LASER POWDER BED FUSION OF LATTICE STRUCTURES FOR THERMOMECHANICAL APPLICATIONS

Sam Catchpole-Smith

This thesis is submitted to the University of Nottingham for the degree of Doctor of Philosophy (PhD)

March 2020

For my grandad,

Phil

ABSTRACT

Laser powder bed fusion (LPBF) is increasingly being adopted in high-value industries such as aerospace because of its design freedoms. An example of LPBF design freedom is incorporation of lattice structures within components. These structures exist in forms including strut-type, consisting of beam elements connected at nodes, and mathematically defined surface-based geometries, where triply periodic minimal surface (TPMS) lattices are found. Strut-type lattices have already found application in end-use components where they are typically used to reduce component mass due to their high specific strength properties. Lattice structures also show promise in heat transfer applications, but there is a lack of research in evaluating performance in this area.

This thesis explores the path taken to manufacture and evaluate lattice structures manufactured via LPBF, including process development for nickel-based superalloys that are desirable in the gas turbine industry. Materials for LPBF are limited by high thermal gradients that are experienced during the process. Fractal scan strategies aiming to reduce thermal gradients were demonstrated in LPBF. This achieved a reduction in cracking of the nickel-based superalloy CM247LC. Although not successful in complete crack mitigation, the study suggested that thermal gradients in LPBF can be altered using alternative scan strategies. This finding may be extended to other alloys that are currently not processable via LPBF.

A range of lattice structures manufactured in Hastelloy-X (HX) via LPBF were evaluated for compressive performance in the as-LPBF and heat-treated conditions. It was demonstrated that TPMS lattice structures exceed the strength and modulus of strut-type geometries in every case. Further, heat treatment resulted in up to 20 % decrease in lattice modulus and 50 % decrease in lattice yield strength. This was linked to the increase in grain size observed after heat treatment. The HX lattices exhibited ductile structural compression throughout, except for a single geometry in which fracture failure of the

lattice elements was observed. The failure sites were investigated using X-ray computed tomography, where shear was identified as the primary failure mode.

Custom thermal evaluation apparatus were developed, providing a capability for determining thermal conductivity and convective heat transfer performance of lattice structures. Experimentation deduced that the bulk material thermal conductivity has the primary effect on lattice thermal conductivity, with some secondary effects from natural convection that are related to the sample geometry. Design equations were developed for lattice thermal conductivity and demonstrated through manufacture and testing of samples with a specific thermal conductivity. Further, volume fraction grading was used to manufacture a lattice structure sample with a custom thermal profile in 2-dimensions.

The convective heat transfer apparatus was used to evaluate TPMS lattice structures for pressure drop and convective performance. TPMS geometries showed enhanced convective heat transfer over a pin-fin benchmark in every flow condition, particularly for applications where high pressure drop is acceptable if heat transfer is maximised. Therefore, such geometries are suitable for gas turbine component applications such as turbine blades or nozzle guide vanes, where a coolant fluid pressure drop of 3 – 5 bar is available. Calculation of thermal performance curves for each geometry provides the data in a format that is required by design engineers to implement lattice structures.

This investigation has, therefore, advanced the understanding and applicability of lattice structures under mechanical, thermal or thermomechanical applications across a range of industries. Case studies were used to demonstrate this enhanced performance through use of lattice structures in a real use application.

ACKNOWLEDGEMENTS

First and foremost, I would like to thank my family for always letting me choose my own path in life and giving me the support I need regardless of what those choices might be, in the past and the future. For a family that had never experienced the world of university, it was probably quite puzzling when I decided to dodge a 'real job' for a further 4 years after graduation and start a PhD! But they never questioned my choices and I hope I have made you proud. Thank you for understanding my mind-set and just letting me 'get on with it' – I really appreciate you for this, and I hope you know I couldn't have asked for any more from you.

Thanks to my supervisor, Adam Clare, who believed in me throughout the PhD and again mostly just let me get on with it! In the five years I have known you, your brilliant and sometimes wacky ideas have kept me thinking outside of the box when I needed it the most. The team Adam has assembled in ACEL is truly first-class. Alex Jackson-Crisp, tech-wizard, deserves special mention for spinning multiple machine-tool shaped plates simultaneously, as well as being there for some great chats when my vision has turned pixelated and 16:9 ratio from staring at Word for too long! If I was the Dean of Engineering, I'd give you an honorary PhD.

Mark and Mark of CfAM, thanks to them for letting me loose on equipment as and when I needed. Mark Hardy in particular who trusted me in things that would probably make him feint if he saw somebody else doing. Being hands-on is very important to me and having the trust of technical staff is invaluable.

Finally, thanks to my industrial sponsor, Siemens Industrial Turbomachinery, Lincoln for the funding for this work. Having access to world class facilities and consumables has been invaluable. The apparatus and samples in this thesis wouldn't have been possible without the extra funding they provided. Special thanks to Tony Davis who

took me under his wing during my brief internship at the company. You clearly have a depth of knowledge that I could only hope to absorb over the next few decades.

LIST OF PUBLICATIONS AND CONFERENCES

PUBLICATIONS IN PRESS:

- **Catchpole-Smith, S.**, Aboulkhair, N., Parry, L., Tuck, C., Ashcroft, I. A., & Clare, A. T. (2017). *Fractal scan strategies for selective laser melting of 'unweldable'nickel superalloys*. Additive Manufacturing, 15, 113-122.
- **Catchpole-Smith, S.**, Sélo, R. R. J., Davis, A. W., Ashcroft, I. A., Tuck, C. J., & Clare, A. T. (2019). *Thermal Conductivity of TPMS Lattice Structures Manufactured via Laser Powder Bed Fusion*. Additive Manufacturing, 100846.

CONFERENCE PRESENTATIONS AND PROCEEDINGS:

- Solid Freedom Fabrication Symposium (SFF) 2015, Austin, Texas, USA, August 10th – 12th 2015. Talk: *Fractal scan strategies for selective laser melting of 'unweldable' nickel superalloys*, **Catchpole-Smith, S.,** & Clare, A. T.
- Additive Manufacturing and Powder Metallurgy (AMPM) 2019, Phoenix, Arizona, USA, June 23rd – 26th, 2019. Talk and proceedings: *Application of Additively Manufactured Lattice Structures for Convective Heat Transfer*, **Catchpole-Smith, S.,** & Clare, A. T.

AWARDS:

- 3rd place in Innovation category, EPSRC Photography Competition, 2018. Title: *Building blocks for a lighter future*, **Catchpole-Smith, S.**

CONTENTS

1 INTRODUCTION 1

1.1 AIMS AND OBJECTIVES 4

1.2 OUTLINE OF THE THESIS 6

2 LITERATURE REVIEW 8

2.1 INTRODUCTION 9

2.2 LASER POWDER BED FUSION 9

2.2.1 LPBF in the gas turbine industry 13

2.3 NICKEL-BASED SUPERALLOYS FOR LPBF 16

2.3.1 Superalloy chemistry and microstructure 16

2.3.2 CM247LC 19

2.3.3 Hastelloy-X 21

2.3.4 Scan strategies for LPBF manufacture of nickel superalloys 24

2.4 LATTICE, POROUS AND CELLULAR STRUCTURES 27

2.4.1 TPMS lattice structures 29

2.4.2 Mechanical properties of lattice structures 30

2.4.3 Porous structures summary 34

2.5 APPARATUS FOR DETERMINING HEAT TRANSFER PROPERTIES 34

2.5.1 1-dimensional conductive heat transfer 35

2.5.2 Convective heat transfer 38

2.6 COMPONENT DESIGN FOR HEAT TRANSFER 41

2.6.1 Conventional heat transfer structures 42

2.6.2 Conventionally manufactured porous structures as heat transfer devices 43

2.6.3 Additively manufactured heat transfer structures 46

2.6.4 Industry-specific heat transfer applications *49*

2.7 THE RESEARCH GAP 53

3 METHODOLOGY 56

3.1 INTRODUCTION 57

3.2 FEEDSTOCK POWDER CHARACTERISATION 57

3.2.1 Particle size distribution *57*

3.2.2 Chemical composition *58*

3.3 LASER POWDER BED FUSION MANUFACTURE 58

3.3.1 Software pre-processing *58*

3.3.2 Support generation *60*

3.3.3 Lattice structure specific support requirements *61*

3.3.4 Slicing and applying process parameters *63*

3.3.5 LPBF machine procedure *64*

3.4 METALLOGRAPHIC TECHNIQUES 65

3.4.1 Metallographic sample preparation *65*

3.4.2 Metallographic grinding and polishing *66*

3.4.3 Etching to reveal microstructure *68*

3.5 SAMPLE CHARACTERISATION 69

3.5.1 Optical microscopy (OM) *69*

3.5.2 Scanning electron microscopy (SEM) *71*

3.5.3 Energy dispersive X-ray spectroscopy (EDS) *72*

3.6 MECHANICAL TESTING 73

3.6.1 Micro-hardness testing *73*

3.6.2 Compressive testing *73*

4 MATERIAL AND PROCESS EVALUATION FOR MANUFACTURE OF LATTICE STRUCTURES 74

4.1 INTRODUCTION 75

4.2 MATERIAL CHARACTERISATION 77

CM247LC *77*

4.2.1 feedstock powder characterisation *77*

Hastelloy-X f *80*

4.2.2 eedstock powder characterisation *80*

4.3 CM247LC PROCESS DEVELOPMENT 82

4.3.1 Steps towards reduction of cracking *82*

4.3.2 Scan Strategies and Manufacture *83*

4.4 CRACK REDUCTION RESULTS AND DISCUSSION 86

4.4.1 Crack locations and morphology *86*

4.4.2 Microstructure and cracking mechanisms *92*

4.4.3 Quantitative crack analysis *97*

4.4.4 Fractal scans for manufacture *101*

4.4.5 Failure in process and material *102*

4.5 HASTELLOY-X PROCESS CHARACTERISATION 104

4.5.1 Bulk density *105*

4.5.2 Microstructure *106*

4.5.3 Sample surface characterisation *111*

4.6 CONCLUSIONS 120

5 EVALUATING MECHANICAL PERFORMANCE OF LATTICE STRUCTURES 121

5.1 INTRODUCTION 122

5.2 MICRO HARDNESS 123

5.3 COMPRESSIVE PERFORMANCE 125

5.3.1 Bulk sample compressive testing *125*

5.3.2 Lattice Structure Samples *127*

5.4 CONCLUSIONS 148

6 A NEW APPROACH TO EVALUATION OF LATTICE THERMAL PERFORMANCE 150

6.1 INTRODUCTION 151

6.2 THERMAL CONDUCTIVITY TESTING 153

6.2.1 Apparatus Design and Operation *153*

6.2.2 Calculation of Thermal Conductivity *155*

6.2.3 Uncertainty Analysis *156*

6.3 CONVECTIVE HEAT TRANSFER TESTING APPARATUS 157

6.3.1 Specimen Design *157*

6.3.2 The Testing Apparatus *159*

6.3.3 Data capture *161*

6.3.4 Testing methodology *162*

6.3.5 Data Processing and Calculations *165*

6.4 SUMMARY 168

7 EVALUATING THE THERMAL CONDUCTIVITY OF LATTICE STRUCTURES 169

7.1 INTRODUCTION 170

7.2 UNIT CELLS UNDER INVESTIGATION 171

7.3 GEOMETRIC PROPERTIES OF THE SAMPLES 172

7.4 SAMPLE PREPARATION AND TESTING 174

7.5 RESULTS AND DISCUSSION 174

7.5.1 Solid samples *174*

7.5.2 Lattice structure samples *175*

7.6 DEVELOPMENT OF SAMPLES WITH GRADED THERMAL CONDUCTIVITY 184

7.7 CONCLUSIONS 189

8 ENHANCING CONVECTIVE HEAT TRANSFER USING LATTICE STRUCTURES 191

8.1 INTRODUCTION 192

8.2 EXPERIMENTAL SETUP 193

8.2.1 Lattice structures under investigation 193

8.2.2 Pin-fin benchmark sample 195

8.3 EXPERIMENTAL RESULTS 196

8.3.1 Pressure drop – AlSi10Mg 196

8.3.2 Heat transfer performance – AlSi10Mg 202

8.3.3 Thermal performance indices – AlSi10Mg 205

8.4 HASTELLOY-X LATTICE CHARACTERISATION 210

8.4.1 Pressure drop – Hastelloy-X 210

8.4.2 Heat transfer performance – Hastelloy-X 213

8.4.3 Thermal performance index - TP_{norm} 214

8.4.4 Thermal performance index TP_{mod} 216

8.5 CONCLUSIONS 219

9 APPLICATION OF LATTICE STRUCTURES FOR HEAT TRANSFER 221

9.1 INTRODUCTION 222

9.2 APPLICATION CASE-STUDIES 223

9.2.1 Lightweight, small-package heatsink for electronic chips 223

9.2.2 Gas turbine nozzle guide vane with modified internal cooling 230

9.3 CONCLUSIONS 233

10 CONCLUSIONS AND FUTURE WORK 234

10.1 FINAL CONCLUSIONS 235

10.2 FUTURE WORK 239

REFERENCES **243**

APPENDIX **263**

SECTION 1 – CONDUCTIVE HEAT TRANSFER APPARATUS 264

SECTION 2 – CONVECTIVE HEAT TRANSFER APPARATUS 271

LIST OF TABLES

Table 2.1 - List of Ni-based superalloy alloying elements and their function 17

Table 2.2 - Periodic trigonometric functions for the TPMS lattice structures under investigation in this thesis. 30

Table 3.1 - Process parameter options in the LPBF software with examples given where applicable. 63

Table 3.2 - Steps taken to grind and polish a sample for metallographic inspection. Different routes are taken depending on whether manual or semi-automated sample preparation methods are used. The grit sizes and equivalent micron-sizes are given along with any special grinding or polishing disc required 67

Table 3.3 - Metallographic etchants used to reveal microstructure for the alloys featured in this thesis. The name and composition of the etchant is provided 68

Table 4.1 - Elemental composition of the CM247LC powder supplied by LPW compared to the nominal composition specified for the alloy [66] 79

Table 4.2 - Elemental composition of the Hastelloy-X powder supplied by Oerlikon compared to the nominal composition specified for the alloy 80

Table 4.3 - Parameter combinations (laser power and laser scan speed) used to produce a total of 16 fractal scan samples (eight Hilbert and eight Peano-Gosper)..... 85

Table 4.4 - Bulk density of the Hastelloy-X in each condition of supply as measured using image analysis. 105

Table 4.5 - Surface roughness characteristics for the Hastelloy-X as-LPBF XY plane (top surface) as measured using focus variation microscopy 116

Table 4.6 - Surface roughness parameters for the Hastelloy-X as-LPBF and HIP + HT YZ plane (side surface) as measured using focus variation microscopy. 118

Table 4.7 – Surface roughness parameters for the AlSi10Mg as-LPBF YZ plane (side surface) as measured using focus variation microscopy. 120

Table 5.1 - Hardness data for HX at each condition of supply, giving mean, minimum, maximum and standard deviation results. 124

Table 5.2 - Unit cell types and cell sizes under investigation. 'X' denotes sample is included in the compressive testing. 127

Table 7.1 - Parameters used for the manufacture of a total of 18 lattice test samples .. 172

Table 7.2 - Surface area and volume data for each lattice sample tested based upon the computer models. Note the large variation in surface area to volume ratio between the unit cell types, giving rise to the differences in conductivity seen in Figure 7.3 177

Table 7.3 - Curve fitting parameters for the linear equations relating apparent thermal conductivity to actual volume fraction for each of the unit cell types 179

Table 7.4 - Design parameters and experimental test data for the three target thermal conductivity lattice samples manufactured in Hastelloy-X. 180

Table 9.1 - Properties of the GPU heatsinks analysed here. Note the difference in mass and volume between the stock and lattice heatsinks 225

LIST OF FIGURES

Figure 1.1 - Chart detailing the order of Chapters in this thesis. 7

Figure 2.1 - Schematic of the laser power bed fusion machine (a) with the process for melting of a single layer in the build process (b). 10

Figure 2.2 – (a) LPBF manufactured fuel nozzle by GE, achieving a 20 – 1 component consolidation and a 25 % reduction in mass (b) LPBF manufactured gas turbine blade by Siemens Industrial Turbomachinery Ltd. Validated at full-load conditions of 13,000 rpm and 1,250 °C for 100 hours. 14

Figure 2.3 – Burner tip repair via LPBF by Siemens Industrial Turbomachinery Ltd using a modified EOS M290 machine. 15

Figure 2.4 - 'Weldability' diagram for a range of Ni alloys as a function of their Ti and Al alloy element composition. Weldability is considered poor above the dashed line and deteriorates with increasing Ti and Al content. CM247LC is found above this weldability line whilst Hastelloy-X is found in the lower ‘weldable’ region. All data taken from associated alloy specification documents [4, 66, 69-72]. 20

Figure 2.5 - After a crack is closed by HIP (a), particulates segregated at the closed crack boundary (b) can form stress concentration points, leading to the crack re-opening (c) and propagating along the weakly bonded crack boundary (d). 21

Figure 2.6 – Illustration of the 10 x 10 mm island scan strategy. Initially, a single wall thickness contour scan is performed followed by the raster scans to form four 5x5 mm ‘islands’ 24

Figure 2.7 - Hilbert (a) and Peano-Gosper (b) fractal patterns used for LPBF. Start and end points indicated. 26

Figure 2.8 - Tree diagram of types of cellular solids. This thesis concentrates on non-stochastic 3D lattice structures. Images taken from Gibson et al. 28

Figure 2.9 - TPMS lattice structures used in this thesis alongside the BCC (strut-type) lattice in the bottom right corner. 30

Figure 2.10 - Ductile compression of IN625 lattice structures with extended plateau stress curve (a) versus staged brittle fracture of AlSi10Mg gyroid lattice with distinct rippled stress-strain plot (b). 32

Figure 2.11 - Thermal conductivity measurement standards applicable to measurement of lattice structures. C158-17 appears simpler but requires two expensive heat flux meters. E1225-13 is simpler in operation. 37

Figure 2.12 - A selection of apparatus layouts taken from the literature. (a) Kirsch et al., (b) Marques et al., (c) Wong et al., (d) Tian et al. 40

Figure 2.13 - A selection of heat exchangers using conventional manufacturing methods. 45

Figure 2.14 – (a) LPBF manufactured pin-fin heatsink by Kirsh et al. and (b) LPBF manufactured strut-type lattice heatsink by Wong et al. 48

Figure 2.15 - Cooling strategies for a gas turbine blade (NGV cooling uses similar features). Ribs and pin-fins used for enhancing heat transfer may be replaced by lattice structures. Image taken from [175]. 52

Figure 2.16 - A demonstration of the use of fluid-fluid heat exchangers in the CANDU nuclear reactor, including one closed-loop system (a) and one open-loop system (b). 52

Figure 3.1 - Illustration of the effect of .stl triangle size (resolution). If too low of a resolution is used, smooth curved surfaces will be rendered as facets (a) and build

quality and dimensional accuracy will be degraded. A correct resolution results in smooth curved surfaces (b). 59

Figure 3.2 - Block supports generated in Magics, with and without border teeth. Removing border teeth aids part adhesion with the build platform. 61

Figure 3.3 - Lattice structures that require additional supports. (a) Small cylinders are added to attach the overhanging feature to the build plate for the gyroid network geometry. The same sample as built (b). In (c), the supports were not added, resulting in build interruption (d). 62

Figure 3.4 - Illustration of the XY and YZ sections cut from a LPBF sample for bulk density and microstructural analysis. 66

Figure 3.5 - Sequence for crack and pore filtering using image processing software ImageJ. A threshold is applied to the raw image leaving only the pores and cracks in black against a white background. Despeckle is used to remove any small noise pixels left behind. The cracks and pores are filtered independently by altering parameters for the aspect ratio of thresholded features. 70

Figure 3.6 - Interaction between the high-energy electron beam of an SEM and the sample surface. The depths from the sample surface at which secondary electrons, backscattered electrons and characteristic X-ray signals are released are given. ... 71

Figure 4.1 - a) CM247LC laser diffraction powder size distribution histogram, b) 200X SEM micrograph showing the distribution of particle sizes and c) 1000X SEM micrograph showing largely spherical particles but with some satellites and irregular shapes. 78

Figure 4.2 - a) Hastelloy-X laser diffraction powder size distribution histogram, b) 200X SEM micrograph showing the distribution of particle sizes and c) 1000X SEM

micrograph showing higher overall sphericity than the CM247LC powder, fewer particles with satellites and minimal conjoined particles.....81

Figure 4.3 - Illustration of the novel scan strategies generated using the (a) 3rd order Hilbert and (b) 2nd order Peano-Gosper mathematical area filling curves. The 100 µm characteristic scan vector length is shown. Approximate weld track thickness is shown in blue on the Hilbert fractal path (a). 84

Figure 4.4 - Identification of the increased cracking and porosity regions in the island intersections. Note that the cracking has a distinct directionality at 0 ° and 90 ° to the island borders, aligned with the laser scan vectors. 86

Figure 4.5 - Optical micrographs showing the cracking in a range of Hilbert samples. Highest density achieved at 100 W 600 mm.s^{-1} (c) and lowest density at 75 W 500 mm.s^{-1} (a). CO = crack origin; note the very similar placement of cracking for each fractal scan type. 87

Figure 4.6 - Optical micrographs showing the cracking in a range of Peano-Gosper samples. Highest density achieved at 75 W 600 mm.s^{-1} (a) and lowest density at 100 W 500 mm.s^{-1} (c). CO = crack origin; note the very similar placement of cracking for each fractal scan type. 88

Figure 4.7 - (a) Hilbert [100W, 600mm.s^{-1}] and (b) Peano-Gosper [75W, 600mm.s^{-1}] scanning strategies approximately overlaid on to the deposits formed via SLM. Note that the cracking does not seem to follow the scan vectors as with the long vector length samples. 89

Figure 4.8 - Illustration of the mechanism causing cracking to appear in the same regions for each fractal samples (Peano-Gosper used in this case). The scan area is completed in regions in the order given in (a). After each region completes, it shrinks during

cooling (b). This forms preferential paths for crack growth between the scan regions (c). 91

Figure 4.9 - Illustration of solidification cracking in welding, where cracking propagates through the liquid phase of the partially solidified weld pool. Figure taken from Ploshikhin et al. 93

Figure 4.10 - Backscatter electron micrographs in the XY plane of the Hilbert 100W 600mm.s^{-1} sample showing: (a) bi-directional crack origin at intersection between fine and coarse equiaxed grains; (b) high angle cracking with (inset c) some sub-micron size precipitates identified along the crack surface 94

Figure 4.11 - EDS line scan of the island scan sample showing elemental distributions across the crack surfaces. Note the lack of elemental peaks that would signify the presence of thin films at the crack boundaries. 95

Figure 4.12 - Backscatter electron micrograph of the YZ plane of the island scan sample showing: (a) the melt pool shape in red giving rise to coarse columnar grains in the core and finer, equiaxed grains at the boundary; (b) a crack following the line of intersection between a fine, equiaxed grains and coarse, columnar grains; (c) columnar dendrite surface exposed by the solidification cracking mechanism 96

Figure 4.13 - Bulk density data for the samples in the XY plane (left) and YZ plane (right). The island sample is represented in grey whilst the Hilbert and Peano-Gosper are in blue and red, respectively. Each pair of columns constitutes a single process parameter set, identified on the x-axis labels. 98

Figure 4.14 - Crack length density data for the island (grey), Hilbert (blue) and Peano-Gosper (red) scan strategies 99

Figure 4.15 - Crack area density data for the island (grey), Hilbert (blue) and Peano-Gosper (red) scan strategies. 101

Figure 4.16 - OM micrographs of the HX XY plane in as-LPBF and HIP + HT conditions. Porosity is clearly visible before HIP treatment with some larger pores highlighted with arrows. 106

Figure 4.17 - Etched microstructures of YZ plane for the HX in as-LPBF (a), (b), HIP (c), (d) and HIP + HT conditions (e), (f). Note the fine grain structure of as-LPBF (b) is coarsened after HIP (d), and the grain boundary thickness is reduced after HT (f). 107

Figure 4.18 - SEM micrographs of the HX YZ plane in as-LPBF (a), (b), (c) and HIP + HT (d), (e) conditions. Melt-pool boundary (a) and grain boundary precipitates shown in (b) with arrows. Note the change in size and shape of the grains after HT. 108

Figure 4.19 – Etched microstructures of XY plane for the HX in as-LPBF (a), (b), HIP (c), (d) and HIP + HT conditions (e), (f). Note the melt pools visible in (a), and the change in microstructure through HIP and HT, particularly the shift to blocky grains after HT (c). 110

Figure 4.20 - SEM micrographs of the XY plane (top surface) of the HX sample at 40X (a) and 200X (b) magnification. The double contour scan is clearly visible in (b). 112

Figure 4.21 - Focus variation microscopy image of the HX sample XY plane (top surface) detailing the raised edges and corner due to the contour scan strategy. A line scan across plane B-B (c) shows this variation, with in increase in height of approximately 75 µm at the sample edge. 114

Figure 4.22 - Focus variation microscopy image showing false colour height maps of the HX sample XY plane (a) and (b), and a line profile across section A-A (c) to demonstrate the waviness inherent to LPBF.....115

Figure 4.23 - Focus variation microscopy images of the YZ plane of Hastelloy-X in as-LPBF (a), (b) and HIP + HT (c), (d) conditions. The isometric view in (a) shows a larger proportion of high areas (pink), with some flat regions that occurred during post-processing. 117

Figure 4.24 - Focus variation microscopy false-colour images of the AlSi10Mg YZ plane. 119

Figure 5.1 – Micro-hardness grid results displayed as colour contour plots. HX material in (a) as-LPBF, (b) HIP and (c) HIP + HT conditions. Scale bar is common between all plots. Placement of indents on HIP + HT sample shown in (d).....123

Figure 5.2 - Stress-strain curves for the Hastelloy-X solid samples, used to evaluate the bulk mechanical properties. The as-LPBF sample exceeded the load limit of the testing machine before onset of plastic deformation. 126

Figure 5.3 - Young's modulus values for the bulk samples in both conditions of supply. The modulus of as-LPBF exceeds that of HIP+HT by 5.4 %.....126

Figure 5.4 - Lattice Young's modulus against volume fraction for the full set of samples. As-LPBF are highlighted in red, HIP+HT matrix phase in blue, HIP+HT network phase and BCC in green.....129

Figure 5.5 - Lattice Young's modulus results for the as-LPBF (a) and HIP + HT (b) samples, sorted by ascending volume fraction as shown on the secondary y-axis. 130

Figure 5.6 - Lattice yield strength (0.2 % offset method) against volume fraction for the full set of samples. As-LPBF are highlighted in red, HIP+HT matrix phase in blue, HIP+HT network phase and BCC in green. 132

Figure 5.7 - Lattice yield strength [0.2 % offset] results for the as-LPBF (a) and HIP + HT (b) samples, sorted by ascending volume fraction as shown on the secondary y-axis. 134

Figure 5.8 - Specific lattice mechanical properties for the full sample set. Highest performance is found in the upper-right corner of the plot. 136

Figure 5.9 - Stress-strain plots for each of the as-LPBF 0.2 10 m cell size lattice samples. All data beyond 50 % lattice strain is truncated. Similar loading response is observed across all unit cell types and sizes. No evidence of sudden failure typical of cracking can be seen. 137

Figure 5.10 - Images captured during compressive testing at lattice strain values of 0 % - 50 %. Sample name is given on the left side of each row. The failure mode of the SCH P unit cell is bending, whilst buckling failure dominates for the GYR M unit cell. The DIA N buckles and layers collapse along a 45 ° plane. The BCC struts bend with the nodes acting as pivot points. 139

Figure 5.11 - Stress-strain plots for a selection of the HIP+HT lattice samples. All data beyond 50 % lattice strain is truncated. Structural failure of the DIA N 3.3 sample occurs in stages up to 40 % lattice strain (a). At 47 % lattice strain (b), the structure undergoes a significant failure leading to a large drop in applied stress. 140

Figure 5.12 - X-ray µCT scans of the DIA N 3.3 sample showing (a) a slice in the top view and (b) an enlarged region with numerous fracture sites highlighted. 3D reconstruction of a fracture site (c) and (d) demonstrates the failure location within the DIA N geometry. 142

Figure 5.13 - X-ray μCT scans of the DIA N 3.3 sample from the side view (a) showing an enlarged view of further sites of failure (b) and 3D representation of the shear failure (c). 143

Figure 5.14 - Lattice Young's modulus results for the as-LPBF 0.5 volume fraction samples sorted by ascending volume fraction as shown on the secondary y-axis. 144

Figure 5.15 - Lattice yield strength [0.2 % offset] results for the as-LPBF 0.5 volume fraction samples sorted by ascending volume fraction as shown on the secondary y-axis 145

Figure 5.16 - Images captured during compressive testing of the as-LPBF 0.5 volume fraction samples at lattice strain values of 0 % - 50 %. Sample name is given on the left side of each row. 146

Figure 5.17 - Specific lattice mechanical properties for the full sample set including as-LPBF 0.5 volume fraction. 0.2 volume fraction samples are shaded in grey. 147

Figure 6.1 – (a) Schematic of the thermal conductivity testing apparatus used to measure the thermal conductivity of the lattice samples using the ASTM E1225-13 comparative-longitudinal heat flow technique. (b) Enlarged view of the test stack indicating the position of the measurements taken for the calculation of apparent thermal conductivity of the sample 154

Figure 6.2 - Dimensions of the sample used in the convective heat transfer testing rig. The sandwich design places a 1 mm skin on the top and bottom of the 'region of interest', shown in blue; the cooling air is forced through the centre of the sandwich structure along the x- and y-direction. 158

Figure 6.3 - Exploded view of the main body of the test apparatus showing the assembly of the sample within the test stack and the position of the pressure transducers along the flow direction. The components are named in the attached table. 160

Figure 6.4 - Flow chart showing the method of data acquisition and processing for the convective heat transfer experiments. 163

Figure 7.1 - Single unit-cell models with lattice dimensions [1, 1, 1] for each of the three unit-cell types used in this study. 171

Figure 7.2 - Thermal conductivity of Hastelloy-X bulk material across the temperature range 25 - 120 °C as taken from the material data sheet [185], with the measured conductivity of the as-LPBF HX sample shown. 7 % error shown. 175

Figure 7.3 - Apparent thermal conductivity against actual volume fraction for all Hastelloy-X lattices. The unit cell type is denoted, but the cell size is ignored for this plot. The star markers are the results of the 'specified conductivity' test. Error bars consistent with 7 %. 176

Figure 7.4 - Normalised conductivity vs cell size for Hastelloy-X lattice samples with (a) 0.2 volume fraction and (b) 0.5 volume fraction. 181

Figure 7.5 - An illustration of the change in wall thickness across different unit cell sizes despite a constant volume fraction (0.2 in this case). 183

Figure 7.6 - Demonstration of 1D functional grading of Hastelloy-X lattice structures to sweep through a prescribed range of apparent thermal conductivities through variation of volume fraction following (a) a simple gradient and (b) a cosine squared gradient. 185

Figure 7.7 - A demonstration of 2D functional grading of Hastelloy-X lattice structures based on the $\sin(x^2 + y^2)^{-1}$ function, showing prescribed apparent thermal

conductivity within the range 1.875 - 4.5 $W.m^{-1}.K^{-1}$). On the left is the digital model of the lattice structure generated and the 2D volume fraction map is shown on the right. 186

Figure 7.8 - University of Nottingham logo and text embedded into a lattice sample using variation in volume fraction. The .stl file can be seen in (a) along with the manufactured sample in (b) after spraying matt black. The logo is barely visible to the naked eye until it is heated and the variation in temperature due to the volume fraction grading is captured with an infrared camera, (c). Temperatures shown in °C. 188

Figure 8.1 - Full set of unit cells under investigation in this study. One unit cell is shown per column, with the isometric view on the top row and the frontal view as seen by the fluid flow on the bottom row. Each represents a 10 x 10 x 10 mm section with 5 mm unit cell size. Surface area to volume ratio (SA:vol) is given in the bar charts and relates to the volume of solid material within each cell. 194

Figure 8.2 - Geometry data for the pin-fin benchmark coupon with spanwise spacing S_s = 5 mm, streamwise spacing S_x = 5 mm, pin diameter D = 2 mm and pin length L = 10 mm. This provides a ratio L/D = 5. This layout can be seen in 3D on the right-hand side (top wall removed for clarity). 195

Figure 8.3 - Friction factor augmentation (f/f_0) across the Reynolds number range for all matrix phase lattice samples. Note the negative correlation between cell size and friction factor augmentation. 197

Figure 8.4 - Friction factor augmentation (f/f_0) at Re = 20,000 for the GYR M and DIA M 2.5 mm and 10 mm cells only. This demonstrates the effect on frictional losses as cell size is decreased. 198

Figure 8.5 - Illustration of the change in boundary layer area (red) and free flow area (blue) when moving from 10 mm (a) to 2.5 mm (b) cell size. 199

Figure 8.6 - Friction factor augmentation (f/f_0) across the Reynolds number range for all network phase lattice samples. Colours refer to unit cell type, marker fill refers to cell size. Note the improved frictional losses compared to the matrix phase (Figure 8.3). 200

Figure 8.7 - Friction factor augmentation (f/f_0) at Re = 20,000 comparing the performance of the matrix phase against network phase for the GYR and DIA unit cell type at 5 mm cell size. 201

Figure 8.8 - Nusselt number for all lattice samples tested across the full Reynolds range. The minimum and maximum Nu of 300 and 7000 respectively demonstrates the wide range of operation possible using lattice heat exchange geometries. 202

Figure 8.9 - Nusselt number augmentation plots for the matrix phase lattice samples across all unit cell sizes 204

Figure 8.10 - Nusselt number augmentation for the network phase lattice structure samples across all cell sizes 205

Figure 8.11 - Thermal performance metric TP_{norm} [Nu/f] against Reynolds number for the matrix phase (top) and network phase (bottom) lattice structure samples. Note the modest performance increase between the lattice samples and the pin-fin benchmark using this performance metric. 207

Figure 8.12 - Thermal performance metric TP_{mod} against Reynolds number for the matrix phase (top) and network phase (bottom) lattice structure samples. Note the relatively flat relationship between performance and Re using this metric. 209

Figure 8.13 - Friction factor augmentation (f/f_0) across the Reynolds number range for all Hastelloy-X samples. Note the negative correlation between cell size and friction factor augmentation. 211

Figure 8.14 - Comparison of friction factor augmentation between HX and AlSi10Mg for the GYR M 5 mm and DIA N 5 mm samples. All data taken at Re = 20,000..... 212

Figure 8.15 - Nusselt number augmentation for all HX samples across the full Re range. 213

Figure 8.16 - Thermal performance metric TP_{norm} [Nu/f] against Reynolds number for the HX lattice structure samples. 215

Figure 8.17 - Comparison of thermal performance index TP_{norm} between HX and AlSi10Mg for the DIA M 5 mm and GYR N 5 mm samples. All data taken at Re = 20,000..... 216

Figure 8.18 - Thermal performance metric TP_{mod} against Reynolds number for the HX lattice structure samples. 217

Figure 8.19 - Comparison of thermal performance index TP_{mod} between HX and AlSi10Mg for the GYR M 5 mm and DIA N 2.5 mm samples. All data taken at Re = 20,000 218

Figure 9.1 - The stock GPU heatsink with 2x fans for forced convection. Heat pipes draw heat away from the GPU which is in contact with the GPU surface plate. Heat transfer efficiency is impeded by the lack of metallurgical bond between the fins (a) and between the heat pipes and surface plate (b). 224

Figure 9.2 - Illustration of the lattice GPU heatsink design. A gyroid matrix lattice is used with a graded volume fraction in the Z-direction, from 30% at the hot surface to 15%

at the top. Compressed air is supplied from a single inlet and travels across the heatsink in the X-direction. 226

Figure 9.3 - AlSi10Mg lattice GPU heatsinks after manufacture via LPBF (a), (b). The heatsink as installed in place on the GPU is shown in (c). The small volume occupied by the heatsink is evident when compared to the stock heatsink. 227

Figure 9.4 - Temperature vs. time plots comparing the stock heatsink (blue) to the lattice heatsink (orange) whilst running GiMark and PixMark Piano benchmarking tests. Throughout, ambient temperature is 21 °C. 228

Figure 9.5 - Demonstration nozzle guide vane models: (a) a single wall geometry with a core region filled with diamond network lattice with constant volume fraction; (b) a double wall geometry with gyroid network lattice region sandwiched between the walls; (c) a trailing edge featuring a slot for film cooling. 231

Figure 9.6 - Demonstrator NGV sections manufactured in Inconel 718 superalloy via LPBF. These sections show the capability of incorporating fine lattice features into a high-value component. 232

Figure 9.7 - Demonstration fluid-fluid heat exchanger manufactured in transparent resin via SLA. Dyed water is used to illustrate the separated flow paths. 233

1 INTRODUCTION

Laser powder bed fusion (LPBF) is an additive manufacturing process that is increasingly being implemented across high value industries such as aerospace, with substantial academic research efforts driving to advance the technology further. LPBF is desirable for its design freedoms with the potential for increasing system efficiency, reducing component counts and costs, and minimising development cycle times. Importantly for the gas turbine industry, components with high complexity can be manufactured in expensive and difficult to machine alloys in near-net shape form. As a result, the number of operations from raw material to final part can be minimised, and the proportion of initial raw material weight to final part weight is maximised (known as buy-to-fly ratio in the aerospace industry).

Whilst some benefit can be gained simply by manufacturing updated versions of existing components via LPBF, the true value is gained through application of design for AM (DfAM) principles in the early design phase. This may include part consolidation, reducing wall thickness and removing unnecessary internal volumes, and using topology optimisation software tools to iteratively generate designs to reach a given design goal. One DfAM tool is lattice structures, a family of different geometries, random or structured, that are typically used to reduce component mass. The most interesting of these can only be manufactured via AM. Research and application in end-use components has shown lattice structures to be effective in retaining mechanical performance whilst reducing component mass. In addition to their mechanical advantages, some lattice structures also show promise in heat transfer applications, making them ideal for components under thermomechanical loading.

One challenge in this area is a lack of design software that allows a design engineer to harness lattice structures in a way that is compatible with existing workflows. Many research groups in the AM field have custom software tools that enable incorporation of

lattice structures into simple components, but the flexibility of these tools and compatibility with commercial computer aided design (CAD) packages is not at the level required for industrial applications. New software tools are emerging that bridge this gap, and as a result, the use of lattice structures in end-use components will gather pace.

Beyond the ability to implement lattice structures in software, the challenge remains of understanding and characterising their performance. Mechanical performance is relatively well understood and simple to evaluate for a new structure or material system. However, research into heat transfer applications for LPBF is limited and further narrows when considering lattice structures. If the aforementioned advantages are to be realised, the heat transfer properties must be determined. This is not trivial using computational methods due to the complexity of the lattice structures, particularly convective heat transfer characterisation, for which resource-intensive computational fluid dynamics (CFD) is required. Furthermore, the unique surface properties of LPBF manufactured components means that existing CFD models developed for conventionally machined components with regular, easily defined surface features may not provide accurate results. To overcome this, experimental evaluation of the heat transfer properties must be performed. This can then be used to inform CFD models at a later date, from which detailed component design can be conducted.

This thesis aims to understand the mechanical and thermal performance of a specific sub-set of lattice structures, triply periodic minimal surface (TPMS) structures. Experimental methods will be used to evaluate these properties, revealing the strengths and weaknesses of different geometries. This will allow design engineers to make an informed decision over what components and applications may benefit from lattice structures, and which geometries to use for the maximum performance. As a result, confidence will be gained in the abilities of lattice structures and their use in components under thermomechanical loading will proliferate.

1.1 AIMS AND OBJECTIVES

The aims of this thesis are to improve the understanding of the performance of TPMS lattice structures for application in components under thermomechanical loading. The methods to achieve this are through experimental determination of lattice properties, which will be divided into four main areas:

- Characterisation of lattice mechanical properties. The compressive strength and Young's modulus of TPMS lattice structures will be evaluated. Through selection of a number of unit cell types, cell sizes and volume fractions, the mechanical performance for lattice structures across a large design window can be determined. Further, samples will be evaluated in the HIP + HT condition in order to understand how post-process heat treatments effect the mechanical properties. This is important as practitioners commonly require heat treatments to ensure the alloy microstructure is suitable for creep or fatigue performance. The specific mechanical performance of the lattice structure samples will also be calculated, demonstrating how lattice structures can help meet mass reduction targets whilst retaining mechanical integrity. The data produced from this study will enable the selection of an appropriate lattice unit cell and cell size to meet engineering load requirements.
- Characterising lattice thermal conductivity. Using a custom-built apparatus based on ASTM standards, the apparent thermal conductivity of lattice structure samples will be evaluated. An important distinction is made between thermal conductivity of the solid material that comprises the alloy, and that contributed by the air that occupies the internal volume of the sample. This combination of heat transfer mechanisms is difficult to evaluate via simulation. Design equations will then be developed, and design case-

studies will be described, including the manufacture and testing of a component to demonstrate the ability to create custom thermal conductivity profiles in 2D. Using the design equations specified, it will be possible to specify lattice structures for a range of thermal conductivity functions, from thermal insulation layers or heat shields, through to enhancing thermal conductivity via graded material density.

- Characterising convective heat transfer performance of lattice structures. Forced convection heat exchangers require flow channels to include geometries tailored to enhancing heat transfer. TPMS lattice structures pose as promising replacements for classic geometries such as pin fins. By experimentally characterising the performance of a range of TPMS geometries for this purpose, a new category of heat exchange geometries can be specified that are only possible to manufacture via LPBF. This will demonstrate the potential of LPBF lattice structures for high-performance heat transfer applications.
- Case-study design utilising TPMS lattice structures. Using the performance data acquired, case-study heat exchange components will be developed, exploring new design spaces that are enabled through LPBF. This includes a heatsink for high-power electronics, demonstrating performance parity with existing technologies but at a significantly reduced mass and volume. Further, proposed designs for gas turbine nozzle guide vanes will provide potential solutions for reducing component temperatures within the engine by using lattice structures to enhance heat transfer. Such a design would be a step-change in the design of internal cooling of hot-section gas turbine components, made possible via LPBF.

Additional to the aims for lattice evaluation, attempts are made to reduce the cracking present in an unweldable Ni-alloy by implementing new scan strategies based on fractals or space filling curves. These scan strategies are unlike any other available in commercial LPBF software packages and are designed to homogenise the thermal profile within each built layer during the LPBF process. Such scan strategies have not been shown in LPBF before and offer a unique processing method for application across a range of materials that suffer from high residual stresses after manufacture.

1.2 OUTLINE OF THE THESIS

The overall outline of the thesis is given in Figure 1.1. In the literature review, the current state of the art research in LPBF, and LPBF for the gas turbine industry in particular, is explored. Lattice structure research forms the main focus, with both mechanical and thermal performance research identified. Chapter 3 details the methodology for the processes used in this thesis, including specific requirements for manufacture of lattice structures via LPBF. The results chapters begin at Chapter 4, where process parameter optimisation for an alloy considered unsuitable for LPBF manufacture is described. After failure to achieve acceptable material quality in this alloy, samples of a new alloy were manufactured and analysed for porosity, microstructure and surface properties. In Chapter 5, the compressive strength and Young's modulus for lattice structure samples manufactured via LPBF was determined. Chapter 6 describes the design and manufacture of two custom thermal property evaluation apparatus: one for 1D thermal conductivity measurement, and a second for determining convective heat transfer properties including pressure drop. These apparatus are then used to evaluate the thermal conductivity and convective heat transfer performance of lattice structure samples in Chapters 7 and 8 respectively. In Chapter 9, the performance data obtained previously is used to demonstrate how lattice structures can be implemented into components under

thermomechanical loading. Finally, conclusions are drawn and recommendations for further work are given in Chapter 10.

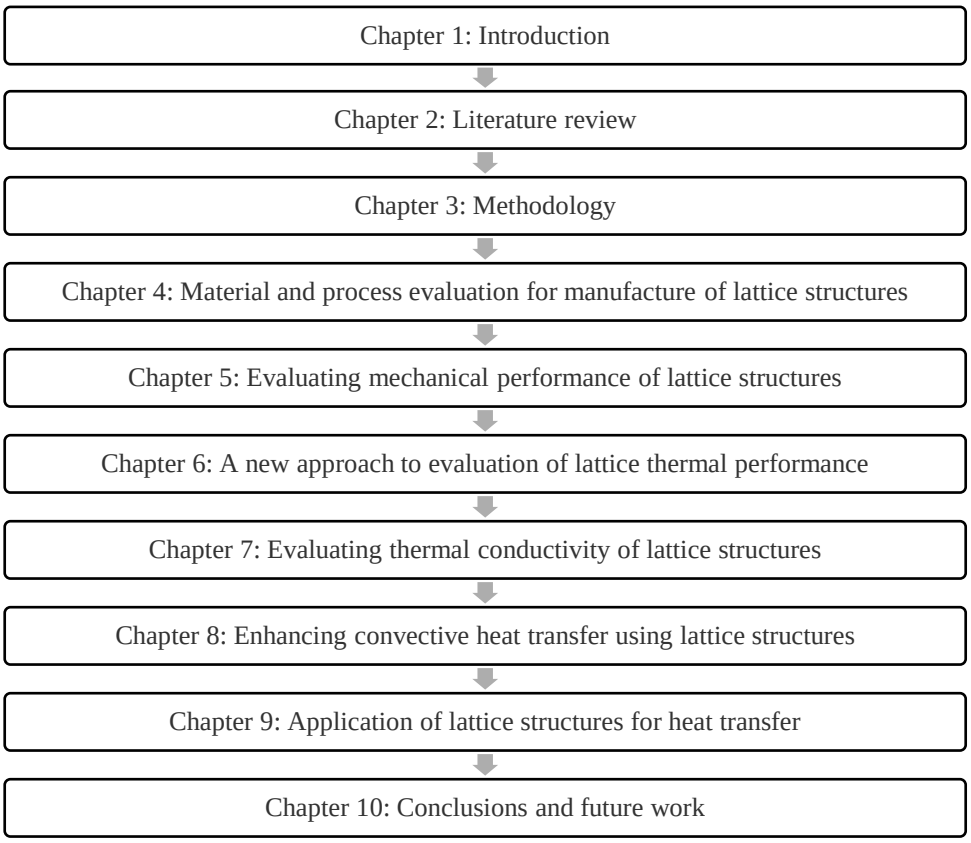


Figure 1.1 - Chart detailing the order of Chapters in this thesis.

2 LITERATURE REVIEW

2.1 INTRODUCTION

This Chapter aims to provide a review of the existing literature, research and industry activity surrounding AM and specifically laser powder bed fusion. It describes the foundation of the LPBF process, its uses in the aerospace industry and the details of two nickel alloys that were used for manufacture of samples throughout this thesis. A background in porous and cellular structures is then provided, with derivation of the sub-family of TPMS structures that were evaluated in later Chapters. Further, it summarises the methods taken by other researchers to determine the thermal characteristics of similar structures and provides a basis from which the apparatus built for this thesis were developed. Finally, it explores the existing methods of enhancing heat transfer for high performance components, including those using conventional manufacturing methods and AM. From this review of existing literature, the research gap is defined.

2.2 LASER POWDER BED FUSION

Laser powder bed fusion (LPBF) is a sub-category of additive manufacturing (AM). It utilises a computer-controlled scanning laser beam to manufacture complex components by melting feedstock powder in a layer-by-layer fashion, direct from a 3D computer model. This feedstock may be a polymer, where the laser partially melts (sinters) the particles together to form a solid [1-4], or a metallic alloy, where the laser energy fully melts the feedstock powder before it cools and consolidates to form the part. While the types of lasers used in these systems vary greatly in type and power, the general machine layout and operating procedure is similar (Figure 2.1 [5]). In this thesis, only metallic LPBF processes will be discussed and hence LPBF will relate to metallic feedstock powders only from hereon. This layer-by-layer method of manufacture enables design freedoms [6-9], not possible in conventional machining methods, that can be

leveraged to add value to components through reducing weight [10, 11], increasing performance, consolidating part counts [12] and reducing manufacturing lead times [13].

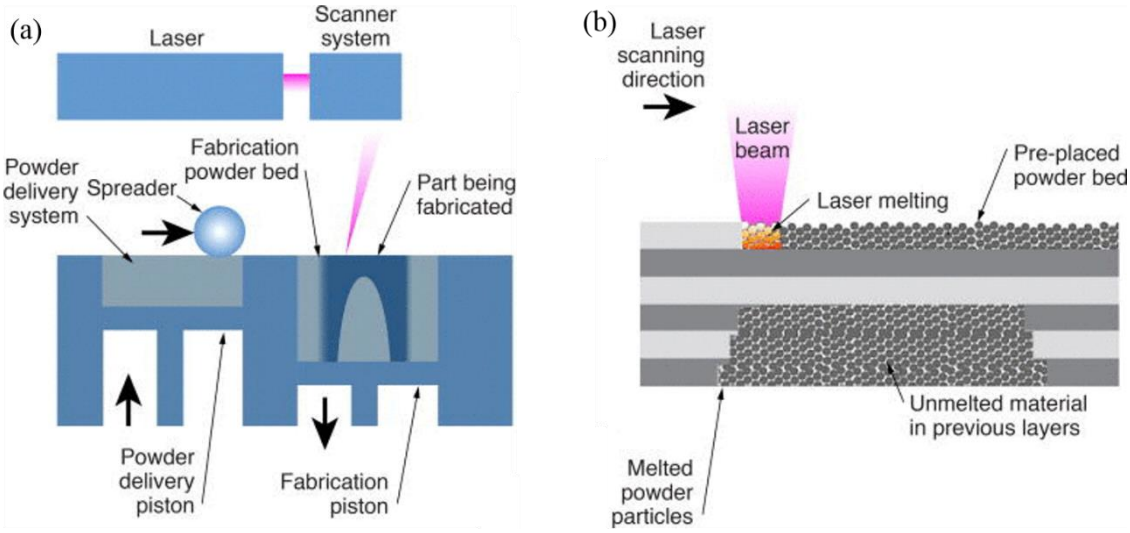


Figure 2.1 - Schematic of the laser power bed fusion machine (a) with the process for melting of a single layer in the build process (b).

The LPBF workflow can be described as seven basic steps [14]:

1. Creation of a digital model
    - Typically using commercial CAD program but many software packages tailored for AM now exist. May include topology optimisation or other simulation-driven modelling.
2. Conversion of CAD model into the Standard Tessellation Language (.stl) [15]
    - Representation of the CAD model surface using a watertight mesh of triangular elements. This is a somewhat legacy file type that has been replaced by certain open-source and proprietary options [16-18], but is still the standard procedure in the industry despite many issues with file errors and bloated file sizes.
3. Set-up of the .stl model in the AM specific software pre-processor

- This includes component orientation and placement in the build volume, along with nesting of multiple components and crucially, definition of support structures for surfaces exceeding a certain angle relative to the build plate (typically 45 °) [19-21].

4. Assignment of process parameters
    - For LPBF, this includes laser power, scan speed, layer thickness, hatch distance and scan strategy amongst others. These will depend upon the material in use and may also change depending on the geometry of the component being built. The .stl file will also be sliced into layers of the defined thickness and the process parameters will be applied, typically being converted into a machine-specific proprietary file format at this stage.
5. Manufacture or build process
    - The stage is common across all layer-by-layer AM processes, but for LPBF constitutes the deposition of a thin layer of alloy powder, followed by exposure to laser irradiation in the cross-section defined in the slice file. A new layer of fresh powder is then spread over the build area and the process repeats.
6. Removal of component from build platform
    - For LPBF, this includes removal of all loose powder and removal of the component from the build platform using wire-EDM (alternatively, a cut-off saw can be used).
7. Post-processing
    - Any support structures are removed here usually manually with hand tools. Depending on the material and finish requirements, heat

treatments and final dimensioning steps may be needed such as CNC or manual machining, grit blasting and polishing.

AM and 3DP have traditionally been seen as prototyping tools, enabling design engineers to move from concept to finalised design more rapidly [22]. Being able to manufacture a functional prototype enables the form, fit and function of a component to be easily evaluated. Whilst some AM processes are still mainly restricted to prototype use, for example fused deposition modelling (FDM) [23-26] and resin stereolithography (SLA) [27-29], LPBF has been used in the manufacture of a wide range of end-use components. Alloys of Ti [30, 31], Fe [32, 33], Ni [34, 35], and Al [36, 37] have been processed via LPBF with near 100% bulk density and good mechanical performance. Therefore, the process is potentially applicable for manufacturing components for virtually any industry providing that the component size fits within the build volume of the LPBF machine.

As the technology matures further, the environments in which LPBF manufactured components operate is becoming more demanding. However, due to the current cost of manufacture via LPBF, it is mostly confined to high-value industries where the performance gains are sufficient to outweigh the increased costs [38]. Such industries include medical and orthopaedic [39, 40], aerospace [41] and gas turbine manufacture, mould and tool manufacture [42, 43] and high-performance automotive [44]. The typically cited barriers to entry of LPBF adoption including high capital and raw material costs[45], limited material selection [46], low productivity of AM systems [47] and lack of AM specific software packages are slowly being eroded by the combined efforts of many industries. As a result, the business case for using LPBF over conventional manufacturing processes is becoming more viable and the market for end-use components will continue to grow.

2.2.1 LPBF IN THE GAS TURBINE INDUSTRY

In this section, a brief overview of the use of LPBF for the aerospace industry, and more specifically gas turbine engines. Gas turbine operating conditions place high mechanical and thermodynamic demands on components. Only recently have some large industrial companies begun to implement AM components in-service that operate under high temperature conditions. In the gas turbine industry, LPBF is utilised to achieve additional component value in a variety of ways, including: increased performance by exploiting AM design freedoms; lightweighting; part consolidation; reducing the need for joining processes such as welding; and near-net shape manufacture of components in alloys typically considered difficult to machine. This enabled time and cost savings in the manufacture of these components.

One prominent example of the use of LPBF is the fuel nozzle manufactured by General Electric (GE) (Figure 2.2 (a)), of which 30,000 units have been manufactured prior to October 2018. The previous manufacturing route was intricate and complex, involving welding and brazing of 20 individual components. LPBF allowed these to be consolidated into a single component, eliminating the failures that would typically manifest at the component joint interfaces, hence significantly increasing the durability and life of the fuel nozzle. Additionally, a 25 % reduction in mass was achieved, further enhancing the value of the re-designed AM component in an industry where mass reduction is highly desirable.

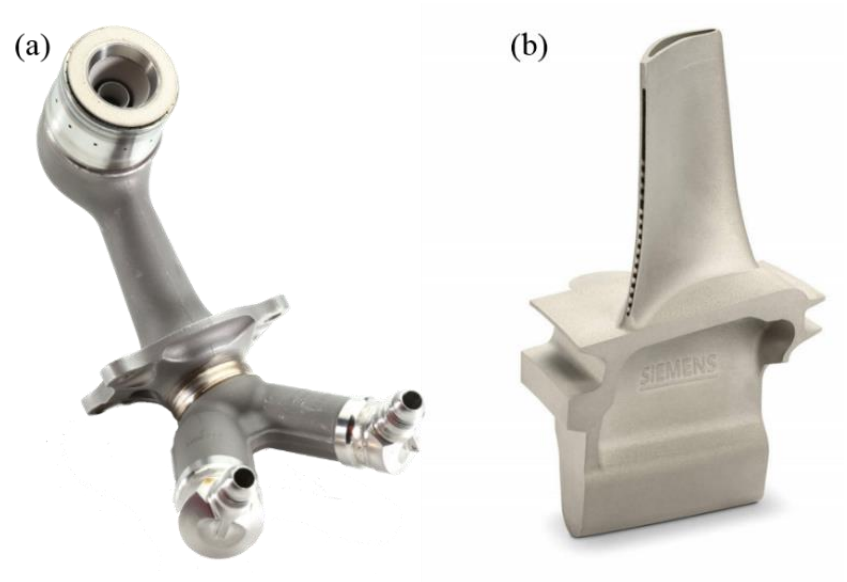


Figure 2.2 – (a) LPBF manufactured fuel nozzle by GE, achieving a 20 – 1 component consolidation and a 25 % reduction in mass (b) LPBF manufactured gas turbine blade by Siemens Industrial Turbomachinery Ltd. Validated at full-load conditions of 13,000 rpm and 1,250 °C for 100 hours.

In the case of the GE fuel nozzle, the component operates at high temperature but does not have to bear any structural load. This reduces the demand on the material properties and internal defects of the component, two areas where LPBF currently encounters some problems. Siemens Industrial Turbomachinery Ltd performed 100 hours of full-load testing on a gas turbine blade manufactured by LPBF in the nickel superalloy CM247LC (Figure 2.2 (b)). This is a significant achievement as the full-load conditions of 13,000 revolutions per minute at gas temperatures of 1400 °C subject the turbine blade to high thermomechanical loads. Revised internal cooling geometries that cannot be achieved using investment casting were included in some of the test blades, demonstrating the capability of AM to advance the design of high-performance components. The validation of the AM turbine blade at full-load conditions indicates that LPBF has reached the maturity level required for manufacture of high-performance

components. However, ensuring life expectancy of the component matches that of conventional manufacturing remains a challenge for the industry.

A further use of LPBF by Siemens was in repair of burner tips for large gas turbine engines [48]. During service, the tip of the burner becomes heavily oxidised and combustion efficiency decreases. This large component is life-limited by the tip and therefore a repair was the most cost-effective maintenance method. The damaged burner tip was first machined back to a clean surface and then fitted into a modified EOS M290 LPBF machine. Fresh material was then deposited on to the burner tip, replacing the oxidised material and returning the component to a suitable state for use (Figure 2.3). This component was not originally manufactured via LPBF but demonstrates the flexibility of the process and the value it can add to the supply chain in the manufacture of high-value components. The repair methodology used prevents a large component from being scrapped due to wear on a small region and likely reduces the lead time in engine overhaul as an entire new component does not need to be manufactured.

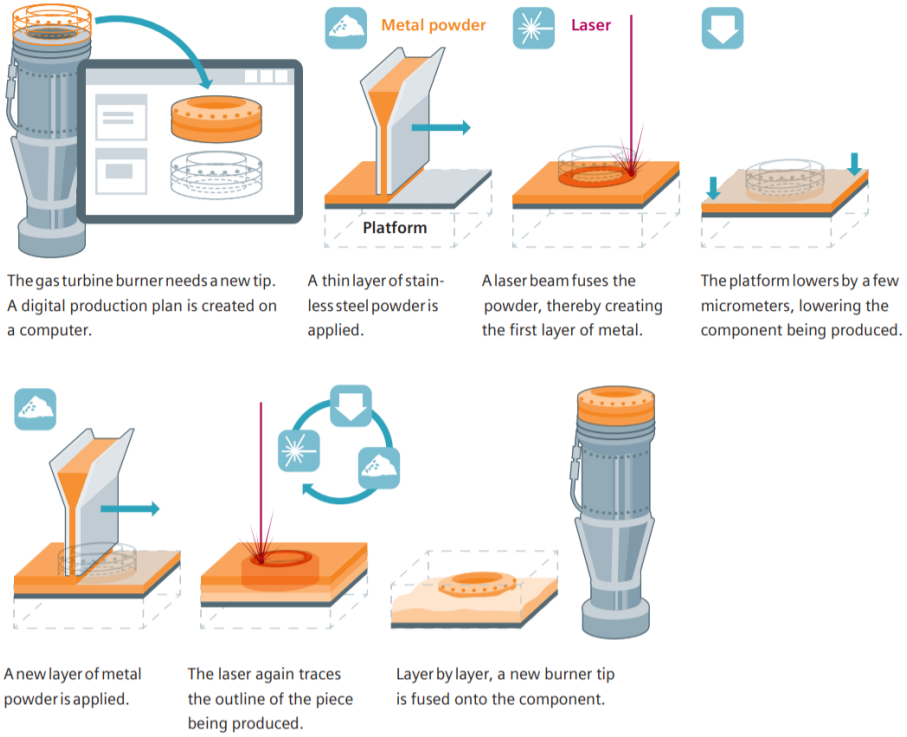


Figure 2.3 – Burner tip repair via LPBF by Siemens Industrial Turbomachinery Ltd using a modified EOS M290 machine.

2.3 NICKEL-BASED SUPERALLOYS FOR LPBF

The term ‘superalloy’ was first used to describe alloys developed after WWII which retained high mechanical strength at temperatures above 600 °C [49]. Ni-based superalloys remain of significant interest for their performance in the high-temperature, load-bearing environments found in the aero and industrial gas turbine industry. Manufacturers are constantly pushing for components that can withstand higher operating temperatures as increasing thermodynamic efficiency, and hence fuel efficiency of gas turbine engines is directly related to increasing turbine inlet temperatures [50]. This relationship is governed by the Carnot efficiency cycle which states that theoretical engine efficiency is directly proportional to the difference between the temperatures of the inlet gases and exhaust gases. To enable components to withstand increasing combustion temperatures, specialist alloys are required. Superalloys are the material of choice for hot gas path components due to their excellent creep and thermal fatigue strength, oxidation resistance and hot corrosion resistance [51]. Some examples of such components manufactured in Ni-superalloys are turbine blades, discs [52], vane segments [53] and casings [54].

2.3.1 SUPERALLOY CHEMISTRY AND MICROSTRUCTURE

Over the years, superalloy chemistry has become increasingly complicated with the addition of multiple alloying elements that all play a specific role. These elements and their primary function can be seen in Table 2.1. The simplest superalloys gain their strength via solid solution strengthening, making them suitable for use in high-temperature, corrosive environments. Interstitial hardening is possible with alloying elements with atomic radii significantly smaller than that of the Ni-matrix, of which C is the only suitable element. Substitutional hardening is possible with a range of elements with atomic radii greater than that of the Ni-matrix, with Mo and W being the most potent [55]. These elements also have very low atomic diffusion rates in Ni. This is of

significance as creep is controlled by atomic diffusion; use of low-diffusion rate alloying elements increases the creep performance of the alloy [56]. However, performance of solid solution strengthened alloys remains inferior to precipitation hardened alloys for high mechanical loading at elevated temperatures.

Table 2.1 - List of Ni-based superalloy alloying elements and their function

Function	Alloying element
Gamma formation (γ)	Co, Cr, Mo,W, Fe
Gamma-prime formation (γ')	Al, Ti, Nb, Ta, Hf
Carbide formation	Cr, Mo, W, Nb, Ta, Ti
Grain boundary segregation	B, C, Zr

Superalloys with high-strength at elevated temperatures are obtainable via combined solid solution hard strengthening and precipitation hardening of the face-centred cubic (FCC) gamma matrix phase (γ-phase). Precipitation hardening is achieved primarily with $Ni_3(Al,Ti,Nb)$ intermetallic compounds, known as the gamma-prime phase (γ'-phase). Via heat treatment, γ'-phase is arranged in a structure, size and distribution such that the microstructure remains stable up to within 10 % of the melting temperature (0.9 T_m) [57]. The low lattice parameter mismatch (~0 – 1.0 %) and high degree of chemical compatibility between the γ-matrix and γ'-phase allows homogeneous precipitation in the bulk material with excellent stability even at high temperature [58]. Further, the ductile nature of the γ'-phase increases the strength of the alloy without diminishing its fracture toughness. Al and Ti are the most common γ'-phase forming alloying elements and can result in a γ' volume fraction of up to 70 % in modern superalloys. In alloys with a low γ' fraction, the γ'-phase forms spherical precipitates due to the desire for minimised surface energy during precipitation. However, at larger γ' fractions, the interfacial energy

of many spherical precipitates with the γ-matrix becomes too large. Instead, the precipitates form cubes which have a greater packing efficiency and hence minimise the interfacial energy. This cubic microstructure is also known as blocky.

The performance of precipitation hardened alloys is further enhanced by formation of thermally stable carbides. The most potent carbide forming elements include Ti, Ta, Nb, W and Cr, forming a range of metallocarbohedryne (MC) carbides with structures MC, $M_{23}C_6$, M_6C and M_7C_3 [59, 60]. The function of these MC carbides is to: reduce the rate of grain boundary slip and hence increase creep performance; increase tensile strength; and provide a preferential reaction source for undesirable elements that would otherwise impede the high-temperature stability of the alloy. The carbides tend to form along grain boundaries and can become more numerous in the component during operation at high temperature. In superalloys with a large number of grain boundaries, carbides in these regions are deemed to be beneficial to the rupture strength at high temperature. However, in some instances the carbides can act as crack initiation sites, having a detrimental effect on the alloy performance. This is a key material quality indicator for AM processing due to the very fine grain structure in comparison to wrought or cast conditions. LPBF components are often heat treated after manufacture to produce a homogeneous grain structure and increase the grain size. This is particularly important for high creep strength as one creep mechanism, grain boundary sliding, is exacerbated by the high number of grain boundaries inherent with a small grain size microstructure. For this reason, modern turbine blades employ directional solidification [61, 62] or single crystal microstructures [63-65] that eliminate grain boundary sliding. However, such microstructures cannot currently be obtained using LPBF, even after heat treatment.

2.3.2 CM247LC

CM247LC [66] was initially developed as a directional solidification nickel alloy for the investment casting of turbine blades, particularly designed for high creep strength. It is a low carbon derivative of MAR-M-247 with reduced Zr and Ti content, and tightened control on Si and S. CM247LC consists of a γ/γ′ dual-phase, face-centred cubic (FCC) crystal structure with preferential solidification in the <001> direction. Its strength arises from the precipitation of the coherent intermetallic γ′-phase, with basic composition Ni_3(Al, Ti), within the γ nickel matrix. Addition of refractory elements facilitates the precipitation of primary metallocarbohedryne (MC) type carbide structures (preferentially TaC, TiC and HfC) [67]. CM247LC was chosen by the industrial partner for this work as it is a desirable alloy for the LPBF manufacture of turbine blades. Directional solidification alloys retain the alloying elements required for grain boundary strengthening, whilst single crystal alloys are not suitable for LPBF as these strengthening elements are not present. Therefore, the current state-of-the-art alloy for turbine blade manufacture is not viable for LPBF.

Nickel alloys with high γ/γ′ volume fraction often exhibit poor weldability [68], a term used to denote high propensity for cracking, due to their sensitivity to high thermal gradients. The weldability of Ni alloys can be considered as a function of the content of γ′-phase forming elements, Al and Ti, as shown in Figure 2.4 for a range of alloys [4, 66, 69-72]. An alloy with Al + Ti composition >4.5 Wt% can typically be considered ‘unweldable’[73]. LPBF combines a high energy density laser source with high traverse speeds, with the resultant high thermal gradients producing thermally induced residual stresses. If these residual stresses become greater than the ultimate tensile strength (UTS) of the material, cracking will occur. Hence, LPBF is not an ideal candidate manufacturing process for such alloys. However, with the unique design freedoms of LPBF, there is a

market push to adapt the process or the material to improve compatibility to a level that enables manufacture of high-performance components.

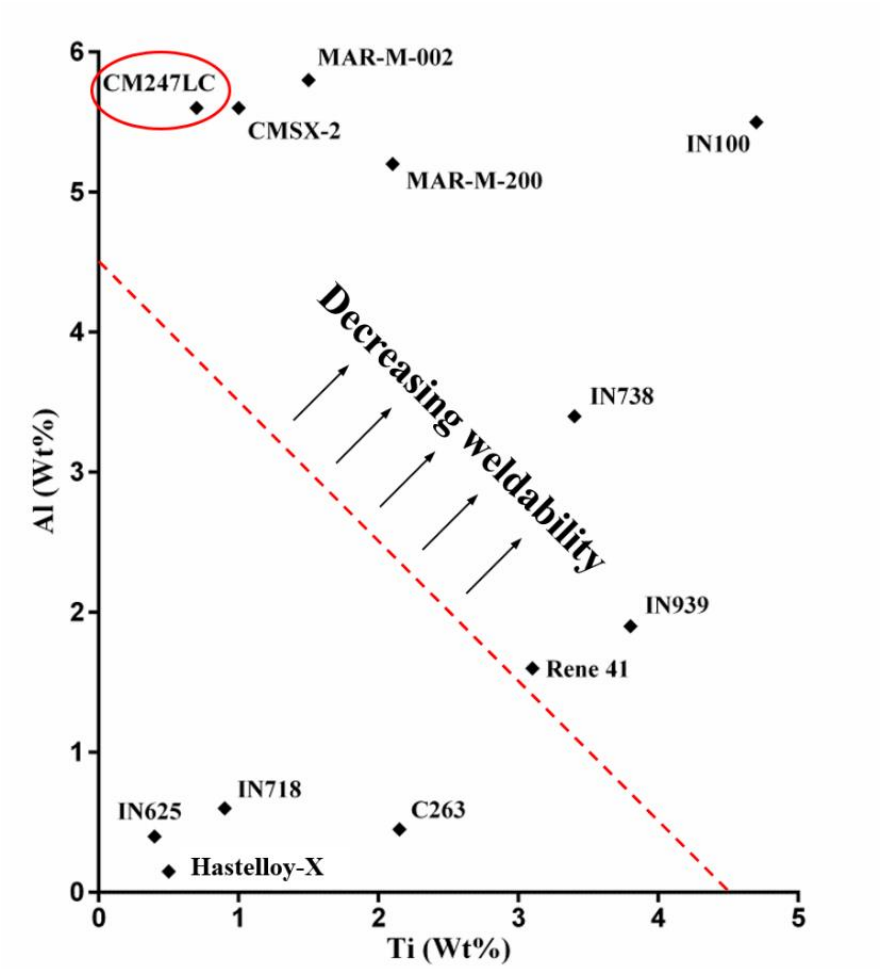


Figure 2.4 - 'Weldability' diagram for a range of Ni alloys as a function of their Ti and Al alloy element composition. Weldability is considered poor above the dashed line and deteriorates with increasing Ti and Al content. CM247LC is found above this weldability line whilst Hastelloy-X is found in the lower 'weldable' region. All data taken from associated alloy specification documents [4, 66, 69-72].

The poor weldability of CM247LC results in the need for post-processing to heal defects present in LPBF manufactured samples. Hot isostatic pressing (HIPing), as discussed by Kunze et al. [74] for IN738LC and by Carter et al. [73] for CM247LC, has been shown to close micro-cracks. However, post-HIP processing, precipitate traces have been observed in the regions of healed crack zones in samples produced via LPBF, with

increasing precipitate coarseness with original crack length. This results in a weakened material condition due to the potential for crack initiation at precipitate sites. Zhao et al. [75] concluded that the diffusion bonding mechanism on which HIP acts is not sufficient to eliminate segregation of carbide forming elements, hence these weakly bonded regions remain post-HIP. The mechanism by which this occurs is shown in Figure 2.5, where in-service loading such as fatigue and creep can cause the weakly bonded prior-crack boundaries to separate again. Thus, it is desirable to minimise the cracking density in the as-deposited part in advance of any subsequent processing; the success of crack healing via HIP is directly related to the integrity of the material in the as-LPBF state.

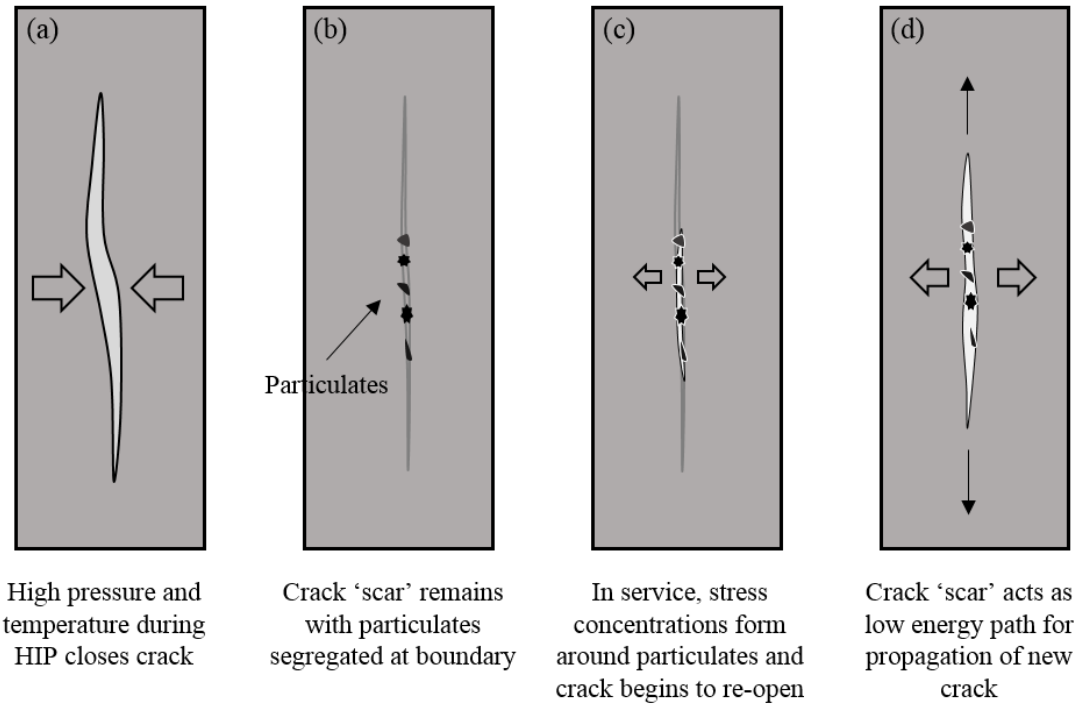


Figure 2.5 - After a crack is closed by HIP (a), particulates segregated at the closed crack boundary (b) can form stress concentration points, leading to the crack re-opening (c) and propagating along the weakly bonded crack boundary (d).

2.3.3 HASTELLOY-X

Hastelloy-X (hereafter abbreviated as HX) is a trademark nickel-chromium-iron-molybdenum alloy from Haynes International (Kokoma, Indiana, USA). It is frequently

used in the gas turbine industry for manufacture of components in and around the combustion zone [76-78], including combustor cans, ducting, injection nozzles and afterburners. The alloy develops a well-bonded protective oxide layer which does not easily spall, therefore providing excellent oxidation resistance at high temperatures [79]. HX also performs well in corrosive and reducing environments, important for combustion zone components due to the corrosive/oxidative nature of the by-products of fuel impurities such as sulphur.

The high mechanical performance of HX comes from solid solution strengthening primarily via Mo-rich carbides (M_6C and $M_{12}C$), with additional strengthening from Cr-rich carbides ($M_{23}C_6$). HX does not have a γ/γ' microstructure, in contrast to CM247LC. Therefore, it is considered significantly more weldable, as evidenced by its positioning in the lower left corner of Figure 2.4. However, challenges remained when first processing HX, with a range of solutions proposed by researchers studying its applicability for LPBF. Wang et al. concluded that cracks remain in LPBF manufactured parts regardless of the process parameters chosen [80], which although can produce samples that have a higher UTS than hot forged equivalents [81], the creep and fatigue performance of such components is likely to be severely impaired. Wang et al. have noted that HIP can repair the cracks found in the as-LPBF samples, however a crack-free microstructure before HIP is desirable for optimal performance.

Further research is focussed around the modification of alloy chemistry, reducing the propensity for hot cracking during solidification and hence improving the as-LPBF density. It was proposed by Tomus et al. [82] that high content of Si and C, and the subsequent formation of a significant amount of M_6C carbides, results in increased cracking in HX when subjected to the high thermal residual stresses generated in LPBF. The small grain size of approximately 1 µm makes LPBF material particularly sensitive to cracking as there are a large number of grain boundaries at which carbides

preferentially segregate to under the rapid cooling conditions. These carbides act as crack initiation sites under the high residual stresses present in LPBF material. When compared to conventional polycrystalline material with a grain size of greater than 50 μm [83] and a more isotropic carbide distribution, it is clear that a reduction of the elements responsible for carbide formation is desirable for a LPBF feedstock material. Further, through computational thermodynamic simulations [84], it was shown that higher Si and C content increases the proportion of eutectic phase and reduces the window of solidification temperatures. Sudden freezing of the material prevents residual stresses from dissipating during cooling resulting in a greater chance of cracking. An alternative approach was taken by Harrison et al. [85] who proposed that by increasing the UTS of the material, the stresses at which cracking occur would not be reached during material solidification. Through increasing the solid solution strengthening elements Cr, W, and Mo, it was demonstrated that cracking density can be reduced when compared to the nominal HX composition.

The most recent articles concerning the use of HX in PBF manufacture has shown that the issue of cracking has been mitigated to the point that near-100 % bulk density can be achieved [86]. This was through a combination of alloy composition optimisation and efforts by machine manufacturers to supply optimised process parameter files [87]. As a result, LPBF is now considered to be a viable manufacturing method for Hastelloy-X components. Hastelloy-X was chosen for manufacture of samples in this thesis for the combination of process suitability and also the alloys frequent use in gas turbine engines, representing a good baseline Ni-superalloy for which the performance of lattice structures can be evaluated.

2.3.4 SCAN STRATEGIES FOR LPBF MANUFACTURE OF NICKEL SUPERALLOYS

Material condition in the as-LPBF state is dependent upon the process parameters chosen for manufacture. Process parameter optimisation for reduction of cracks and pores is typically based upon altering scan speed, laser power, hatch distance and layer thickness [34, 88-91]. However, an important factor to consider is the path the laser takes to fill in an area in the build plane, known as the hatch scan strategy. In its most basic form, a scan strategy describes whether the laser is always travelling in a single direction (uni-directional [92]) or back and forth within the scan area (meander or zig-zag scan [93]). The scan strategy to fill in an area can be altered by rotating the hatch scan between layers [94], or sub-dividing the scan area into separate regions depending upon the outcome desired. In the context of this thesis and process development for CM247LC, the important outcome is the reduction of residual stress. One method commonly employed in the LPBF industry to minimise residual stress build-up during manufacture is the use of short scan vector lengths [95].

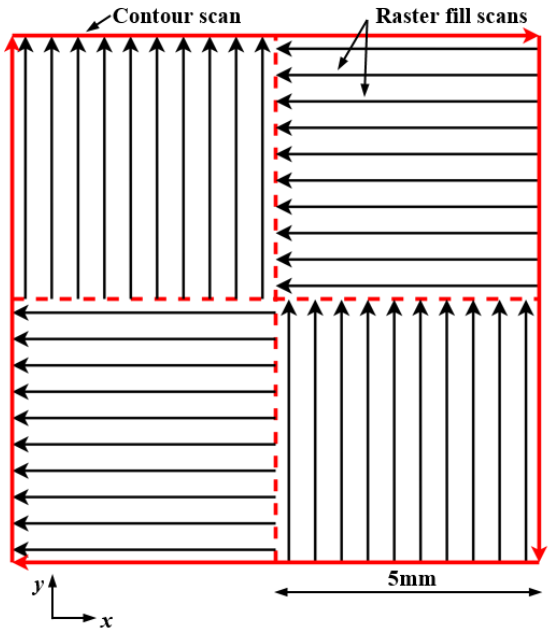


Figure 2.6 – Illustration of the 10 x 10 mm island scan strategy. Initially, a single wall thickness contour scan is performed followed by the raster scans to form four 5x5 mm 'islands'

A strategy for implementing short vector lengths is to divide the laser scanned area of each layer into smaller square sections referred to as ‘islands’ or ‘checkerboard’ [96], comprised of a border (contour) and inner raster scan region (as illustrated in Figure 2.6). The result is a large area broken up into many smaller sections, constraining the residual stresses formed in the hatch scan region to a localised area that is less likely to cause macro-scale distortion or cracking. Further, by rotating the hatch scan direction by 90 ° between neighbouring islands, residual stresses act to balance each other out over a larger area. This is an important technique for high aspect ratio components or large areas (>400 mm^2) which may otherwise distort in a way that disrupts the LPBF process by obstructing the re-coat sequence or bring the component outside of dimensional tolerance. In the case of CM247LC, the residual stresses are partially relieved through macro cracking within the bulk material.

The relationship between scan vector length and residual stress was experimentally explored by Kruth et al. [97] by manufacturing cantilever specimens. An indicator of residual stress, curling angle, was correlated with scan vector length, where it was seen that using 2 mm vector lengths provided a 13 % reduction in curling angle compared to a reference part manufactured using 20 mm vector lengths. However, no experiments were conducted using vector lengths below 2 mm. Parry et al. [98] identified that longitudinal residual stress increases with scan vector length, hence reducing the vector length as far as possible should prevent the stress build-up in LPBF.

In attempt to reduce cracking in IN718, Lu et al. [99] conducted a comprehensive analysis on the effect of varying the island sizes. It was seen that reducing the island size below 3 x 3 mm produced a significant increase in cracking density, as the large number of island intersections resulted in poor metallurgical bonding and the formation of pores. Variation in cracking density using island scanning in CM247LC deposits was also reported by Carter et al. [100]. This was attributed to a bimodal grain structure, consisting

of columnar grains aligned with the build direction within the hatch region surrounded by fine equiaxed grains positioned along the intersection of the scanned islands. The high cracking density within the fine equiaxed region precluded island scanning from being an effective method in this case.

Despite the benefits in using island scanning, there has been only limited exploration of alternate scanning strategies with very short vector lengths (<500 µm) or novel scan patterns, such as mathematical area filling curves, or ‘fractals. Fractals in the context of this thesis are patterns comprising of many short sections with frequently changing directions. The fractals used here, Hilbert and Peano-Gosper (Figure 2.7), can fill an area using a single continuous line. For LPBF this means that a large area can be scanned without turning the laser off and there are only two start and end points to the laser scan path in any one layer.

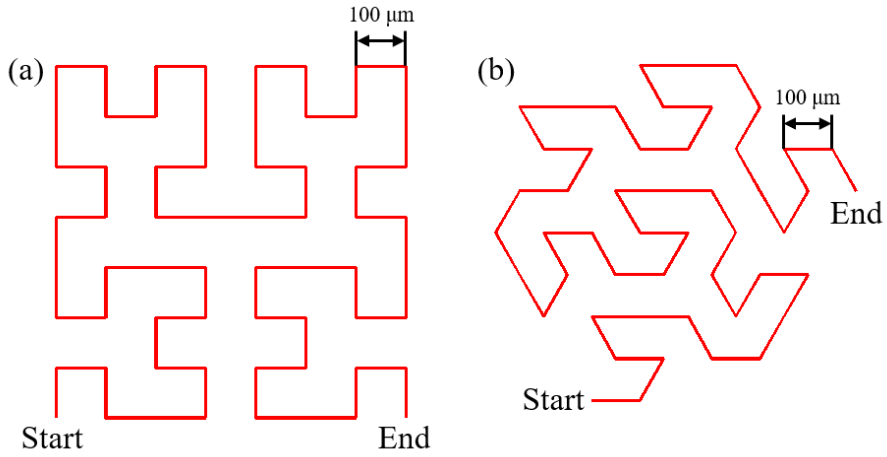


Figure 2.7 - Hilbert (a) and Peano-Gosper (b) fractal patterns used for LPBF. Start and end points indicated.

Ma et al. [101] simulated the temperature and stress variations seen during selective laser sintering (SLS) of polymer powder, comparing a standard meander scanning pattern to the Hilbert fractal scanning pattern. It was concluded that the Hilbert scan pattern produces a more symmetrical temperature field and smaller plate distortion than the meander scan pattern. Further SLS simulation tests by Yang et al. [102] also concluded

that the use of the Hilbert curve results in lower thermal gradients and decreased residual stress in SLS components. Experimental tests indicated more consistent sintering and higher tensile strength in components manufactured using Hilbert curve scanning strategies. With exception of the article published as part of this thesis [103], no literature is known that details the application of fractal scan strategies to metal additive manufacturing (AM) processes. This is an interesting avenue of research for its potential in reducing the cracking of alloys such as CM247LC in LPBF and was explored later in this thesis.

2.4 Lattice, Porous and cellular structures

The previous section has outlined the Ni-based superalloys that will be used in later Chapters. The main body of work in this thesis does not focus on process parameter optimisation or characterisation of these alloys, but rather the potential that lattice structures manufactured in these alloys via LPBF have to improve component performance.

Lattice structures belong to the family of porous and cellular structures, which are those comprised of interconnected networks of solid struts, surfaces or faces (Figure 2.8) [104]. These structures may be two-dimensional (2D) or three-dimensional (3D) forms with an ordered structure, known as non-stochastic, for example honeycombs constructed from hexagonal cells. Alternatively, the pores may be un-structured, randomly distributed and orientated (stochastic) to form structures categorised as foams [105]. Foams can have individual cells or pores with no connection to neighbouring cells, known as closed-cell foams, or interconnected cells with a pathway for fluid flow through the structure, known as open-cell foams. Stochastic foams can be found in nature as bone, wood, fungi and sponge amongst others [106]. They can also be manufactured using relatively simple methods, for example by: introducing inert gas into melted polymer and using a low-

pressure atmosphere to expand the gas, forming a porous network [107]; introducing volatile hydrocarbon gases into polymer beads which are placed into a mould, where under high temperature and pressure the gas rapidly expands to form a porous network (expanded polystyrene, [108]). Metallic foams, typically aluminium or copper alloys due to their low melting temperature, can be manufactured in a similar way: inert gas is bubbled through the liquid alloy, rising and becoming entrapped in a layer of cooled, solid alloy at the surface. The cooled foam is continuously drawn away from the surface to allow new gas bubbles to reach the surface and form more foam [109]. Alternatively, foaming (blowing) agents such as TiH_2 can be added to the molten alloy, which release gaseous hydrogen during heating, creating a foamed liquid which after cooling forms a metallic foam structure [110]. Foams, particularly closed-cell foams, are not ideal for LPBF manufacture due to difficulties in removing the loose powder inside the structure after the build.

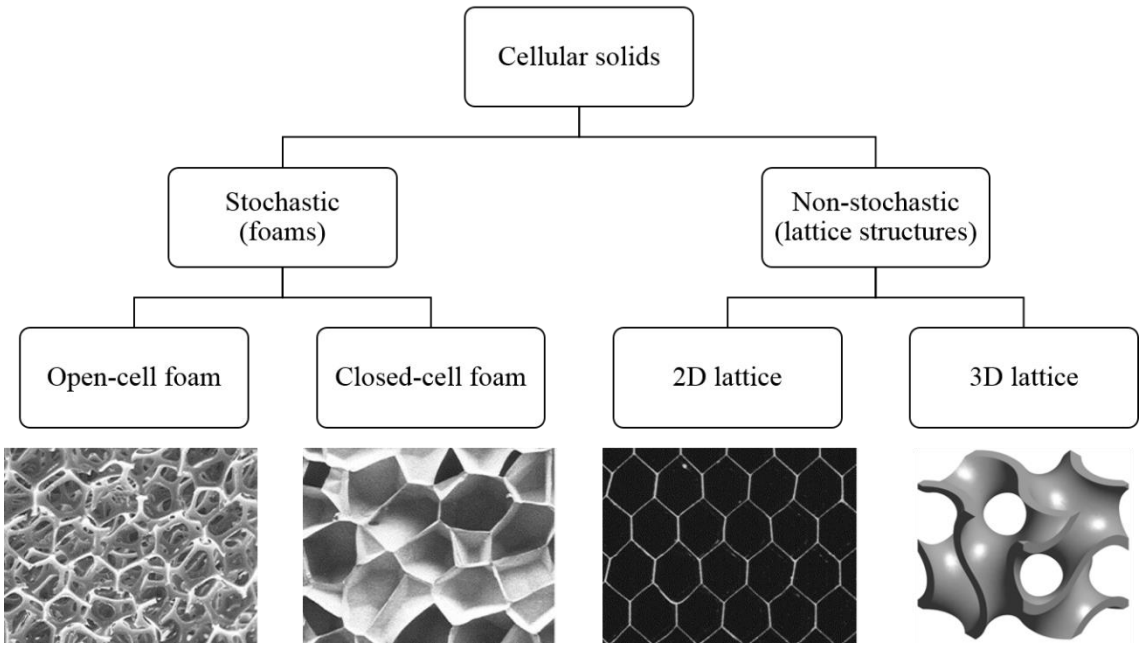


Figure 2.8 - Tree diagram of types of cellular solids. This thesis concentrates on non-stochastic 3D lattice structures. Images taken from Gibson et al.

Lattice structures occupy a separate category of 3D cellular structures due to their strictly defined unit cell (non-stochastic) which is repeated and tessellated in three dimensions to form a solid. Non-stochastic structures cannot be manufactured using the conventional methods used for metallic foams, but rather must be manufactured in a controlled, programmed way. AM and PBF processes in particular are suitable for lattice structure manufacture due to the ability to manufacture complex structures in a layer-by-layer method. Subtractive manufacturing methods are unable to create many of these structures due to tool access requirements. Casting methods are limited by geometric complexity and can only be used to manufacture simple 3D lattice structures with limited feature size [111, 112]. Simple strut-type lattice structures can be manufactured by welding, brazing or soldering wire struts at nodes to form a 3D geometry [113-115], but this introduces many points of potential failure and is a lengthy and high-cost process, especially considering the low complexity that is possible when compared to PBF manufacture.

2.4.1 TPMS LATTICE STRUCTURES

A sub-category of 3D non-stochastic structures is the triply periodic minimal surface (TPMS) lattice structure (Figure 2.9). The TPMS structures are defined by a set of equations (Table 2.2) [116, 117] that describe a surface with zero thickness. To create a sample with volume, the surface is ‘thickened’ to provide a certain proportion of solid material per volume, termed the volume fraction. In this thesis, 0.2 and 0.5 volume fractions were used, i.e. 20 % and 50 % solid material by volume. This represents the upper and lower bounds of volume fractions useful for engineering design. Below 0.2 volume fraction at 2.5 mm cell size, the features become too small to manufacture via LPBF; greater than 0.5 volume fraction, lattice structures lose value as a method of lightweighting and the drawbacks of the increased design complexity outweigh the performance benefits.

Table 2.2 - Periodic trigonometric functions for the TPMS lattice structures under investigation in this thesis.

TPMS	Periodic trigonometric function
Diamond	$\phi(r) = \cos(X) + \cos(Y) + \cos(Z) = 0$
Gyroid	$\phi(r) = \cos(X)\cos(Y)\cos(Z) - \sin(X)\sin(Y)\sin(Z) = 0$
Schwarz Primitive	$\phi(r) = \sin(X)\cos(Y) + \sin(Z)\cos(X) + \sin(Y)\cos(Z) = 0$

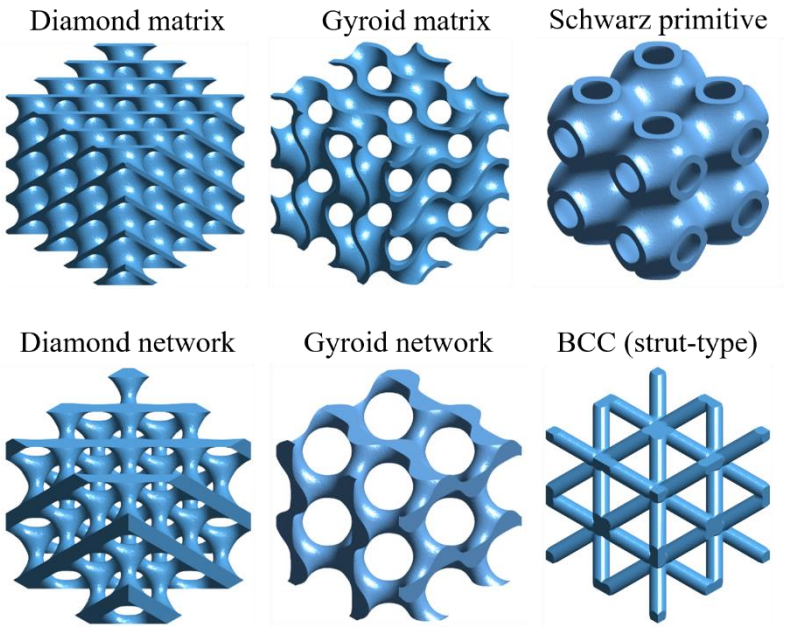


Figure 2.9 - TPMS lattice structures used in this thesis alongside the BCC (strut-type) lattice in the bottom right corner.

2.4.2 Mechanical properties of lattice structures

The most frequently leveraged benefit of porous or cellular materials is their high-specific mechanical properties, or high-strength to weight ratio [118-120]. This makes them ideal for lightweighting components by replacing large areas of bulk material with the low-density porous structure, designed and implemented such that the required strength is maintained. Further, the properties of these structures are geometry dependent and hence once knowledge is gained of how each type of structure performs under

loading, specific structures can be selected based upon the mechanical performance required.

Existing research has determined the mechanical performance and failure modes of a range of lattice structures. Ataee et. al [121] identified the compressive failure mode of Ti6Al4V EBM-manufactured gyroid network lattice samples to be bending at the joints of the lattice followed by shear fracture at a 45 ° angle to the loading direction. This supports the categorisation of the gyroid network lattice as a bending dominated structure under loading. Ataee et al. also revealed the effect of manufacturing accuracy on the mechanical performance of the lattice samples, where smaller cell sizes tended to result in distortion of circular channels through the lattice. Consequently, some samples exhibited mechanical anisotropy, with reduced elastic modulus and yield strength in the build direction (for example, E = 637 ±45 MPa in the build direction vs 1084 ±160 MPa in the transverse direction for sample G2). This highlights the importance of choosing the correct lattice type and cell size for each manufacturing process or application.

Inconel 625 (IN625) strut-type lattice structures manufactured via LPBF were investigated by Leary et. al [122] under compressive loading. Both BCC and FCC structures exhibited higher compressive yield strength at smaller cell sizes, with the addition of a vertical strut (BCC*Z* and FCC*Z*) resulting in increased yield strength. Furthermore, the failure mode transitioned from bending dominated in *x*CC form to stretch dominated in *x*CCZ form. This is due to the Z-component providing support at the node intersection where strut bending occurs, effectively constraining the deflection seen here. The IN625 samples were noted for their high ductility, where under extreme compressive load leading to densification, no strut fracture was observed (Figure 2.10 (a)). The inversely proportional relationship between cell size and compressive yield strength is also reported by Yan et. al [123]. Testing of gyroid network LPBF manufactured 316L samples with cell sizes in the range 2 – 8 mm demonstrated this trend,

where the 2 mm cell size sample had approximately 36 % higher yield strength and 27 % greater elastic modulus than the 8 mm cell sample. Images captured during testing and the smooth deformation seen in associated stress-strain plots support the mechanism of bending without fracture failure of the gyroid network lattice geometry.

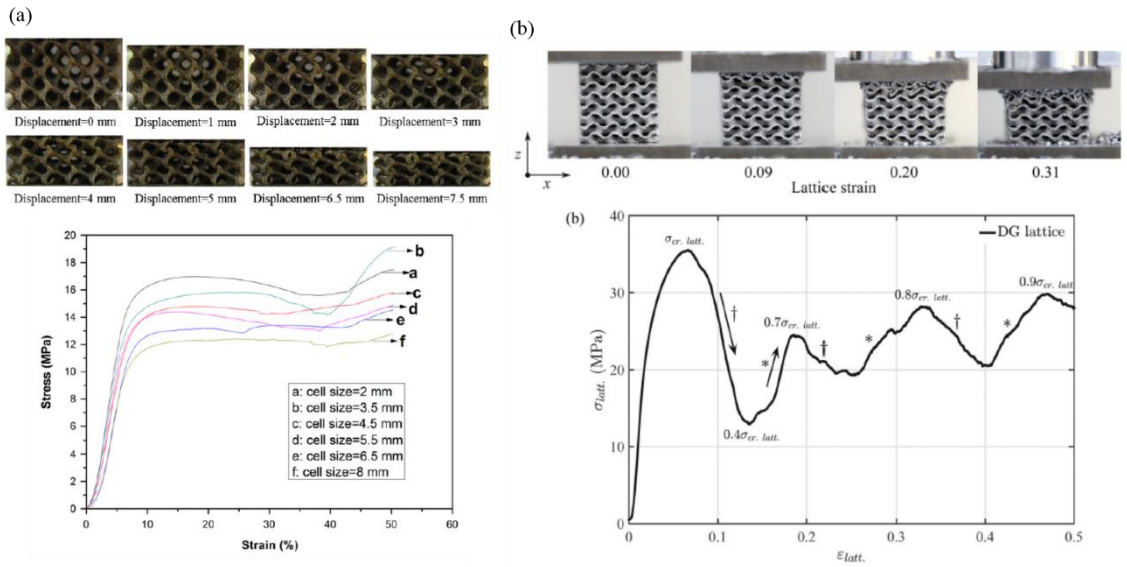


Figure 2.10 - Ductile compression of IN625 lattice structures with extended plateau stress curve (a) versus staged brittle fracture of AlSi10Mg gyroid lattice with distinct rippled stress-strain plot (b).

Gyroid matrix TPMS lattice structures evaluated by Maskery et. al [124] were observed to have approximately three times the specific energy absorption capability when compared to BCC lattice samples [125]. However, this was only achieved after heat treating the AlSi10Mg, which although was seen to reduce the ultimate tensile strength of the material by 12 %, significantly improves the ductility. Before heat treatment, the material was too brittle to bend and failed in 45 ° shear bands relative to the loading direction directly through the cubic sample, the plane of maximum shear stress under uniaxial loading. The influence of this T6-like heat treatment for LPBF manufactured AlSi10Mg is explored in full by Aboulkhair et. al [37], which can be considered a necessary post-processing step if ductility is required.

Maskery et al. also evaluated the failure of BCC lattices with a graded volume fraction, demonstrating that preferential failure regions can be designed in to a structure [125]. Layers collapsed in order of increasing volume fraction, a feature that could be leveraged for a crash structure where a gradual increase in is energy required to further deform the structure may prevent complete structural failure. A further application may be in biomedical implants, where graded structures may provide protection from dynamic loading including shock absorption, torsion and compression that may occur simultaneously in some cases [126]. Staged failure exhibits a rippled stress-strain curve (Figure 2.10 (b)), a feature that can help identify this failure mode where it may not be immediately apparent from the sample exterior. For example, the rippled curve could signify multiple internal struts fracturing at the same stress level, highlighting a potential weakness in a given geometry. However, the rippled stress-strain curve alone cannot identify the failure mode of a lattice structure. It also appears in samples manufactured in maraging steel, where in the testing by Al-Ketan et al. [127] it was shown to be a result of layers failing sequentially under bending in Schwarz primitive, diamond network and octet-truss geometries – without any fracture failure. Therefore, it must only be used as an identifier for a failure across multiple sites simultaneously rather than for a specific failure mode. Failure of individual elements within the structure may not provide sufficient deformation to result in a stress decrease of the magnitude seen in Figure 2.10 (b).

Staged failure is a characteristic of many further geometries investigated in the literature including gyroid network [128], D-FCC [129], F2-BCC [130] and cuboctahedron [131], even with constant (i.e. not graded) volume fractions. This can be avoided by using a ductile material as demonstrated by Leary et al. [122] with Inconel 625 BCC and FCC structures. Here, the stress-strain curves plateaued after the elastic limit and remained relatively flat until the lattice began to densify via bending of the struts

at the onset of high strain (>5 %). This signifies distribution of the loading stress within the whole sample rather than stress concentrations forming at element intersections or vertices in the geometry. This is a desirable feature when seeking a high-strength lattice structure as minimising the potential for stress concentration points leads to a decrease in the likelihood of exceeding the UTS of the material and the fracture or failure that would follow.

2.4.3 POROUS STRUCTURES SUMMARY

The use of porous structures is an effective method for reducing the weight of a component whilst retaining high mechanical strength and has been applied in engineering components using conventional manufacturing methods. LPBF enables manufacture of non-stochastic lattice structures that cannot be made in any other way. These structures have many advantages over stochastic structures including their ability to be tailored for anisotropic loading applications. The mechanical properties of lattice structures has been shown to be a product of the geometry and the properties of the material used for manufacture. To identify the best geometry for an application, it is necessary to perform mechanical testing on a wide range of samples. Many geometries have been investigated previously, including strut-type lattices and the gyroid TPMS, however there is need for experimental characterisation of a wider range of TPMS lattice structures. To date, many authors have focussed on aluminium alloys due to the potential for component lightweighting. TPMS lattice structures are also of interest to the gas turbine manufacturing industry, where Ni-superalloys are a requirement in many cases. This is the focus for evaluation of lattice mechanical properties in the later Chapters.

2.5 APPARATUS FOR DETERMINING HEAT TRANSFER PROPERTIES

Previously, lattice structures were shown to have good performance in mechanical loading. Further value can be gained by using lattice structures in thermal applications

such as heat exchangers or thermal insulation (heat shields). However, no commercial solution exists to determine the thermal properties of the lattice structures, as like for mechanical properties, both geometry and material must be considered. In order to evaluate the lattice structures, new thermal characterisation apparatus was required. This section outlines the literature used to inform the design and layout of the apparatus used in later Chapters for thermal conductivity and convective heat transfer evaluation.

2.5.1 1-DIMENSIONAL CONDUCTIVE HEAT TRANSFER

A number of methods exist for measurement of thermal conductivity but each has limitations including material type (fibrous insulation, polymers, metals), material state (solid [132, 133], liquid [134], paste, powder) and measurement direction (bulk, through-thickness [135, 136], in-plane). Sample geometry presents a problem, where most apparatus that can measure thermal properties of metallic samples require thin sections or powders and therefore can only measure the properties of the constituent material. The challenge posed by measurement of lattice structures is that of anisotropy within the sample and effects of natural convection within the lattice itself. This combination of solid and air conductivity requires determination of a value for the apparent thermal conductivity of the sample (i.e. the sum of conductivity through solid and air). Whilst determining the thermal conductivity of the lattice alone by testing under vacuum may appear to be the most desirable method, these structures would be mostly used under atmospheric or increased air pressure applications. Therefore, it is important to determine the effect of the air contained within the lattice so that performance of lattice structures in heat transfer can be fully understood.

The two standards that are applicable to the thermal conductivity measurement of lattice structures are ASTM C518-17 [137] (Steady-State Thermal Transmission Properties by Means of the Heat Flow Meter Apparatus) and ASTM E1225-13 [132]

(Thermal Conductivity of Solids Using the Guarded-Comparative-Longitudinal Heat Flow Technique). C158-17 uses a heat flux meter, a thin polymer membrane with a precise electrically conductive path running inside it. This sensor measures the exact heat energy that passed through the membrane and as such can be used to calculate the heat energy input or output of a system. However, this sensor has a high cost (>£500 for a size appropriate for lattice evaluation) and for the highest accuracy apparatus conforming to C158-17, two sensors would be required (heat input and output of the lattice sample). The main advantage of this standard is the speed of measurement acquisition, as the heat flow meters do not require the system to be at steady state to determine the thermal conductivity. This capability is not necessary for the lattice structure thermal conductivity measurement and so the high cost of implementing the heat flux sensors can be avoided by using a different measurement method and apparatus.

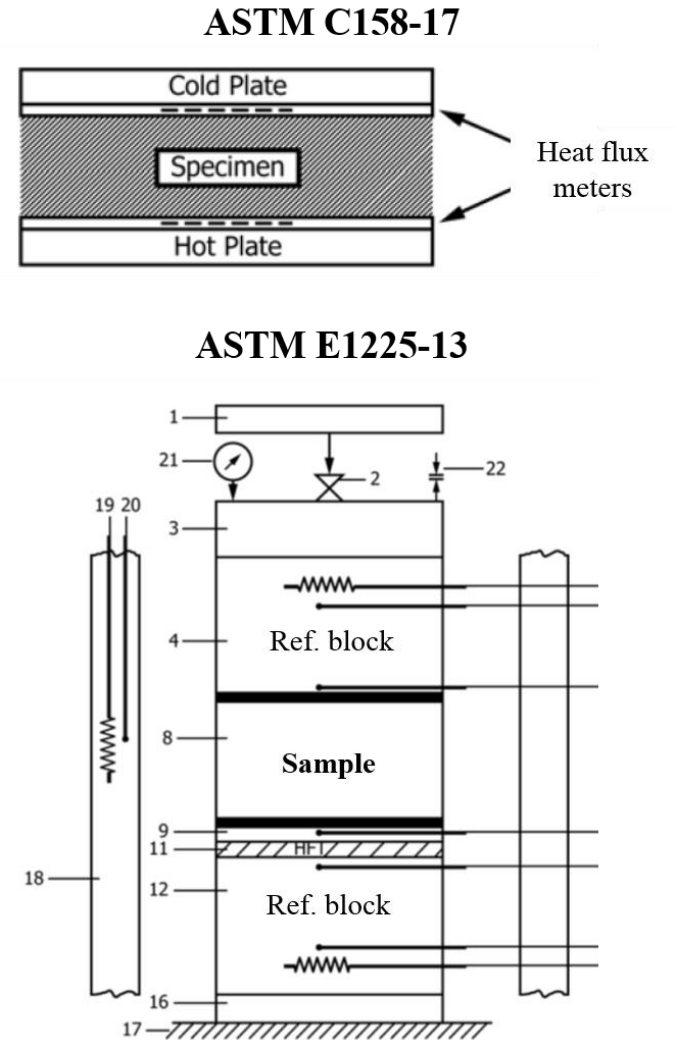


Figure 2.11 - Thermal conductivity measurement standards applicable to measurement of lattice structures. C158-17 appears simpler but requires two expensive heat flux meters. E1225-13 is simpler in operation.

E1225-13 takes a much simpler approach of using the test sample sandwiched between two reference blocks of a known conductivity (the test stack). Setting up a thermal gradient across the test stack and measuring the temperature at each interface while at steady state allows the thermal conductivity to be calculated. The weakness of this system is that the time taken to reach steady state can be lengthy (>30 mins), however this was deemed to be acceptable for the number of samples considered in later experiments. A benefit of this apparatus is that the components required are relatively low cost off-the-shelf and easily acquired in the event of a breakage or failure. As the test

stack will be arranged manually for each sample, component wear is likely especially for fragile thermocouples and therefore component cost and availability is important. Further, the system can be flexible to the test sample dimensions as the only requirements are that the cross-section of the reference blocks must be equal to that of the sample. As flexibility and low cost are desirable, and there is no requirement for fast measurement acquisition times, E1225-13 is the ideal standard to follow for measurement of lattice structure thermal conductivity. The methods and apparatus used to achieve this outcome are described in Chapter 6.

2.5.2 Convective heat transfer

The geometrical complexity of lattice structures makes simulation of convective heat transfer via computational fluid dynamics (CFD) computationally expensive. Furthermore, the behaviour of fluid flows in such geometries cannot be directly inferred from existing models due to the difference in characteristic surface roughness profile between current class LPBF [138] and conventionally manufactured components. Experimental methods are therefore seen as the most viable method to characterise lattice structure heat transfer devices. Whilst apparatus to test heat transfer properties of AM components exist in the literature, currently there is no standardised method. Apparatus has been used previously by Kirsch et al. in testing of LPBF manufactured heat transfer devices (Figure 2.12 (a)), namely wavy micro-channels [139] and pin-fin arrays [140], targeting use in gas turbine components. The apparatus used by Kirsch et al. provides all of the data required for evaluation of thermal performance, however the sample size is too small for effective testing of a range lattice geometries as it is tailored for evaluation of gas turbine internal cooling geometries only.

A similar scale apparatus was developed by Marques et al. [141] for testing of pin-fin geometries used in the trailing edge of gas turbine blades manufactured via LIGA

(lithographie, galvanoformung, abformung, translated from German as ‘lithography, electroplating, and molding’) micro-manufacturing. Whilst the 500 µm channel height in this apparatus was also too small for lattice samples, the topology was considered to be effective. The use of an O-ring sealed body for the apparatus Figure 2.12 (b) allowed for easy replacement of the sample during experimentation and was adopted for the apparatus detailed in section 6.3.

Wong et al. developed a custom apparatus to characterise the heat transfer performance of a number of LPBF manufactured geometries that are considered ‘conventional’: pin-fins, diamond fins and diagonal wavy struts [142]. A lattice-type geometry was added to further work by the same authors [143]. This apparatus accommodates samples of approximately the size required (50 x 100 mm), with the samples manufactured on extruded aluminium substrates which were used as heat spreaders during the experiments. The topology seen in Figure 2.12 (c) was considered during the design stage of the new apparatus, however the specimen size was reduced and the orientation of samples on the build plate was altered to enable a greater number of samples to be manufactured on a single LPBF build plate.

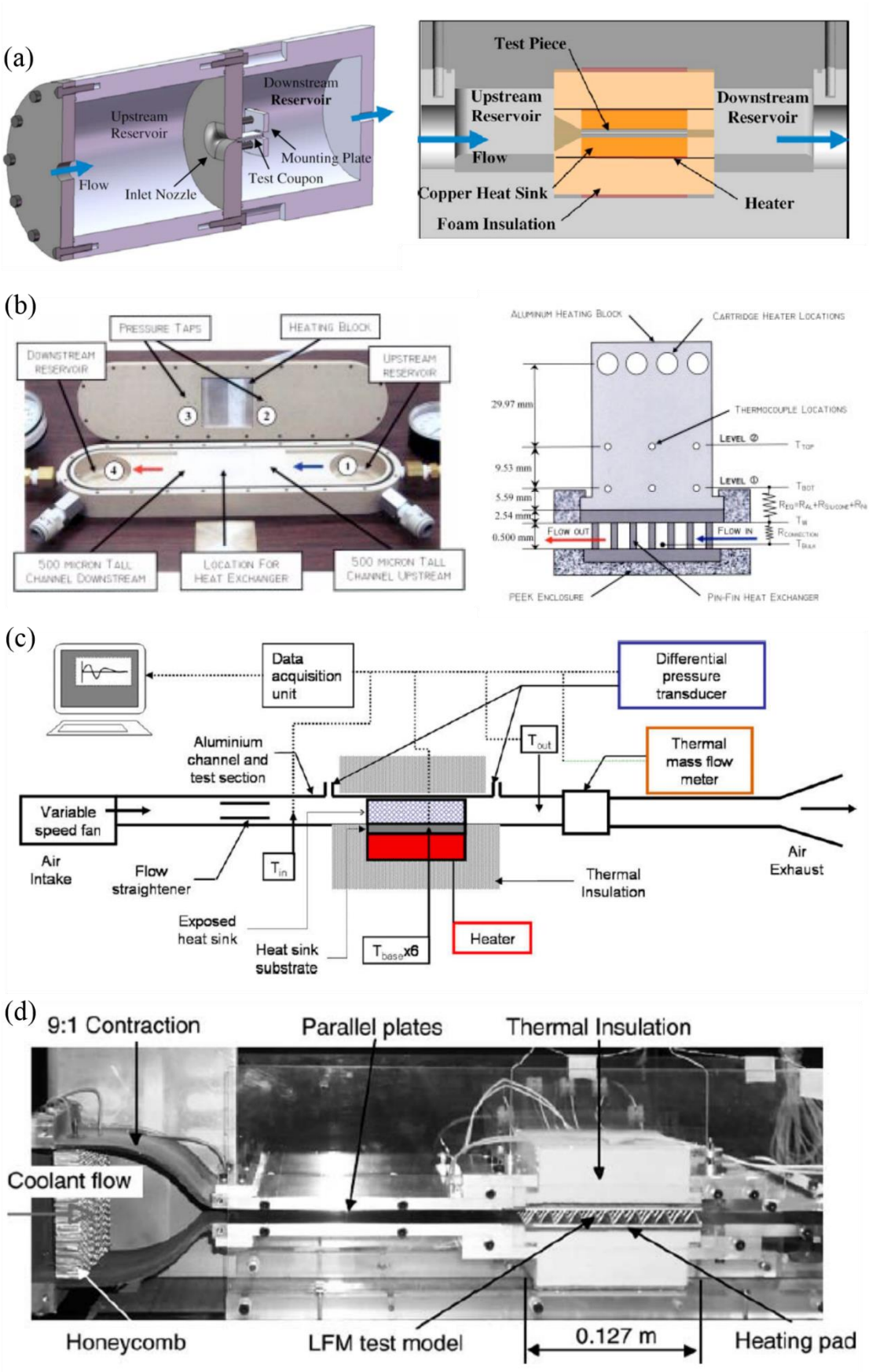


Figure 2.12 - A selection of apparatus layouts taken from the literature. (a) Kirsch et al., (b) Marques et al., (c) Wong et al., (d) Tian et al.

Further testing using convective heat transfer apparatus has been performed on samples that are not manufactured using AM. Some of the geometries investigated by Tian et al. [144] are analogous to those seen in AM literature, such as tetrahedral and pyramidal strut-type unit cells, but lack the complexity possible using AM and are complicated in their method of manufacture. Similar structures are manufactured using the same wire and brazing method by Joo et al. [145], with the testing apparatus providing pressure drop and heat transfer data. Whilst the layout and operation of the apparatus in Figure 2.12 (d) is suitable for lattice testing, the scale of the samples used is too large for cost-effective LPBF manufacture. Pressure drop and heat transfer results are demonstrated by Kim et al. across a range of publications, studying lattice-frame samples on a small scale in aluminium [146] [147] and in larger scale polycarbonate samples [148] [149]. In these publications, thermochromic liquid crystals (TLC's) are used to great effect in demonstrating the flow paths of the coolant through the lattice structures. However, the method is not directly applicable to metallic lattice samples as the TLC's are sprayed onto and their emission is viewed via transmission directly through transparent polycarbonate samples.

2.6 COMPONENT DESIGN FOR HEAT TRANSFER

For high-performance engineering components, heat transfer and the management of excess heat is often a key performance consideration. Operating temperatures of components can vary greatly depending on the application, from rocket propellant storage tanks at the temperature of liquid oxygen, through to gas turbine blades operating in combustion gas temperatures of 1450 °C. For some components, passive heat transfer, i.e. heat transfer that occurs via methods that do not require an energy input from the engineering system, are sufficient. At the more extreme temperature scales, heat transfer requires some form of work to be performed and hence has a negative effect on the

efficiency of the engineering system. This is often the pumping of a fluid such as air or water which carries heat away from the component via conduction and convection across a heat transfer device or surface. Whilst the demands on such cooling systems are increasing in the pursuit of component performance gains, the package volume available for heatsinks and ancillaries is not increasing accordingly [150-152]. AM can potentially enable highly efficient cooling designs that provide excellent heat transfer per unit volume or unit mass. Only limited investigations into AM for heat transfer, however, have been undertaken.

One method to increase the heat transfer performed by a device is to reduce the hydraulic diameter for the flow. This in turn increases the heat transfer coefficient by increasing the surface-area-to-volume ratio of the heat exchanger, forcing more interaction between the working fluid and the geometry [153, 154]. The drawback of this method is an increased pressure drop across the heat transfer device. In many cases, this causes an undesirable efficiency penalty in the system. To minimise the energy required to perform the heat transfer, such devices must be optimised for performance. TPMS lattice structures may provide the combination of a geometry that enhances flow interaction for increased heat transfer, whilst retaining a relatively free flow path to prevent excessive pressure drop. In this section, the function and performance of such devices is described, and the conventional manufacturing methods are compared to the new methods made available with AM.

2.6.1 Conventional heat transfer structures

Heatsink geometry is typically varied to optimise the heat transfer coefficient and the working fluid pressure drop across the heat transfer region. Heat transfer geometries are heavily constrained by conventional manufacturing methods such as sheet forming, extrusion [155], welding [156] or investment casting. This is especially true for

components with internal cooling features such as turbine blades, where complex cooling channels can provide the greatest benefit but simply cannot be implemented effectively via conventional investment casting manufacture [157-159].

Heat transfer surfaces within heat exchangers come in a variety of forms including tubes, corrugated/wavy walls, straight fins, bent-fins and pin-fin arrays. For high-performance components that require internal cooling, pin-fins are commonly used. Whilst these geometries are effective at increasing the surface area available for heat transfer, performance enhancement using such designs is limited. A further problem with conventional heat transfer structures is that they are mono-functional – they are only used to perform heat transfer and have limited secondary functionality. This is a problem for components that are under large mechanical loads as typically the volume that the heat transfer structures occupy reduces the overall strength or mechanical performance of the component. Pin-fins for example are restricted by their geometry to providing uniaxial tensile or compressive strength. As soon as loading is applied perpendicular to the pin-fin, the structure becomes liable to failure through shearing or bending. Other structures such as honeycombs are known for their high specific strength and stiffness, but again this is not an isotropic bulk property; the honeycomb must be deliberately orientated to take advantage of this. Further, the orientation desired for mechanical strength and that for which the structure has the best heat transfer performance is often mismatched. Hence, optimisation can only be achieved for one property.

2.6.2 Conventionally manufactured porous structures as heat transfer devices

Research has been conducted into characterising porous structures of many types that were manufactured using techniques other than AM across a range of materials and intended applications. Lu, T.J. [160] simulated laminar flow through channels containing micro-cell aluminium honeycombs (Figure 2.13 (a)). It was stated that whilst the heat

transfer performance was doubled by including the honeycomb core, further improvements could be obtained using a geometry that stimulates turbulent flow. TPMS lattice structures have ideal geometrical features that can provide disruption to the flow that results in higher turbulence. Further studies on honeycomb and corrugated structures manufactured from sheet material were conducted by Wen et al. [161]. They concluded that honeycomb structures are superior in thermal performance than metal foams, lattice-frame materials or woven structures, providing a higher heat transfer rate at a constant pumping power. However, many TPMS lattice types are more analogous to the continuous-wall honeycomb structures than to the other examples given, highlighting their potential as heatsinks. Further, the manufacture of SLM lattice structures is simplified in comparison to the stamping, forming, assembling and brazing process used by Wen et al.

Kim et al. [147] manufactured tetrahedral lattice-frame materials (LFM) from an aluminium alloy with an array of struts of 2 mm diameter for a relative density of 6% (Figure 2.13 (b)). They found that greater than 50 % of the heat input to the structure was conducted through the struts and then transferred to the coolant fluid via convection from the strut surface. This highlights the importance of ensuring the geometry chosen has good flow interaction for effective heat transfer. TPMS lattices with wall-type geometries may be particularly effective in this regard due to their high surface area to volume ratio.

Porous structures including the Schwarz Primitive TPMS structure (Figure 2.13 (c)) have been investigated by Krishnan et al. [162], where the heat transfer efficiency and pressure drop across the structures was analysed via computational methods and experimentally. It is clear that all of the porous structures tested experimentally, slotted-hexagon, fin-foam and Schwarz P, provide significant improvements in heat transfer efficiency when compared to a parallel plate arrangement. This comes with a pressure drop penalty, however, which in the case of the Schwarz P, is large enough that it cannot

be considered the best performer. Schwarz P is particularly susceptible to causing a large fluid pressure drop due to the low percentage of free-flow area in the cross-section. With direct manufacture of TPMS structures via LPBF, a more desirable TPMS can be chosen.

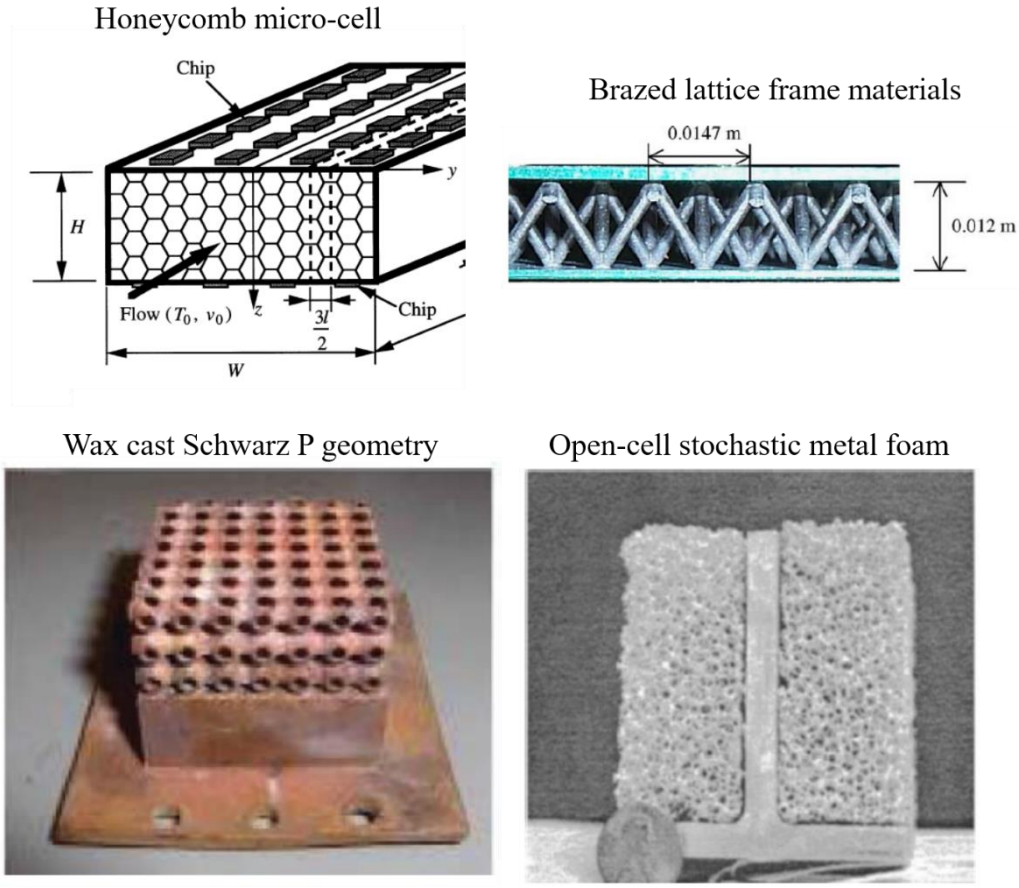


Figure 2.13 - A selection of heat exchangers using conventional manufacturing methods.

Stochastic foams were investigated by Bhattacharya et al. [163] for application in cooling of electronic chips (Figure 2.13 (d)). 90 % porosity aluminium foams with pore sizes 5 – 20 pore per inch (PPI) were joined to an aluminium heatsink frame using conductive epoxy and tested under forced convection using air as the working fluid. Even with this high-thermal resistance (when compared to metallurgical bonding) between the foam and the frame, the heat transfer coefficient was enhanced by a factor of 6 when compared to typical a finned heatsink. Using LPBF, heat transfer could be enhanced further by the metallurgical bond between the heat transfer surface and the frame.

However, this performance comes at the cost of significantly greater fluid pressure drop; with limits placed on pressure drop, performance enhancements of 1.5 – 2 times can still be achieved. Further, the foams with larger pores (5 PPI) provided a better heat transfer coefficient per unit fan power, indicating that increasing the surface area to the flow is not always beneficial to heat transfer performance. Despite the potential performance gains of stochastic foams, control of pore distribution for techniques such as functional grading is limited by the conventional manufacturing methods. Whilst the pore size and overall density can be controlled, the material cannot be placed exactly where it is desired, unlike with LPBF. This is highlighted by the 'lumping' of metal seen at the intersection of pores [164], which increases the overall density of the foam but provides no benefit to thermal transport.

2.6.3 Additively manufactured heat transfer structures

LPBF manufactured lattice structures have the potential to replace pin-fins [141, 165], honeycombs [160, 161] and sandwich panels [145, 166] traditionally employed in high performance heat transfer applications. Existing research has evaluated the convective heat transfer performance of strut-type lattice structures, however no known literature covers TPMS geometries. These geometries, particularly the wall-based (matrix phase) TPMS structures, can potentially provide greatly increased heat transfer over pin-fins or similar conventional heat transfer enhancement methods.

Kirsch et al. [140] used SLM to manufacture channels with pin-fin heat exchange arrays with a range of spanwise and streamwise spacings (Figure 2.14 (a)). Whilst the results regarding pin-fin spacing are not directly transferrable to TPMS structures, it was stated that the high surface roughness inherent to the LPBF process provides significant improvement in heat transfer due to greater interaction between the coolant flow and the geometry. Importantly, minimal gain in heat transfer was achieved through significantly

increasing the density of the pin array. Combined with the negative effects of increased pressure drop, it was demonstrated that increasing the surface area in contact with the coolant flow is not always beneficial to the overall performance of the heat exchanger.

LPBF has been used to manufacture a range of strut-type lattices, characterised by the node and element topology, where the elements are 'thickened' to form structures typically with continuous cross-section struts. Such examples are the body-centred cubic (BCC) unit cell [30] and the BCC-Z unit cell [167]. However, these LPBF manufactured lattices have not been characterised for use in heat transfer applications. This is despite conventionally manufactured samples of similar geometry being shown to perform well in convective heat transfer [148], with the potential for bi-functionality when used in combined thermal and mechanical loading [146]. The use of lattice structures in dual load applications was also identified by Gu et al. [168], who demonstrated that continuous cross-section lattice sandwich panels can be optimised for combined thermal and mechanical performance. It was shown that optimisation favoured either structural stiffness or thermal performance; both factors could not be optimised concurrently due to the geometry of the chosen strut-type lattices. The triangular geometry that provided the highest stiffness had lower thermal performance than the other geometries and the honeycomb structure with the best thermal performance had reduced mechanical strength in comparison to the triangular geometry. TPMS lattice structures have the potential to improve upon these results by providing the high specific stiffness required to meet targets for mass reduction alongside an enhanced thermal performance over strut-type lattice structures.

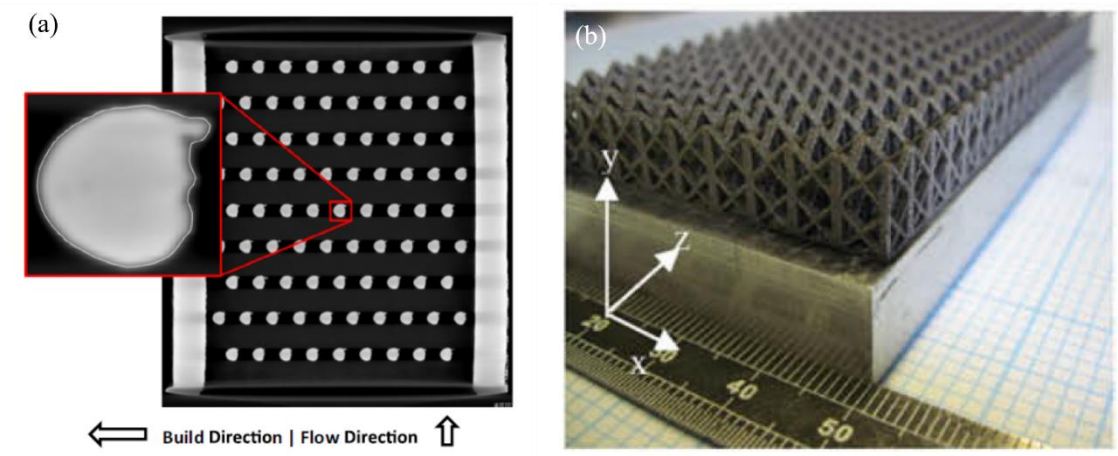


Figure 2.14 – (a) LPBF manufactured pin-fin heatsink by Kirsh et al. and (b) LPBF manufactured strut-type lattice heatsink by Wong et al.

Wong et al. [142] used LPBF to manufacture pin-fin heat exchanger designs in stainless steel (316L) and aluminium (6061). The geometries included circular and diamond cross-sections, with an additional lattice type structure consisting of elliptical cross-sections built at an angle to the substrate. The best performing geometry was the diamond as a result of the geometry forcing fluid flow to interact with each fin in such a way as to prevent a thick boundary layer from forming. This study was extended in subsequent work with a strut-type lattice that was said to be modelled on the geometries typically used as support structures in LPBF (Figure 2.14 (b)) [143]. Whilst the lattice structures chosen by Wong et al. significantly increased the surface area to volume ratio, typically the driver for effective convective heat transfer, the struts had insufficient thickness to conduct heat efficiently. Hence, the undefined BCC-Z strut-type lattice sample resulted in the lowest heat sink efficiency index rating of all geometries tested. Further, the fluid flow has poor interaction with the geometry of the lattice due to alignment of features in the fluid flow direction evidenced by the low pressure drop in comparison to its surface area. With TPMS lattices, both of these failures can be addressed. Dependent on the application, unit cells can be chosen that force the coolant fluid to frequently change direction or divert around a feature, resulting in increased fluid

interaction with the structure. Further, thick wall sections that are a feature of some TPMS structures can join hot-side to cold-side to provide a high thermal conductivity path to draw heat away from a source. Volume fraction grading can be utilised to provide this increased conductivity where it is required but keep mass to a minimum by removing material in cooler regions of the structure.

Strut-type lattices have been evaluated using custom convective heat transfer apparatus by a number of authors. However, no investigation of TPMS lattice structures is known. Certain geometrical features of the TPMS lattices, such as meandering flow paths through the structure, may be ideal for convective heat transfer. Combining this heat transfer potential with the high mechanical performance as identified earlier, the potential for implementing lattice structures in components under thermomechanical loading is clear.

2.6.4 Industry-specific heat transfer applications

To demonstrate the wide-ranging potential of lattice structures for thermomechanical applications, three case study areas are explored including two that are outside of the gas turbine industry. These were chosen as they represent potential opportunities to increase component performance using LPBF, or to demonstrate novel design features that are made possible using TPMS lattice structures.

2.6.4.1 High-power electronics

Regardless of advances in computing performance and efficiency, Ohmic heating will always generate waste heat as current flows through electronics. Excess heat acts to significantly reduce the lifespan of these components and decreases the mean time between failures, hence careful consideration of cooling designs must be taken to ensure adequate cooling of components. As computational power becomes essential to the operation of an increasing number of engineering systems, electronic chips are being used

at a higher density and in more restrictive packages. This presents a problem of removing sufficient heat from the components without dedicating large volumes of space to heatsinks. LPBF manufacture of lattice structures for use in heat transfer applications may be able to provide a lightweight, low-profile solution.

The highest performing heatsinks for electronics are achieved using water cooling or phase-change cooling [169], in some cases even fully submerging the electronics in a dielectric fluid [170] [171]. Such methods are too complex in many scenarios, requiring additional systems dedicated to cooling. This often leaves air cooling as the only viable option. For low-power components or those under intermittent thermal loading, heatsink designs which aid in natural convection are sufficient [172]. For high-power components, forced convection using a fan is the common method to achieve greater cooling power. This generally involves large, heavy heatsinks that are manufactured from aluminium or copper using methods including extrusion, machining, bonding and skiving [173]. As the axial fans used for convection cannot provide a high-pressure airflow, even with ducting, the pressure drop across the heatsink must be low. Pressure drop is directly proportional to the surface-area-to-volume ratio (SA:vol), hence cooling performance is limited by the available coolant pressure in high SA:vol heatsinks.

2.6.4.2 Gas turbine nozzle guide vane

Gas turbines operate at the extreme of high-temperature operating environments, where components have to endure gas temperatures of above 1400 °C continually for a typical operating life of 30,000 hours between component overhaul [174]. Whilst material science innovations such as thermal barrier coatings have pushed this operating temperature above the melting temperature of the nickel superalloys used in hot-section turbine components, further operating temperature increases are limited by the ability to cool the base material. Nozzle guide vane (NGV) internal cooling passages use bleed air from the compressor stage of the turbine engine to force air at high-pressure (3 – 5 bar

above ambient turbine section pressure) through cooling passages. These passages are augmented with ribs or pin-fins that increase the surface area for heat transfer and enable greater cooling efficiencies (Figure 2.15) [175]. The complexity of the internal cooling features is limited, however, by the accuracy and repeatability of the current class manufacturing method, investment casting [176]. Using LPBF, these limitations can be overcome, and new cooling geometries can be explored. Lattice structures are an ideal candidate for this application due to the high surface-area-to-volume ratio, enabling a large surface area for heat transfer to be placed in narrow passage or in thin regions between walls. Further, the material density or flow permeability of the structures can be easily adjusted to provide tailored heat transfer performance in different regions of the component. Mechanical integrity of the components is also improved by implementing lattice structures. For an NGV, impact resistance is an important mechanical design aspect as any foreign object ingested into the turbine, or any component failure upstream of the turbine section, will risk damaging the NGV. Design engineers also have the opportunity to optimise the lattice for energy absorption alongside thermal performance, utilising lattice structures for multiple functions.

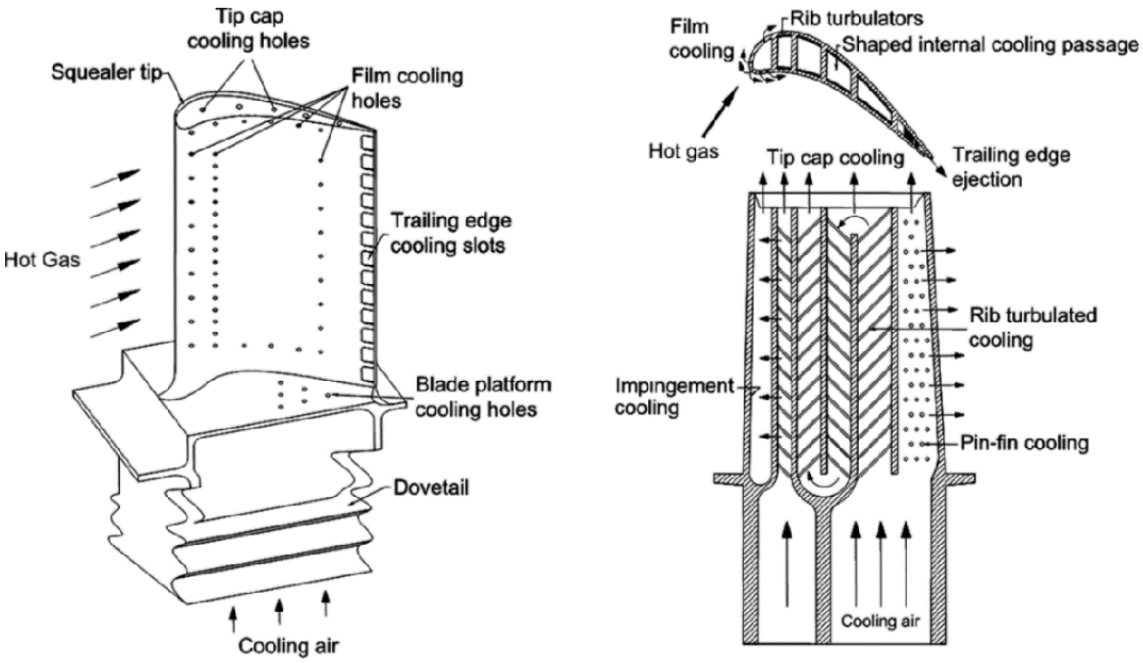


Figure 2.15 - Cooling strategies for a gas turbine blade (NGV cooling uses similar features). Ribs and pin-fins used for enhancing heat transfer may be replaced by lattice structures. Image taken from [175].

2.7 THE RESEARCH GAP

Nickel superalloys with a high γ/γ' ratio microstructure have the best high-temperature performance for gas turbine applications. In order to be used in LPBF, attempts must be made to adapt the process to reduce the thermal gradients that result in cracking of these alloys. The options for scan strategies in current-class machine software may be improved with the aim of reducing cracking. If new scan strategies can be developed that provide a more isotropic thermal profile, high-performance alloys such as CM247LC can be adopted for LPBF. Fractal patterns show promise from simulations in the literature, but no research has tested the experimental application of these scan strategies. Further, knowledge gained with these scan strategies can be applied to other material systems that suffer from high residual stresses in LPBF, such as Ti6Al4V. This would improve the overall performance of LPBF systems and would enable further materials to be adapted for the process, a current weakness of AM over conventional manufacturing methods.

Hastelloy-X is still developing as an alloy for use in LPBF. Manufacturers require this alloy for its versatility in hot and corrosive environments across the gas turbine, power generation and chemical industry. The majority of research on this alloy focuses on process parameter optimisation, with little research developing lattice structures manufactured in this alloy for end-use LPBF components. With the mechanical and thermal performance of lattice structures manufactured in Hastelloy-X, the industrial value of this alloy for LPBF is increased. Confidence can be gained in the performance of lattice structures for high-temperature, corrosive environments, as well as for the suitability of Hastelloy-C for LPBF. Without this important work, existing Hastelloy-X components that would benefit from a design incorporating lattice structures may be overlooked.

Lattice structure mechanical properties have been explored in the literature however the focus is generally on a narrow set of geometries or evaluation of a specific feature such as failure modes. For an effective design tool to be developed, it is necessary to evaluate a wide range of structures in the same material and manufactured using the same process to ensure an even playing field. By evaluating the thermal performance of seven different structures in Hastelloy-X, this can be achieved. Further, through testing pre- and post-heat treatment, the effect of material condition can be evaluated. This is an important step for industrial use where heat treatment of LPBF components is considered a necessity in most applications. Currently, a comprehensive study on TPMS lattice structures that incorporates these features is not available in the literature.

Academic research of heat transfer structures manufactured by AM is limited, even when considering conventional geometries such as pin-fins, honeycombs and narrow channels. Whilst the end-use gas turbine components identified earlier are design optimised for manufacture by LPBF, they do not utilise lattice structures to enhance the performance of the components. This is a result of a lack of performance data regarding lattice structures in areas outside of mechanical properties, or restricted funding to pursue the necessary low-level research internally. This highlights the need for fundamental research on the characteristics of lattice structures for such geometries to be adopted by the industry.

To fully understand the thermal performance of different lattices, the modes of heat transfer, conduction and convection, must be analysed separately. The high degree of complexity makes simulation of heat transfer very computationally expensive. Moreover, confidence in the results cannot be assured due to the geometries being unlike those for which the conventional FE and CFD software are developed and optimised for. Therefore, the most accurate and efficient method of determining the properties is via experimentation. No commercially available apparatus exist for characterising these

properties. To satisfy the requirements of industry for application of lattice structures in heat transfer, it is proposed that a custom apparatus must be developed that is tailored for thermal evaluation of lattice structures.

To the knowledge of the author of this thesis, there are no available literature resources regarding TPMS lattice structures for convective heat transfer outside of those published as part of the work towards this thesis. The performance of TPMS lattice structures under pure conductive heat transfer must be explored before continuing to characterise forced convection heat transfer. The results of the pure conduction heat transfer experiments will enable their use in basic applications and act as a precursor to understanding the convective heat transfer performance of lattices. The performance curves that will be generated from the convective heat transfer testing apparatus can be directly used to specify an appropriate lattice structure for a given heat transfer application. Once this outcome is achieved, the data from experimentation can be fed back into simulation software as required to verify the model, enabling iterative design techniques and lattice optimisation for a given component.

The gap in research providing a comprehensive evaluation of lattice structures for mechanical and heat transfer applications impedes industrial adoption of these geometries in component design. This thesis aims to provide the data required for design engineers to implement TPMS lattice structures in components that are under mechanical, thermal or thermomechanical loading.

3 METHODOLOGY

3.1 INTRODUCTION

This Chapter outlines the equipment and techniques used in the characterisation of the experimental work. Samples for the work in this thesis were manufactured on a variety of commercial LPBF machines and the analysis of the samples required a range of techniques in areas such as sample preparation, microstructural characterisation, heat treatment and mechanical testing. The methodology of these techniques is described in this Chapter.

3.2 FEEDSTOCK POWDER CHARACTERISATION

3.2.1 PARTICLE SIZE DISTRIBUTION

Particle size distribution (PSD) is an important characteristic of the feedstock powder that determines its ability to be spread and packed evenly and consistently in LPBF. If the feedstock does not have the correct PSD, processing defects such as porosity, increased surface roughness and build failure can occur. The PSD of the feedstock powder is determined using a Malvern Mastersizer 3000 laser diffraction particle size analyser with Aero S dry powder dispersion unit (Malvern Instruments Limited, Malvern, UK). In this apparatus, a falling stream of dry, dispersed powder passes through a chamber where two laser beams (red: 632.8 nm, blue: 470 nm) illuminate the particles. A number of detectors measure the intensity of the laser light scattered by the particles from a range of different angles. This laser intensity data can be directly correlated to the size and size distribution of the powder particles using the Fraunhofer diffraction theory and Mie scattering theory, automatically calculated in the Mastersizer 3000 software. The size range of measurable particles is 0.1 – 3500 µm and the measurements have an accuracy of < 0.6 % with a repeatability of < 0.5 % variation.

3.2.2 Chemical composition

Determining the chemical composition of the feedstock powder can be a lengthy and complicated process requiring multiple analysis techniques. Wherever possible, chemical composition of the powder is obtained from the manufacturer. Data obtained in this way is clearly marked in the later sections. Where chemical analysis is performed internally, the first technique used is EDS. This is the most accessible technique in the lab and provides accurate data on metallic alloying elements. However, it cannot accurately quantify oxides and lighter elements.

3.3 Laser powder bed fusion manufacture

Manufacture via LPBF requires specific pre- and post-processing steps to turn a computer model (CAD model) into a part. These include software and hardware processes that are sometimes universally applied regardless of the component or may be proprietary steps exclusive to certain machine manufacturers or steps required only in certain circumstances. The process taken to manufacture the parts under investigation in this thesis are described in this section.

3.3.1 Software pre-processing

Computer models that are to be printed are first exported in .stl file format using the CAD software. This format is the standard for 3D models in AM and is not proprietary to any manufacturer. However, the models are prone to errors due to their use of a mesh of triangles to represent the part as described in the section 2.2. Such errors include overlapping or intersecting triangles, holes in the mesh and noise shells (small internal or external volumes). All fixing steps are performed in the software package Magics (Materialise, Leuven, Belgium). The .stl files can also be optimised in this step to improve the geometry or reduce file size. Due to the triangulation of surfaces, smooth surfaces can only be approximated. The required resolution of this approximation is dependent on the

resolution of the AM process and the geometry of the component. For LPBF with a resolution of ~100 µm, a minimum triangle size of 20 µm provides a surface representation that is sufficiently accurate to manufacture the component whilst ensuring the file sizes do not become bloated. Further, if the component contains curved faces with tight radii, a small triangle size must be chosen to prevent the curve being represented as a series of facets that will result in dimensions being out of tolerance (Figure 3.1 (a)). This is particularly important for lattice structures as they contain a number of smooth surfaces with tight radii that can become highly distorted if an incorrect .stl resolution is chosen. It is desirable to appropriately define this during the initial .stl generation. Using Magics, the triangle mesh can be refined as necessary if the geometry is too rough, or coarsened to reduce file size if the mesh resolution exceeds the resolution of the AM process. Once the fixing has been performed and the mesh errors have been solved, this mesh is now described as 'watertight' and can be advanced to the next pre-processing step.

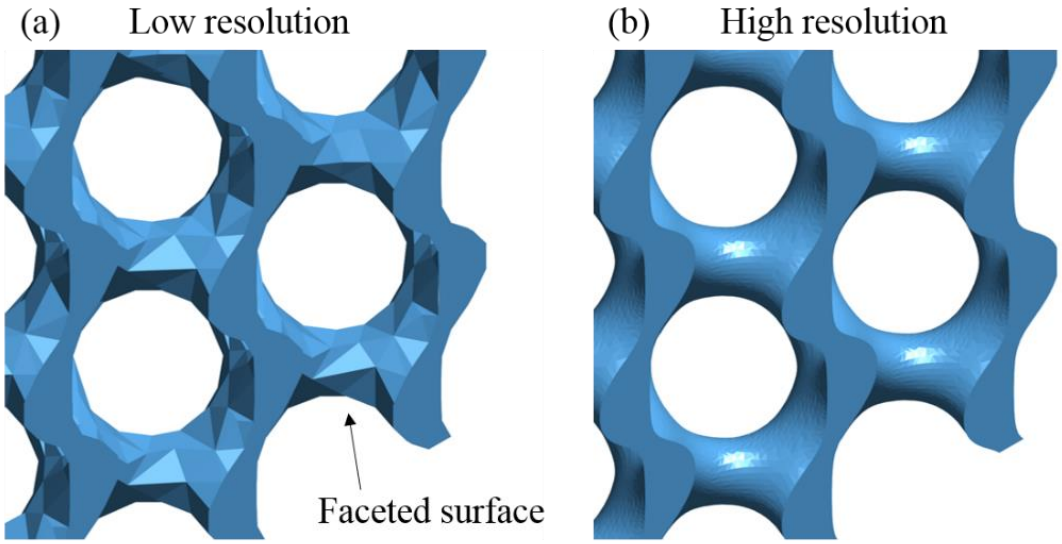


Figure 3.1 - Illustration of the effect of .stl triangle size (resolution). If too low of a resolution is used, smooth curved surfaces will be rendered as facets (a) and build quality and dimensional accuracy will be degraded. A correct resolution results in smooth curved surfaces (b).

3.3.2 SUPPORT GENERATION

In most cases, even for simple parts such as cubes, support structures are required. They form an interface between the part and the baseplate, anchoring the part to secure it during the LPBF process. Due to rapid heating and cooling that occurs in the LPBF process, large residual stresses can build up in the parts resulting in forces that act to deform the part. Support structures act to constrain this deformation which may otherwise result in geometrical inaccuracies or build failure if the part comes into contact with the powder re-coating system. Further, the support structures act as a conduction pathway to draw some heat away from the part during the build. For small, simple parts such as cubes used for process parameter development, support structures also provide an easy and quick way to remove the part from the baseplate using a hammer or other hand tools. This is in contrast to using wire-EDM for part removal, the more costly and time-consuming method required for larger LPBF builds.

Support structures can be automatically generated in Magics. The type and placement of support structures varies greatly depending on the part geometry. Typically, all angles greater than 45 ° relative to the build plane need to be supported. For all cube samples manufactured as part of this thesis, ‘block’ and ‘line’ supports were used in Magics (Figure 3.2), with a spacing between walls appropriate for the size of sample being manufactured. Removing the border teeth leaves a single thin wall around the border of the part that provides improved adhesion of the part to the built platform.

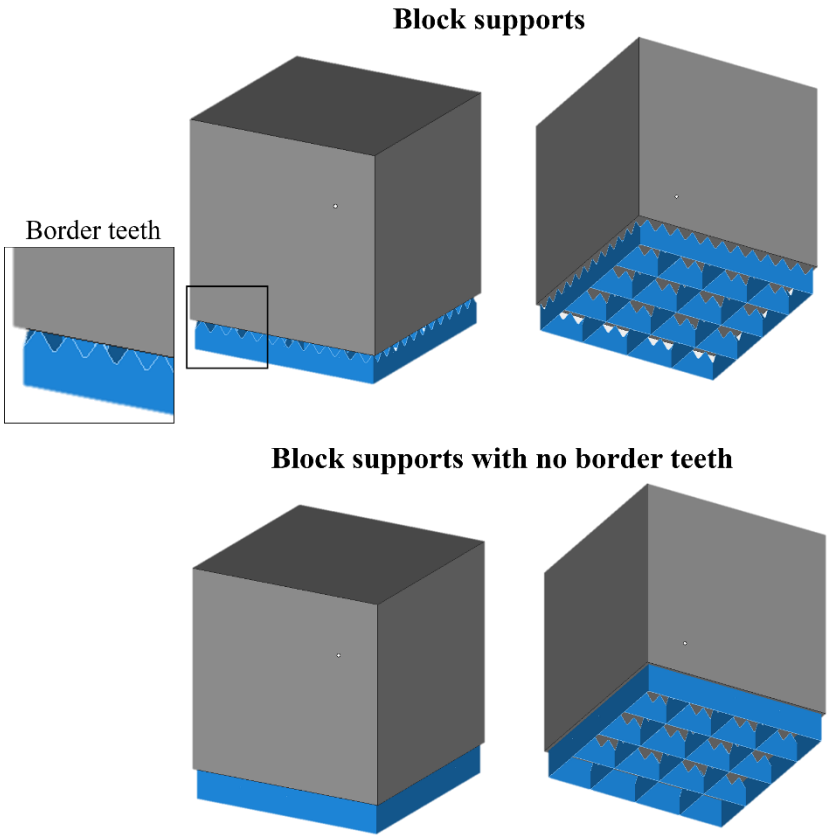


Figure 3.2 - Block supports generated in Magics, with and without border teeth. Removing border teeth aids part adhesion with the build platform.

3.3.3 LATTICE STRUCTURE SPECIFIC SUPPORT REQUIREMENTS

Many lattice geometries are self-supporting in principle, however if they are not contained within a component where the outer lattice cells are connected to a wall, there are often overhanging features. Overhangs will begin to build directly on the loose powder without any solid material connected directly beneath. This will result in inaccurate manufacture of these regions and may also result in warped features that interrupt the re-coat wiper and will cause the build to fail. To prevent this, care must be taken to analyse each sample to ensure there are no unconstrained overhangs.

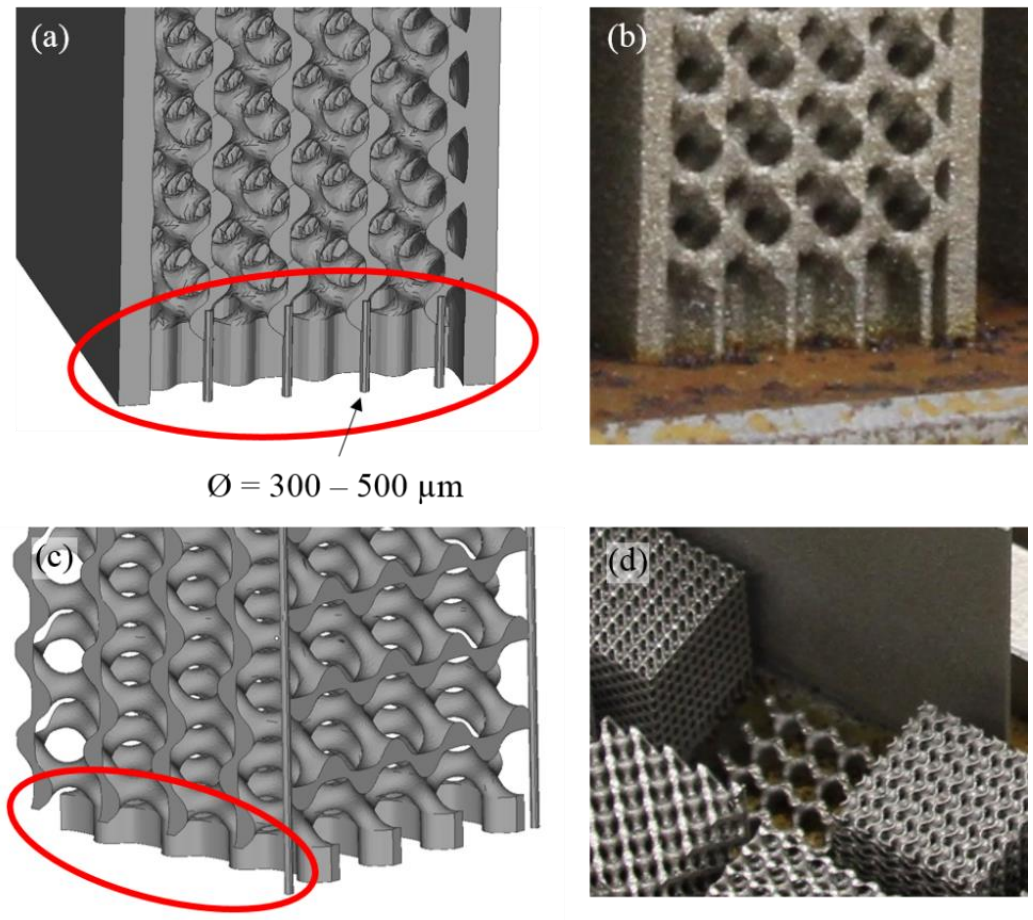


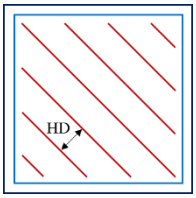
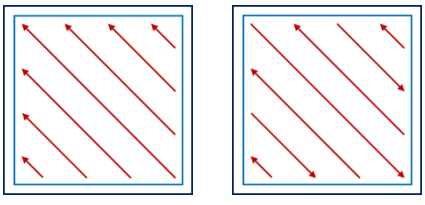
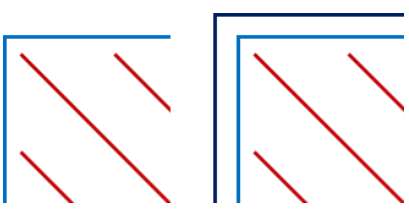
Figure 3.3 - Lattice structures that require additional supports. (a) Small cylinders are added to attach the overhanging feature to the build plate for the gyroid network geometry. The same sample as built (b). In (c), the supports were not added, resulting in build interruption (d).

The placement of these supports is illustrated in Figure 3.3 for the gyroid network lattice structure. In Figure 3.3 (a), despite the structure being mainly contained by solid walls, four small overhanging regions remain. These were supported using 300 µm diameter cylinders which can be easily removed using side cutters after the build. In Figure 3.3 (c), these same features were left unsupported, resulting in a build failure for this sample (Figure 3.3 (d)). Fortunately, the issue was identified early and the single sample could be simply removed from the build program without interrupting the remaining samples.

3.3.4 SLICING AND APPLYING PROCESS PARAMETERS

The LPBF machines must be supplied with files that contain the solid part and support structure broken down into slices of a constant thickness. These slices are taken in the Z-direction of the part and represent a series of XY-plane cross-sections. Slicing is performed in Magics with a user defined layer thickness, typically 20 µm for a high-resolution build or 40 µm for a shorter build time. CM247LC builds were conducted at 25 µm layer thickness and all Hastelloy-X builds were conducted at 40 µm layer thickness. Process parameters are applied in the LPBF machine manufacturer software. Table 3.1 shows the parameter options available for the Realizer SLM50 using RDesigner software (Realizer GmbH, Borchen, Germany).

Table 3.1 - Process parameter options in the LPBF software with examples given where applicable.

Parameter name	**Unit**	**Range**	**Example**
Laser power	W	0 - 120	
Scan speed	mm/s	0 – 2000	
Hatch distance	mm	> 0	
Hatch pattern (*scan strategy*)	N/A	Uni-directional, meander, island	
Contour scan	N/A	Single, double	

3.3.5 LPBF MACHINE PROCEDURE

The simplified machine diagram in the section 2.2 shows the key components including the build chamber, build plate, powder re-coater system and laser scan head (galvanometer). Ancillaries include an inert gas supply (argon for reactive alloys including aluminium, titanium and nickel; nitrogen for stable alloys including steels), water chiller for cooling the laser and a PC for control. Once the CAD model has been processed into the applicable build files and sent to the machine, the machine can be prepared for operation. The baseplate is degreased using isopropranol and screwed into the machine. It is then manually lowered using the machine control software until the top surface of the build plate is level with the machine bed. The powder hopper is filled with the feedstock powder and the machine control software is used to advance the powder through the feed system and into the re-coat system. The machine door is then closed and secured using the door latch. Once the machine is sealed, the inert gas purging system can be activated to remove all oxygen from inside the build chamber, preventing any oxidation of the feedstock powder during the process [177]. The chamber is purged once the oxygen level reaches 0.05 % or 500 ppm (or lower). If required, the build plate heater is also activated. This is a commonly used method to help reduce distortion resulting from thermally induced stresses in LPBF [178-180]. Throughout the experiments in this thesis, a maximum build plate temperature of 250 °C was used. The final stage is to set the laser focus position to 12.1 mm, which corresponds to a laser spot size of 50 µm. The machine is now fully prepared for the build process.

3.3.5.1 REALIZER SLM50 MACHINE SPECIFICATION

All CM247LC and Hastelloy-X as-LPBF samples were manufactured using a Realizer SLM 50 desktop-scale LPBF machine with a build volume 70 mm in diameter and 80 mm Z-axis height. It is equipped with an IPG Photonics continuous wave ytterbium fibre laser (YLM-100-AC) source with a wavelength of 1070 nm and a

maximum power output of 120 W. During processing, the build chamber was purged and continuously flushed with argon to create a working environment of <0.5 vol% O_2 to inhibit oxidation.

3.3.5.2 EOS M290 MACHINE SPECIFICATIONS

All Hastelloy-X HIP+HT samples were manufactured using an EOS M290 LPBF machine. It is a medium-frame machine with a build volume of 250 x 250 x 325 mm, equipped with a 400 W continuous wave ytterbium fibre laser. As previously, the build chamber is purged with argon throughout the build to maintain a target 100 ppm O_2 working environment to inhibit oxidation.

3.4 METALLOGRAPHIC TECHNIQUES

Samples manufactured via LPBF undergo a range of analysis techniques to assess quality metrics such as porosity, cracking, bulk density, grain structure and geometrical accuracy. This section outlines the preparation procedures and the analysis techniques used in this thesis.

3.4.1 METALLOGRAPHIC SAMPLE PREPARATION

The most common sample preparation technique is resin mounting. This allows samples to be sectioned and polished for easy investigation under OM, SEM and other techniques. Defects can occur between layers (e.g. oxide and spatter inclusion) or during the deposition of a layer (e.g. lack of fusion, balling). Therefore, it is important to section the samples in a way that allows multiple planes or orientations to be analysed. For bulk density and microstructural analysis, the samples are sectioned in the XY and YZ planes (Figure 3.4) using a Brilliant 220 cut-off saw (ATM GmbH, Mammelzen, Germany) with a 125 mm diameter SiC cut-off disc and continuous water coolant flow to prevent microstructural changes due to localised heat input during cutting.

For hot resin mounting, the sample sections are encased in carbon-filled conductive mounting resin. The sample and resin go through a cycle of heating to 177 °C at a pressure of 28 MPa for 9 minutes followed by water cooling for 2 minutes. The mounted sample is then removed from the hot mounting press for grinding and polishing.

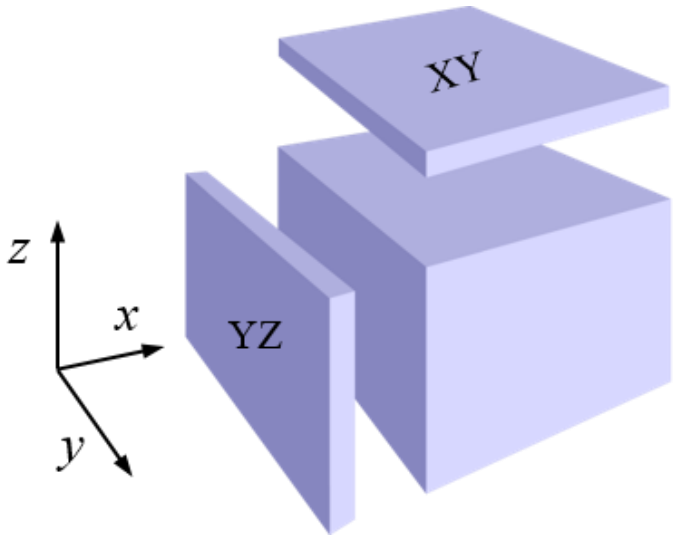


Figure 3.4 - Illustration of the XY and YZ sections cut from a LPBF sample for bulk density and microstructural analysis.

3.4.2 METALLOGRAPHIC GRINDING AND POLISHING

Samples must be taken from the raw mounted form to a near-mirror polish finish for metallographic inspection. This is achieved by progressively finer grit grinding followed by diamond polishing. Grinding is divided into two processes: plane grinding (PG) and fine grinding (FG). PG is the initial high removal rate grinding step that ensures all of the samples have equal, flat (plane) surfaces with no sharp edges or protrusions. FG takes the plane surface and reduces the surface roughness using progressively finer grit abrasives. After grinding, the surface is polished using either diamond paste or a solvent based diamond suspension. This provides a surface that is ready for viewing under OM or SEM.

Depending on the number of samples and the alloy type, the preparation can follow a manual method using SiC grinding discs or a semi-automated method using specialised magnetic grinding discs attached to a Struers LaboPol-5 grinder with LaboForce-3 motorised specimen holder. The steps for both methods are outlined in Table 3.2.

Table 3.2 - Steps taken to grind and polish a sample for metallographic inspection. Different routes are taken depending on whether manual or semi-automated sample preparation methods are used. The grit sizes and equivalent micron-sizes are given along with any special grinding or polishing disc required

	Manual method	**Semi-automated method**
Plane grinding	SiC 240-grit (50 µm)	SiC 240-grit (50 µm)
Fine grinding	SiC 400-grit (18.3 µm)	Struers MD-Piano 500
	SiC 800-grit (7.8 µm)	
	SiC 1200-grit (3.8 µm)	
Polishing	6 µm diamond paste	Struers MD-Largo with 9 µm DiaPro diamond suspension
	1 µm diamond paste	Struers MD-Dac with 3 µm DiaPro diamond suspension
Fine polishing	Struers MD-Chem with 0.04 µm colloidal silica	Struers MD-Chem with 0.04 µm colloidal silica

3.4.3 ETCHING TO REVEAL MICROSTRUCTURE

Grinding and polishing provides a clear view of the sample top surface but does not reveal any microstructural texture. Viewing the microstructure is desirable as it provides clues about cooling mechanisms and rates, metallic and non-metallic phases in the sample and defect formation. Additionally, defects may be concealed by material smearing, leaving a thin film of material over pores or cracks. This problem is especially prevalent with softer materials such as aluminium alloys but can also occur with harder materials such as steels, titanium and nickel alloys. Etching may be performed to dissolve any thin films and reveal the concealed defects.

Etchant type depends on the base alloy; the etchant used for the alloys featured in this thesis are given below (Table 3.3). For Ni-based superalloys, Kalling's No.2 etchant is swabbed over the surface of the sample using cotton wool 5 – 10 times. Regular checks using OM can confirm the level of etching as it varies depending on the sample. In some cases, it is beneficial to over-etch the sample and then repeat the penultimate polishing step as above. However, this etchant did not work for Hastelloy-X in as-LPBF and HIP + HT conditions. Instead, electrolytic etching was used with the etching solution provided in Table 3.3 with an etching voltage of 6 Vdc.

Table 3.3 - Metallographic etchants used to reveal microstructure for the alloys featured in this thesis. The name and composition of the etchant is provided

Alloy	Etchant	Composition
Ni-superalloy (CM247LC, Hastelloy-X)	Kalling's No.2	5 g $CuCl_2$, 100 ml HCl, 100 ml ethanol
	Electrolytic (6 Vdc)	5 g oxalic acid, 95 ml HCl

3.5 SAMPLE CHARACTERISATION

3.5.1 OPTICAL MICROSCOPY (OM)

OM was performed using a Nikon Eclipse LV100D microscope in reflected illumination mode for metallographic inspection. A range of objective lenses (5X, 10X, 20X, 50X) were used as appropriate. For quick visual inspection i.e. when checking etching level, the eyepiece was used alone. For bulk density analysis, high-resolution images were captured using a Nikon Digital Sight DS-Ri1 column camera, with the images stitched together using the Nikon software.

3.5.1.1 CRACK AND PORE ANALYSIS

A high resolution, wide-area view of each polished cross-section was captured via OM. To analyse the cracking and porosity within the samples, the image processing software core package ImageJ [181] with the Fiji plugin bundle [182] was used, following the image processing steps outlined in Figure 3.5. A threshold was applied to each region of interest (ROI) to isolate the cracks and pores, followed by a noise reduction step. The cracks and pores were then isolated independently by applying geometrical constraints. A pore was defined by having a circularity of > 0.50 and an aspect ratio of < 3.0, whilst a crack was defined by having a circularity of < 0.50 and an aspect ratio of > 3.0. These values were determined by testing a range of values and manually quantifying the accuracy of the crack and pore isolation in the images. The image data was exported for quantification of defects and sample density.

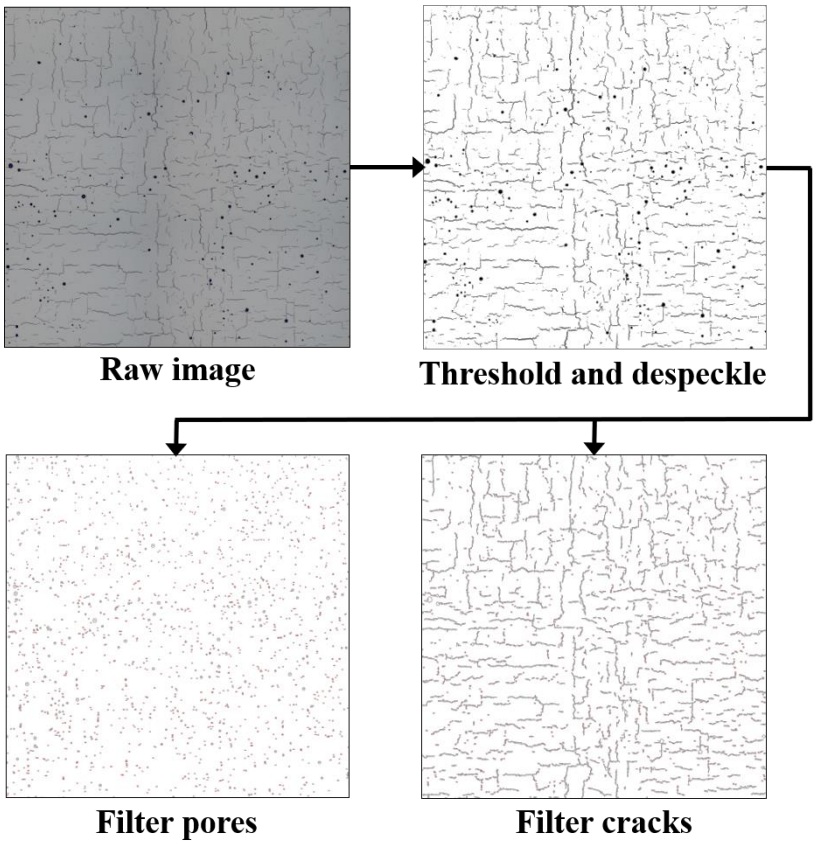


Figure 3.5 - Sequence for crack and pore filtering using image processing software ImageJ. A threshold is applied to the raw image leaving only the pores and cracks in black against a white background. Despeckle is used to remove any small noise pixels left behind. The cracks and pores are filtered independently by altering parameters for the aspect ratio of thresholded features.

3.5.2 SCANNING ELECTRON MICROSCOPY (SEM)

SEM is a versatile method for materials characterisation. A focussed beam of high-energy electrons (5 – 20 kV) bombards the surface of the sample. The incident electrons interact with the atoms that make up the sample and a variety of signals are produced from the surface as a result (Figure 3.6). Low energy (< 50 eV) secondary electrons (2e) are released from the top 10 nm of the surface as a result of ionisation of the sample atoms. As the low energy electrons can only escape from the very near surface, they provide excellent information on surface topography in SEM. Backscattered electrons (BSE) are electrons from the incident beam that are elastically scattered at high energy by the atomic nuclei of the sample. Backscatter is a function of atomic number of the sample material; elements with a high-atomic number scatter electrons more strongly and hence appear brighter in the image. This element-dependent scattering can be used to show contrast between different chemical compositions and is useful in identifying alloy elements and phases in the sample.

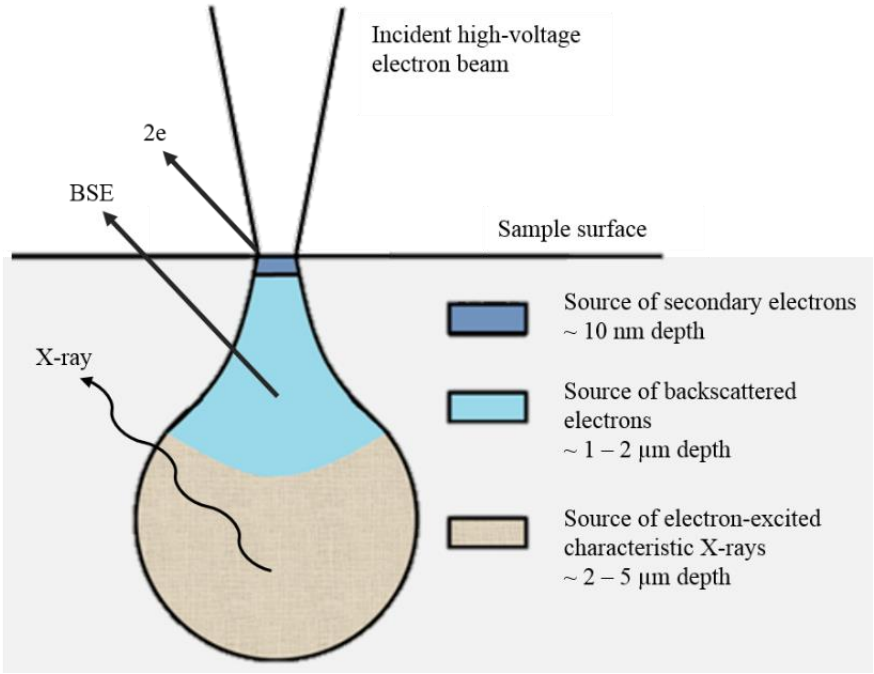


Figure 3.6 - Interaction between the high-energy electron beam of an SEM and the sample surface. The depths from the sample surface at which secondary electrons, backscattered electrons and characteristic X-ray signals are released are given.

3.5.3 Energy dispersive X-ray spectroscopy (EDS)

EDS is a method for determining the chemical composition of samples and the sensors required are typically integrated into SEM. Hence, it is a fast and convenient compositional analysis technique. Electron bombardment from the SEM beam excites electrons in the atoms of the sample, causing ionisation or the release of an electron from the atom shell. When an electron from a higher energy level shell drops into this gap, a characteristic X-ray is released with an energy directly related to the elemental composition of the emitting atom. Through detection of these characteristic X-rays, the chemical composition of the sample can be mapped. These can be 2-D area measurements over a specified region of the sample or line-scan measurements, useful when determining compositional changes over a boundary or between different metallic phases. In this thesis, EDS was performed using a Philips XL-30 SEM equipped with Oxford Instruments X-Max EDS detector, with data processed using the INCA software.

3.6 MECHANICAL TESTING

Two mechanical testing methods were used in this thesis. The testing apparatus data and settings for micro-hardness and compressive testing are given in this section.

3.6.1 MICRO-HARDNESS TESTING

All hardness tests were performed with a Wilson VH3100 automatic hardness tester with a Vickers indenter (pyramid-shaped diamond tip with 136 ° angle) at 0.5 kg load and 10 s dwell time of force application. Testing was conducted in accordance with ASTM E92-17 [183]. Measurement of the indentations was conducted automatically by the testing machine using a 50X magnification objective lens and images taken during measurement were manually verified for correct focus. Where grid arrays of indentation were made, each indentation was placed at 500 µm spacing to avoid the effect of local strain hardening from neighbouring points.

3.6.2 COMPRESSIVE TESTING

Uniaxial compressive testing was performed using an Instron 5958 static testing system with a 250 kN capacity load cell. The samples were loaded in the direction equivalent to the LPBF build direction at a strain rate of 1 mm/min, with the test terminating at 50 % strain. Deformation data for strain measurement was collected using linear variable differential transformer (LVDT) gauges placed on each side of the sample as viewed from the front. Each test was video recorded from the front view at 1920x1080 resolution and 60 frames per second for visual evaluation of the deformation and failure modes. Young's modulus was determined by calculating the gradient of the elastic region on the stress-strain plots. Yield strength was determined using the 0.2 % offset method, using the same gradient line as calculated for Young's modulus.

4 MATERIAL AND PROCESS EVALUATION FOR MANUFACTURE OF LATTICE STRUCTURES

4.1 INTRODUCTION

This Chapter outlines the materials used in later experimental Chapters and the processes used towards adapting the LPBF process for new materials to reach the required standard for manufacturing samples. Initially, the nickel-based alloy CM247LC was chosen due to being the current material of choice for manufacture of nozzle guide vanes by Siemens Industrial Turbomachinery. The high thermal gradients experienced during manufacture via selective laser melting result in cracking of this high γ/γ′ Nickel based superalloy. The commonly employed methods to reduce the build-up of thermally induced stresses, including island scanning and double scanning each layer did could not achieve acceptable density levels or result in eliminating cracking.

To improve upon this, novel fractal scanning strategies based upon mathematical fill curves, namely the Hilbert and Peano-Gosper curve, were explored. Here, short vector length scans, in the order of 100 µm, were used as a method of reducing residual stresses. The effect on cracking observed in CM247LC superalloy samples was analysed using image processing, comparing the novel fractal scan strategies to the conventional island scans. Scanning electron microscopy and energy dispersive X-ray spectroscopy was utilised to determine the cracking mechanisms.

Ultimately, cracking could not be reduced to an acceptable level with the fractal scan strategies, and hence an alternative nickel-based alloy, Hastelloy-X was used for manufacture of samples thereon. This alloy is considered more weldable than CM247LC, resulting in higher bulk density with no cracking. HX is used primarily for hot-section components such as combustors, transition ducts and afterburners for its high corrosion and oxidation resistance. It is not suitable for application in turbine blades or vanes, as is the use case for CM247LC. However, it is an equally important alloy for gas turbine manufacturers as many components manufactured in HX have the potential to be

improved upon using LPBF and lattice structures. As the thermal properties of CM247LC and HX are near-identical, it is possible to translate the results obtained in later thermal evaluation of lattice structures between the two materials. In this respect, there is no penalty associated with using HX to achieve the aims of this thesis as outlined in section 2.3.3. The outcomes from process parameter development for HX is described later in the Chapter.

In characterisation of the HX material, optical microscopy and SEM were used to confirm the near-100 % dense bulk material obtained using the optimised parameter set. The improvement in density seen after HIP was also evaluated. Further, micrographs of the samples after etching showed the evolution of grain structure seen from as-LPBF condition through HIP and HT. This grain structure is used later in the thesis as reasoning for changes in mechanical properties of the manufactured samples (section 5.2 onwards).

Finally, focus variation microscopy was used to investigate the surface morphology and roughness of the manufactured samples. This is an important factor to consider when evaluating the performance of lattice structures in convective heat transfer (section 8.3 onwards), as surface roughness affects the degree of interaction between the fluid and the geometry, and as a result, the pressure drop and heat transfer characteristics.

4.2 MATERIAL CHARACTERISATION

4.2.1 CM247LC FEEDSTOCK POWDER CHARACTERISATION

The powder used for experimentation was supplied by LPW Technology Ltd. Analysis with a Malvern Mastersizer 3000 indicated the particle size distribution seen in Figure 4.1 (a) with range 11.2 – 76 µm, D_{10} = 19.8 µm, D_{50} = 32.8 µm, and D_{90} = 53.0 µm. SEM micrographs of the bulk powder confirmed a morphology characteristic of the gas atomisation powder manufacturing method. These properties are conducive to satisfactory flowability and close packing density in the powder bed. However, numerous particles has satellites (smaller particles adhered to the outside) and conjoined particles (particles of roughly equal size joined together) were frequently seen. Despite this and the presence of many irregular shaped particles dispersed throughout Figure 4.1 (c), the powder was determined to have a flowability index of 14.62± 0.4 s/50g, using a Hall flowmeter funnel in accordance with the ASTM standard B213 [184]. This indicates a high powder flow rate which was confirmed from qualitative evaluation during use, with excellent flowability and no clumping seen.

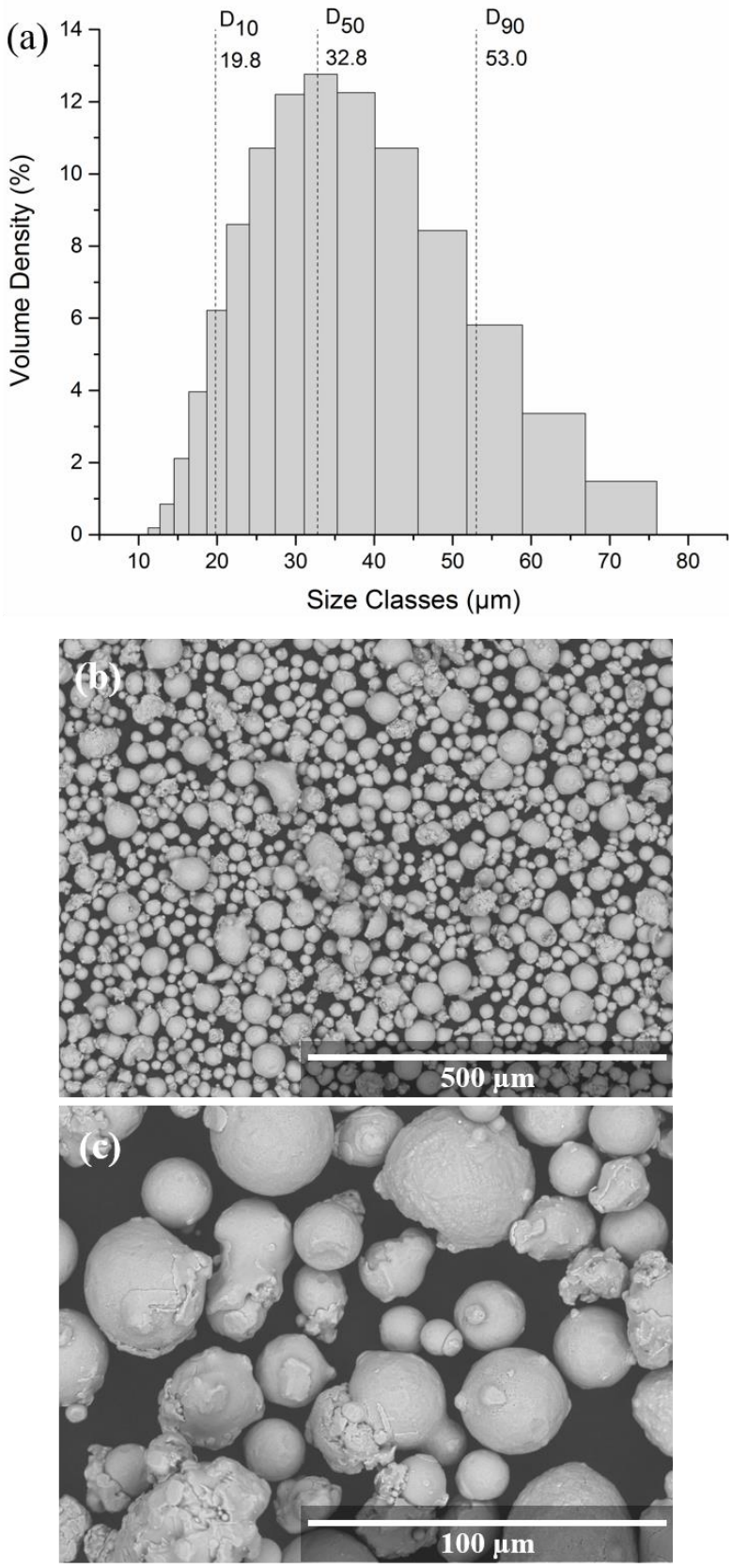


Figure 4.1 - a) CM247LC laser diffraction powder size distribution histogram, b) 200X SEM micrograph showing the distribution of particle sizes and c) 1000X SEM micrograph showing largely spherical particles but with some satellites and irregular shapes.

The elemental composition of the virgin powder was analysed by EDS with the composition given in Table 4.1, calculated as an average of three square maps with a count time of 300 seconds per map. It can be seen that the actual composition of the feedstock has a decreased weldability than the nominal composition due to the greater quantity of aluminium and titanium, the alloying elements that dictate the overall weldability [103]. The relationship between weldability and Ti/Al content is given in section 2.3.2. Overall, the actual feedstock has a greater contribution of every alloying element except for tungsten when compared to the nominal composition. However, each element remains within the limits specified. Some elements could not be quantified due to the low concentrations and detection limits of the EDS sensor.

Table 4.1 - Elemental composition of the CM247LC powder supplied by LPW compared to the nominal composition specified for the alloy [66]

	Ni	**Al**	**Cr**	**Co**	**Ti**	**Ta**	**Mo**
Nom.	61.7	5.6	8.1	9.2	0.7	3.2	0.5
Act.	64.6	6.8	8.5	9.2	0.9	5.1	0.7
	W	**Hf**	**C**	**B**	**Zr**	**Si**	**S**
Nom.	9.5	1.4	0.07	0.015	0.015	<0.03	<15 ppm
Act.	5.9	2.5	-	-	-	-	-

4.2.2 HASTELLOY-X FEEDSTOCK POWDER CHARACTERISATION

Laser diffraction testing of the Hastelloy-X feedstock powder provided the particle size distribution seen in Figure 4.2 (a) with range 12.7 – 76 µm, D_{10} = 22.4 µm, D_{50} = 35.1 µm, and D_{90} = 54.2 µm. SEM micrographs of the bulk powder (Figure 4.2 (b) and (c)) showed a higher degree of sphericity than that seen in the CM247LC. Fewer particles had satellites and there were minimal conjoined particles. These characteristics resulted in a high flowability and no clumping, ideal for the LPBF process.

The chemical composition of the powder is given in Table 4.2 with all elements shown to be within the specification of the alloy [185]. The composition was provided by Oerlikon and relates directly to the powder batch used to manufacture the samples in this thesis.

Table 4.2 - Elemental composition of the Hastelloy-X powder supplied by Oerlikon compared to the nominal composition specified for the alloy

	Ni	**Fe**	**Cr**	**Co**	**Mo**	**W**	**C**
Nom.	Bal	17.0 – 20.0	20.5 – 23.0	0.5 – 2.5	8.0 – 10.0	0.2 – 1.0	0.10 max
Act.	Bal	18.2	21.5	2.1	9.4	0.9	0.04
	Si	**Mn**	**Al**	**Ti**	-	-	-
Nom.	1.00 max	1.00 max	0.5 max	0.15 max	-	-	-
Act.	0.5	0.1	0.1	0.1	-	-	-

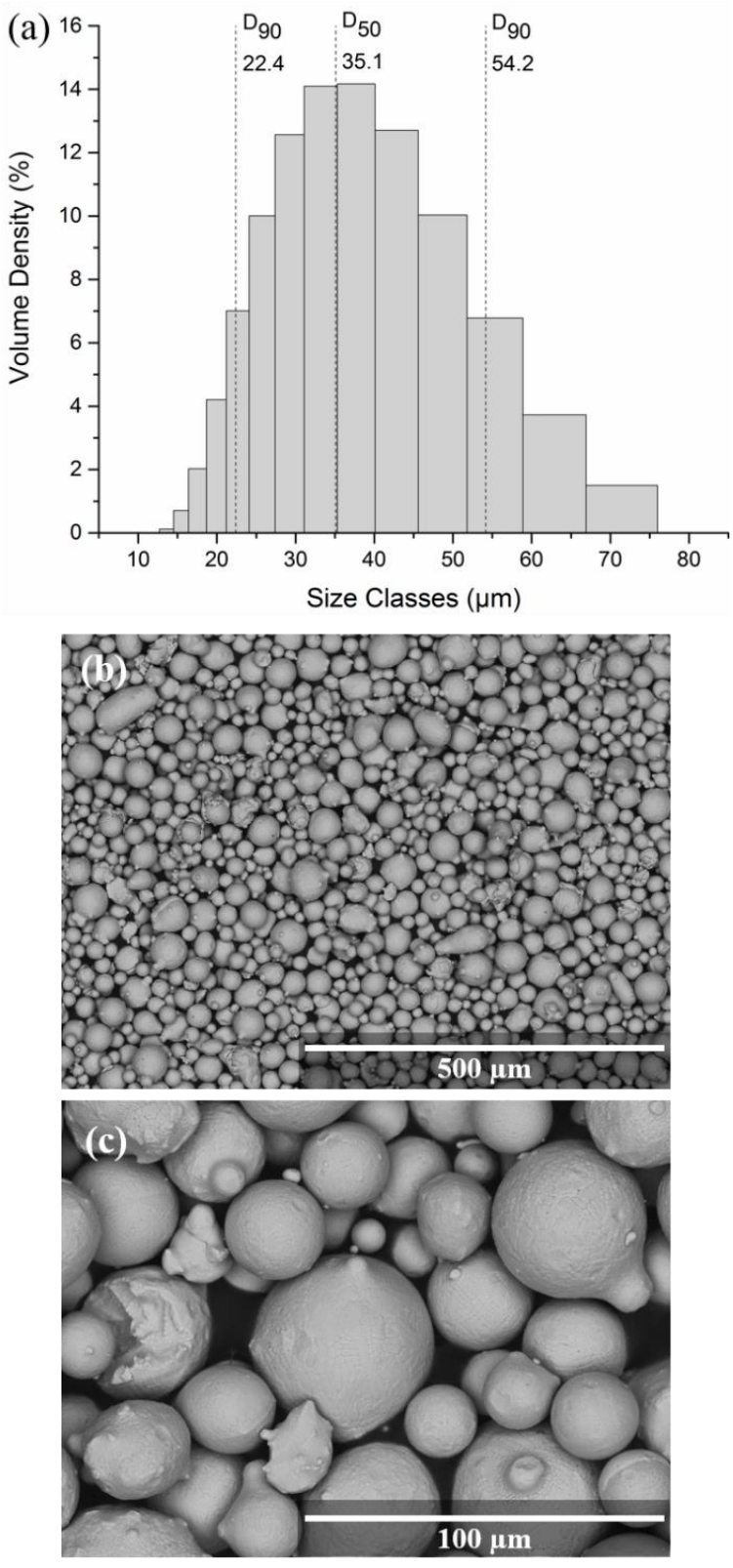


Figure 4.2 - a) Hastelloy-X laser diffraction powder size distribution histogram, b) 200X SEM micrograph showing the distribution of particle sizes and c) 1000X SEM micrograph showing higher overall sphericity than the CM247LC powder, fewer particles with satellites and minimal conjoined particles.

4.3 CM247LC PROCESS DEVELOPMENT

This section details the progress towards reduction of cracking in the alloy CM247LC processed via LPBF. Conventional scan strategies are compared to fractal scan strategies, with bulk density and crack density calculated.

4.3.1 STEPS TOWARDS REDUCTION OF CRACKING

As highlighted in the literature review, CM247LC falls into the category of 'unweldable' Ni-alloys due to its high Al and Ti content [103]. As a result, manufacture of crack free components via LPBF is difficult with the scan strategies that are available as standard in pre-processing software. The choice then must be made to either adapt the alloy chemistry to mitigate cracking in LPBF, or to optimise the process to prevent the occurrence of thermal gradients that result in the cracking behaviour. Adapting the alloy is expensive and time consuming, particularly for complex alloys such as CM247LC with 12 alloying elements. Additionally, manufacturers have strict alloy elemental compositions for aerospace applications and modifications to the alloy can quickly result in the composition falling outside of the specification. As a result, the new alloy would have to pass through an extensive testing and validation procedure. In this instance, optimising the LPBF process was chosen as the method which is most suitable for the intended outcomes of the project.

Attempts to mitigate the cracking via use of island scanning, stripe scanning and pre- or post-melt scans (i.e. two scans per layer) were unsuccessful. More sophisticated scan strategies are required that consider the development of the thermal gradients responsible for stress induced cracking. Such scan strategies may be necessary for the manufacture of high-density components in the as-LPBF state, eliminating or minimising the need for post-processing steps such as HIPing. In order to reduce the incidence of cracking in this alloy, novel scanning strategies based on fractals were developed. The aim was to reduce

the large thermal gradients and residual stress build-up responsible for cracking in CM247LC manufactured via LPBF by using short scan vector lengths (<300 µm), with neighbouring scan vectors at >60 ° orientation mismatch. In theory, this should produce many small areas of residual stresses that are acting in different directions, which when summed across a large area, can cancel each other out and reduce the incidence of cracking. Currently, no data is available on how fractal scan strategies influence integrity post-LPBF outside of the article published as part of this thesis. However the in-situ methods for reducing thermal gradients in SLS demonstrated by Ma et al. [101] and Yang et al. [102] can be inferred to be applicable to LPBF due to strong similarities in the material thermal history between the processes.

4.3.2 Scan Strategies and Manufacture

Alongside the fractal scan samples, an island scan sample was produced with dimensions 10 x 10 x 5 mm [*XYZ*], with the *XY* plane divided into four equal 5 x 5 mm discrete islands (*see* Figure 2.6). This island size was determined to be optimal by Lu et al. [99] and was also consistent with the samples produced by Carter et al. [100], [186]. The island samples serve as a control to compare the later scan strategies against. Initially, the entire 10 x 10 mm sample cross-section was contour scanned to give a single track thickness wall around the perimeter, then the island regions were in-filled using a meander hatch scan (Table 3.1). Samples were produced using a 25 µm layer thickness, 100 W laser power and a 400 $mm.s^{-1}$ scan speed, determined to be the optimum processing parameters in an earlier parametric study. This sample was used as the baseline for comparison with the novel fractal scan strategies as it is an established method of reducing residual stresses in LPBF manufacture.

A range of samples were manufactured using fractal scanning strategies based upon the mathematical area filling curves *Hilbert* [187] and *Peano-Gosper* [188]. These curves

were chosen as the distance between adjacent lines remains constant, an important feature due to the constant laser spot size and hence constant melt pool width. The characteristic scan vector length in each case was defined as 100 µm, whilst no single vector length was permitted to exceed 300 µm; illustrations of the fractal scan strategy paths are shown in Figure 4.3. The use of short vector lengths to reduce residual stress underlies the island scanning strategy. However, this can result in anisotropic stress distribution over a part cross-section due to differentials in temperature distribution at the ends of the scan vectors, forming spatially distinct cooling rates. Hence, simply substituting short vector lengths into island patterns may not result in an overall stress reduction. However, application of a fractal scan pattern, as a single, continuous path that covers a wide area, can potentially provide a more uniform temperature distribution compared to the cyclic heat input that is associated with unidirectional, straight line raster fill scans.

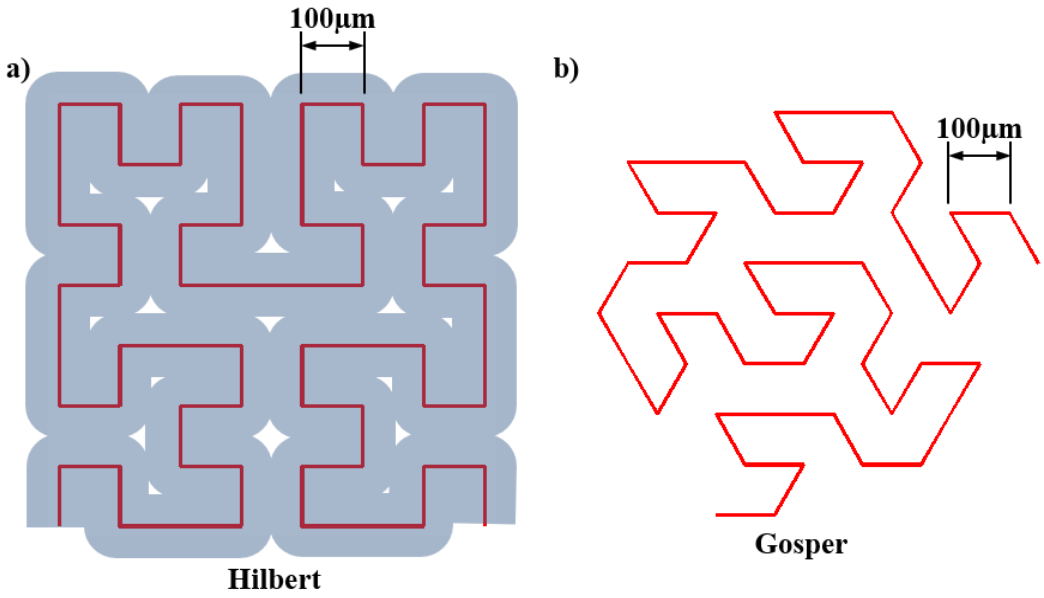


Figure 4.3 - Illustration of the novel scan strategies generated using the (a) 3rd order Hilbert and (b) 2nd order Peano-Gosper mathematical area filling curves. The 100 µm characteristic scan vector length is shown. Approximate weld track thickness is shown in blue on the Hilbert fractal path (a).

A MATLAB script (written by Dr. Luke Parry, a research assistant at the Centre for Additive Manufacturing, University of Nottingham in 2015) was used to add appropriate laser spot size and hatch spacing parameters to the fractal curve generation code. Melt pool width of approximately 120 µm results in the area being filled as demonstrated using the blue shading in Figure 4.3 (a). The script also defined material and process parameters and output a machine file directly readable by the LPBF machine. With the hatch spacing defined as 50 µm, the resultant samples were formed by a single continuous scan path that filled an area of 5 x 5 mm and 3.3 x 3.3 mm for the Hilbert and Peano-Gosper paths, respectively. For each fractal scan strategy, scan speeds of 500, 600, 700 and 800 $mm.s^{-1}$ and laser powers of 75 W and 100 W laser were used to explore the processing parameter window. A summary of the process parameter sets is given in. The samples were produced with 25 µm layer thickness and a total height of 5 mm excluding strut support structures.

Table 4.3 - Parameter combinations (laser power and laser scan speed) used to produce a total of 16 fractal scan samples (eight Hilbert and eight Peano-Gosper)

Laser power (W)	**Scan speed ($mm.s^{-1}$)**			
75	500	600	700	800
100	500	600	700	800

4.4 CRACK REDUCTION RESULTS AND DISCUSSION

4.4.1 CRACK LOCATIONS AND MORPHOLOGY

All sample builds were superficially successful, with no warping or lifting from the support structures and no macro-scale surface cracking or porosity. However, micro-cracking was prevalent in every case. In the island scan control sample, cracking and porosity varied greatly within the cross-section, particularly at the island intersection region, where defects were most prevalent. The intersection was identifiable due to its position at 50 % side length (image shown in Figure 4.4 is cropped). These bands of low density were associated with long cracks predominantly parallel to the border of each island, along with smaller cracks perpendicular to the border that extended into the bulk area (Figure 4.4). In the island hatch scan area, the cracking has a distinct directionality that followed the laser scan vector; i.e. a cracking pattern at 0° and 90° to the sample edges as a result of the 90° rotation of the raster fill scan between each layer.

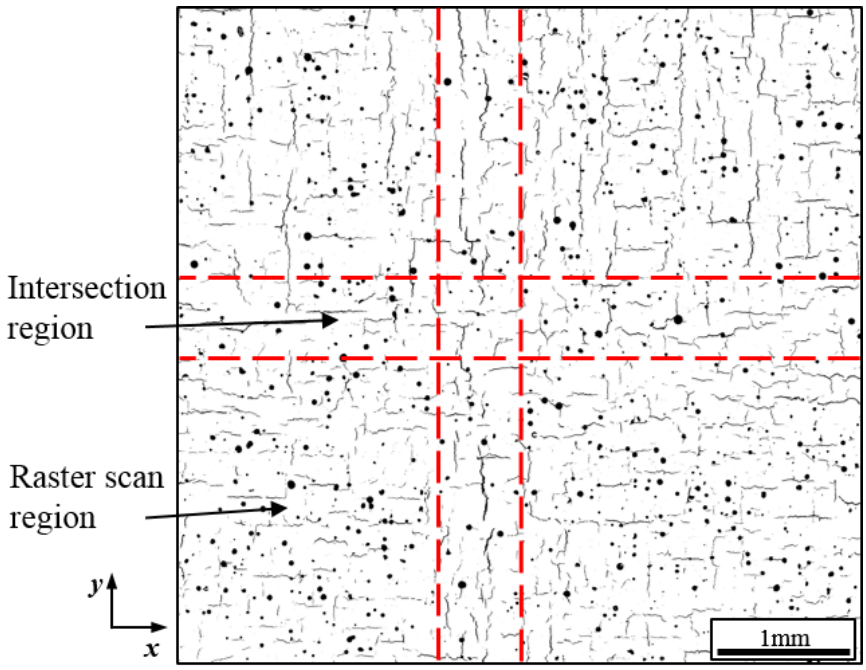


Figure 4.4 - Identification of the increased cracking and porosity regions in the island intersections. Note that the cracking has a distinct directionality at 0 ° and 90 ° to the island borders, aligned with the laser scan vectors.

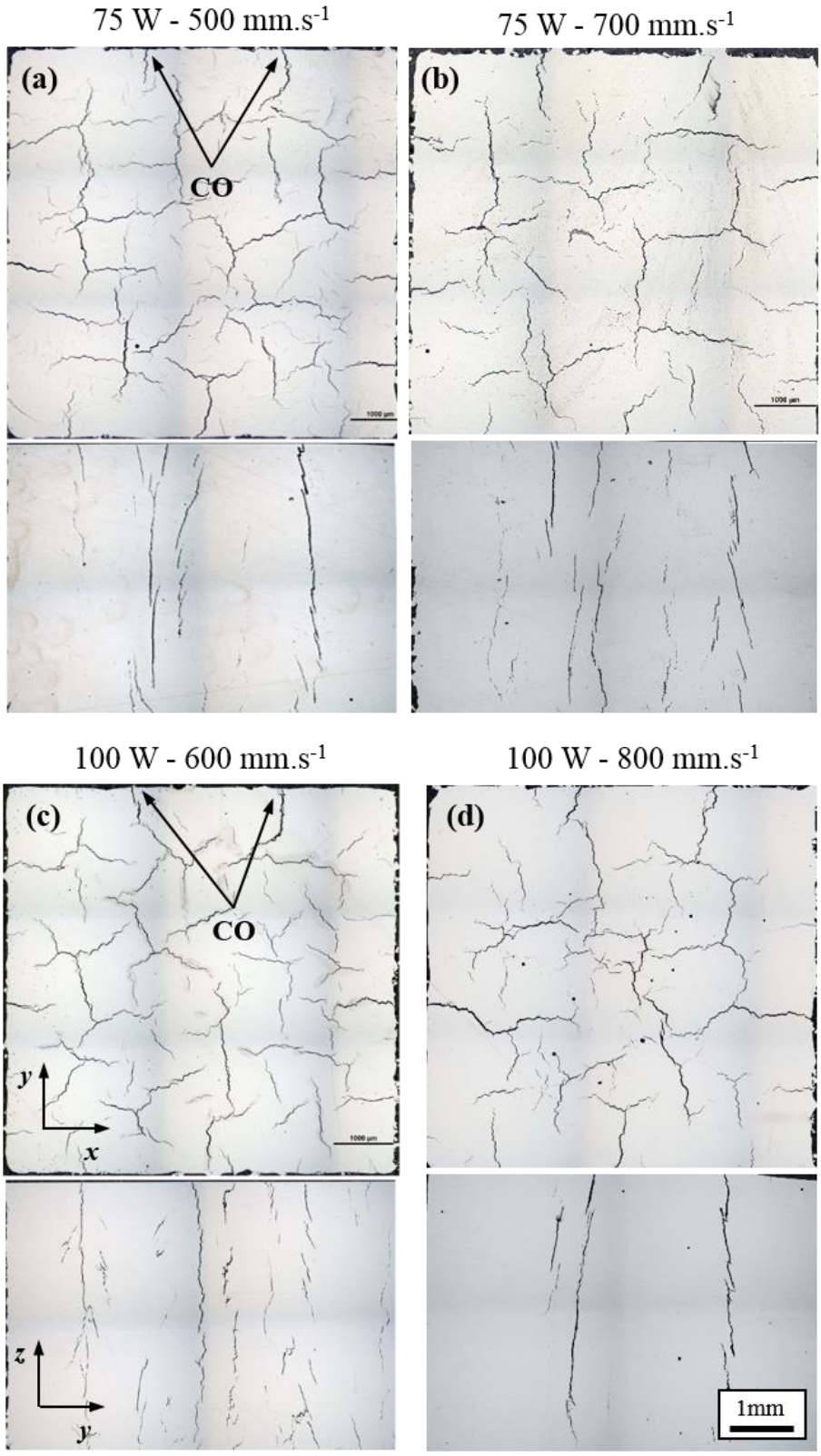


Figure 4.5 - Optical micrographs showing the cracking in a range of Hilbert samples. Highest density achieved at 100 W 600 mm.s^{-1} (c) and lowest density at 75 W 500 mm.s^{-1} (a). CO = crack origin; note the very similar placement of cracking for each fractal scan type.

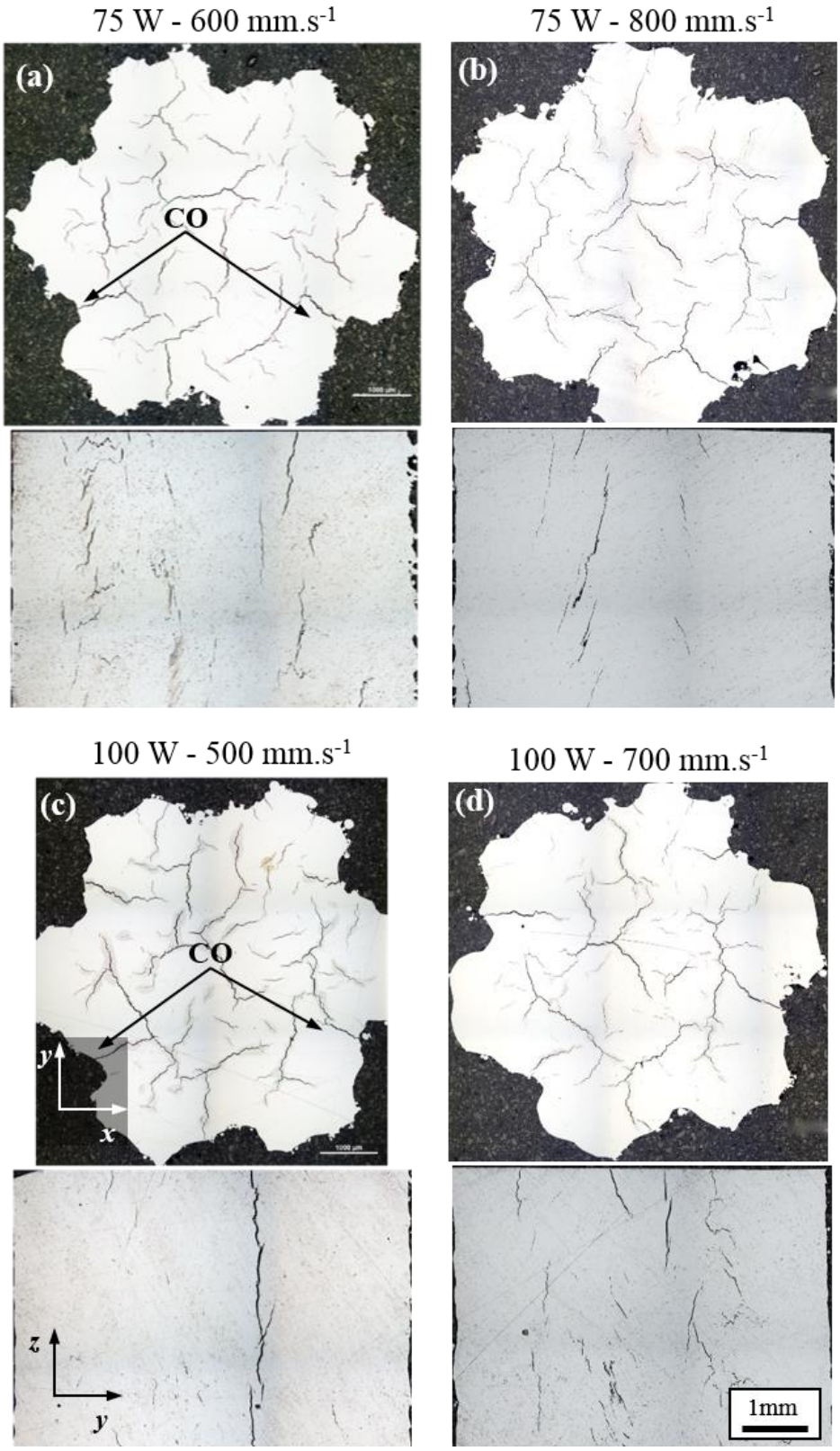


Figure 4.6 - Optical micrographs showing the cracking in a range of Peano-Gosper samples. Highest density achieved at 75 W 600 mm.s^{-1} (a) and lowest density at 100 W 500 mm.s^{-1} (c). CO = crack origin; note the very similar placement of cracking for each fractal scan type.

In the fractal scan samples, the origin and appearance of large cracks occurred in approximately the same place for every sample in the *XY* plane (*see* Figure 4.5 and Figure 4.6), across all process parameter sets. Further, the cracking did not follow the scan vector lines as in conventional scanning strategies, as evident when overlaying the scanning strategy onto the deposit micrograph, as in Figure 4.7. This indicates that repeatable stress concentration points are developed by the fractal scan patterns. In the Hilbert samples, cracking occurred along scan vectors but also at an angle to the scan vectors, indicating that the build-up of residual stress in the fractal samples is more complex than in raster scan strategies as a result of the rapidly varying scan vectors.

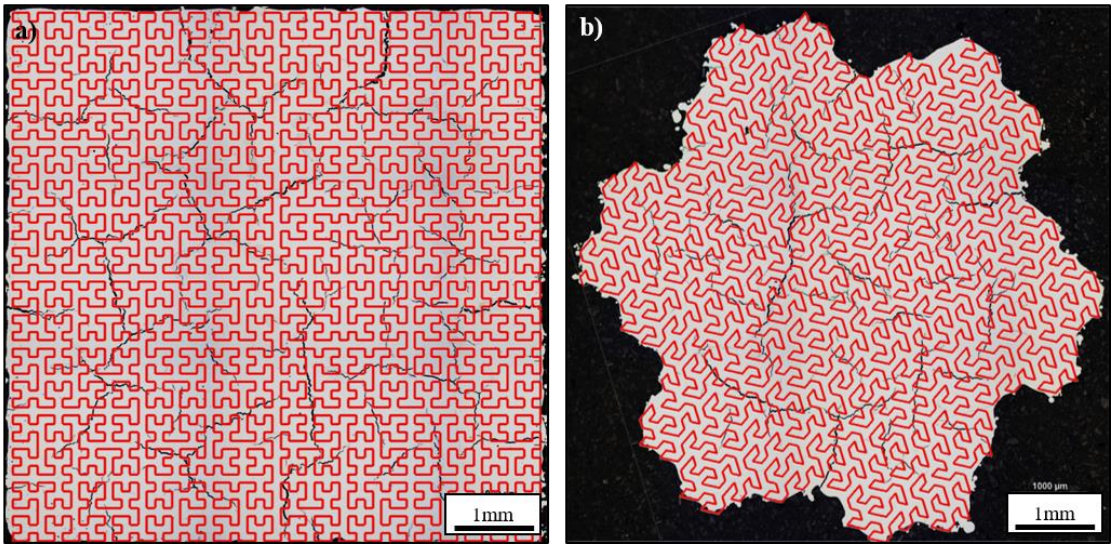


Figure 4.7 - (a) Hilbert [100W, 600mm.s^{-1}] and (b) Peano-Gosper [75W, 600mm.s^{-1}] scanning strategies approximately overlaid on to the deposits formed via SLM. Note that the cracking does not seem to follow the scan vectors as with the long vector length samples.

Cracking is also multi-directional in the Peano-Gosper samples, however this is to be expected due to the addition of a scan vector that is at a 65° angle to the *X* or *Y* axis. It is hypothesised that the cracking seen here is as a result of localised micro-scale stress vectors combining to form stress concentration points. As a result, cracks can form at an angle to or perpendicular to the direction expected from conventional understanding of

stress build-up using long vector length scans. The stress concentration theory would explain the propensity for crack initiation and growth in the same location and direction for each fractal scan sample. The scan path results in the area being divided into regions which will cool and shrink at differential rates (Figure 4.8 (a, b)). This leaves preferential paths for crack growth between the regions (Figure 4.8 (c)) which match the pattern of cracking seen in Figure 4.6 (c) and (d). In the *YZ* plane, large cracks were seen parallel to the build direction and frequently coalesced to form one continuous crack, spanning the full height of the deposit in a number of cases. Some deposits contained a number of these long cracks whilst others contained single, typically longer and wider, cracks.

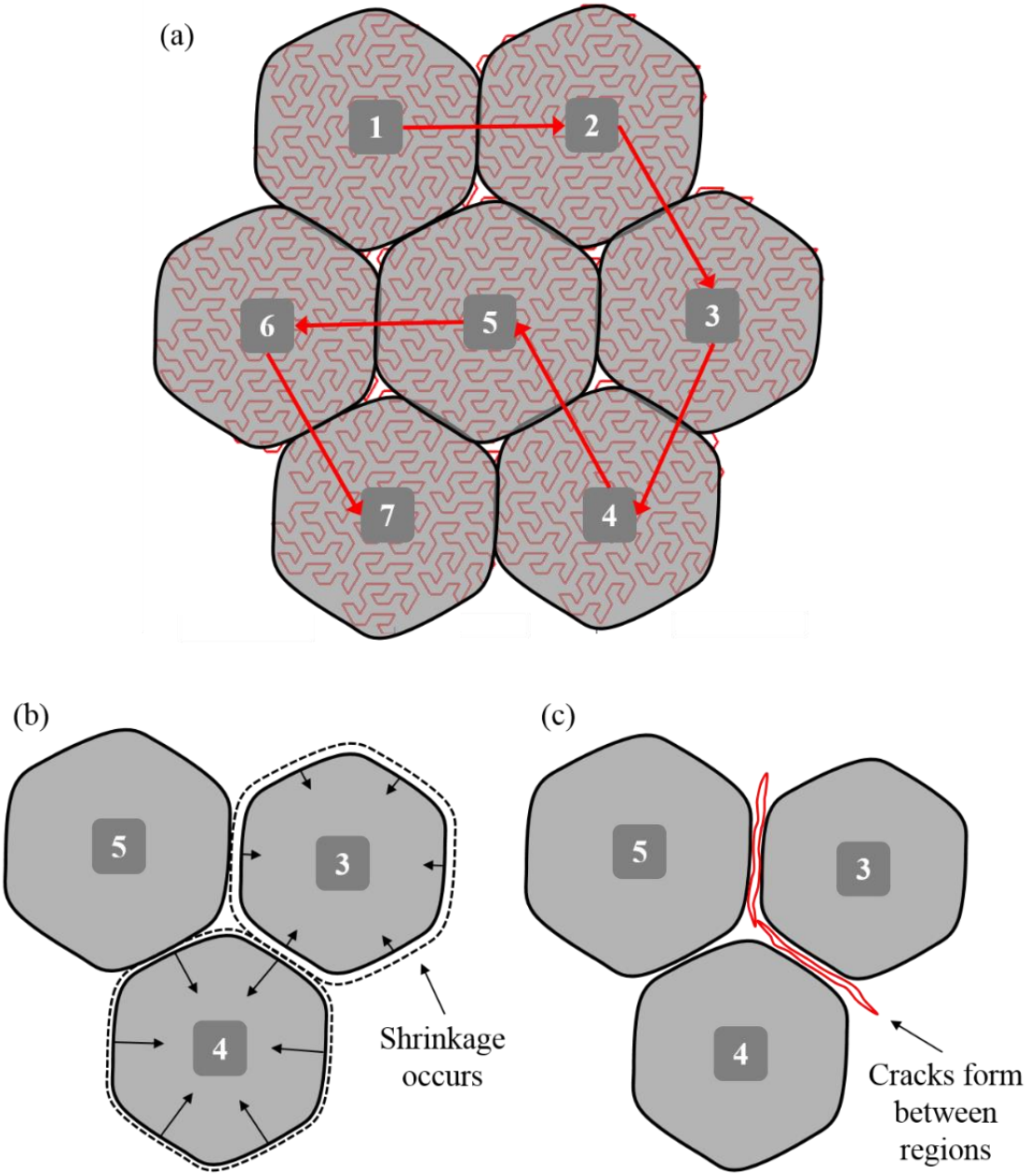


Figure 4.8 - Illustration of the mechanism causing cracking to appear in the same regions for each fractal samples (Peano-Gosper used in this case). The scan area is completed in regions in the order given in (a). After each region completes, it shrinks during cooling (b). This forms preferential paths for crack growth between the scan regions (c).

4.4.2 MICROSTRUCTURE AND CRACKING MECHANISMS

The Ni-based superalloy CM247LC is susceptible to two main types of cracking during LPBF processing: solidification cracking and grain boundary liquation cracking. Solidification cracking can occur in the fusion zone of a melt pool where the newly deposited material is cooling at a higher rate than the surrounding material. Alloys with a large number of alloying elements tend to have a wide solidification temperature range and are hence more susceptible to solidification cracking. As the melt pool cools, partial solidification of the lower melting point elements forms a two-phase liquid-solid composition [189] of dendrites or small grains surrounded by interdendritic (or intergranular) liquid. Before the melt pool fully solidifies, tensile strains result in contraction of the solidified material, with the remaining liquid films surrounding the solid acting as low energy paths for crack propagation. This mechanism is illustrated in Figure 4.9 [190]. Liquation cracking can occur during LPBF in the partially-melted zone created when solid material in a previous layer is re-melted by the laser beam when processing the current layer [191]. This again forms a two-phase solid-liquid composition, which provides a low energy path for cracking under thermal stresses induced during cooling. However, in this case cracking occurs in the previously solidified material. Due to both mechanisms acting along the grain boundaries, the microstructure is particularly significant when analysing cracking in CM247LC, as discussed below.

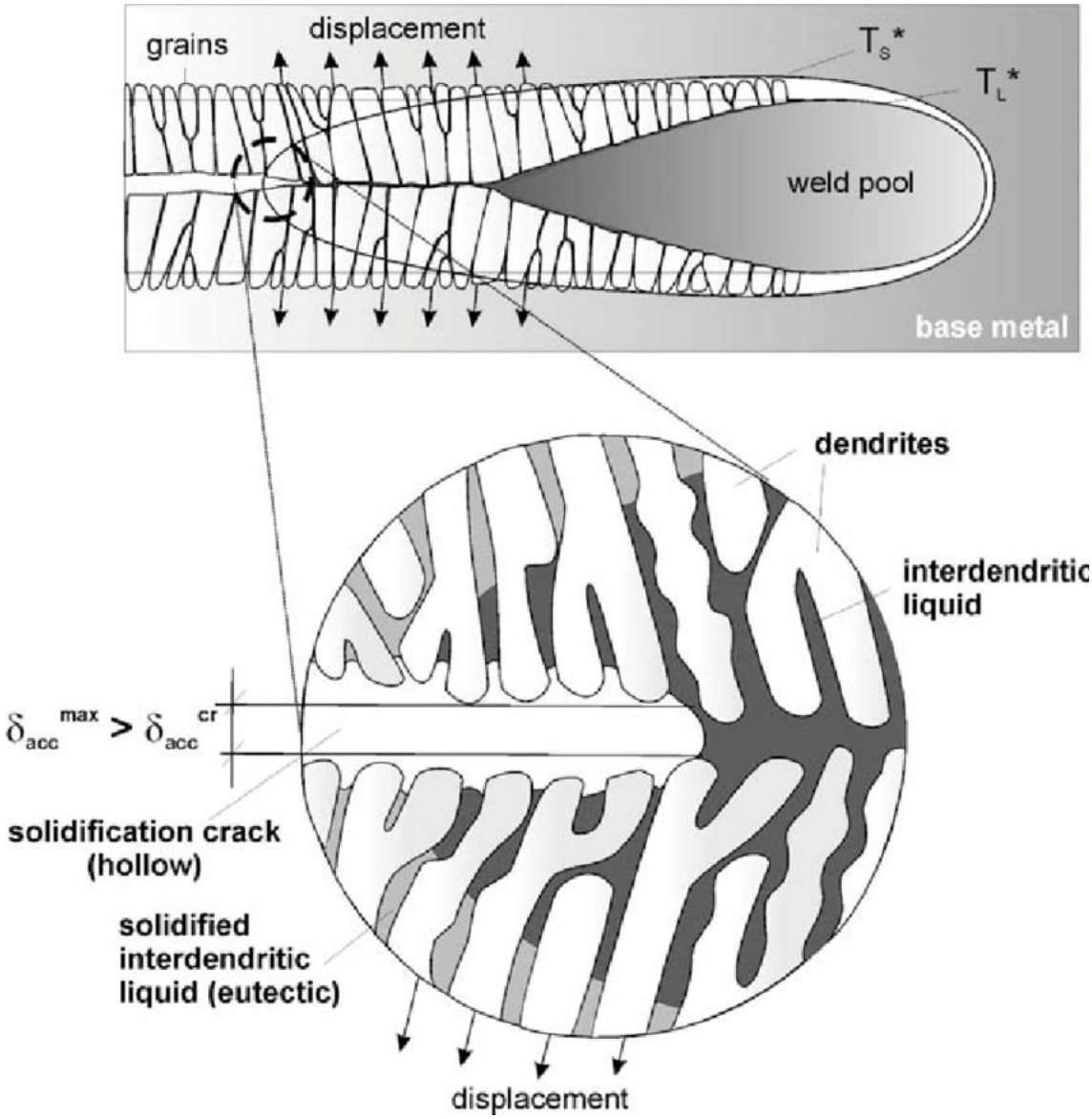


Figure 4.9 - Illustration of solidification cracking in welding, where cracking propagates through the liquid phase of the partially solidified weld pool. Figure taken from Ploshikhin et al.

In the *XY* plane, a bi-modal grain structure was formed consisting of a mix of fine and coarse equiaxed grains for the island and fractal scan samples. Cracking occurred where coarse equiaxed grains intersected fine grain regions (Figure 4.10, (a)), or where a colony of large equiaxed grains ruptured to form a crack (Figure 4.10, (b)). The bi-modal structure appeared to have no obvious pattern in the *XY* plane. In the fractal scan samples, the complexity of the rapidly changing ~100 µm scan vectors formed a cooling regime

that had no preferential grain growth direction in the *XY* plane. This may serve to remove any obvious patterning. In the island samples, a 90 ° rotation of the raster fill scan between each layer resulted in a cross-over of the laser scan vectors, preventing growth of the distinct grain texture that results from using equal scan vectors in each layer. However, despite Divya et al. [192] using a 67° rotation of the scans between layers, a bi-modal grain structure was clearly visible in their samples in the *XY* plane using EBSD analysis, suggesting that a higher laser energy density can result in preferential grain growth regardless of using rotation between layers.

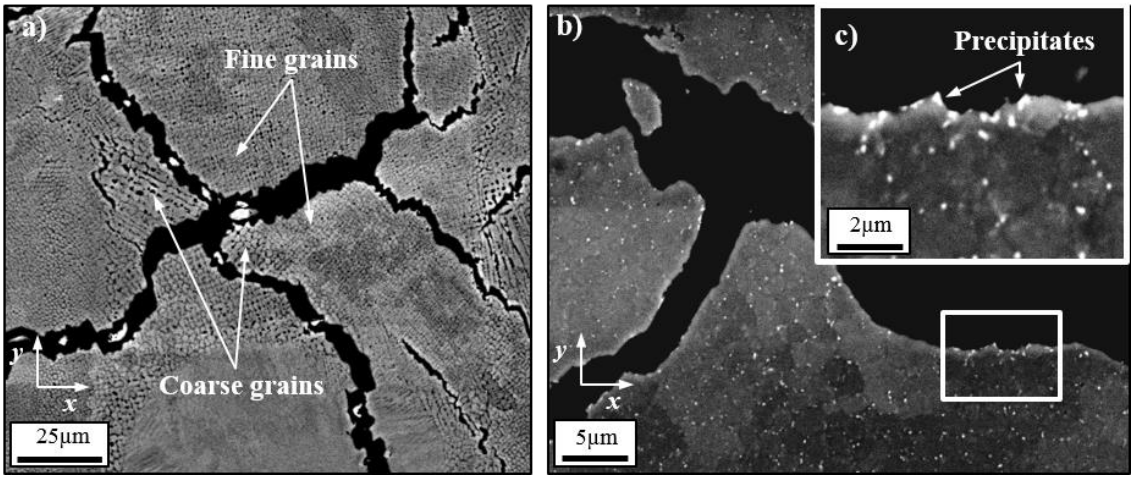


Figure 4.10 - Backscatter electron micrographs in the XY plane of the Hilbert 100W 600mm.s^{-1} sample showing: (a) bi-directional crack origin at intersection between fine and coarse equiaxed grains; (b) high angle cracking with (inset c) some sub-micron size precipitates identified along the crack surface

Precipitates were observed at grain boundaries and appear as bright spots in the backscatter electron images due to their relatively higher atomic mass (Figure 4.10, (c)). The precipitates can be found uniformly distributed within the bulk material and despite their common occurrence along crack boundaries, there was no clear indication that they were the sole cause of crack initiation or higher crack formation propensity. To investigate the possibility of carbide thin films at crack boundaries, EDS line scans were

taken across crack boundaries and assessed for elemental concentrations, as seen in Figure 4.11. Cloots et al. [193] suggested that Zr may be responsible for solidification cracking in LPBF processed IN738LC as it acts to significantly lower the solidus temperature at grain boundaries. However, EDS line scans showed no peaks in Zr elemental concentration near the crack boundaries in this work. Further, no peaks corresponding to carbide forming elements were seen at the crack boundaries, indicating that there are no detectable thin films of carbides initiating cracking. Drop-off and pick-up signals of elements such as Ti, Mo and Zr can be seen at the crack boundaries, however these trends are also exhibited by major constituent elements such as Al and Ti and hence do not indicate elemental concentration greater than that seen in the bulk material. However, the resolution of the EDS method used here is limited and may not be able to detect thin films in the sub-micron thickness range.

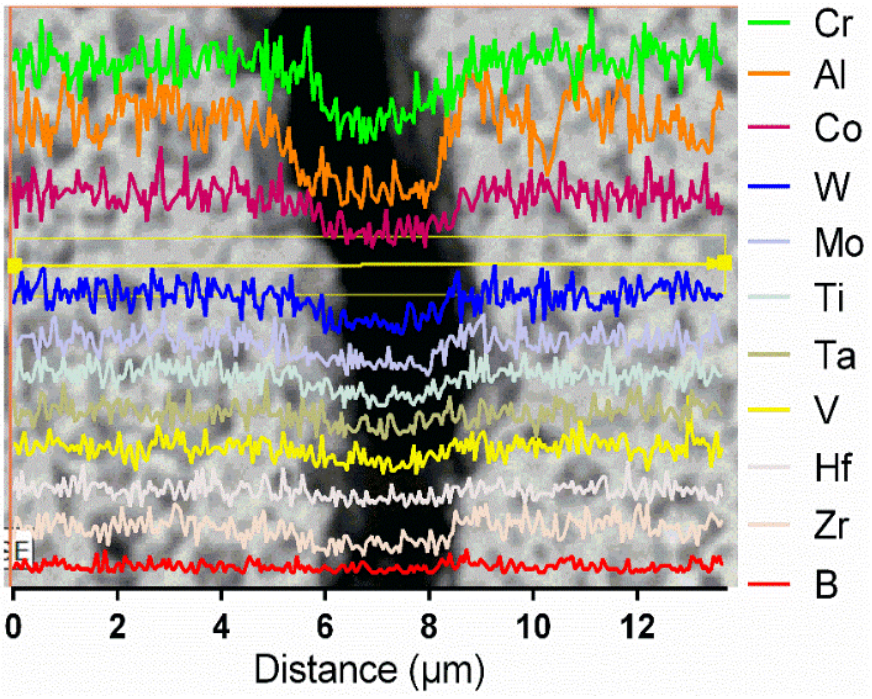


Figure 4.11 - EDS line scan of the island scan sample showing elemental distributions across the crack surfaces. Note the lack of elemental peaks that would signify the presence of thin films at the crack boundaries.

In the *YZ* plane, cracking appears to follow grain boundaries with preference for regions where longer, columnar grains interact with shorter, more equiaxed grains (Figure 4.12, (a)). This bi-modal grain structure was repeatedly identifiable in the *YZ* direction as coarse columnar grains at the core of each melt pool and fine equiaxed grains at the boundary. This follows on from the theoretical understanding of melt pool cooling, in which the core material retains heat and hence cools at a slower rate than the boundary. The fast cooling boundary solidifies as fine grains whilst the core has sufficient time to form a columnar grain structure. Further, the directional growth of columnar grains from the core of the melt pool follows the expected path parallel to the greatest heat flux lines, extending towards the heat source.

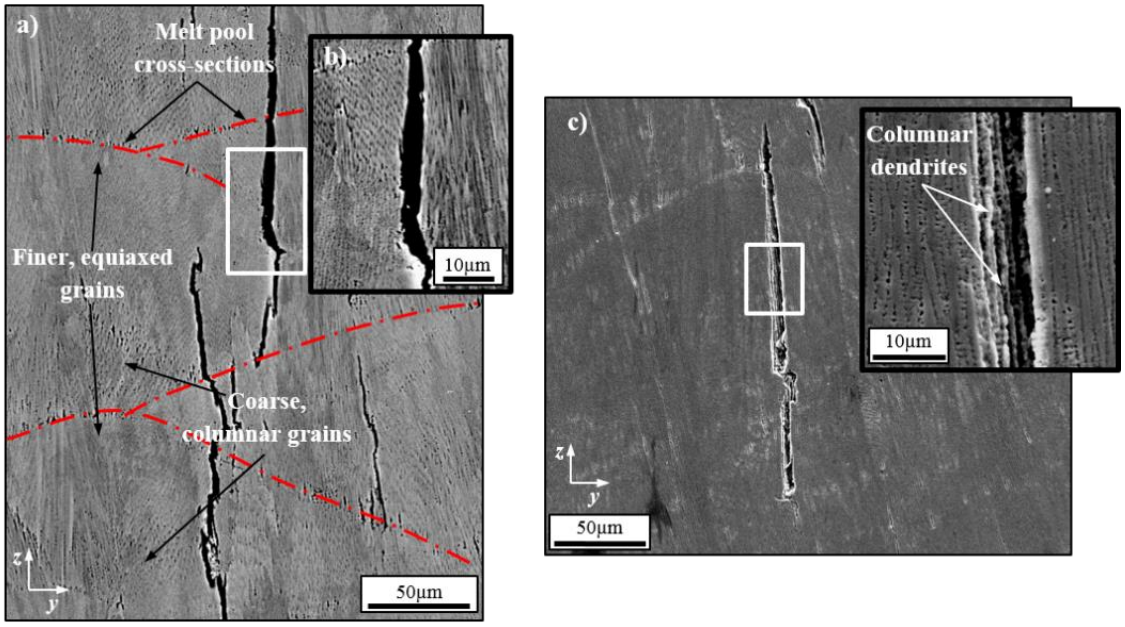


Figure 4.12 - Backscatter electron micrograph of the YZ plane of the island scan sample showing: (a) the melt pool shape in red giving rise to coarse columnar grains in the core and finer, equiaxed grains at the boundary; (b) a crack following the line of intersection between a fine, equiaxed grains and coarse, columnar grains; (c) columnar dendrite surface exposed by the solidification cracking mechanism

For shorter, more isolated cracks, particularly those only spanning the height of a single build layer, the mechanism of solidification cracking is supported by the appearance of cracks clearly separating individual columnar dendritic grains in the *YZ* direction as seen in Figure 4.12 (b). These solidification cracks can act as initiation sites for liquation cracking as the build continues. The serrated, deformation-free appearance and mirrored morphology of the crack surfaces either side of the cracks shown in Figure 4.12 (c) suggests cracking after partial re-melting, characteristic of liquation cracking [194]. In consecutive layers, these liquation cracks are repeatedly partially re-melted, initiating further crack growth that extends through multiple build layers, as evident in Figure 4.12 (a). It is difficult to attribute a single cracking mechanism to each crack, particularly as solidification and liquation cracking act via similar mechanisms and both follow grain boundaries, however there is evidence of both cracking mechanisms acting in the samples, particularly in the *YZ* plane.

4.4.3 Quantitative crack analysis

The crack length density (total length of cracks per bulk area) and crack area density (total area of cracks per bulk area) were calculated separately. The distinction between crack length density and crack area density was made as using crack length alone does not necessarily reflect the severity of cracking within a sample. For example, narrow cracks will respond more favourably to HIPing than wide cracks. Separating the measurements provides a better representation of the condition of the as-built LPBF samples, as well as a secondary metric to compare the scanning strategies used in the experiments. The bulk density of each sample was calculated by subtracting the crack and pore area from the bulk sample area analysed.

4.4.3.1 BULK DENSITY

The overall bulk density data for all samples is given in Figure 4.13. The highest *XY* plane bulk density of 98.0±0.1 % was achieved using the Peano-Gosper scan at 75 W laser power and 600 mm.s^{-1} scan speed. This is significantly higher than the *XY* plane bulk density of the island scan sample at 96.0±0.6 %. This is attributed to the large amount of spherical porosity seen in the island sample, whereas porosity was rarely seen in any of the fractal scan samples. Further, the fractal scan samples typically had less variation in the bulk density across the three ROI analysed when compared to the island scan sample. In the *YZ* plane, the bulk density of the fractal samples was also significantly higher than the island sample. However, the variation in density is larger due to difficulty in repeatable cross-sectioning of the samples; the complex scan strategy results in a higher propensity for *YZ* plane cracking in some regions and so crack density can vary depending on the location of the cross-section taken.

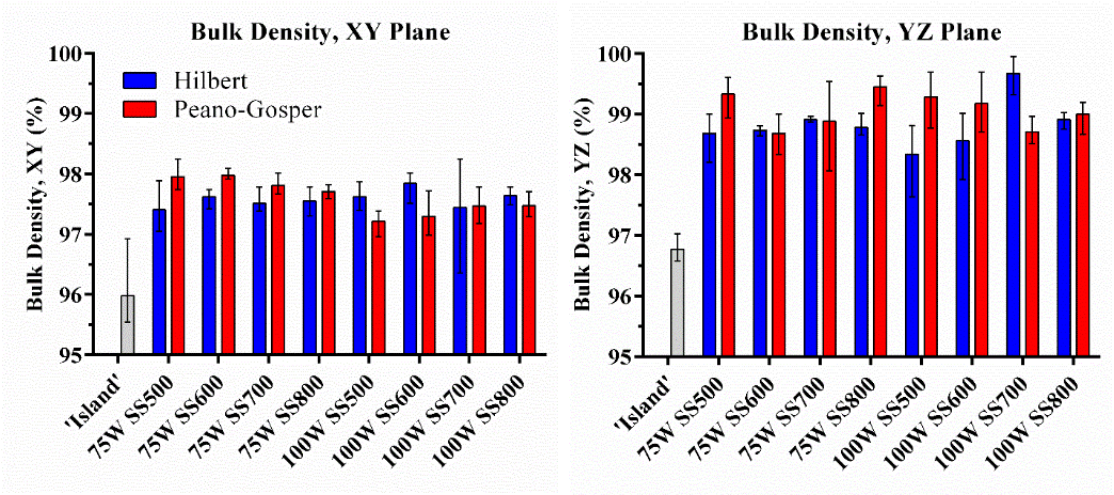


Figure 4.13 - Bulk density data for the samples in the XY plane (left) and YZ plane (right). The island sample is represented in grey whilst the Hilbert and Peano-Gosper are in blue and red, respectively. Each pair of columns constitutes a single process parameter set, identified on the x-axis labels.

4.4.3.2 CRACK LENGTH DENSITY

When comparing the crack length density in Figure 4.14, it is again clear that the fractal scan samples provide an improvement over the island scan. Overall, the crack length density was lower in the *YZ* plane than the *XY* plane, as expected from the bulk density results. For every process parameter set, the upper and lower bounds of the crack length density measurements overlap, indicating that the two fractal scan strategies are very similar in cracking propensity due to their thermal profile and hence stress build up within the sample. The lowest mean *XY* plane crack length density of 0.82±0.40 mm/mm^2 was in the Hilbert scan, 100 W and 700 mm.s^{-1}, compared to 2.71±0.47 mm/mm^2 for the island sample. The crack length density was also the lowest using this Hilbert fractal scan, providing an even greater magnitude of improvement over the island sample. Again, the samples show a greater variation in *YZ* plane crack length density across the process parameter sets, attributed mainly to the differences in cross-sectioning. However, the results still demonstrate the improvement made by the fractal scans to reduce the prevalence of cracks in the CM247LC samples.

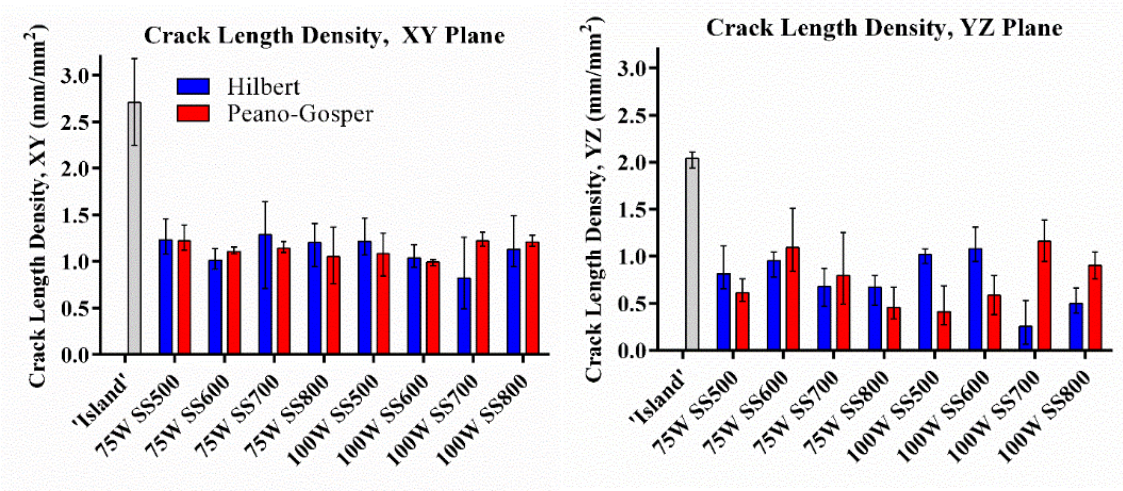


Figure 4.14 - Crack length density data for the island (grey), Hilbert (blue) and Peano-Gosper (red) scan strategies

4.4.3.3 CRACK AREA DENSITY

Finally, the crack area density for each sample is given in Figure 4.15. The importance of differentiating between crack length and crack area is evident by the less significant improvement made by the fractal scan samples. However, a reduction in crack area density was still seen in 81 % of the *XY* plane and 94 % of the *YZ* plane of the fractal scan samples, demonstrating that the novel scan strategies are effective across all quantification metrics used in this study. The crack area density data confirms the observation from the optical micrographs that the cracks in the fractal samples are shorter, but wider than those seen in the island samples. This could pose a problem for HIP treatment whereby wide cracks cannot be fully consolidated (*see* section 2.3.2 for an illustration of how cracks remain post-HIP). However, the cracks are still in the micro-scale with a typical width <50 µm. Of greater value from the fractal scan samples is the reduction in the crack length density and hence the reduction in the number of healed sites that would remain post-HIP. Such heal sites often contain thin films of precipitates, such as carbides, which result in a weakly bonded interface [75] that is susceptible to re-opening during the service life of the component. Occurrence of this weakly bonded interface is proportional to the crack length in the sample, hence the reduction in crack length density that the fractal scan strategies can provide is more desirable than a reduction in crack area density. Further, the fractal scans also resulted in a large reduction in porosity and hence the bulk density was significantly greater than in the island samples, highlighting the benefit of using fractal scans for porosity reduction as well as crack reduction. As such, fractal scans may also be beneficial when applied to alloys where the principal density issue is porosity rather than cracking.

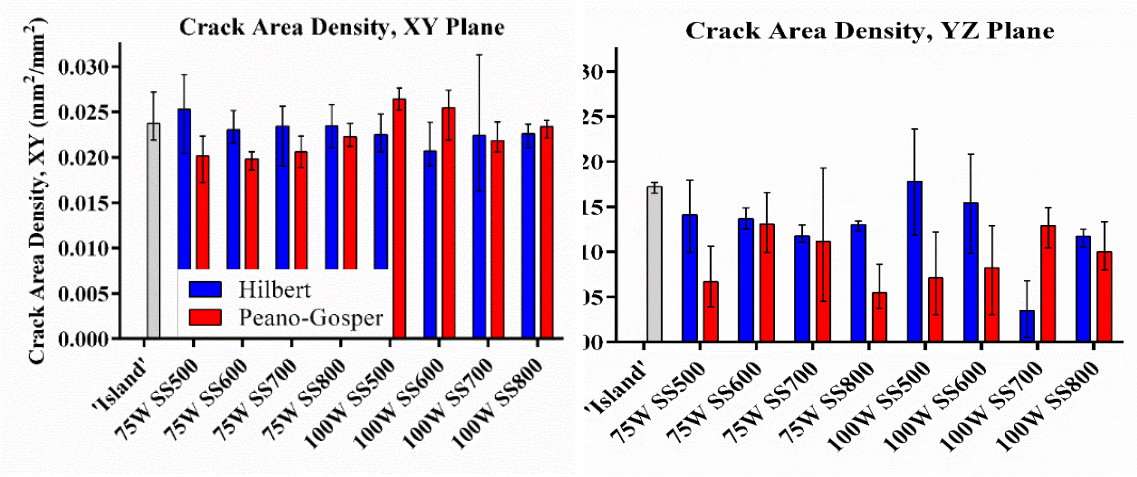


Figure 4.15 - Crack area density data for the island (grey), Hilbert (blue) and Peano-Gosper (red) scan strategies.

4.4.4 Fractal scans for manufacture

Of significance from this study is the dependence of the crack morphology, position and direction on the scan strategy, or more specifically, the scan vector. The novel fractal scan strategies demonstrated here, whilst still resulting in cracked samples, produce a repeatable defect pattern. With knowledge of how cracks may develop in each scenario, defects could be more reliably detected mitigated, reducing the number of scrap parts manufactured. Further, there exists the possibility to apply different scanning strategies to individual areas of a part cross-section dependent upon crack susceptibility, as a result of part geometry, to reduce the probability of cracks developing in these areas. Eliminating cracking is of paramount importance for the manufacture of components via LPBF. Whilst HIPing can improve the density post-LPBF, defects will remain that are susceptible to re-opening during service. This is especially significant for load-bearing components that undergo thermal cycling, where potential catastrophic failure could result. Conventional scan strategies have limited scope for optimisation, relying on laser power and scan speed as the primary parameters. Hence, novel scan strategies, such as the fractal scans proposed here, should be explored further. However, it is clear that the

highly crack susceptible properties of CM247LC cannot be mitigated completely by the fractal scan strategies alone that were studied here. Modification of the alloy chemistry may also be required alongside process parameter and scan strategy optimisation. As discussed previously, this is an expensive and time-consuming process, and one that can drive the alloy outside of its specifications, resulting in the need for extensive re-evaluation. This procedure is outside the scope of work for this thesis.

4.4.5 Failure in process and material

Novel fractal scan strategies based upon the Hilbert and Peano-Gosper curves were developed and experimentally tested via LPBF. Comparison with conventional island scan samples showed that a significant increase in bulk density can be achieved by implementing the fractal scans. Optical micrographs and quantification of cracking data was used to highlight the importance of using multiple metrics to assess cracking to determine material quality. However, crack reduction and material quality was not sufficient through any processing method to be suitable for manufacturing lattice structure samples. With regards to modifying scan strategies for non-weldable alloys, including implementation of fractal scans, the following conclusions were drawn:

- Cracking propagates along and parallel to scan vectors in island scanning with long vector lengths, however, with fractal scan strategies, cracks propagate parallel to and at an angle to the scan vectors
- Process parameter optimisation for island scan strategies must consider the intersection region in order to achieve isotropic material density
- Crack origins and paths are repeatable in the fractal scan samples, irrespective of process parameters

- Sub-micron scale precipitates exist throughout the microstructure but are not necessarily responsible for crack initiation. This is supported by a lack of elemental concentration in EDS line scans across crack boundaries
- Partial re-melting of previously consolidated layers drives liquation cracking, resulting in cracks that span multiple build layers
- Crack length density and crack area density should be analysed separately in order to accurately determine the quality of a sample; bulk density alone is not sufficient
- The presence of porosity is independent of cracking and porosity-free samples can be manufactured using fractal scan strategies, even when cracking remains

The basis for implementing fractal scan strategies within LPBF has been explored here. Due to the increased complexity compared to island scan strategies, further optimisation must be performed to exploit the greatest reduction in cracking density of CM247LC samples. New fractal patterns may be introduced depending upon component cross-sectional area or presence of geometrical features such as thin walls, increasing the efficacy of their implementation further. For the current generation of LPBF machines, fractal scan strategies show promise as a method of altering the thermal profile of the process without the requirement for external heating of the build volume. However, they were not successful in overcoming the challenges of CM247LC as a particularly crack-susceptible material. The high thermal gradients of LPBF remain regardless of the scan strategy chosen. It may be necessary to implement features such as high-temperature build volume heating or high power, large spot diameter secondary laser energy sources to control the cooling rates sufficiently to avoid cracking.

4.5 HASTELLOY-X PROCESS CHARACTERISATION

The issue of cracking in CM247LC is not trivial to resolve and would require a thorough investigation including heat treatment, HIP and potentially LPBF machine customisation for a high temperature build volume. With the aim of this thesis to manufacture and test lattice structures, a different alloy was required that can be reliably processed with high bulk density. The weldability of Hastelloy-X is significantly greater than CM247LC (see Figure 2.4) and poses fewer problems in regard to obtaining a > 99 % dense bulk material via LPBF processing. However, as this material had not been processed using the Realizer SLM 50 before, process parameter optimisation was required. Using process parameters developed for CM247LC and nickel-iron alloy IN718 as a guideline, the processing window was restricted to a sensible range of laser power and scan speed values, preventing unnecessary sample manufacture and analysis. The process parameter optimisation is not given in detail here as it follows the standard parametric method seen frequently in the literature [195-197]. Micrographs of the HX material are shown later to demonstrate the high quality and density (99.958 %) of the bulk material in the as-LPBF condition.

Later HX builds were completed by Siemens Industrial Turbomachinery Ltd in Finspång, Sweden. Large samples used in the convective heat transfer testing would not fit within the Realizer SLM50 build volume and so it was determined that the samples should be manufactured by Siemens so as to ensure that they developed the capability to manufacture TPMS lattice structures internally to a high degree of reliability. The samples manufactured by Siemens were evaluated at two conditions of supply:

- as-LPBF (no post-process heat treatment)
- HIP + solutionising heat treatment
    - HIP: 1180 °C at 100 MPa argon atmosphere for 240 mins
    - HT: 1177 °C for 360 mins

4.5.1 BULK DENSITY

The Hastelloy-X material was high density even in as-LPBF condition as seen in Table 4.4 with only 0.042 % porosity in the XY plane. After HIP, this was reduced to 0.007 % porosity, raising slightly after HT to 0.014 %. However, this rise in measured porosity is within the expected deviation at different planes within the sample. In the OM micrographs, a large number of small pores (<30 µm diameter) were visible at 10X magnification for the as-LPBF sample (Figure 4.16). After HIP, this porosity was no longer visible, with exception of an occasional pore of similar size as in the as-LPBF condition but with a less spherical shape. This suggests that the pores were affected by the HIP process, causing them to change shape, but were not fully closed. This can be an issue for porosity in LPBF, where the pores are filled with a gas comprising of the build volume shield gas (argon in this case) and/or some vapour from alloying elements such as aluminium being heated by the laser beam. As a result, these pores are difficult to close during HIP as the gas is either compressed inside the pore preventing it from closing, or is forced to diffuse into the bulk material.

Table 4.4 - Bulk density of the Hastelloy-X in each condition of supply as measured using image analysis.

Condition	XY density (%)	YZ density (%)
as-LPBF	99.958	99.945
HIP	99.993	99.995
HIP + HT	99.986	99.995

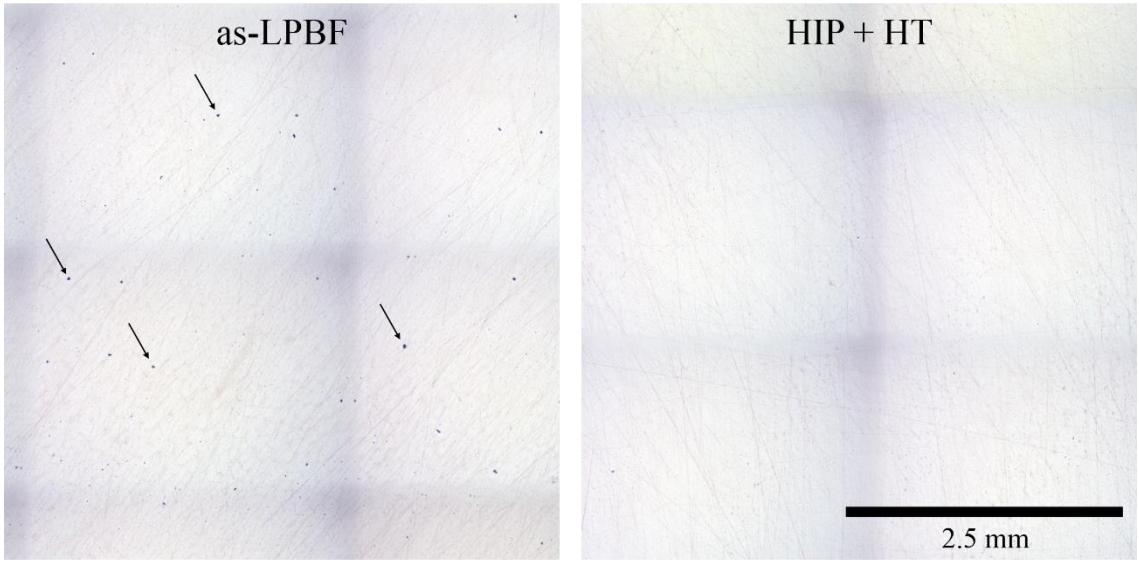


Figure 4.16 - OM micrographs of the HX XY plane in as-LPBF and HIP + HT conditions. Porosity is clearly visible before HIP treatment with some larger pores highlighted with arrows.

4.5.2 MICROSTRUCTURE

After micrographs were taken for density analysis, the samples were etched using the electrolytic method as described in section 3.4.3. Interestingly, the HX HIP condition was etched revealing the grain structure by Kalling's No.2 etchant as used for CM247LC with approximately 3-5 s etch time. However, the as-LPBF and HIP + HT conditions were impervious to this etchant, remaining mirror polished even after full submersion of the surface for >30 s. Further, the HIP condition did not etch as well as the as-LPBF and HIP + HT using the electrolytic method. OM micrographs for the YZ plane are shown in Figure 4.17. Distinct melt pool cross-sections are seen in the as-LPBF samples (Figure 4.17 (a) and (b)) as is typical for LPBF material before any HT. Some elongated grain structures span multiple build layers of the sample, however the main microstructural texture is from the melt pools themselves, particularly the boundary region of each melt pool which is signified by the dark curved line.

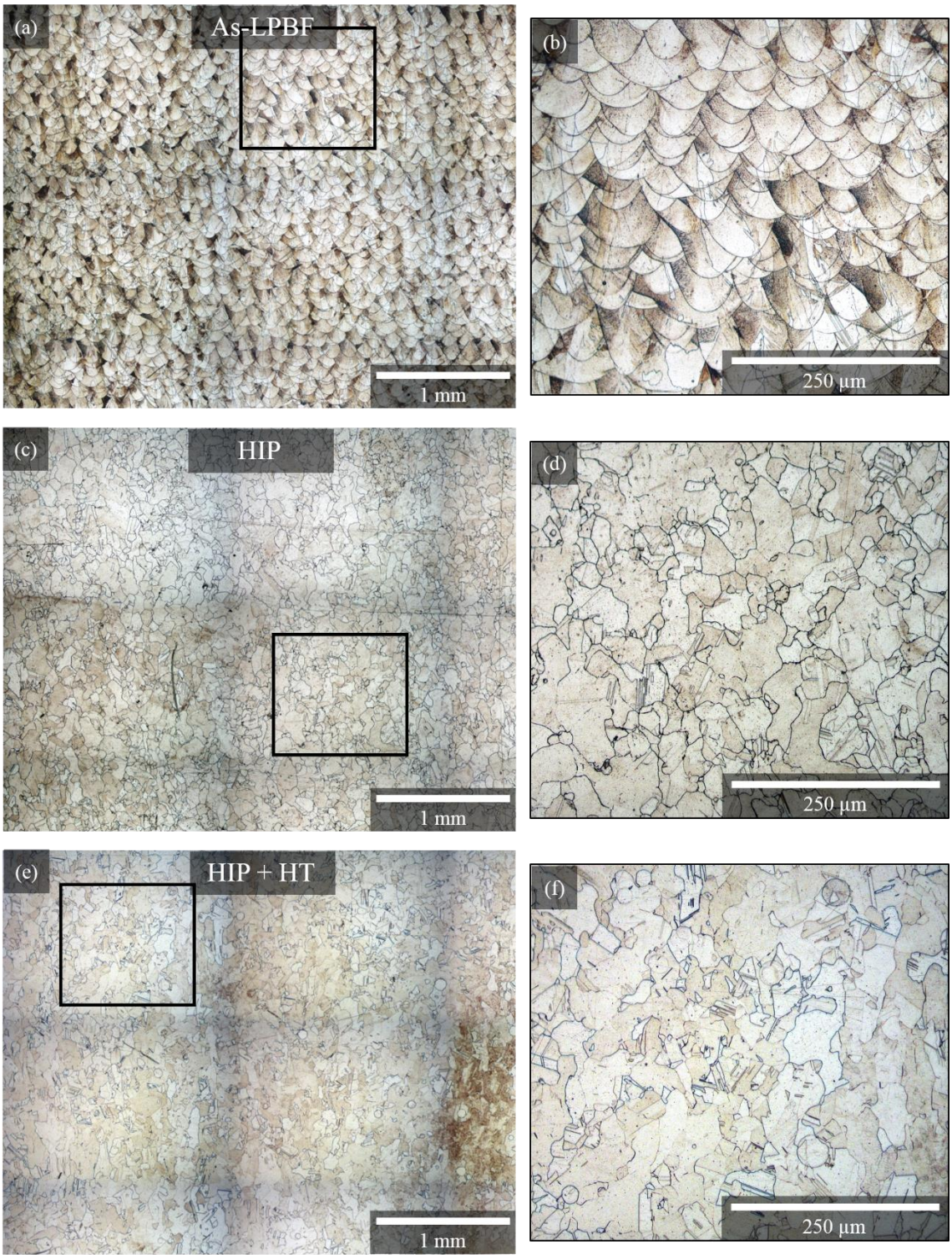


Figure 4.17 - Etched microstructures of YZ plane for the HX in as-LPBF (a), (b), HIP (c), (d) and HIP + HT conditions (e), (f). Note the fine grain structure of as-LPBF (b) is coarsened after HIP (d), and the grain boundary thickness is reduced after HT (f).

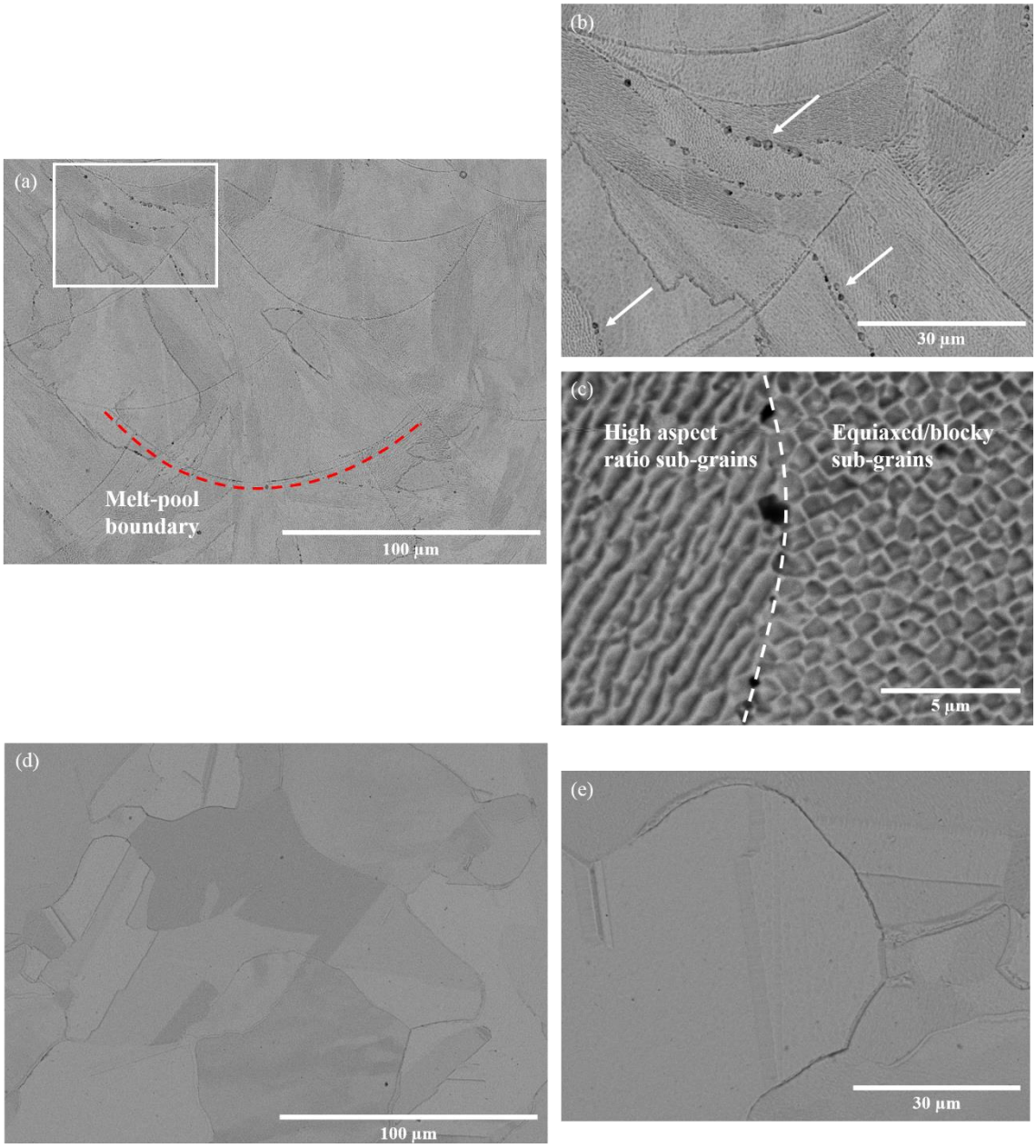


Figure 4.18 - SEM micrographs of the HX YZ plane in as-LPBF (a), (b), (c) and HIP + HT (d), (e) conditions. Melt-pool boundary (a) and grain boundary precipitates shown in (b) with arrows. Note the change in size and shape of the grains after HT.

Within these grains outlined by the melt pool shapes, a very fine sub-grain structure is observed (Figure 4.18 (c)) with a sub-grain size of <1 µm. This sub-grain structure changes frequently across melt-pool boundaries from high-aspect ratio grains to blocky, equiaxed grains. This was also seen in the CM247LC as-LPBF grain structure (Figure 4.10) and is characteristic of the fast cooling rate of the LPBF process, with different grain morphologies based on the magnitude and direction of the thermal gradients during

cooling. After HIP, the clustered cell LPBF grain structure is completely removed and no evidence of the melt pool structure can be observed (Figure 4.17 (c) and (d)). The fine, isotropic grain structure is replaced with coarse, more equiaxed grains of varying shapes and sizes. Further, no directionality is seen. After solutionising HT, the grain structure in the YZ plane remained similar to that seen after HIP with larger, equiaxed grains of varying size and shape (Figure 4.17 (e), (f) and Figure 4.18 (d), (e)). The grain boundaries became less prominent due to the precipitates diffusing into the grain area itself. This is the purpose of the solutionising step and hence was expected.

OM micrographs of the XY plane show a similar progression in microstructure through the post-process heat treatments (Figure 4.19). In the as-LPBF micrograph, the melt pool shapes are clearly visible at approximately 30 ° inclination. The melt pools are not aligned due to a 67 ° rotation in hatch angle between each layer and hence multiple layers of melt pools are visible in this image. In Figure 4.19 (b), two of these melt pools are measured as 85 µm and 91 µm width, narrower than expected but the micrograph does not necessarily show the mid-point or widest region of the melt pool. Within each melt pool are fine grained structures that vary in a similar way to those in Figure 4.18 (b) – no preferred orientation, a range of grain shapes and pronounced grain boundaries.

After HIP, this texture is completely removed and replaced with rounded equiaxed grains as seen in Figure 4.19 (a). These vary in size from approximately 25 µm in diameter to >300 µm diameter and have no preferential growth direction. This is as expected from the HIP treatment as the sample is homogeneously heated and so no thermal gradients are present to drive grain directionality. After solutionising HT, the rounded grains are transformed into blocky structures with right angle or acute-angle grain boundaries in many cases. High aspect ratio grains are now present occurring as needle-like structures in some cases. As with the HIP sample, there is no detectable directionality to the grain structure.

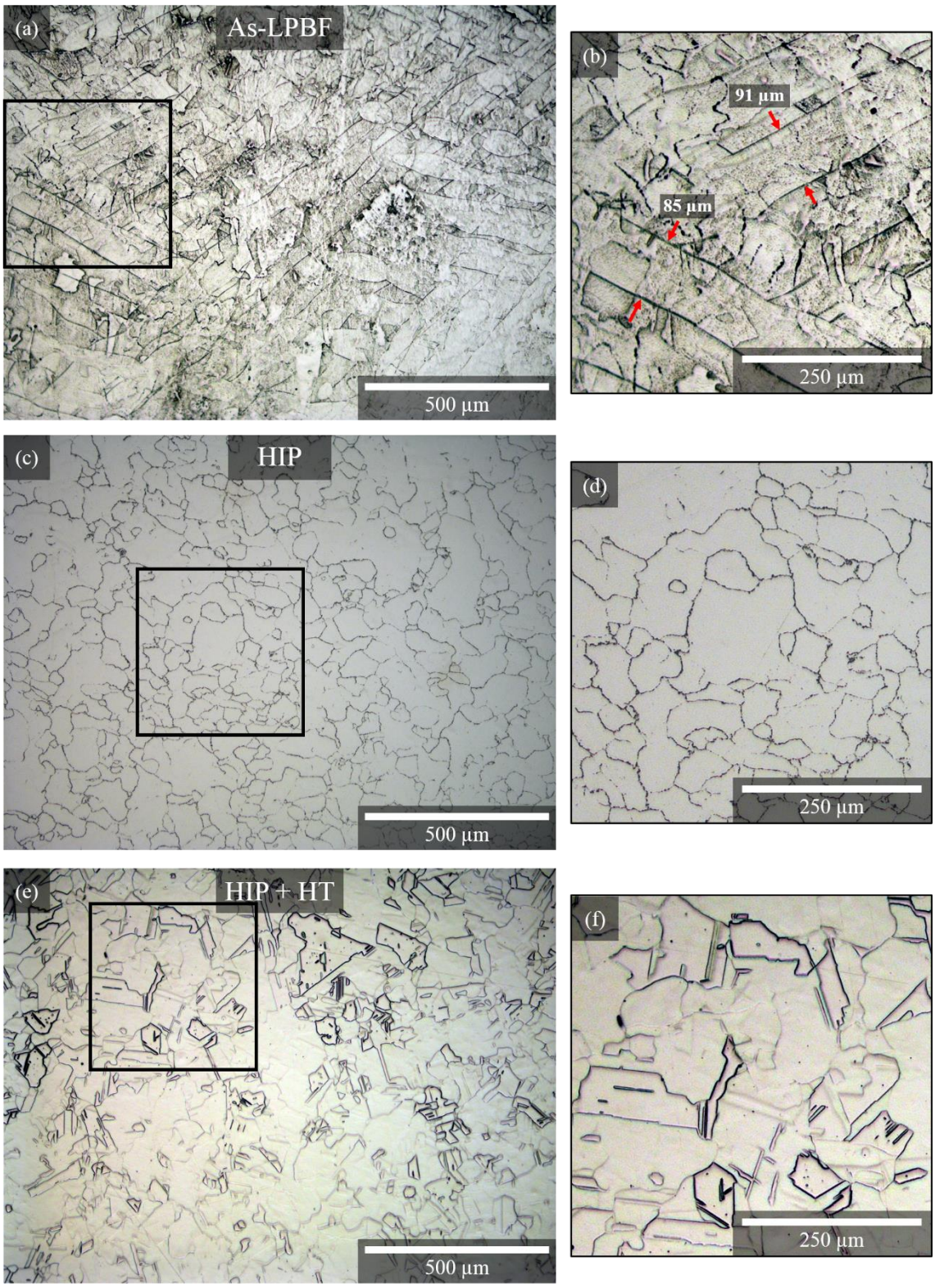


Figure 4.19 – Etched microstructures of XY plane for the HX in as-LPBF (a), (b), HIP (c), (d) and HIP + HT conditions (e), (f). Note the melt pools visible in (a), and the change in microstructure through HIP and HT, particularly the shift to blocky grains after HT (c).

4.5.3 SAMPLE SURFACE CHARACTERISATION

It is important to consider the surface qualities of a PBF manufactured component as the surface roughness profile characteristic of the process has an impact on performance, both mechanical and thermal. For mechanical applications, partially fused particles and near-surface porosity can act as crack initiation sites, significantly reducing the life expectancy of a component. This is especially important for components that must be resistant to creep or fatigue. Therefore, minimum surface roughness is desirable for these applications. When considering thermal applications, surface roughness can be an advantage, particularly for convective heat transfer. A rough surface can induce turbulence and disrupt the boundary layer that forms at the surface of the geometry. As a result, interaction between the heat transfer fluid and the surface is increased, enhancing the heat transfer performance. Rough surfaces may cause fouling of the flow and introduce unacceptable pressure losses. Surface roughness is influenced by processing parameters but is also a characteristic of the material and particle size distribution of the powder feedstock.

The ripples formed within the melt tracks are minimised by using a specific top-skin melt strategy that applies higher laser power to this region in order to achieve greater flatness and lower surface roughness. The higher laser power also minimises the number of particles adhered to the top surface, however some remain. Further, a double contour strategy is used (Figure 4.20 (b)), where the inner contour has a full-width melt track whilst the outer contour is narrower due to interaction with the loose powder. This double contour strategy is used to reduce the chance of porosity between the hatch and contour scans. Near-surface porosity is critical to the mechanical performance of the component as they can act as crack initiation sites, hence simple optimisations like this can improve the service life or ultimate mechanical strength of a component.

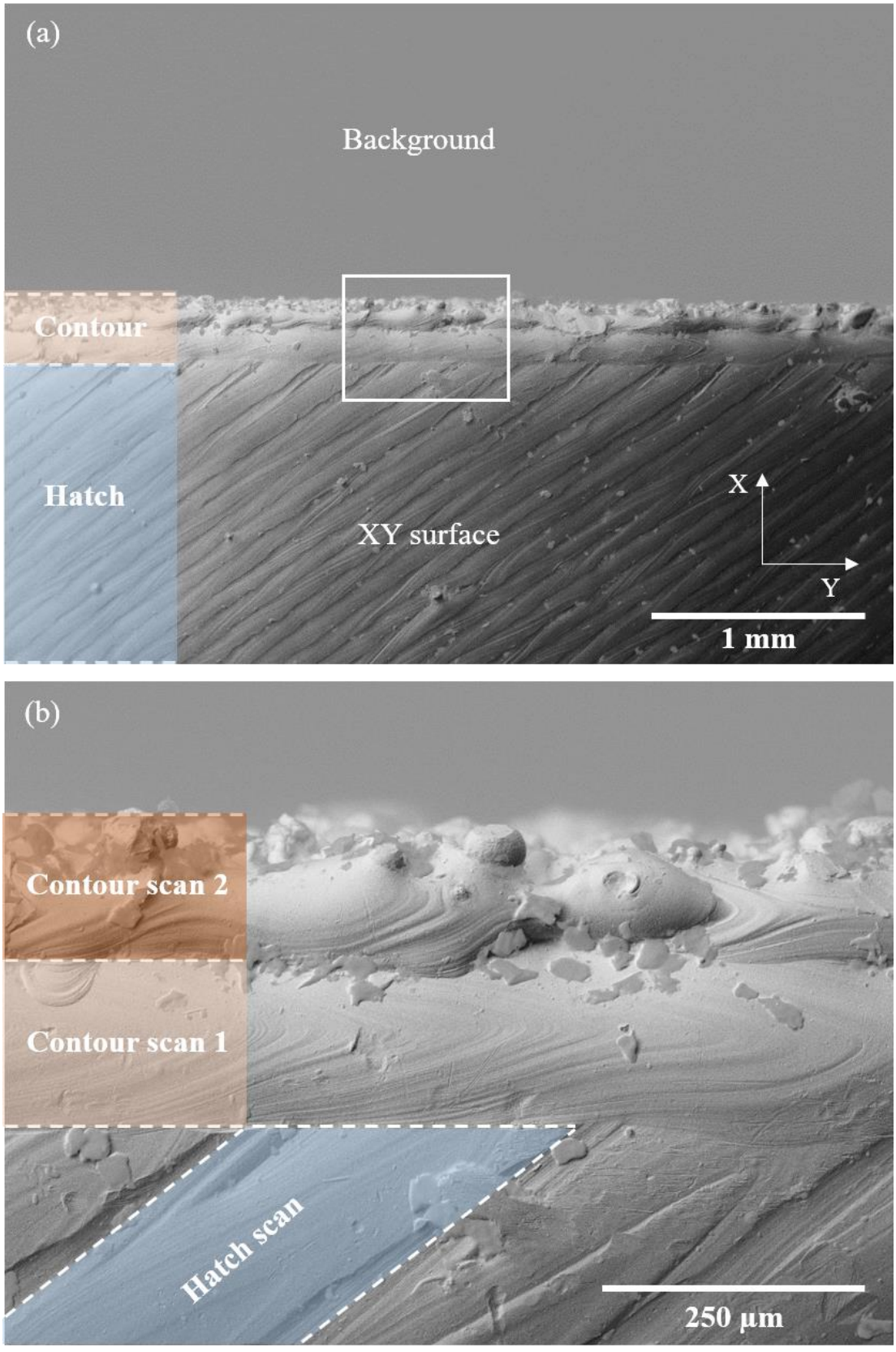


Figure 4.20 - SEM micrographs of the XY plane (top surface) of the HX sample at 40X (a) and 200X (b) magnification. The double contour scan is clearly visible in (b).

Focus variation microscopy was used to evaluate the effect of the contour scan on the XY plane surface height (Figure 4.21). The double contour scan ensures that no near-surface porosity is present, however it can have the effect of increasing the layer thickness in these regions by drawing in excess powder from the area surrounding the part. The colourised surface height map (Figure 4.21 (a) and (b)) clearly show raised regions surrounding the sample, with the greatest height increase at the corner. Here, the laser has to rapidly change direction and as a result is effectively travelling at a reduced speed compared to the straight section. The resulting increased energy input causes a raised feature here. The line profile scan (Figure 4.21 (c)) shows the straight region of the contour is raised by approximately 75 µm from the mean surface height across the sample – this is nearly twice the thickness of a single layer, 40 µm in this instance. This can have important implications in component manufacture, where a dimensional inaccuracy of 75 µm can prevent components from interfacing and fitting correctly. Features such as this can be removed easily in post-processing if easily accessible, however access is not always possible. Therefore, process anomalies such as this must be considered during component design for AM.

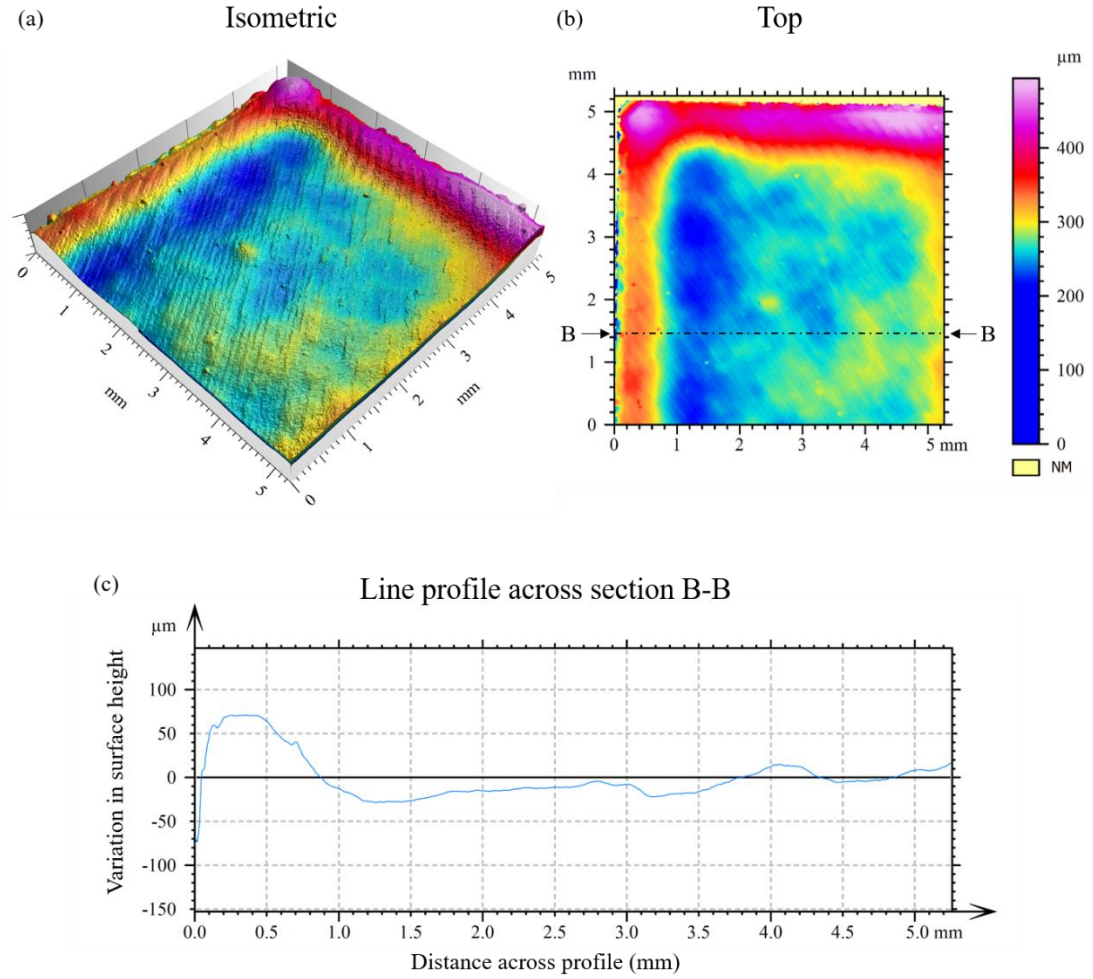


Figure 4.21 - Focus variation microscopy image of the HX sample XY plane (top surface) detailing the raised edges and corner due to the contour scan strategy. A line scan across plane B-B (c) shows this variation, with in increase in height of approximately 75 µm at the sample edge.

Further focus variation microscopy analysis was performed on the XY plane to show the surface waviness inherent to the LPBF process. A profile line scan across section A-A (Figure 4.22 (c)) illustrates the peak and trough form of the top surface, a pattern that is a result of the overlapping melt tracks of the hatch scan. The height across this region varies by approximately ±2.5 µm from the mean surface height and the average track width (trough to trough) is approximately 110 µm. The geometry of the melt tracks extracted in the line profile appears to be more angular than in reality due to the scanning

method of focus variation microscopy, where the surfaces approaching 90 ° to the viewing axis are not captured accurately (the instrument is line-of-sight only). A rotation of the scan head in the X- or Y-axis would be required to capture full detail of the sides of the melt tracks, greatly increasing the scan time. Despite this, the minimum and maximum surface heights are accurate as these surfaces are plane with the focal plane of the instrument, therefore including scan head rotation in this study was not deemed to be necessary. The surface roughness parameters of the XY (top) surface are as given in Table 4.5, showing a low S_q and S_a characteristic of the XY surface.

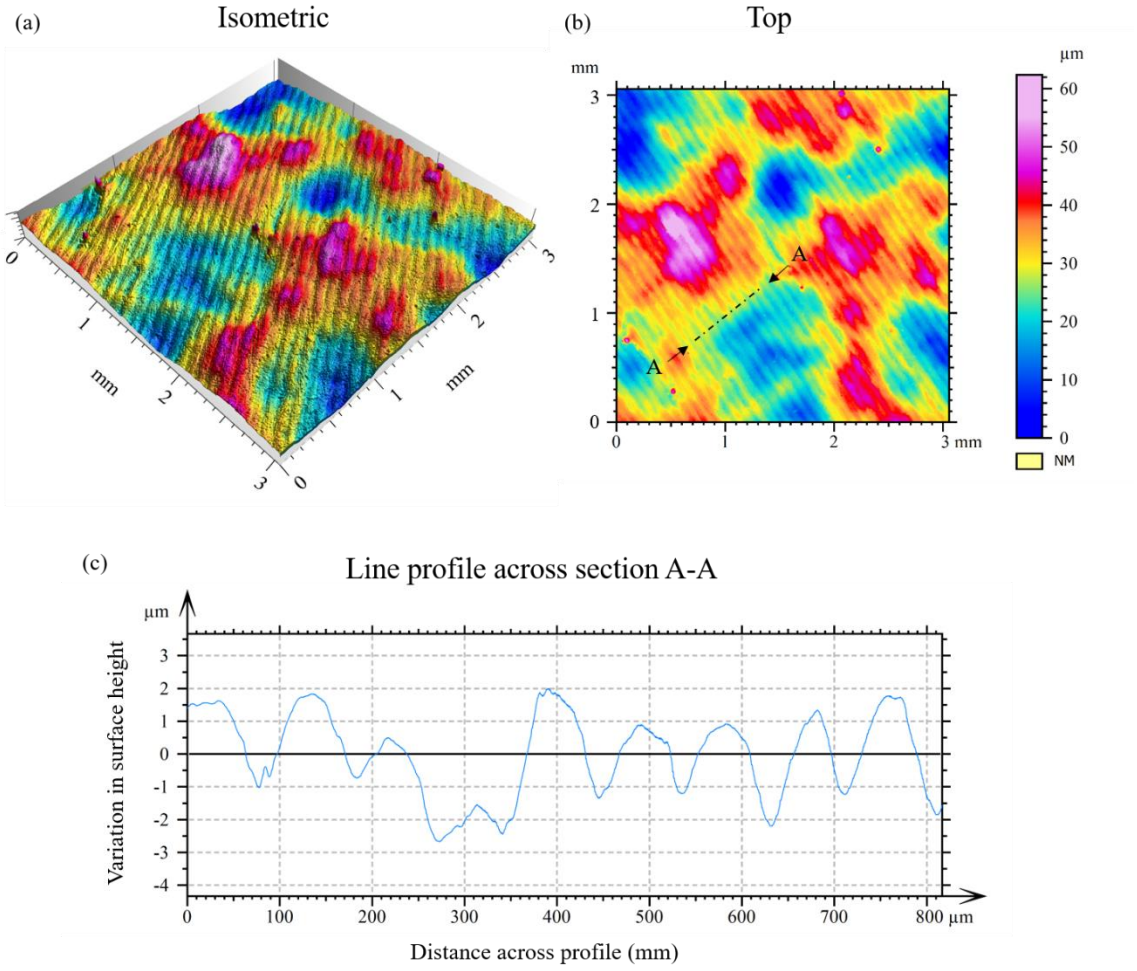


Figure 4.22 - Focus variation microscopy image showing false colour height maps of the HX sample XY plane (a) and (b), and a line profile across section A-A (c) to demonstrate the waviness inherent to LPBF

Table 4.5 - Surface roughness characteristics for the Hastelloy-X as-LPBF XY plane (top surface) as measured using focus variation microscopy

Sq (µm)	Ssk	Sp (µm)	Sv (µm)	Sz (µm)	Sa (µm)
9.37	-0.153	32.7	29.7	62.4	7.5

To investigate if the HIP + HT cycle affected the surface roughness of the HX samples, focus variation microscopy was used to compare the YZ (side) surfaces. The occurrence of partially fused particles is more frequent on this surface and more closely represents the surface found on real components manufactured via LPBF; the XY plane surface roughness only holds for surfaces exactly parallel with the powder bed. This is particularly true for lattice structures, where the organic geometries rarely have large flat areas, but rather are comprised of continuously changing surfaces and so surface roughness does not remain constant.

The change in surface roughness between as-LPBF and HIP + HT condition of supply can be seen in Figure 4.23. After heat treatment, fewer high spots (pink colouration) were present, indicating that the heat treatment process has flattened some of these regions. However, no evidence of particle melting could be observed in Figure 4.23 (c), so it is not clear by which mechanism this may have occurred. It is important to note that some flattening of the high spots on the as-LPBF sample occurred during sample handling and can be seen in Figure 4.23 (a). The surface roughness values for the YZ plane in as-LPBF and HIP + HT conditions are given in Table 4.6. From this it is clear that the YZ surface has considerably higher roughness than the XY surface. This is due to the angle of incidence of the laser beam relative to the surface and the scan parameters used for up-skin surfaces, which are optimised to provide a smoothening effect. This is not as effective for the YZ plane as the laser is always incident at 90 ° to the surface.

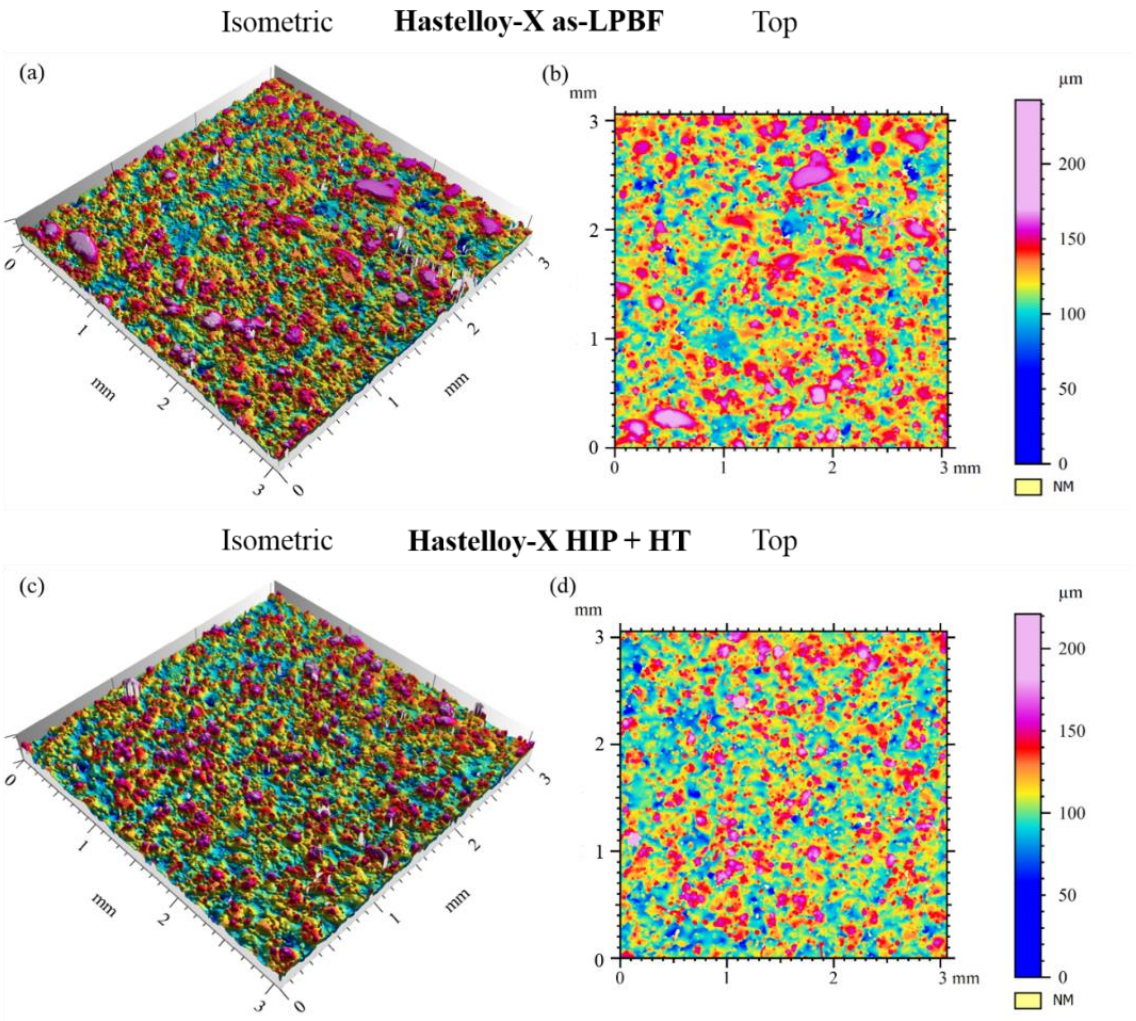


Figure 4.23 - Focus variation microscopy images of the YZ plane of Hastelloy-X in as-LPBF (a), (b) and HIP + HT (c), (d) conditions. The isometric view in (a) shows a larger proportion of high areas (pink), with some flat regions that occurred during post-processing.

Table 4.6 - Surface roughness parameters for the Hastelloy-X as-LPBF and HIP + HT YZ plane (side surface) as measured using focus variation microscopy.

Condition	Sq (µm)	Ssk	Sp (µm)	Sv (µm)	Sz (µm)	Sa (µm)
as-LPBF	19.5	-0.042	120.4	122.3	242.7	15.5
HIP + HT	22.5	0.523	109.9	111.3	221.2	17.8

There is an approximately 10 % increase in Sq and Sa after HIP + HT for the YZ plane – however, the Sz is decreased after HIP + HT. This is unexpected and may be an artefact of the measurement process due to differences in reflectivity of the surfaces. After HIP + HT, a dark coating covered the sample surface that could not be completely removed without changing the surface roughness (i.e. could not be removed with non-contact methods). The as-LPBF surface remained a relatively bright and reflective surface with light silver colour. As a result, some of the peaks in the measurement were blown-out and no height data could be collected. This may have resulted in the reduced Sq and Sa values. With minimal variation in surface roughness when this is taken into account, it can be considered that HIP + HT had no significant effect on surface roughness in this case.

4.5.3.1 AlSi10Mg SURFACE ROUGHNESS

In section 8.3, AlSi10Mg LPBF manufactured lattice structures were used for evaluation of a large number of unit cells, before a smaller batch was manufactured in HX. This was to save time and cost as Ni-alloy raw materials are expensive and manufacture of the samples had to be outsourced to Siemens Industrial Turbomachinery Ltd. Surface roughness is a key element of the convective heat transfer performance as previously described, and so it was important to characterise the samples made in

AlSi10Mg. The focus variation microscopy images are shown in Figure 4.24, which when compared with Figure 4.23, the average size of the roughness features is higher for the AlSi10Mg. Many fine hemispherical partially-fused particles on the HX are replaced with large agglomerated fused particles on the AlSi10Mg. The AlSi10Mg feels to have higher roughness when handling the samples, however the focus variation microscopy analysis provides lower roughness values than for HX across all metrics. This shows the difficulty in characterising LPBF surfaces using metrological equipment, a topic that has been research in depth by Newton et al. [198], [199] and for which it is clear that there is a degree of 'art' to the process of capturing high-quality surface data. This is not to say that the measurements obtained are incorrect, but rather that the values may not represent what is intuitively derived through physically interacting with the sample surfaces – in this case, the AlSi10Mg would be evaluated by a human as having a higher surface roughness and overall lower quality surface finish than that of the HX samples. What is important is the effect the surface roughness has on component performance; the link between measured surface roughness and convective heat transfer performance will be explored later in Chapter 8.

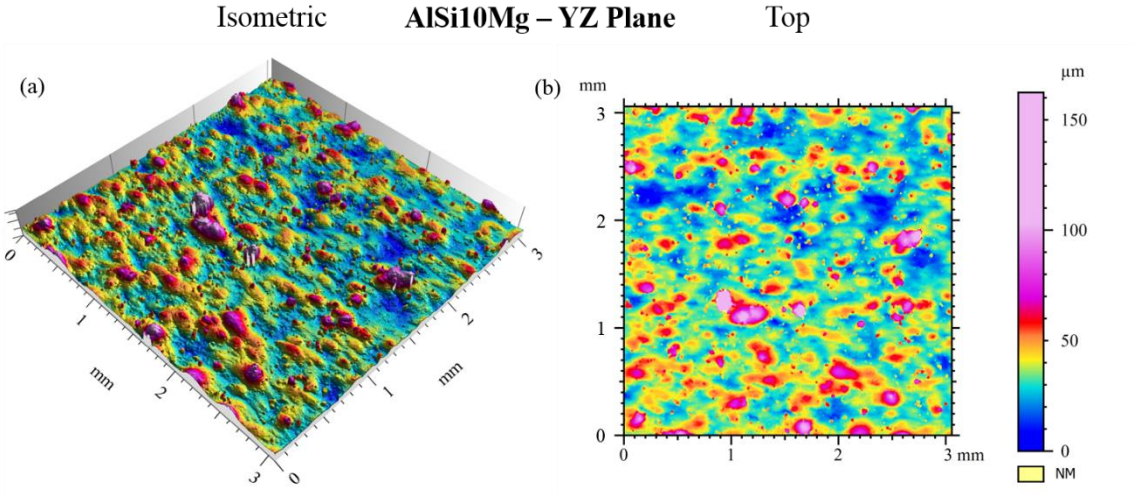


Figure 4.24 - Focus variation microscopy false-colour images of the AlSi10Mg YZ plane.

Table 4.7 – Surface roughness parameters for the AlSi10Mg as-LPBF YZ plane (side surface) as measured using focus variation microscopy.

Material	Sq (µm)	Ssk	Sp (µm)	Sv (µm)	Sz (µm)	Sa (µm)
AlSi10Mg	13.9	1.95	123.7	36.6	160.3	9.8

4.6 CONCLUSIONS

A new scan strategy using fractal patterns was introduced for LPBF, yielding solid samples with good material properties. However, this method could not alleviate the propensity of CM247LC for cracking under high thermal gradients during cooling. New methods such as high-temperature build volumes or controlled heating using a secondary laser beam may be required to achieve a crack-free material without the need for HIP. Therefore, a Hastelloy-X was chosen for manufacture of samples for the remainder of this thesis. It was demonstrated that HX is a good candidate for LPBF with overall bulk density values of >99.9 %, before HIP + HT. The microstructure of the HX in all conditions of supply was also given and will be referred to in section 5.2 onwards in relation to mechanical performance. Surface roughness values for the samples were also obtained using focus variation microscopy as these will have an effect on the convective heat transfer performance of the lattice structures in later experiments (section 8.3).

5 EVALUATING MECHANICAL PERFORMANCE OF LATTICE STRUCTURES

5.1 INTRODUCTION

This Chapter details the methods and results associated with evaluating the mechanical properties of the bulk Ni-base superalloys manufactured via LPBF and the mechanical performance of a range of lattice structures manufactured by the same. Micro-hardness testing is used to evaluate material properties of the bulk alloys on the micro-scale. Compressive testing evaluated the macro-scale properties of both the bulk alloys and the lattice structures. In addition, the effect of a HIP + HT cycle on the mechanical properties of Hastelloy-X was studied. Stills taken from videos of testing were used to analyse the failure modes of the lattice structures where possible, with one sample investigated further using X-ray micro-CT. Whilst heat treatment will be performed on end-use components as a matter of course in the majority of cases, some beneficial mechanical properties can be obtained by retaining the fine-grained microstructure inherent to as-LPBF material. Therefore, it is important to understand the performance of lattice structures both with and without heat treatment.

The data included here is for Hastelloy-X across two conditions of supply, the details of which were provided earlier. Throughout this Chapter, the following colour and shading convention will be used to allow for simple and quick identification of samples and patterns within the data:

Colour – Cell type [all]	
GYR M	
DIA M	
SCH P	
GYR N	
DIA N	
BCC	
BCC AN.	

Shading – Cell size [bar charts]	
10 mm	
5 mm	
3.3 mm	
2.5 mm	

Line style – Cell size [line plots]	
10 mm	——
5 mm	- - -
3.3 mm	·····
2.5 mm	- · -

Marker style – Cell size [scatter plots]	
10 mm	□
5 mm	⊞
3.3 mm	▨
2.5 mm	■

5.2 MICRO HARDNESS

Micro hardness indentations were performed on the HX samples at each condition of supply. A grid of indentations was made with 500 µm spacing between each indentation, sufficient spacing to prevent distortion of the hardness results due to local strain hardening caused by neighbouring indentations. The values obtained from these grids was plot as a colour map as shown in Figure 5.1, and numerical data for mean, maximum, minimum and standard deviation of hardness values is given in Table 5.1.

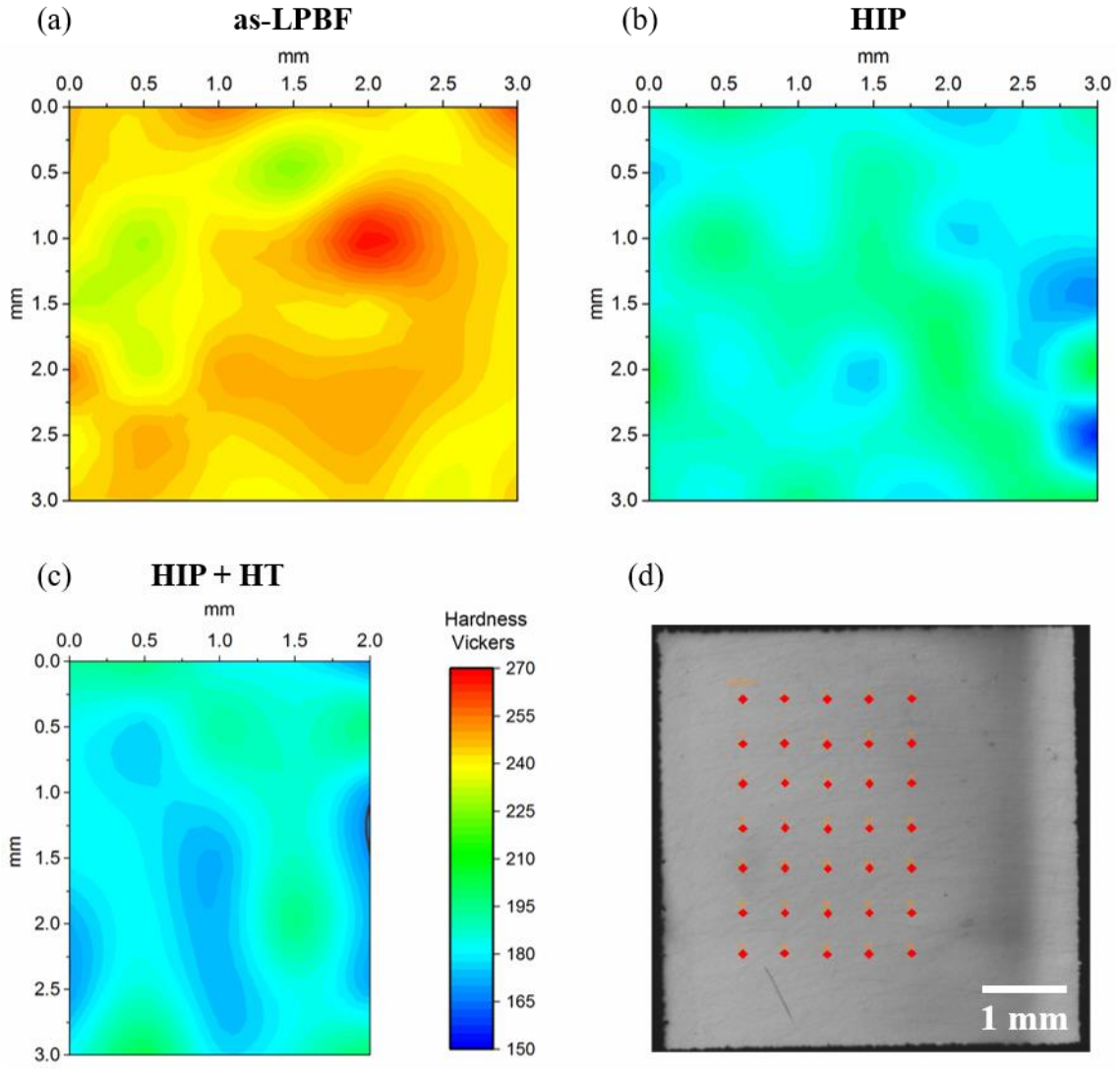


Figure 5.1 – Micro-hardness grid results displayed as colour contour plots. HX material in (a) as-LPBF, (b) HIP and (c) HIP + HT conditions. Scale bar is common between all plots. Placement of indents on HIP + HT sample shown in (d).

Table 5.1 - Hardness data for HX at each condition of supply, giving mean, minimum, maximum and standard deviation results.

Condition	Mean HV	Min. HV	Max. HV	Std. Dev.
as-LPBF	243.5	224.9	269.0	7.3
HIP	185.7	152.7	206.3	9.9
HIP + HT	182.8	169.9	202.4	8.9

The hardness of the HX drops by approximately 25 % after HIP, with the subsequent HT cycle resulting in no significant change in hardness (within the measurement standard deviation). This is due to the change in grain structure seen in the micrographs in section 4.5.2 – the small grains characteristic of the as-LPBF material are conducive to high hardness due to grain boundary strengthening [200]. The Hall-Petch relationship states that yield strength is inversely proportional to the grain size of the alloy (above a critical grain size, ~10 nm). Grain boundaries act to impede dislocation motion and therefore dislocation motion in a bulk material with a high grain boundary density (number of grain boundaries per unit area) will require more energy than in a material with low grain boundary density. In the larger grains present after HIP + HT, dislocations can move through the grain area for a longer distance before encountering a grain boundary and therefore lower energy input is required to deform the material. The load applied and therefore energy input to the material during hardness testing is constant and so this mechanism manifests as a larger deformation in the HIP + HT samples; the measurement of this deformation is what is used to calculate the material hardness and deformation size is inversely proportional to hardness The as-LPBF hardness is aligned with that seen by Tomus et al. [201], however the HIP + HT samples fall approximately 10 % lower (200 – 220 reported by Tomus et al.). This may be a result of the lower pressure and longer

soak time during the HIP cycle for the samples in this thesis (100 MPa for 240 mins vs. 150 MPa for 120 mins), resulting in a larger grain size of the HIP + HT material.

5.3 COMPRESSIVE PERFORMANCE

5.3.1 BULK SAMPLE COMPRESSIVE TESTING

Solid 20x20x20 mm cubes of Hastelloy-X were tested to determine the bulk compressive modulus and strength. The stress-strain curves are given in Figure 5.2, it can be seen that the as-LPBF sample did not yield before the maximum compressive load of the machine was reached (220 kN). This corresponds to an applied stress of 518 MPa without plastic deformation. Therefore, no compressive strength value could be obtained for the as-LPBF sample using the available compressive testing apparatus. The HIP + HT sample began to yield at approximately 315 MPa, with a resulting 0.2 % offset yield strength of 326 MPa. The Young's modulus of the two conditions was similar, with the modulus of 66.5 GPa of the as-LPBF exceeding that of the HIP+HT at 63.1 GPa by 5.4 % (Figure 5.3).

The yield strength of the alloy is directly related to the grain size as discussed previously. The large grain structure of the HIP + HT sample exhibits lower yield strength as dislocations within the material can move more freely, allowing plastic deformation to occur with a lower energy input. However, the Young's modulus does not exhibit any significant change after HIP + HT. Modulus is an elastic regime material property, the mechanism of which is dominated by deformation of atomic bonds [202]. Under elastic strain, insufficient energy has been supplied to result in dislocation motion and all strain energy is stored in compression, elongation or rotation of atomic bonds. This property is related to the chemical composition of the alloy and hence modulus is relatively insensitive to the microstructure and is typically unchanged after heat treatment, as demonstrated here.

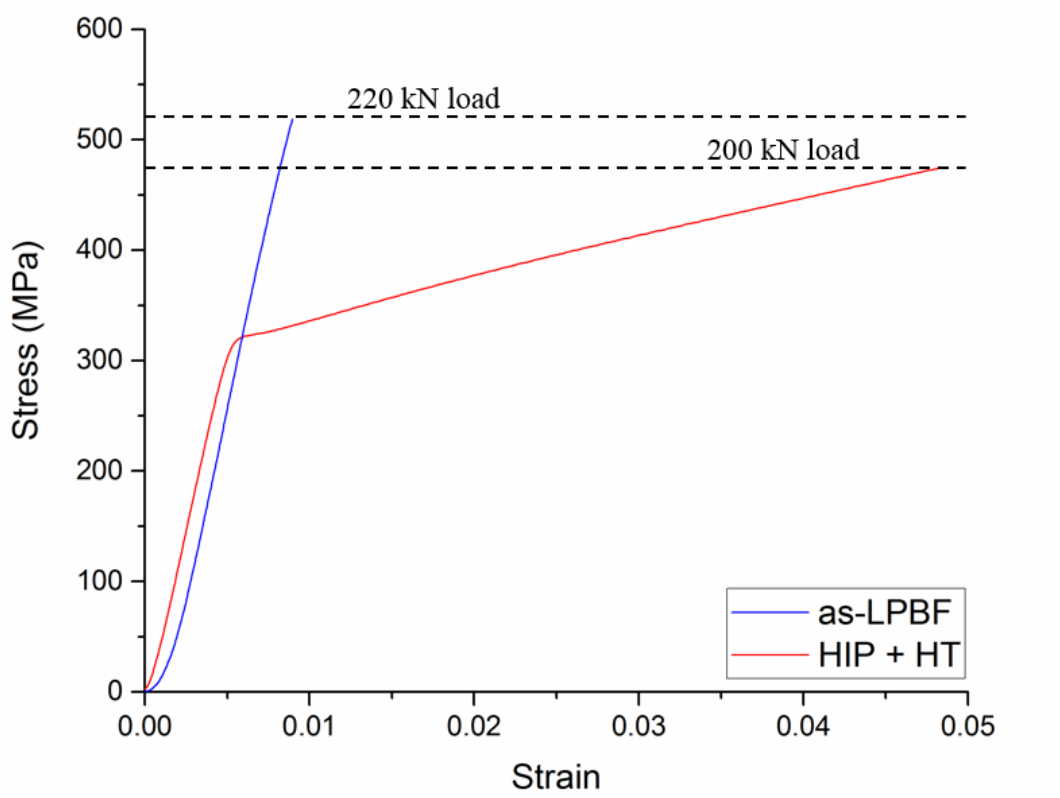


Figure 5.2 - Stress-strain curves for the Hastelloy-X solid samples, used to evaluate the bulk mechanical properties. The as-LPBF sample exceeded the load limit of the testing machine before onset of plastic deformation.

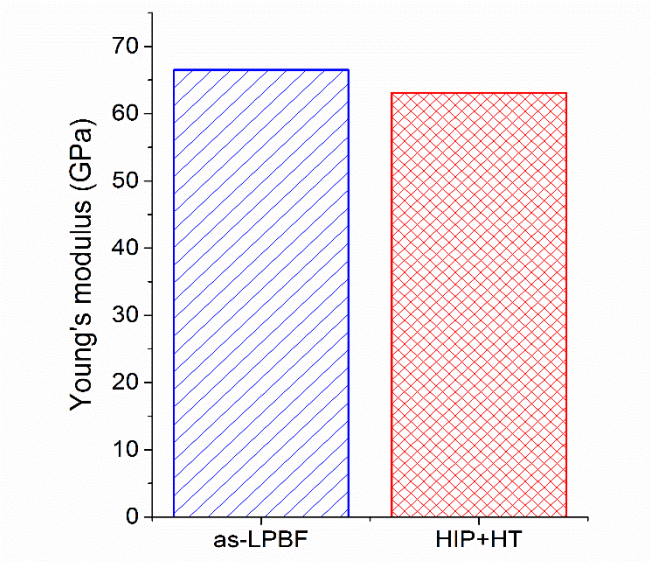


Figure 5.3 - Young's modulus values for the bulk samples in both conditions of supply. The modulus of as-LPBF exceeds that of HIP+HT by 5.4 %

5.3.2 Lattice Structure Samples

The full set of lattice samples under investigation for compressive testing are given in Table 5.2. The samples discussed in the majority of this section had a designed volume fraction of 0.2 (20 %), except those in section 5.3.2.6 which had a designed volume fraction of 0.5 (50 %). For the as-LPBF data set, the sample 'DIA M 3.3' was omitted after repeated build failures due to material expansion above the build plane, leading to collision with the re-coater. A sample with sufficient quality for evaluation could not be manufactured due to the wall thickness being too low, resulting in separation of some layers due to incomplete fusion with previous layers.

Table 5.2 - Unit cell types and cell sizes under investigation. 'X' denotes sample is included in the compressive testing.

	as-LPBF			**HIP + HT**		
Unit cell	10	5	3.3	10	5	3.3
GYR M	X	X	X		X	X
DIA M	X	X			X	X
SCH P	X	X	X		X	X
GYR N						X
DIA N					X	X
BCC					X	X
BCC AN.					X	X

5.3.2.1 Lattice Young's modulus

The lattice Young's modulus of the lattice samples ranged 1.4 – 10.01 GPa, with an overall positive correlation between modulus and volume fraction (Figure 5.4). No correlation could be made between cell size and modulus. There are clear differences between the as-LPBF and HIP+HT matrix phase samples (Figure 5.4, red and blue

regions respectively), demonstrating reduction in lattice modulus after heat treatment. Whilst the modulus of the bulk material was previously discussed to be unaffected by HT, this is not true for the lattice samples as a combination of geometry and material phenomena determine the lattice modulus. Performance of each geometry was similar between the sample sets despite the HIP+HT set having an average of 7.5 % higher volume fraction. The sample with the highest lattice modulus in both conditions of supply, DIA M 5 mm, showed a 17 % reduction in lattice modulus after heat treatment. The microstructural changes that give rise to the reduction in strength have been discussed previously. It is clear that the lattice modulus is driven by material and structural phenomena, therefore care must also be taken to choose an appropriate alloy and heat treatment cycle to obtain the desired material properties alongside choosing an appropriate geometry.

The network phase, BCC and BCC AN. showed significantly lower lattice modulus than the matrix phase samples (Figure 5.4, green region). The matrix phase geometries consist of walls with near-constant thickness that divide the cell volume into a series of voids. The network phase consists of a geometry more analogous to the BCC, with thin elements spanning voids within the cell volume that thicken in the regions where elements combine. As a result, the geometry of the matrix phase lattices naturally provides a higher stiffness, whilst the network phase geometry includes vulnerable regions that undergo premature bending and buckling within the otherwise ‘elastic’ region.

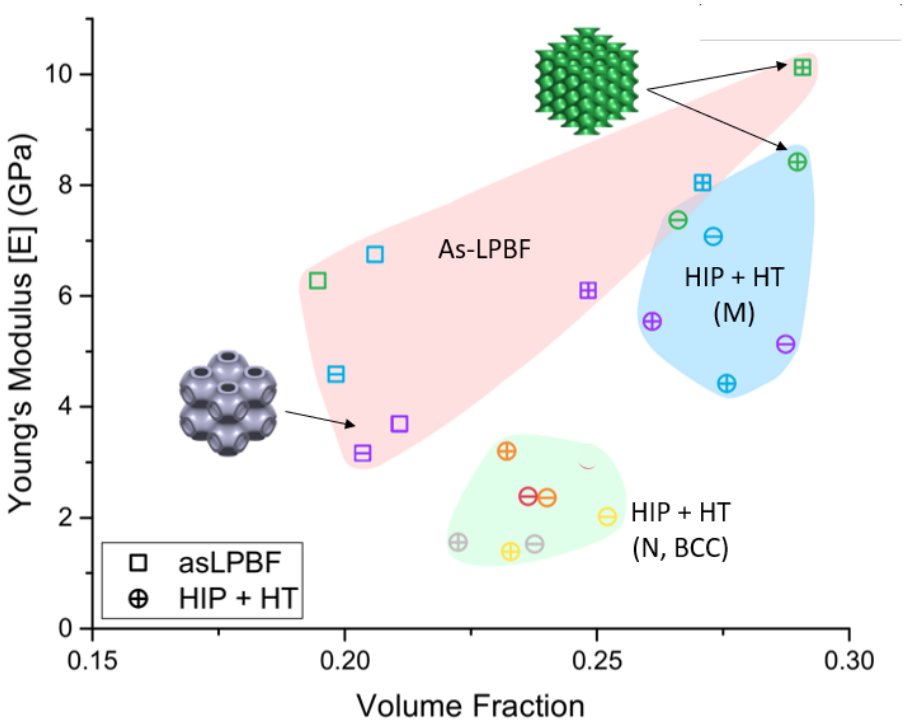


Figure 5.4 - Lattice Young's modulus against volume fraction for the full set of samples. As-LPBF are highlighted in red, HIP+HT matrix phase in blue, HIP+HT network phase and BCC in green.

Sorting the as-LPBF results by increasing volume fraction (Figure 5.5 (a)) the SCH P can be clearly identified as the lowest performance geometry at 20 % volume fraction, particularly the 3.3 mm sample which had half the lattice modulus of the DIA M 10 mm, despite a 0.9 % volume fraction advantage. Further, the lattice modulus of the SCH P 5 mm at 24.8 % measured volume fraction did not exceed that of the DIA M 10 mm at 19.5 % volume fraction. It is clear that at ~20 % volume fraction, the SCH P geometry would not be chosen for applications where high stiffness is required. However, it may be of use in crash structures where energy absorption through deformation of the lattice structure is desirable.

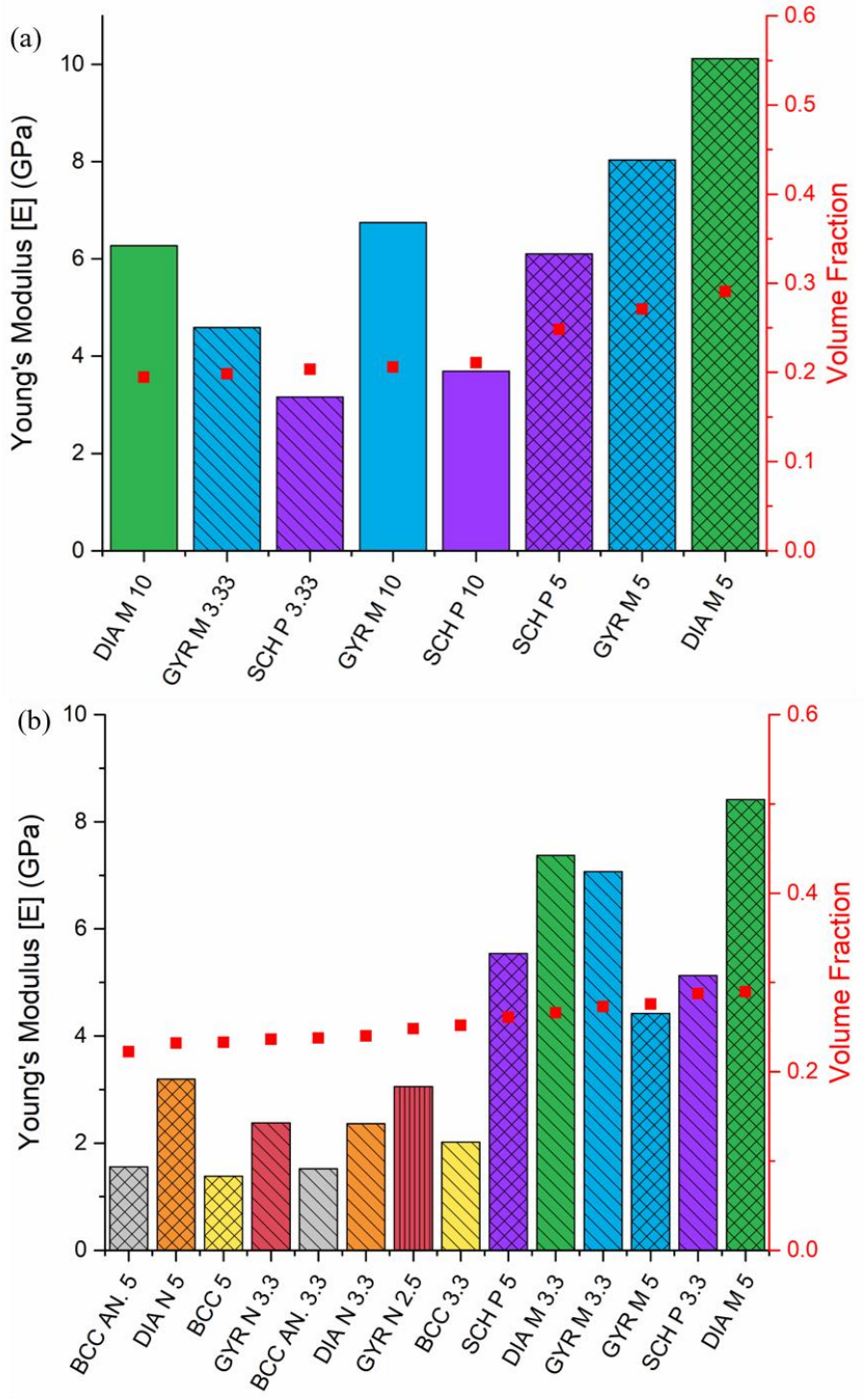


Figure 5.5 - Lattice Young's modulus results for the as-LPBF (a) and HIP + HT (b) samples, sorted by ascending volume fraction as shown on the secondary y-axis.

Results for the HIP + HT samples sorted by ascending volume fraction are given in Figure 5.5 (b). This further demonstrates the high performance of the matrix phase TPMS lattice structures in comparison with the network phase TPMS and BCC-type geometries. Again, the DIA M and GYR M outperformed the SCH P by up to 64 % (SCH P 3.3 mm vs DIA M 5 mm). Both pre- and post-heat treatment, the DIA M 5 mm had the highest performance but was also measured at the highest volume fraction. The CAD model for this sample was verified at 20 % designed volume fraction, therefore the oversizing seen after manufacture was a result of the LPBF process itself.

The network phase TPMS showed improvement in modulus over the classic BCC-type structures, further strengthening the case for adoption of TPMS lattices over strut-type lattices. The DIA N 5 mm showed a 120 % increase in modulus over the BCC 5 mm, indicating that equal performance could be achieved with lower mass through use of DIA N over BCC. Network phase TPMS lattices can be manufactured reliably at lower volume fractions than the matrix phase due to the way material is distributed within the structure – minimum feature size limits of the LPBF process are reached sooner with the matrix phase. Therefore, for applications where minimum weight is the optimisation goal, network phase TPMS lattices may be the most desirable.

5.3.2.2 Yield strength

The reduction in performance from the larger grain structure after heat treatment was also apparent in the lattice yield strength results (Figure 5.6). Overall, samples with a higher lattice modulus also had a higher lattice yield strength. The scatter in lattice yield strength performance was narrowed compared to the modulus data. Again, no correlation between cell size and strength could be determined. The DIA M 5 mm provided the highest lattice yield strength for both conditions of supply (as-LPBF: 88 MPa, HIP+HT: 44 MPa). However, heat treatment resulted in a 50 % decrease in lattice yield strength for this sample. Comparing Figure 5.4 and Figure 5.6, it can be seen that the heat treatment

had a greater effect on the lattice yield strength performance than on the modulus, with the blue region shifting downwards significantly in Figure 5.6.

At each cell size and condition of supply, the SCH P unit cell had the lowest lattice modulus and lattice yield strength of the three matrix-phase unit cells. This is due to the large internal void present in the SCH P unit cell, combined with the lack of material aligned directly in the Z-direction (the axis of loading). This is in comparison with GYR M and DIA M which both have walls that run at least partially along the Z-direction, resulting in increased stiffness and strength.

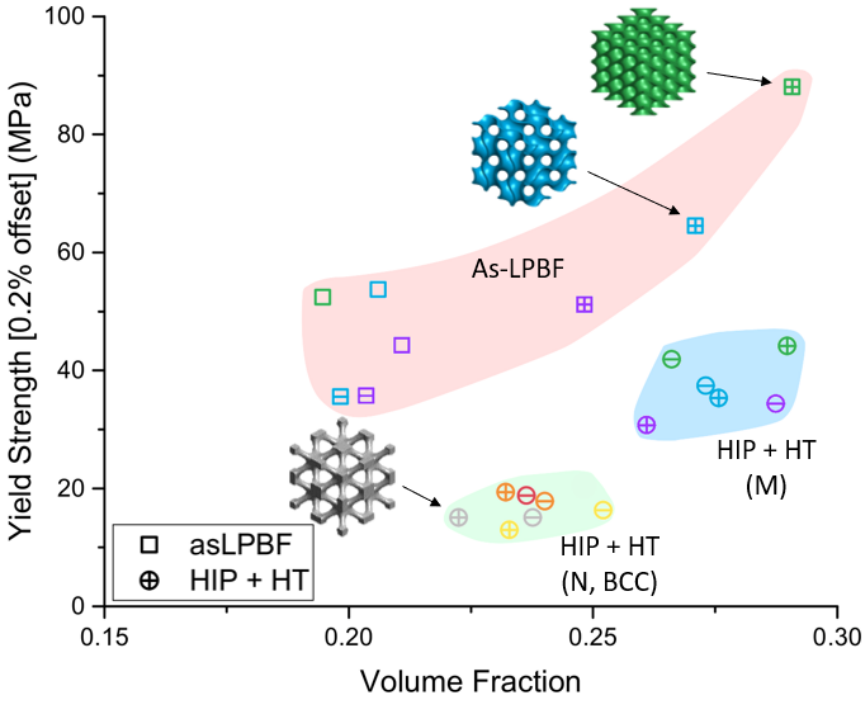


Figure 5.6 - Lattice yield strength (0.2 % offset method) against volume fraction for the full set of samples. As-LPBF are highlighted in red, HIP+HT matrix phase in blue, HIP+HT network phase and BCC in green.

The lattice yield strength data was sorted by volume fraction for the as-LPBF (Figure 5.7 (a)) and HIP + HT (Figure 5.7 (b)) samples. The 10 mm cell size as-LPBF GYR M and SCH P samples have a higher lattice yield strength than the 3.3 mm samples (GYR M: +51 %; SCH P: +24 %), despite less than ±4 % deviation in volume fraction from the

group mean. This suggests that at a 0.2 volume fraction, larger unit cells have a higher mechanical integrity. This may be driven by the change in surface area to volume ratio between 10 mm and 3.3 mm cells (GYR M: 3.31 – 9.52; SCH P: 2.55 – 7.15) and hence decreasing wall thickness as cell size decreases. The surface roughness and thickness of the contour laser scan region remains constant. Consequently, at smaller cell sizes a higher proportion of the mass of the material is comprised of a network of partially fused, low strength powder particles at the surface. As discussed previously, the 5 mm cell size samples were manufactured with a higher volume fraction than the design intent, hence the strength of these samples is greater than the 10 mm and 3.3 mm cell size samples. This pattern of the 5 mm unit cell having the highest strength follows across all three unit cell types, but cannot be directly compared to the 10 mm and 3.3 mm cell size samples due to the volume fraction mismatch.

The decrease in performance seen after HIP + HT also applies to lattice yield strength, where for example the DIA M 5 mm sample saw a 50 % drop in lattice yield strength (88 MPa – 44 MPa). Again, the DIA M and GYR M had the highest performance, with the SCH P being the worst matrix phase TPMS lattice. The network phase lattices showed lower lattice yield strength as expected from the modulus results. However, the performance increase over the BCC-type samples was not as significant. This is a result of the similar bending-dominated deformation modes of these unit cells, with point-to-point connections between cells made at 45 ° to the compressive loading axis rather than the continuous walls, sometimes aligned with the loading direction, seen in the matrix phase lattices. Therefore, compression of these samples occurs at relatively low stress and the geometry collapses in on itself before densifying.

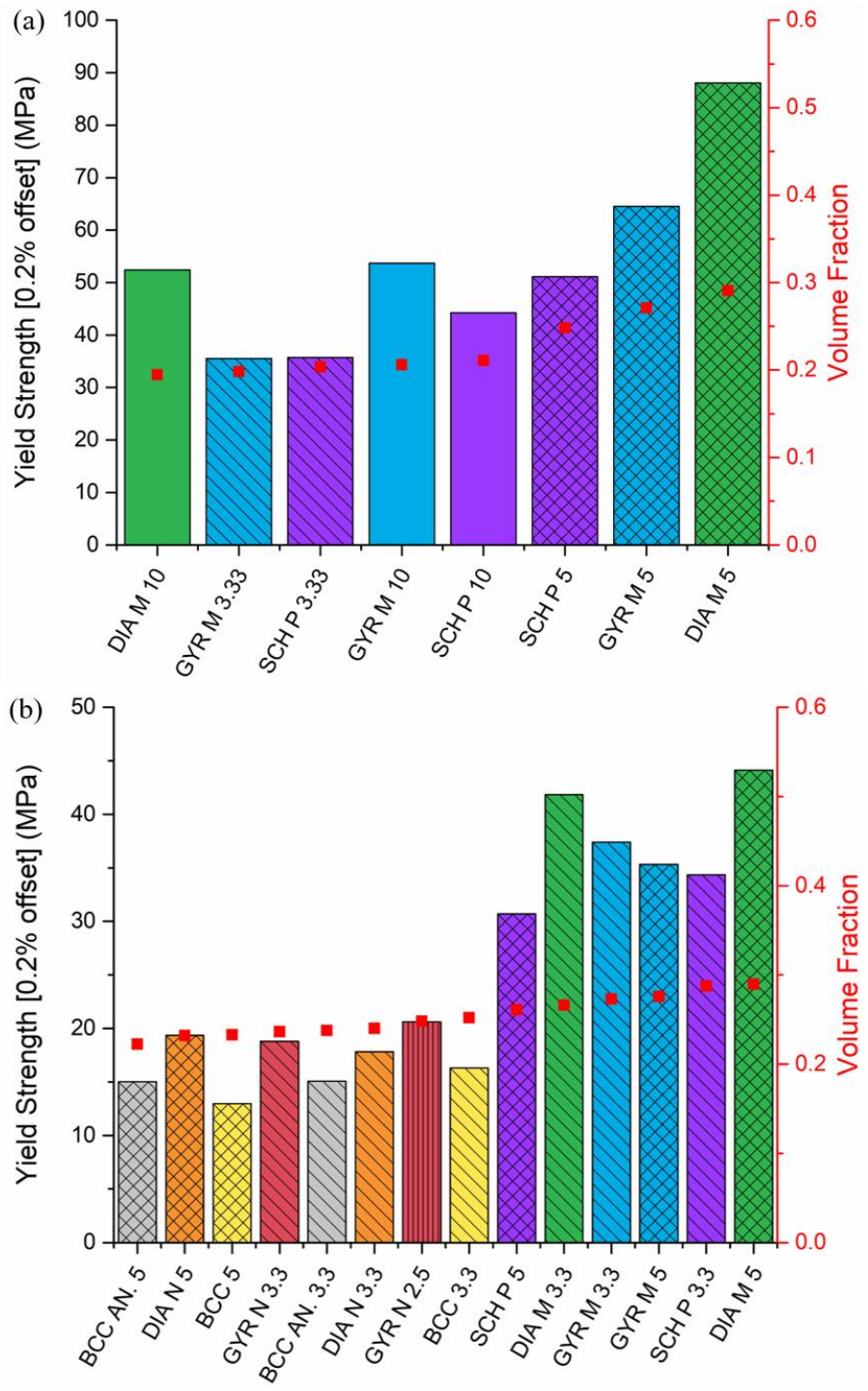


Figure 5.7 - Lattice yield strength [0.2 % offset] results for the as-LPBF (a) and HIP + HT (b) samples, sorted by ascending volume fraction as shown on the secondary y-axis.

5.3.2.3 SPECIFIC MECHANICAL PROPERTIES

Specific mechanical properties are important as they allow selection of materials or geometries that will provide the required performance for the minimum mass. Here, the lattice Young's modulus and lattice yield strength results were divided by the effective density (kg/m^3) of each sample, as measured after manufacture. The highest performance region (upper-right of the plot) is dominated by the as-LPBF sample set, with the HIP+HT set showing decreased performance particularly in specific modulus. This would suggest that the case for implementing lattice structures in the as-LPBF condition is clear. However, the small-grain microstructure that provides this enhanced modulus and yield strength is not desirable in all applications; creep and fatigue performance of as-LPBF components is typically compromised, resulting in reduced component life. Therefore, HT would still be regarded as necessary and the resulting decrease in mechanical performance would need to be accounted for in another way, for example a slight increase in the designed volume fraction of the lattice structure.

Figure 5.8 demonstrates the enhanced performance available using matrix phase TPMS geometries over the conventional strut-type (BCC) lattice structures. A five factor increase in specific lattice yield strength and three factor increase in specific lattice modulus was achieved using as DIA M 5 mm over BCC 5 mm in the HIP+HT condition. This rises to a 5.7 and six factor increase respectively for the as-LPBF condition. The network phase TPMS geometries showed poor performance in specific mechanical properties when compared to the matrix phase, however, still provided a 25 – 125 % increase in specific yield strength over the BCC samples. Specific Young's modulus showed a maximum of 25 % improvement over BCC, demonstrating that the node and element topology of the network phase TPMS results in a significantly lower stiffness than the surface-based topology of the matrix phase.

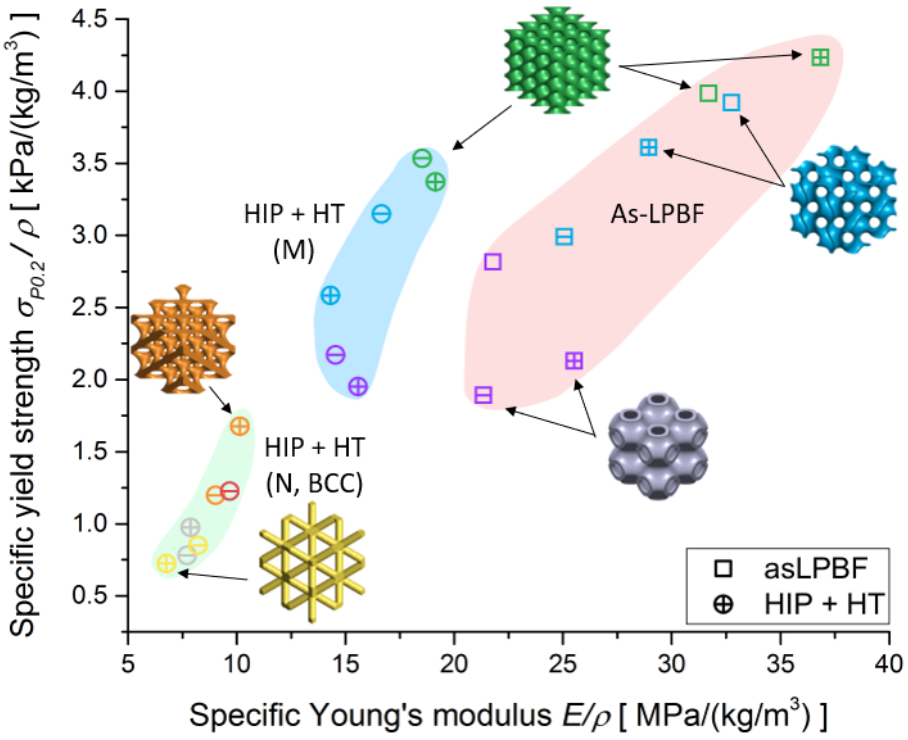


Figure 5.8 - Specific lattice mechanical properties for the full sample set. Highest performance is found in the upper-right corner of the plot.

5.3.2.4 Deformation and failure modes

The stress-strain plots for the as-LPBF 10 mm samples are given in Figure 5.9, with the corresponding still images taken during testing in Figure 5.10 (row 1 and 2). Both demonstrate the ductile deformation seen throughout all samples and conditions of supply. The GYR M unit cell geometry contains sinusoidal-type curved walls than run parallel with the compression direction, aiding in stiffness and strength. As the lattice strain increased in the GYR M 10 mm sample, the sinusoidal wall shapes increased in amplitude and decreased in wavelength until approximately 20 % lattice strain (Figure 5.10, top row), beyond which the stress plateaued and began to decrease as the walls buckled. Between 30 – 40 % lattice strain, the geometry underwent a concertina-like buckling where the walls collapsed into the void space within the cells. At approximately 40 % lattice strain, the walls came into contact and the sample began to densify with a

sharp increase in stress as seen in the stress-strain plot. This is in contrast to the compressive failure mode seen in a GYR M 9 mm sample tested by Maskery et al. [124] in as-LPBF AlSi10Mg material, where the cell walls underwent brittle fracture and structural failure occurred due to crack propagation through the lattice. This indicates that the failure mode of the lattice is highly dependent on the ductility of the material chosen for manufacture.

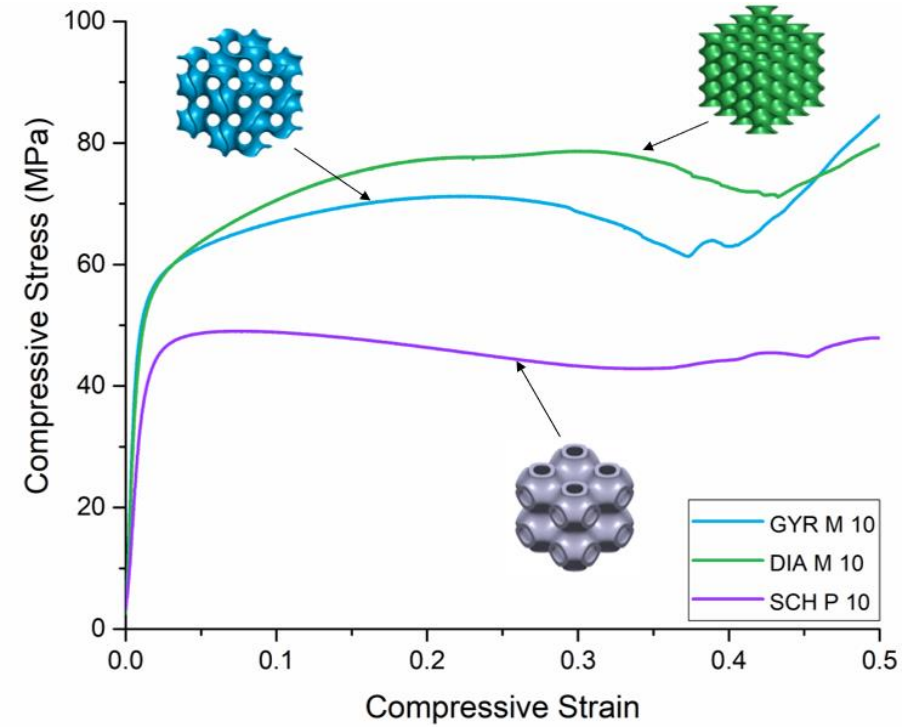


Figure 5.9 - Stress-strain plots for each of the as-LPBF 0.2 10 m cell size lattice samples. All data beyond 50 % lattice strain is truncated. Similar loading response is observed across all unit cell types and sizes. No evidence of sudden failure typical of cracking can be seen.

Deformation of the SCH M 10 mm sample began via bending of the cell walls at approximately 10 % lattice strain (Figure 5.10, row 2). Thereon, the lattice stress value decreased as the walls of the lattice were plastically deformed, with collapse of the lower cells occurring first. At 37 % lattice strain, the stress began to rise again as the internal void closed and the lattice began to densify. The bending at specific points on the SCH P

geometry results in onset of significant plastic deformation soon after the elastic limit (approximately 5 % lattice strain), as seen in the stress-strain plot. In contrast, the stress is more evenly distributed in the GYR M and DIA M geometry, where applied stress increases until 20 % lattice strain. This pattern follows across all cell sizes and highlights an intrinsic mechanical weakness of the SCH P geometry.

The 5 mm and 3.3 mm GYR M and DIA M samples exhibited an extended, flat stress-strain plot when compared to the stress plateau followed by decreasing stress exhibited by the 10 mm cell size samples. This is attributed to the unconstrained walls of the samples – at 10 mm cell size [2 x 2 x 2 cells], 100 % of the cells have three unconstrained sides, allowing for a high degree of deformation to occur in the plane normal to the compression axis. This is particularly evident in Figure 5.10 (top row) for the GYR M 10 mm sample, where the bottom corners of the sample began to bend and deflect outwards beyond 20 % lattice strain. This causes the downward stress trend in the stress-strain plot. For 5 mm [4 x 4 x 4 cells] and 3.3 mm [6 x 6 x 6 cells] cell sizes, only 12.5 % and 3.7 % respectively of the total cells in the sample have three unconstrained sides. Consequently, the samples remained geometrically stable in the plane normal to the compression axis, with minimal deformation resulting from unconstrained features. As a result, the stress-strain curve does not have a negative trend beyond the stress plateau for these samples in Figure 5.9. The SCH P geometry is self-supporting in this regard as its circular cross-section prevents any geometry in contact with the compression ram from deforming relative to the whole sample. Therefore, the stress-strain plot flattens quickly after onset of plastic deformation.

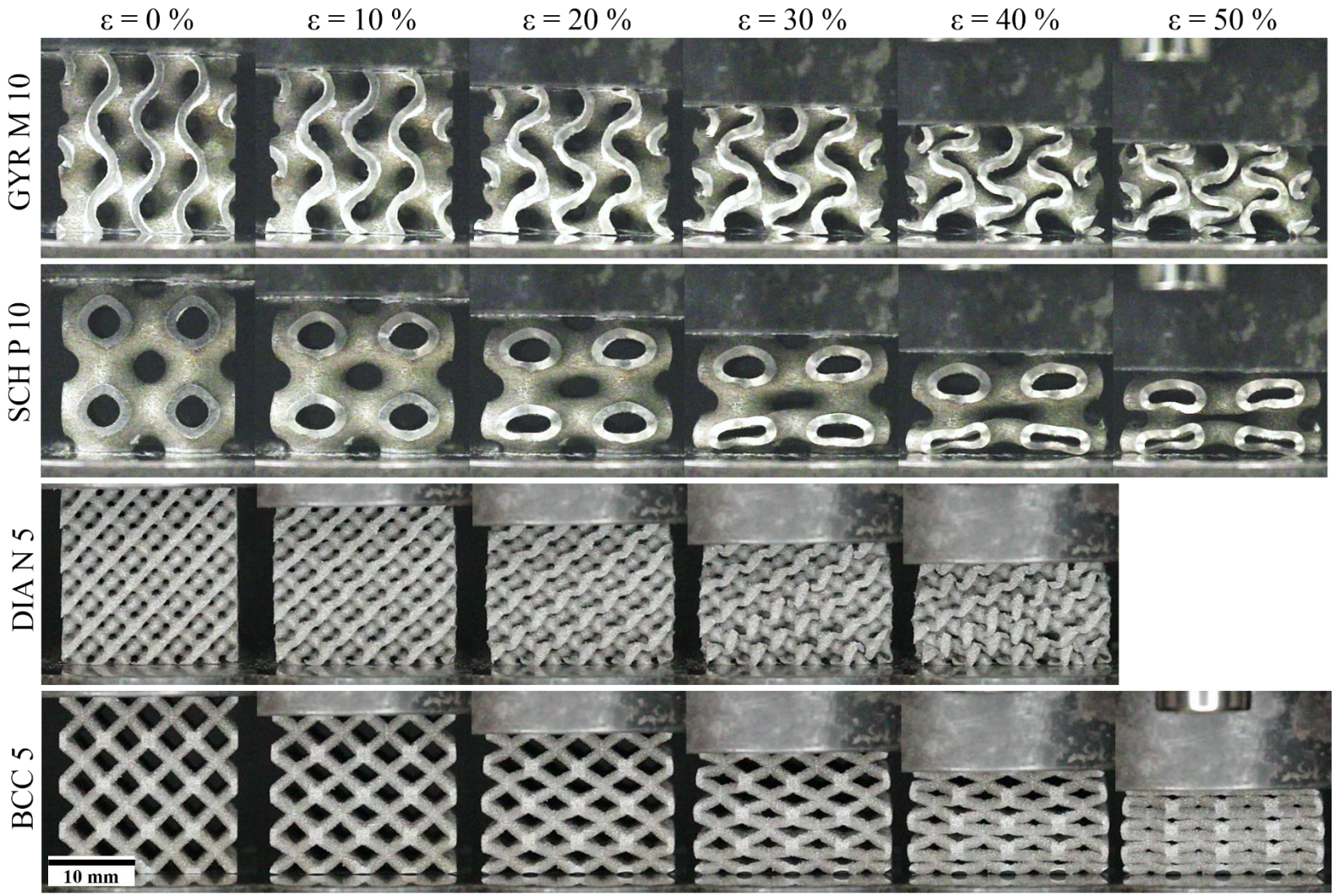


Figure 5.10 - Images captured during compressive testing at lattice strain values of 0 % - 50 %. Sample name is given on the left side of each row. The failure mode of the SCH P unit cell is bending, whilst buckling failure dominates for the GYR M unit cell. The DIA N buckles and layers collapse along a 45 ° plane. The BCC struts bend with the nodes acting as pivot points.

The HIP+HT network phase and BCC lattices also show ductile deformation in the stress-strain plots (Figure 5.11) and still images from testing (Figure 5.10, row 3 and 4). The DIA N geometry had the highest performance but also suffered failures at high lattice strain which are discussed in the following section. The GYR N sample performed in much the same way as the other TPMS lattices with an extended plateau region after the elastic region, followed by densification of the structure. The BCC geometries reached the elastic limit at the lowest compressive stress of all geometries under investigation. The structure deformed via bending of the struts with the nodes as pivot points, with the lower layers collapsing first.

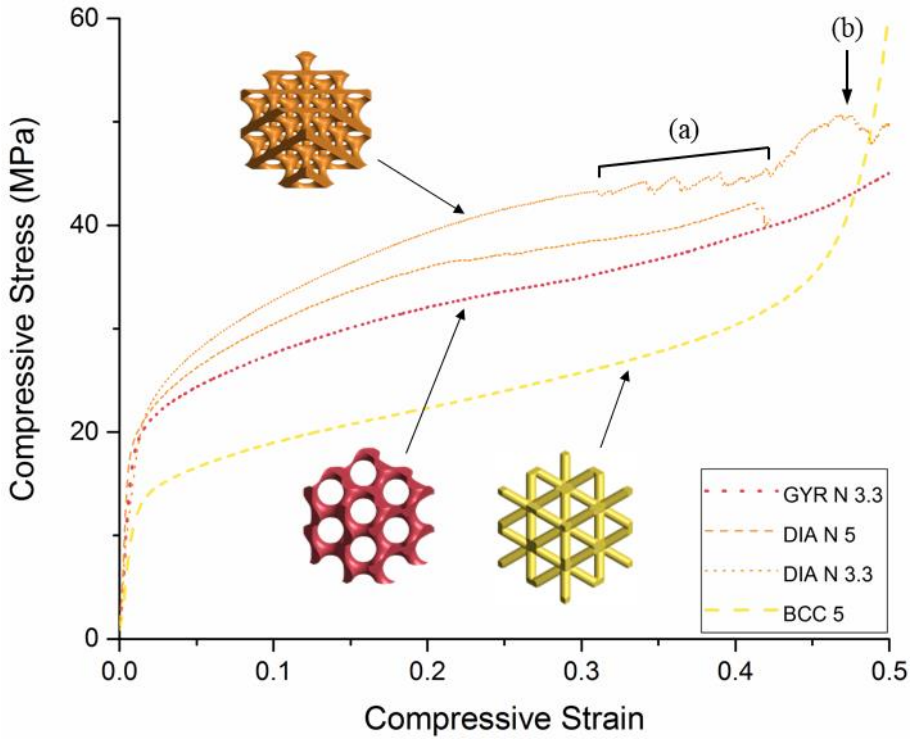


Figure 5.11 - Stress-strain plots for a selection of the HIP+HT lattice samples. All data beyond 50 % lattice strain is truncated. Structural failure of the DIA N 3.3 sample occurs in stages up to 40 % lattice strain (a). At 47 % lattice strain (b), the structure undergoes a significant failure leading to a large drop in applied stress.

Onset of densification occurs at approximately 45 % lattice strain, sooner than the network phase TPMS geometries, as the nodes stack to form a column in the loading direction. The DIA N and GYR N structures collapse in a way that effectively fills in the void space within the cells, leading to densification occurring at a higher lattice strain value (beyond 50 %). For the BCC sample, onset of plastic deformation occurred around 13 MPa and the stress-strain curve remained flat until 40 % lattice strain. This indicates a constant bending deformation as can be seen in Figure 5.10 (bottom row). Maskery et al. [125] observed shear deformation along a plane 45 ° to the compression direction in as-LPBF and heat treated AlSi10Mg BCC samples, followed by failure of the struts and collapse in this same plane. Here, the bending deformation demonstrates the dominance of material properties over geometry effects; a more ductile material such as Hastelloy-X collapses in a controlled manner without fracture as its material properties can accommodate bending. This was not the case for the brittle AlSi10Mg.

5.3.2.5 DIA N FRACTURE FAILURE

The DIA N unit cell type was the only sample to exhibit catastrophic failure of elements within the lattice, defined as complete fracture and loss of mechanical integrity of an element. This was indicated as ripples in the stress-strain curves (Figure 5.11 (a) and (b)) as discussed in section 2.4.2.The stress-strain curve for DIA N 5 mm ends after the sharp drop in lattice compressive stress seen at approximately 40 % lattice strain as the test was aborted in attempt to preserve the failure site for micro-CT analysis. For the DIA N 3.3 mm cell, the test was continued after the initial failure to capture further failure points. Small failures occurred sequentially until approximately 40 % lattice strain, shown as ripples in the stress-strain curve, after which compressive stress rises as collapsed layers densify. Fractures were audible during testing. At 47 % lattice strain, a large failure occurred where a drop in compressive stress indicates a more significant structural failure (Figure 5.11, (b)). X-ray micro-CT analysis of the DIA N 3.3 sample

was used to determine the position and topology of the failures. For each failure highlighted in Figure 5.12 (b), fracture occurred across the thinnest section of an element. The scan resolution is not high enough to evaluate the fracture surface directly. However, the deformation of the lattice and failure at 45 ° planes to the loading direction (Figure 5.10, row 3) suggests that the elements have failed under tension due to shear-type loading as the unit cells are sliding relative to their neighbour. This theory is corroborated by the wide fractures formed in the elements in Figure 5.12 (b) and the misalignment of the element across the fracture in Figure 5.12 (d).

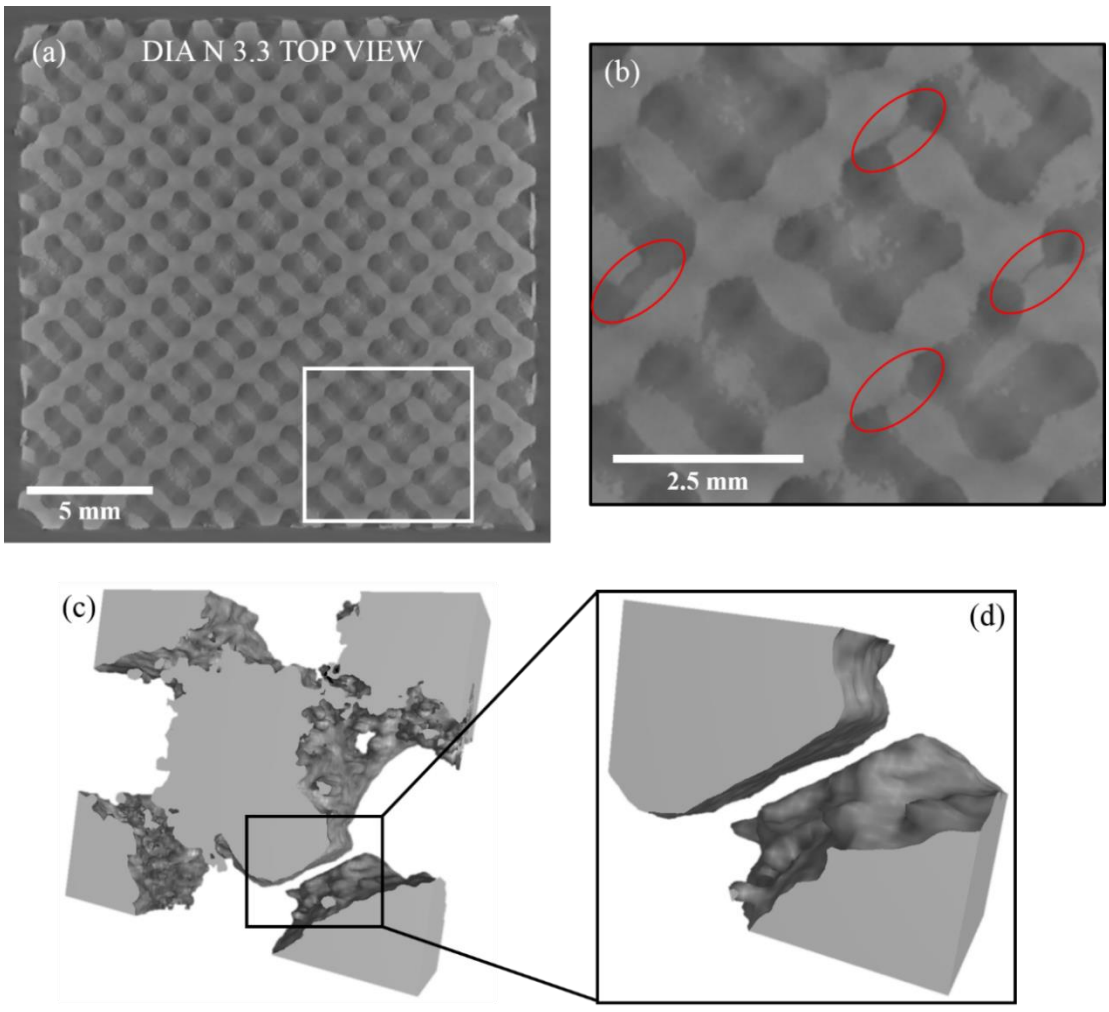


Figure 5.12 - X-ray µCT scans of the DIA N 3.3 sample showing (a) a slice in the top view and (b) an enlarged region with numerous fracture sites highlighted. 3D reconstruction of a fracture site (c) and (d) demonstrates the failure location within the DIA N geometry.

A further site of failure was analysed from the side view of the DIA N 3.3 mm sample (Figure 5.13 (a)). This region also appeared to have failed under shear, with the fracture surfaces showing a high degree of misalignment after failure (Figure 5.13 (b)). A thin section was taken from the 3D reconstruction to demonstrate the appearance of this failure in the context of a lattice unit cell (Figure 5.13 (c)). This single strut has failed whilst neighbouring struts remain intact. It is hypothesised that a small fragment of the strut became detached during the sudden failure (region highlighted in red). This is corroborated by the audible fracture and sample debris on the compressive test apparatus after conclusion of the testing.

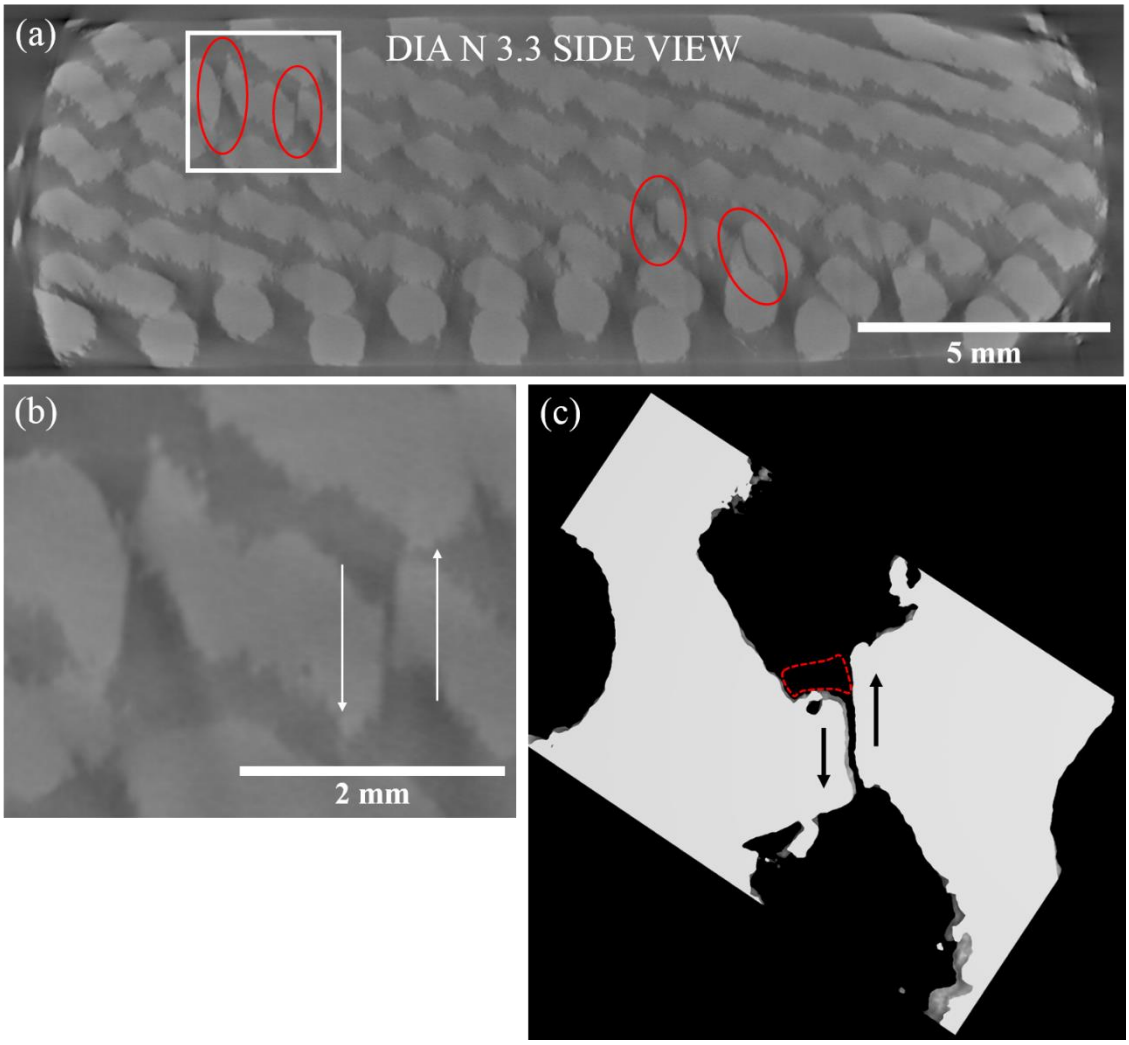


Figure 5.13 - X-ray µCT scans of the DIA N 3.3 sample from the side view (a) showing an enlarged view of further sites of failure (b) and 3D representation of the shear failure (c).

5.3.2.6 50% VOLUME FRACTION SAMPLES

Hastelloy-X as-LPBF samples were also manufactured at 0.5 volume fraction and tested for lattice compressive modulus and yield strength. The lattice Young's modulus results are given in Figure 5.14, sorted by ascending volume fraction. Across all samples, the measured volume fraction remained mostly constant (+1.5 / -0.8 % from the group mean), allowing direct comparison between the samples. As with the 0.2 volume fraction group, no real correlation could be made between cell size and lattice modulus. There was no correlation between the small volume fraction variation and lattice modulus. Further, the unit cell types performed similarly, with the exception of GYR M 3.3 and 5 mm, which had a lower than expected lattice modulus. This may be due to the deformation of unconstrained areas touching the compression plates as described earlier. Overall, the SCH P 5 mm had the highest lattice modulus, taking this geometry from the worst performance at 0.2 volume fraction, to the best performance at 0.5.

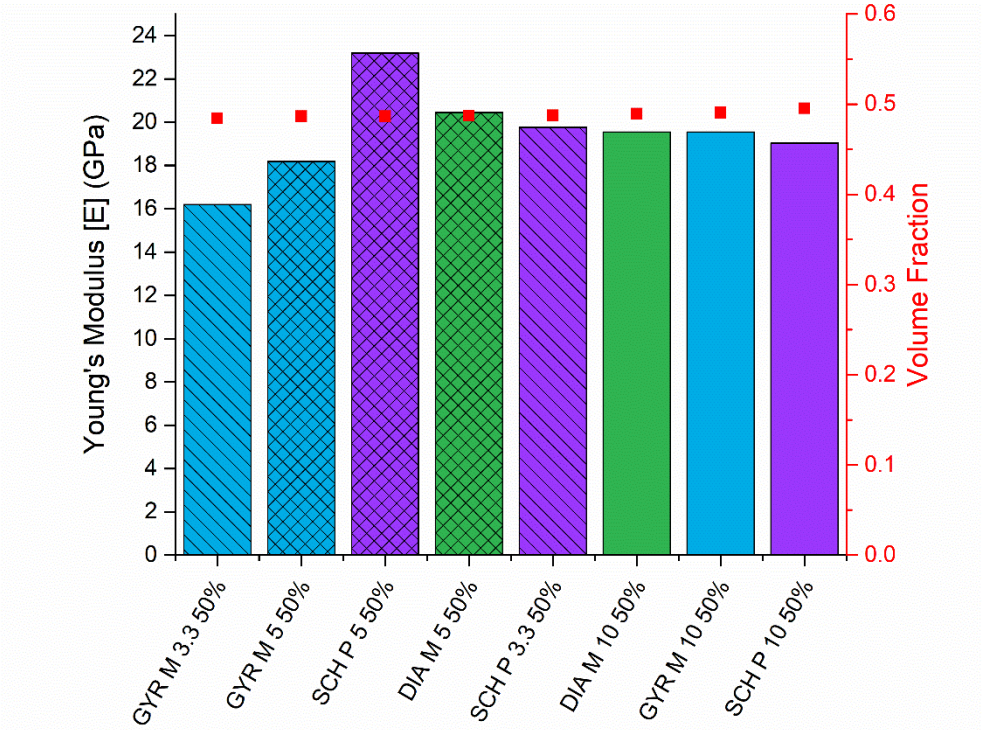


Figure 5.14 - Lattice Young's modulus results for the as-LPBF 0.5 volume fraction samples sorted by ascending volume fraction as shown on the secondary y-axis.

Lattice yield strength is also relatively constant across the various unit cell types and unit cell sizes (Figure 5.15). The SCH P 5 mm again has the highest performance, with the GYR M 3.3 and 5 mm being below expectations. Beyond this, there is little differentiation between the samples, with an average lattice yield strength of 170 MPa. Increasing the volume fraction to 0.5 appears to have desensitised the mechanical properties to unit cell type and size – there is less variation in the results than with the 0.2 volume fraction. The SCH P in particular appears to densify early during compression (Figure 5.16 bottom row) and the thick walls prevent the onset of bending, the method of deformation which prevented the SCH P from high performance under compression at 0.2 volume fraction.

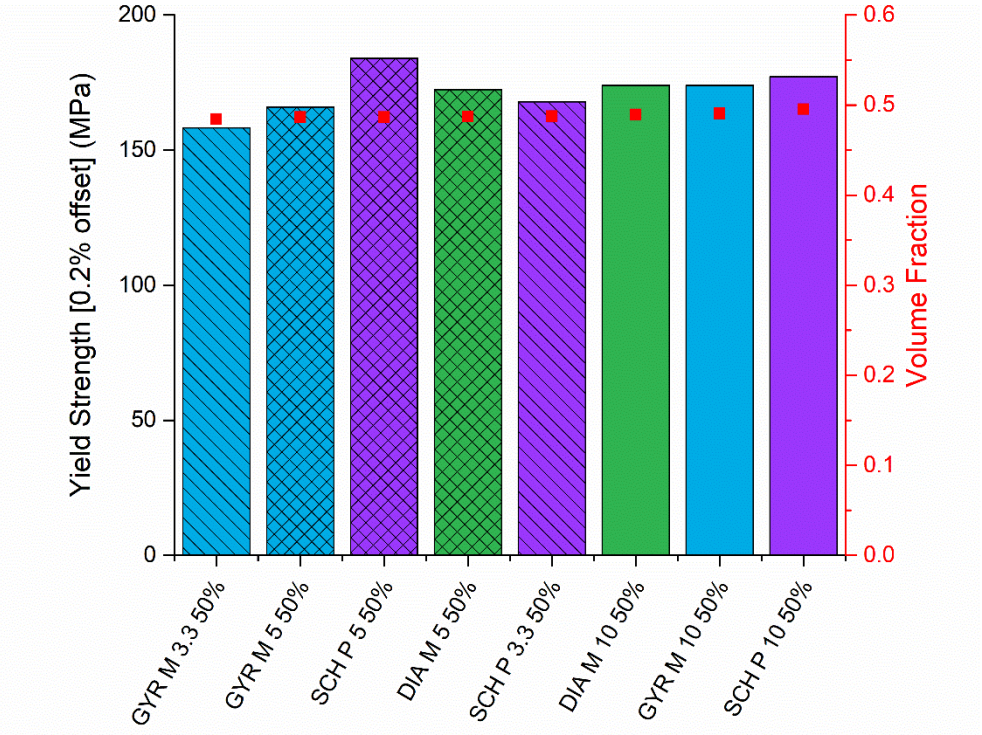


Figure 5.15 - Lattice yield strength [0.2 % offset] results for the as-LPBF 0.5 volume fraction samples sorted by ascending volume fraction as shown on the secondary y-axis

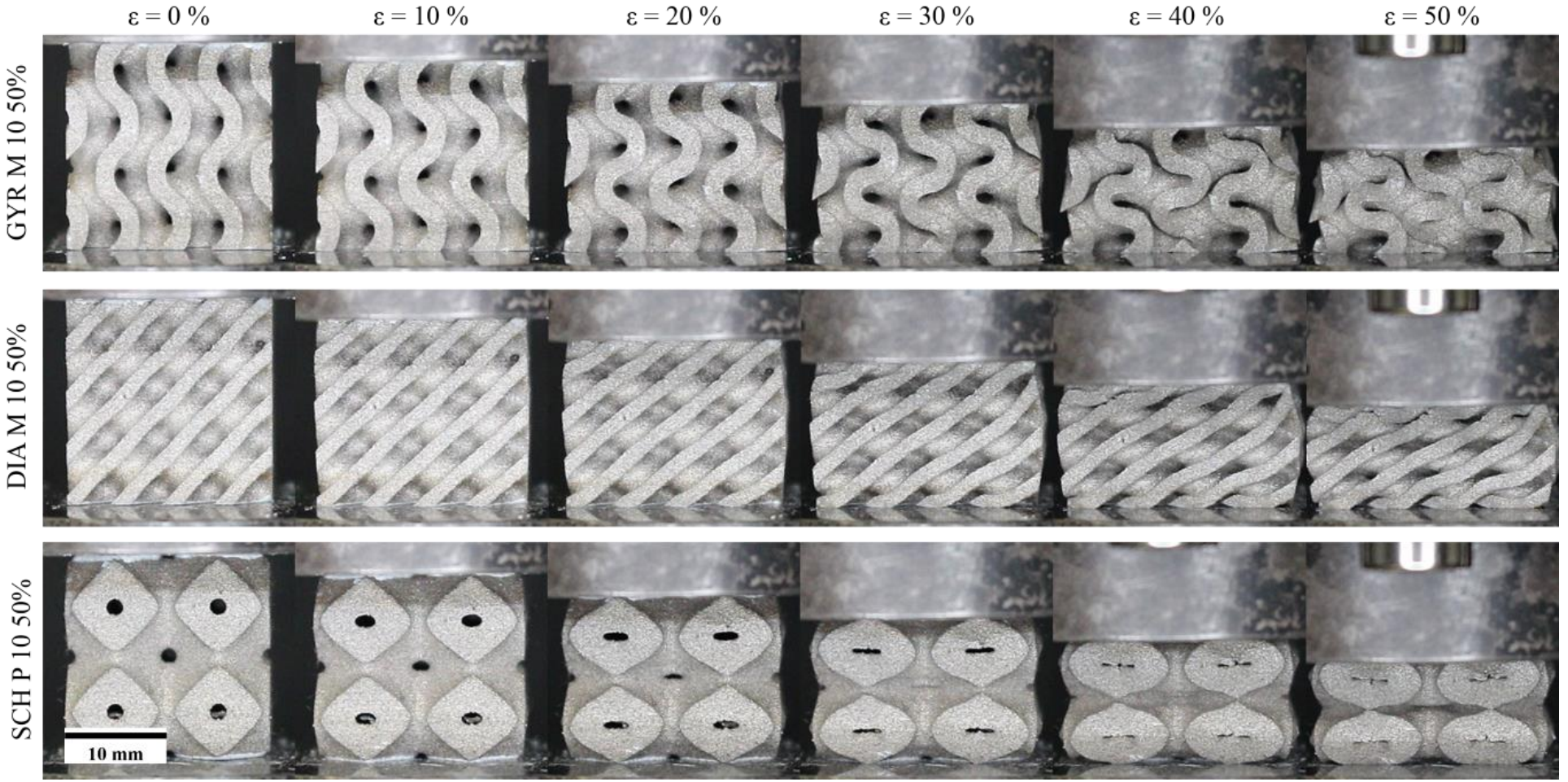


Figure 5.16 - Images captured during compressive testing of the as-LPBF 0.5 volume fraction samples at lattice strain values of 0 % - 50 %. Sample name is given on the left side of each row.

Plotting the 0.5 volume fraction samples on the specific mechanical properties graph (Figure 5.17) it is clear that by increasing the volume fraction, performance can be improved. Therefore, it would be intuitive to assume that a design should incorporate the highest volume fraction possible for the best specific strength. However, with lightweighting being the primary aim of lattice structures in mechanical applications, this would result in a dense, high mass component. Alternatively, solid volumes that do not require the mechanical properties that high material density provides should be replaced with a lattice that has sufficient strength or modulus, but also enables mass to be minimised. A computational optimisation can determine the required volume fraction, in some cases even grading the lattice to provide the strength or stiffness where it is required, whilst minimising mass in areas that are not under high stress or loading.

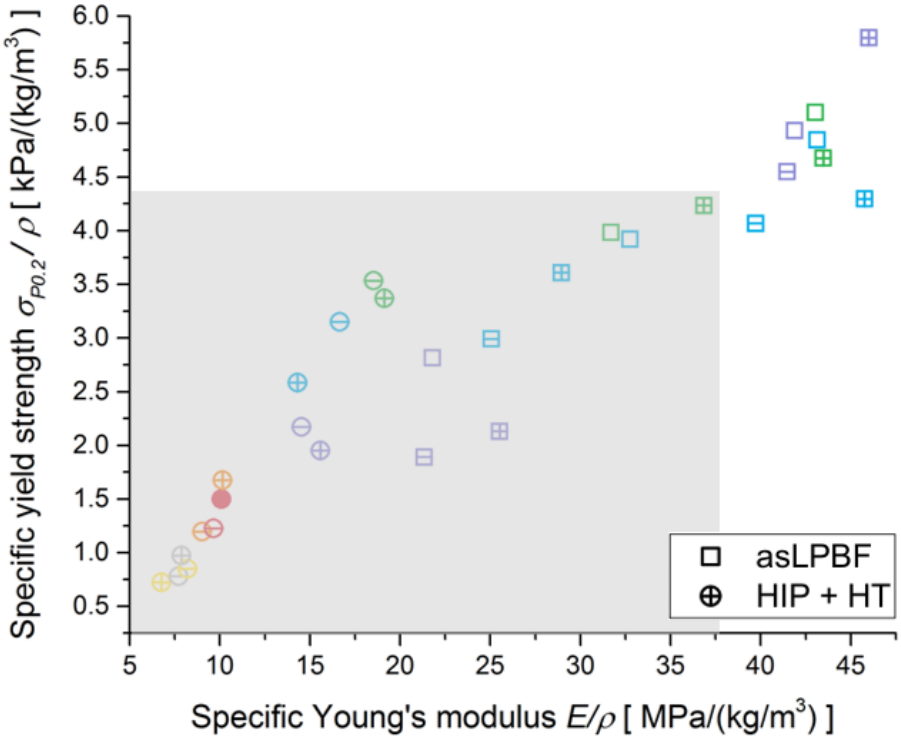


Figure 5.17 - Specific lattice mechanical properties for the full sample set including as-LPBF 0.5 volume fraction. 0.2 volume fraction samples are shaded in grey.

5.4 CONCLUSIONS

Mechanical testing of the HX bulk material and lattice structures was performed in both as-LPBF and HIP + HT conditions of supply. The hardness measurements obtained for the HX as-LPBF bulk material was in line with that seen in the literature, and the hardness in the HIP + HT condition was slightly below that expected, due to the increased HT cycle duration.

After compressive testing, the TPMS lattice structures show clear potential for application in components under compressive loading. The specific strength and modulus improvement over BCC strut-type lattice structures effectively eliminated the use case for the BCC geometry. This is with the exception of applications such as crash structures, where lower stiffness may be desirable. It has been demonstrated that DIA and GYR matrix phase TPMS geometries provide the highest mechanical performance, up to six times that of the BCC, over a range of cell sizes.

For the highest strength and modulus, HX lattice structures should be used in as-LPBF state, but only where microstructures resistant to creep and fatigue are of minimal importance. Optimisation of heat treatment may retain some of the mechanical performance that is lost through the HIP+HT routine used in this study and is ultimately the more desirable method than using components in the as-LPBF condition from a microstructure perspective.

Whilst Hastelloy-X is a ductile material under compression in either condition of supply, certain geometries can result in regions with high stress that lead to fracture, as in the case of DIA N. This is also important to consider for fatigue life as fatigue cracks can quickly propagate from surface roughness defects of LPBF components if stress concentrations are present. However, this is not unique to the TPMS structures but rather

a design consideration whenever component complexity is increased or small features are introduced.

Overall, the TPMS structures exhibit high specific mechanical properties that are desirable for component lightweighting and are an attractive choice for a variety of mechanical loading applications. Care must be taken to ensure the correct combination of geometry and material properties are chosen for the required performance – particularly when HT will be performed. The data given in this Chapter will enable design engineers to filter out certain geometries before selecting those most suitable to conduct their own application-specific performance evaluation. As a result, time and cost will be saved as a more comprehensive performance evaluation will not be required.

6 A NEW APPROACH TO EVALUATION OF LATTICE THERMAL PERFORMANCE

6.1 INTRODUCTION

Before lattice structures can be implemented in heat transfer components, their heat transfer performance under typical operating conditions must be characterised. Evaluation of thermal performance of materials is usually performed to calculate bulk material properties, for example where the thermal conductivity of *a material* is required. The apparatus used to calculate these properties typically requires a thin slice of solid material or a small quantity of powder feedstock, as in the case of the laser flash thermal conductivity and diffusivity method [135]. Such methods are not suitable for determining the thermal properties of macro scale structures or geometries such as lattice structures, however. The performance of these is dependent both upon material composition but also structure since this is implicit to the manufacturing process. This Chapter provides the design methodology, apparatus schematic and standard operating procedure for two custom thermal property apparatus that are tailored for evaluating lattice structures.

The most basic requirement for characterisation of lattice structure thermal properties is to understand the 1-D thermal conductivity. To experimentally determine this, a custom thermal conductivity testing apparatus was developed from ASTM standards. This enabled the nuances of thermal conductivity in the lattice structures to be understood beyond the correlation with volume fraction which simply states that thermal conductivity is proportional to the percentage of material present in the sample by volume. Therefore, true values for apparent thermal conductivity of each geometry could be calculated that account for internal natural convection currents. The convective element that contributes to the apparent thermal conductivity cannot be simply captured using computational finite element analysis (FEA). An approximation may be made but will require validation using experimental methods.

The next stage was to determine the performance of the lattice structures under convective heat transfer, including pressure drop of the working fluid due to interaction

with the geometry. The geometrical complexity makes simulation of convective heat transfer via computational fluid dynamics (CFD) complex and computationally expensive. Further, the behaviour of fluid flows in such geometries cannot be directly inferred from existing models due to the role of surface roughness of AM parts on the heat transfer. The surface roughness structure is different to that seen on conventionally manufactured components and it is difficult to ascribe a representative surface roughness parameter and value that can be used for CFD model input. Experimental methods are therefore seen as the most viable and cost-effective method to study the performance of lattice structure heat transfer devices. This required additional custom testing apparatus to be developed for which no applicable standards documentation exists. The design of this apparatus was based on design requirements drawn from the required output data and from similar equipment described in the literature review. This apparatus enabled thorough understanding of how each lattice structure performs as a convective heat transfer device. This data is key to implementing lattice structures in high-performance heatsink applications such as in a gas turbine NGV.

6.2 THERMAL CONDUCTIVITY TESTING

6.2.1 APPARATUS DESIGN AND OPERATION

The testing apparatus was designed to conform with ASTM E1225-13 for measurement of the thermal conductivity of a sample using the comparative-longitudinal heat flow technique [132]. A schematic layout of the apparatus is given in Figure 6.1 and the full engineering drawings are provided in the Appendix Section 1. The test stack is comprised of a lattice sample, the specimen, placed between two reference blocks of AISI 304 stainless steel (thermal conductivity, λ_M = 16.2 $W.m^{-1}.K^{-1}$ at 293 K) under 5 kg of axial load. Silver sheets (0.5 mm thick) with two metallurgically bonded T-type thermocouples were placed at every interface as shown in Figure 6.1 (b). A layer of thermal grease was applied between each interface to ensure good thermal coupling. The bottom side of the test stack was heated by a PID regulated positive temperature coefficient (PTC) element to a constant 443 ±0.5 K, and the top side was cooled to 295 ±1.0 K using a water-cooled copper heatsink. The aluminium guard cylinder surrounding the test stack was heated to the mean temperature between the hot and cold sides of the stack, 369 ±1.0 K. A fibre blanket (λ = 0.04 $W.m^{-1}.K^{-1}$ at 473 K) was placed between the test stack and the guard cylinder for insulation and to prevent convective heat transfer currents establishing around the test stack.

After assembling the test stack, heating was undertaken, and the test rig was left for a minimum of 60 minutes to reach steady state (defined as < 0.1 K/min drift from the prescribed temperatures). The temperatures at each reference block and sample interface were logged using a Pico TC-08 (Pico Technology, UK) thermocouple data logger at 1 second intervals and stored on a PC.

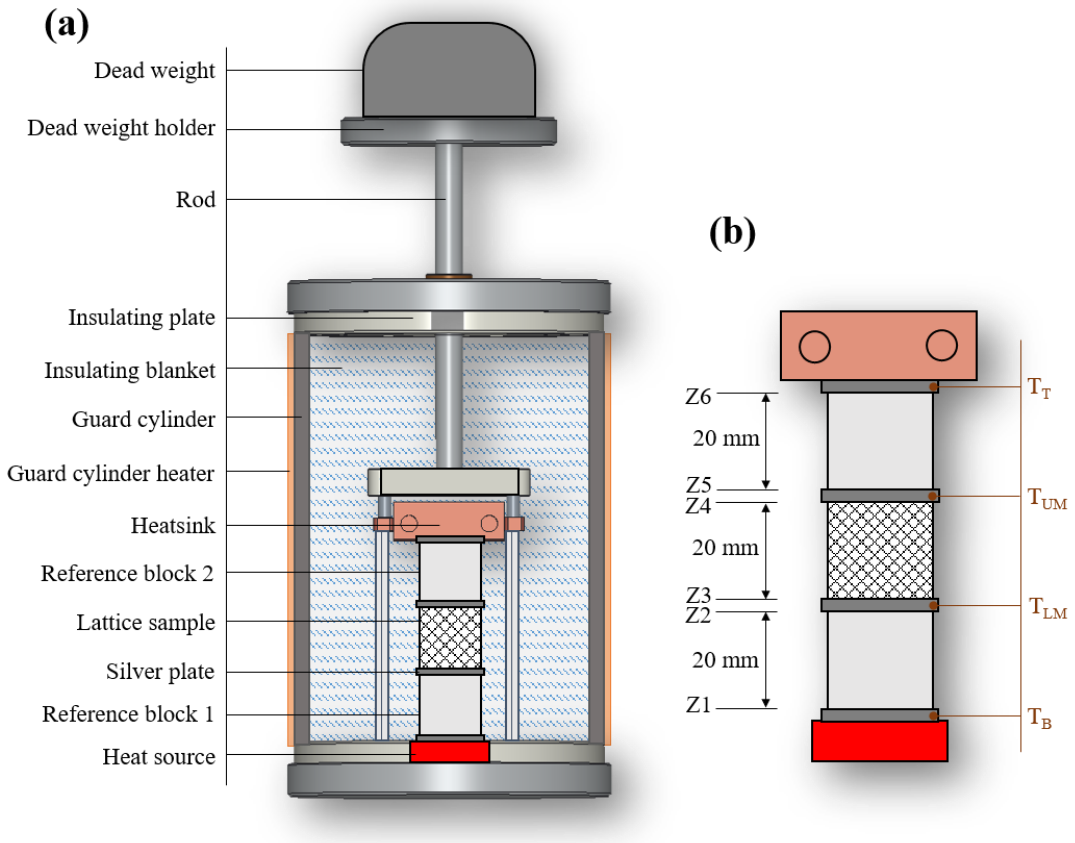


Figure 6.1 – (a) Schematic of the thermal conductivity testing apparatus used to measure the thermal conductivity of the lattice samples using the ASTM E1225-13 comparative-longitudinal heat flow technique. (b) Enlarged view of the test stack indicating the position of the measurements taken for the calculation of apparent thermal conductivity of the sample

6.2.2 CALCULATION OF THERMAL CONDUCTIVITY

The thermal conductivity of the lattice samples was calculated from the temperature gradients set up in the test stack. As the thermal conductivity of the reference blocks is known, it is possible to calculate the thermal conductivity of the sample (λ_S) from the temperature drop across the sample and reference blocks when the system is at thermal steady state, using the following equation taken from ASTM E1225-13 [132]:

$$\lambda_S = \frac{Z_4 - Z_3}{T_{UM} - T_{LM}} \frac{\lambda_M}{2} \left(\frac{T_{LM} - T_B}{Z_2 - Z_1} + \frac{T_T - T_{UM}}{Z_6 - Z_5} \right)$$

The nomenclature used in this equation can be drawn from Figure 6.1 (b). The contribution of the silver sheets to the temperature drop across the stack is assumed to be negligible due to the relatively high thermal conductivity of silver (λ = 420 W.m^{-1}.K^{-1} at 293 K) which is approximately 20 – 60 times that of the base alloys used to manufacture the specimens tested using the apparatus (Hastelloy-X: λ = 11.2 W/m^{-1}.K^{-1} at 373 K). It should be noted here that this standard and the calculation above generally relates to conduction in a solid material. In this case we have a geometric structure consisting of air and metal. Whilst the high conductivity of the metal would indicate that this would be the main heat flow path in the test, heat flow is also possible through conduction and convection in the air. Another factor with the lattice geometry is that it will affect the heat flow path in the metal. For this reason, the test should be considered as measuring an 'apparent conductivity' that is a measure of both material and geometry rather than a pure material property.

6.2.3 Uncertainty analysis

For this experiment, errors that arise from heat exchange between the test stack and the guard, and heat shunting through the insulation surrounding the test stack, were assumed to be negligible. This assumption was tested by altering the temperature of the guard cylinder from room temperature (~294 K) to 373 K, noting that minimal change of measured conductivity for the test specimen was obtained.

For error calculation, the following values were used - maximum uncertainty in thermocouple temperature reading: ±0.2 % of the reading ±0.5 K; uncertainty in the thermal conductivity of the reference blocks: ± 5 %. Indeterminate errors caused by heat exchange between stack and surroundings, heat shunting through insulation, non-uniform interfacial resistance and random uncertainty were minimised by repeating experiments, and were evaluated to be less than ±3 % of the measured value. Therefore, the uncertainty in the measurement of the thermal conductivity of the samples using this method was determined to be a maximum of ±7.0 % for the Hastelloy-X samples.

6.3 CONVECTIVE HEAT TRANSFER TESTING APPARATUS

The convective heat transfer testing apparatus outlined in the literature review demonstrates the varied approaches that are taken to convective heat transfer. Furthermore, they highlight the importance of experimental work over pure computer modelling; the complex geometries under investigation require significant in-depth knowledge of CFD modelling parameters and the calculations are computationally expensive.

There are no applicable standards for the development of a testing apparatus for evaluating the thermal performance of geometries such as lattice structures. Therefore, a suitable apparatus was developed from review of those found in the literature. It is important to define the correct operating procedure to accurately determine convective heat transfer characteristics and other related outputs. This section details the testing apparatus including the methodology of data capture and the processing of the data to obtain the relevant lattice performance metrics.

6.3.1 SPECIMEN DESIGN

The apparatus presented here was developed specifically for testing lattice structure samples that are manufactured via powder bed fusion methods. The sample geometry is shown in Figure 6.2. This is an example of a lattice structure sample, however there are no restrictions to the type or geometry of the sample providing that the sample conforms to the dimensional limits and that the blue shaded ‘region of interest’ occupies the central 10 mm in the z-direction. The overall dimensions were chosen to allow sufficient volume to test a range of unit cell sizes. A ‘region of interest’ height of 10 mm allows for cell sizes in the range of 2.5 mm to 10 mm. Smaller unit cells would result in features that are too small to manufacture current class PBF; larger unit cells are beyond the size scale of the potential end-use components for these structures.

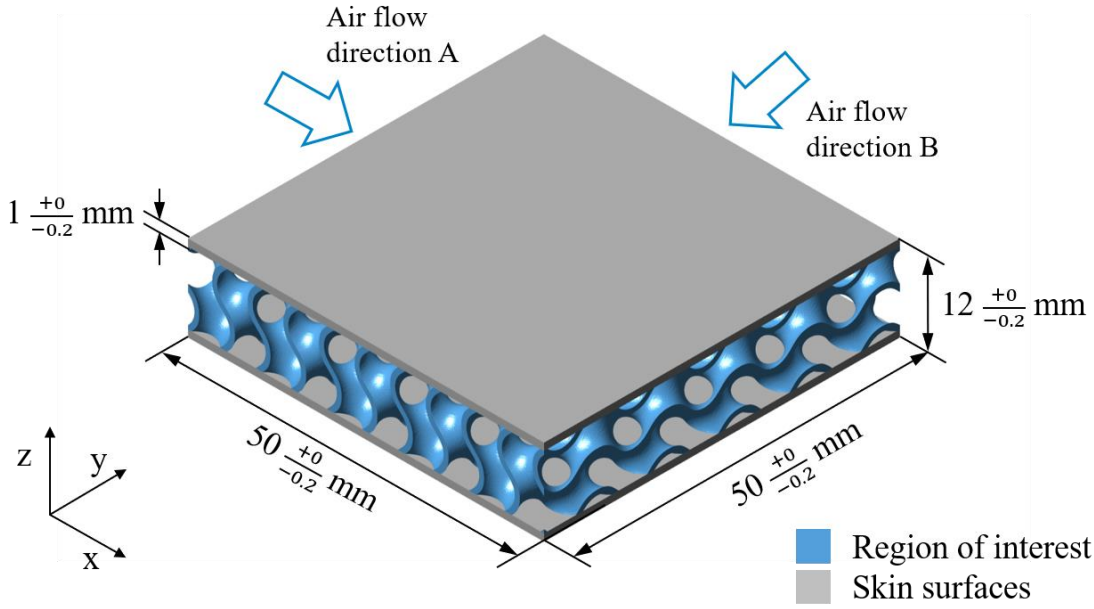


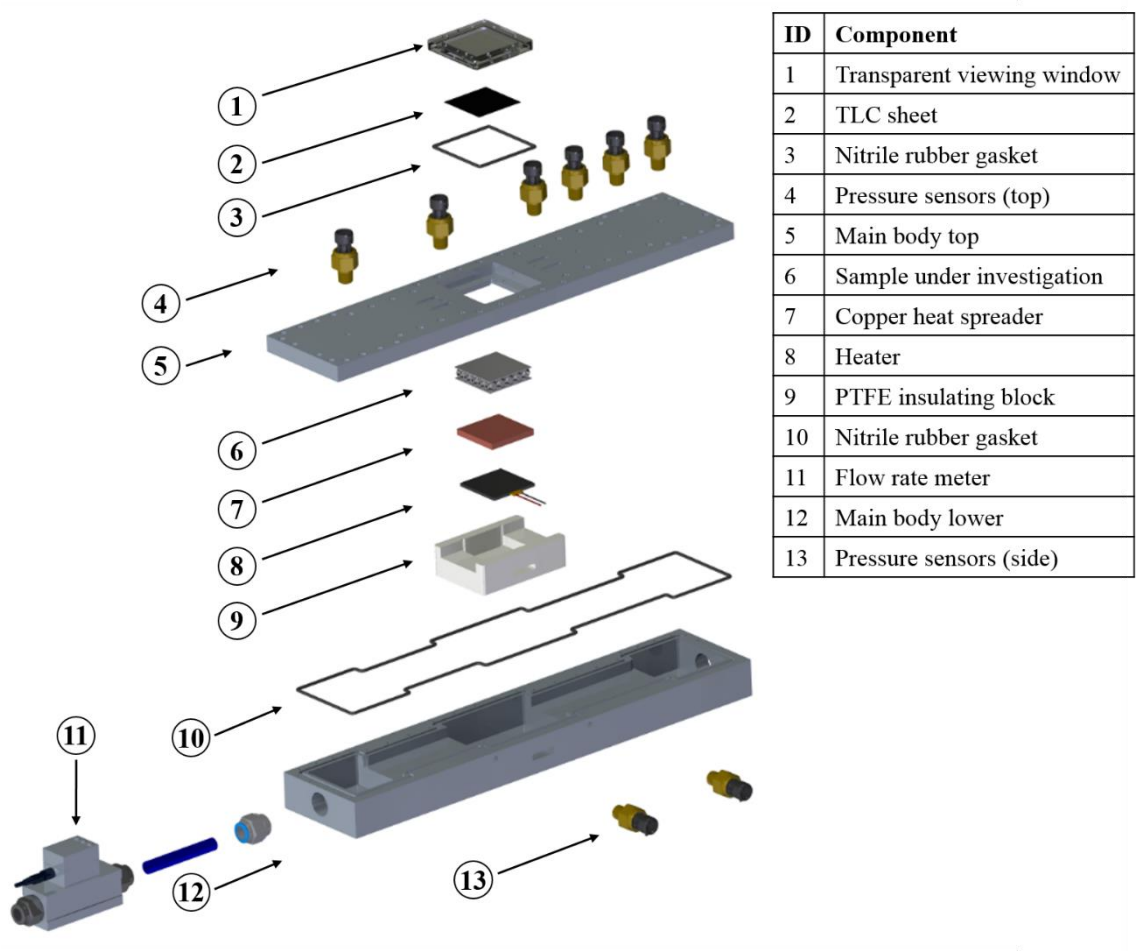
Figure 6.2 - Dimensions of the sample used in the convective heat transfer testing rig. The sandwich design places a 1 mm skin on the top and bottom of the 'region of interest', shown in blue; the cooling air is forced through the centre of the sandwich structure along the x- and y-direction.

Square samples were chosen so that geometries with directionality, i.e. those with a different fluid flow path through the structure in perpendicular directions, can be tested in both directions with a single sample. For additively manufactured samples, the build orientation influences the surface roughness; down-skin regions, those that are facing towards the build plate, are typically rougher than the up-skin regions facing upwards. This variation in roughness can also be tested using the square sample geometry, rotating the sample by 90° between each test. Providing that the geometry of the ‘region of interest’ is self-supporting, the samples can be manufactured in an XZ or YZ orientation on the PBF machine build plate, providing a high component packing density and hence cost-efficient manufacture.

6.3.2 THE TESTING APPARATUS

The main body of the testing apparatus is a machined aluminium section that houses the sample and the sensors used to collect pressure and temperature readings, the layout of which is shown in Figure 6.3 and the full engineering drawing are provided in the Appendix Section 2. In-line flow meters (SMC PFMC7202, 20-2000 $L.min^{-1}$ range and ± 1% full-scale range accuracy) monitor the volumetric flow rate of dry compressed air that is fed through the main body, acting as the coolant fluid for the forced convection testing. A total of six piezoresistive pressure transducers with integrated ASIC signal conditioning and amplification (Honeywell PX3 1–50 bar and ± 0.25% full-scale range accuracy) provide real-time absolute pressure measurements along the length of the channel. A silicon differential pressure sensor with on-chip signal conditioning and temperature compensation (NXP MPX-series) is used to measure the pressure drop across the sample. The model chosen is dependent on the pressure differential range expected for each sample (MPX5010DP [0-10 kPa], MPX5050DP [0–50 kPa] and MPX5100DP [0–100 kPa], all 2.5% full-scale range accuracy). This ensures the maximum resolution and hence accuracy of the measurement. Four K-type (± 0.5 K accuracy) thermocouples are positioned in the coolant flow at the inlet and outlet of the sample to determine the coolant temperature. Heat is applied to the base of the sample by a wire-wound mica heater that is PID temperature controlled. Four thermocouples are embedded in the copper heat spreading block, between the heater and the sample base, to provide temperature readings at regular intervals along the direction of the coolant flow.

The sample sits on a 6 mm thick copper block used to distribute the heat from the mica heater below. This heater stack is placed in a PTFE block, chosen for its low thermal conductivity (0.25 $W.m^{-1}.K^{-1}$), which acts to minimise thermal conduction losses into the aluminium main body. Above the sample is an acrylic viewing window which can be removed to change the sample using eight machine screws. A controlled torque is applied to the screws to ensure that an equal clamping force is applied to each sample under test.



ID	Component
1	Transparent viewing window
2	TLC sheet
3	Nitrile rubber gasket
4	Pressure sensors (top)
5	Main body top
6	Sample under investigation
7	Copper heat spreader
8	Heater
9	PTFE insulating block
10	Nitrile rubber gasket
11	Flow rate meter
12	Main body lower
13	Pressure sensors (side)

Figure 6.3 - Exploded view of the main body of the test apparatus showing the assembly of the sample within the test stack and the position of the pressure transducers along the flow direction. The components are named in the attached table.

6.3.3 DATA CAPTURE

A flow chart of the data capture and processing methodology for the experimental apparatus is given in Figure 3. The thermocouple data is recorded using a PicoLog TC-08 USB thermocouple data logger with integrated cold junction compensation and the data from the remaining sensors is recorded using a PicoLog 1216 data acquisition (DAQ) unit. The multiple channels are recorded consecutively in real-time to a PC via USB. The data recorded during the experiments is saved as a text file and later processed using MATLAB (scripts written by Richard Sélo, PhD student at the Centre for Additive Manufacturing, University of Nottingham). The processing performs the conversion from raw voltage data output from the data loggers into the correct units for the measurement, before calculating outputs such as Reynolds number and ΔP. The data is averaged to provide a smoothed fit for each of the factors that are then plot to explore the effect of sample and flow conditions on the heatsink performance.

The apparatus has the option for logging the temperature of the sample top surface using thermochromic liquid crystal (TLC) sheets since the upper enclosure is transparent. No data using TLC measurement is included in this thesis, however the apparatus was designed to have many possible data acquisition methods for further research activities. When the TLC temperature measurement is in use, a DSLR camera with an on-axis LED ring light is used to capture RAW images of the TLC surface. The ring light and camera lens have opposing direction linear polarising filters attached to minimise the capture of reflections from the acrylic window surface. As the light reflected from the TLC surface is circularly polarised, the TLC information is retained, and the highest image quality is captured. The RAW images are converted to uncompressed TIF images using the Canon Utility, before being converted to hue-saturation-intensity (HSI) colour space in MATLAB. Calibration equations relating HSI values to temperatures are applied to enable a 2D temperature distribution of the sample top surface to be plotted.

6.3.4 TESTING METHODOLOGY

6.3.4.1 PRESSURE DROP TESTING

This test was performed at ambient temperature without the heater activated due to temperature dependence of many air properties, for example, air density and specific heat capacity. The temperature of the air is monitored using the thermocouples described previously to ensure that the air properties can be accurately calculated in the data processing step. After each sample is placed in the test rig, the valve at the outlet of the main body is closed and the rig is pressurised to 1 bar to test for air leaks that may occur due to improperly seated gaskets. If no leaks are found, the rig is de-pressurised by opening the outlet valve and the air flow is ramped down to zero.

To begin testing, the DAQ software is initiated, recording data from thermocouples and sensors at a frequency of 100 Hz. A first record is made without any airflow for one minute to provide a baseline for each sensor at ambient conditions. Using the flow regulator, the air flow rate through the rig is increased from 100 $L.min^{-1}$ to 700 $L.min^{-1}$ in 100 $L.min^{-1}$ increments. A three-minute wait period at each measurement point allows the flow conditions to reach steady state. Steady state conditions are verified during the data processing step by calculating the gradient of ΔP against time via linear regression. This gradient is theoretically zero at perfect steady state conditions. During the experiment, however, if the gradient coefficient is within one standard error of the mean from zero, the regime is considered steady state. If the stationary hypothesis is rejected, the experiment is continued for a further three minutes to allow the system to reach steady state. As the entire apparatus is at thermal steady state for the duration of the testing, it is not necessary to record data for more than 1000 points at each flow rate. After recording 1000 samples, the DAQ is stopped before the air flow rate is ramped down to zero.

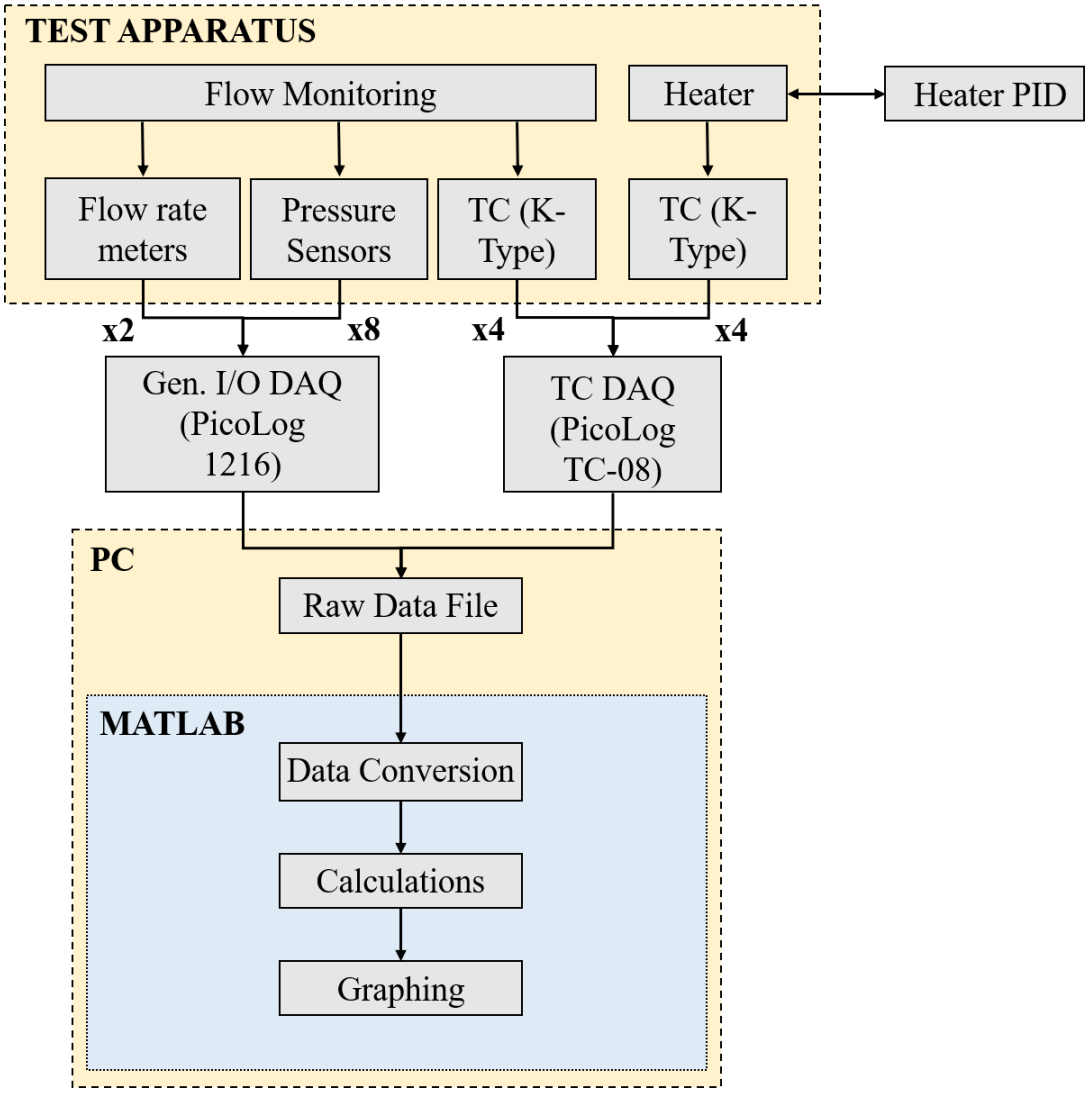


Figure 6.4 - Flow chart showing the method of data acquisition and processing for the convective heat transfer experiments.

6.3.4.2 CONVECTIVE HEAT TRANSFER TESTING

The procedure for convective heat transfer testing is similar to pressure drop testing but now the heater is activated. The regulator is used to set the flow rate at 100 $L.min^{-1}$ before the heater is switched on to prevent the top surface of the sample from becoming too hot and damaging the acrylic window. The heater PID controller is set to 373 K (100 °C), which typically requires constant full power operation at 80 W. Before DAQ is initiated, the heater and sample are left to reach thermal steady state for 15 minutes at the lowest flow rate. Steady state is verified using the same method as for pressure drop, using linear regression to calculate the gradient of air outlet temperature against time. The system is considered to be steady state if the gradient coefficient of the outlet temperature is $< 5x10^{-6}$. At steady state, DAQ is initiated at a sample rate of 1 Hz and 100 samples are recorded. The flow rate is increased through the range at the increments described in the pressure drop testing method. At each increment there is a pause to allow thermal steady state to be reached, which requires 10 minutes. As the change in flow conditions and sample base temperature is relatively small at subsequent test points, the time to reach steady state at these test flow rates is reduced. In each case, 100 samples are recorded once the steady state condition has been reached. At the end of the test sequence, the DAQ is stopped before the air flow is cut off to prevent anomalous data from being captured.

6.3.4.3 APPARATUS UNCERTAINTY ANALYSIS

Measurement uncertainty was calculated using root sum of the squares and was not constant across each dataset. Relative combined uncertainty in the friction factor varied from 50% for the lowest flow rate (100 $L.min^{-1}$) and decreased to 5% at highest flow rate (700 $L.min^{-1}$). Reynolds number uncertainty ranged from 21% to 3% for the lowest to the highest flow rate respectively. The main contributor to uncertainty for Reynolds and friction factor at low flow rate was the ± 1% full-scale range measurement error of the flow rate meter. Error analysis on the heat transfer testing determined a relative combined

uncertainty of Nusselt number ranged between at 100 L.min^{-1} 7% and 24% at 700 L.min^{-1}. The main contribution to error in the Nusselt number was the low temperature difference between the inlet and the outlet at high flow rates.

6.3.5 DATA PROCESSING AND CALCULATIONS

The experiments involve transfer of energy to air as it passes through the samples, hence there is a variation in air temperature and pressure. If air property values are static, large errors will accumulate during calculation of sample performance. The air properties are calculated for each measurement point based upon the mean air temperature and pressure across the sample, T_{ave} and P_{ave}. As the operating pressures of the testing are considered 'low pressure' (< 0.25 MPa above ambient), the effect of changing pressure on the air properties is <0.5 % and hence pressure is omitted from the calculations in most cases. It is included, however, when the dependence upon pressure for a particular property is considered significant.

To calculate air density, the ideal gas law can be used as follows, where $R_{specific}$ is the specific gas constant for dry air:

$$\rho = \frac{P_{ave}}{R_{specific} \cdot T_{ave}} \qquad (1)$$

As the testing all operates at low pressures, i.e. less than 0.2 MPa above ambient, air dynamic viscosity can be approximated using the power law and a reference value of μ_0 taken at a reference temperature T_0, in this case 273 K:

$$\frac{\mu}{\mu_0} = \left(\frac{T_{ave}}{T_0}\right)^{0.7}$$

$$\mu = 17.15E^{-6} \cdot \left(\frac{T_{ave}}{273}\right)^{0.7} \qquad (2)$$

Air kinematic viscosity can be directly calculated from μ and ρ:

$$\nu = \frac{\mu}{\rho} \quad (3)$$

The power law can also be used to calculate the air thermal conductivity with temperature dependence at low pressures, using a reference value of k_0 at a given temperature T_0, 300 K:

$$k \cdot T_{ave} = k_0 \cdot T_0 \cdot \left(\frac{T_{ave}}{T_0}\right)^{0.9} \quad (4)$$

Specific heat capacity of air in the temperature range 273 – 573 K (0 – 300 °C) is calculated using the empirical formula derived by Xiao et al. [203]:

$$c_p = 1.0026 + 5.1E^{-4} \cdot (T_{ave} - 273) \quad (5)$$

The flow and heat transfer values can be calculated now that the air properties are known. The most important of these is Reynolds number as it describes the air flow regime through the system and is used to compare heat transfer and pressure drop characteristics of the samples:

$$Re_{Dh} = \frac{U \cdot D_h}{\nu} \quad (6)$$

Friction factor, a measure of the proportion of energy of the fluid flow lost to frictional effects, is proportional to the first power of velocity and increases with increasing surface roughness. For a fixed sample size, friction factor is also proportional to surface area to volume ratio of the sample, where a larger ratio results in increased fluid-wall interaction and hence higher losses due to friction. The friction factor can be calculated as shown in Equation 7:

$$f = \frac{\Delta P \cdot D_h}{L} \cdot \frac{2}{\rho \cdot V^2} \quad (7)$$

The friction factor of an empty channel, f_0, is used to identify the magnitude by which a geometry increases the frictional effects experienced by the fluid compared to a hydraulically smooth empty channel. In this case, f_0 is assumed to be described by the Blasius smooth wall, fully developed, turbulent flow correlation:

$$f_0 = 0.316 \cdot Re^{-0.25} \quad (8)$$

The convective heat transfer coefficient, ħ, is calculated based on the heated surface area of the sample, A_{base}. It is a mean value for the entire geometry as the convective heat transfer coefficient of a single point cannot be determined. Using this area allows for different geometries to be directly compared without the need to derive geometric descriptors such as mean 'pin diameter' or 'strut width' that are generally not applicable to complex surface type lattice geometries.

$$\bar{h} = \frac{\dot{m} \cdot c_p \cdot (T_{out} - T_{in})}{A_{base} \cdot \left(T_{base} - \frac{T_{out} + T_{in}}{2}\right)} \quad (9)$$

From this, the Nusselt number, representing the ratio between heat transfer from convection to that from conduction alone, can be calculated. The Nusselt number is important as a design metric to compare heat transfer between the different sample geometries as it removes the effect of size scaling. It is the Nu/Nu_0 ratio plot against Reynolds number that is most commonly used when selecting an appropriate geometry for cooling a component.

$$Nu = \frac{\bar{h} \cdot D_h}{k} \quad (10)$$

In the same way that f_0 describes the friction factor for an equivalent smooth wall empty channel, Nu_0 describes the Nusselt number of the same channel. This is used to determine the increase in effectiveness of convective heat transfer achieved using a

specific geometry over that possible using an empty channel. This is calculated using the Gnielinski correlation for fully developed, turbulent flow:

$$Nu_0 = \frac{\left(\frac{f_0}{8}\right) \cdot (Re - 1000) \cdot Pr}{1 + 12.7\left(\frac{f_0}{8}\right)^{0.5} \cdot (Pr^{2/3} - 1)} \qquad (11)$$

In order to compare the overall performance of each sample, a thermal performance (TP) index derived from the Nusselt number and friction factor is calculated [144]:

$$TP_{norm} = \frac{Nu}{f} \qquad (12)$$

This index allows comparison of the heat transfer per unit of pumping power for each of the samples. In this simple form, it places equal weighting on heat transfer and pressure drop to determine overall TP_{norm}. This penalises geometries with a high pressure drop, however – in some cases a geometry that has excellent heat transfer but a high pressure drop would have a poor overall TP_{norm}, resulting in such a geometry being disregarded. A modified version of the TP_{norm} index, TP_{mod}, was therefore calculated, as introduced by Han et al. [152] [204], which places an exponent on the friction factor term to reduce the weight of friction factor on the overall thermal performance.

$$TP_{mod} = \frac{{}^{Nu}/_{Nu_0}}{\left({}^{f}/_{f_0}\right)^{1/3}} \qquad (13)$$

6.4 SUMMARY

Thermal characterisation of lattice structures is challenging to achieve using commercial apparatus. FEA and CFD simulations are complicated and computationally expensive on such geometries, and furthermore, simulation may not capture the range of second order heat transfer effects that are acting in real components. This drove the development of the custom thermal conductivity and convective heat transfer testing apparatus detailed in this Chapter.

7 EVALUATING THE THERMAL CONDUCTIVITY OF LATTICE STRUCTURES

7.1 INTRODUCTION

In this Chapter, the testing apparatus outlined in Chapter 6 (section 6.2.1) is used for characterising the pure conductive heat transfer properties for TPMS lattice types including gyroid, diamond and Schwarz primitives. Unit cell size and volume fraction are varied and thermal conduction performance is analysed.

Thermal conductivity through the solid material can be easily modelled using FEA. Natural convection currents are also set up within the free volume inside each cell, contributing to the effective thermal conductivity of the lattice. Further, some effects of the geometry, such as surface area to volume ratio and surface roughness, may play a role in the thermal conductivity values that cannot be easily predicted in simulations. For these reasons, experimental determination of thermal conductivity properties was deemed to be the most comprehensive method of investigation.

The experimental results were used to generate design equations that enable the manufacture of a component with a custom thermal profile through varying the volume fraction of the lattice. This idea was used to model thermal conductivity grading in both 1D and 2D models. Finally, a sample was designed with the University of Nottingham logo imbedded in the lattice, which was then manufactured, heated and viewed with an IR camera, where the logo was revealed.

7.2 UNIT CELLS UNDER INVESTIGATION

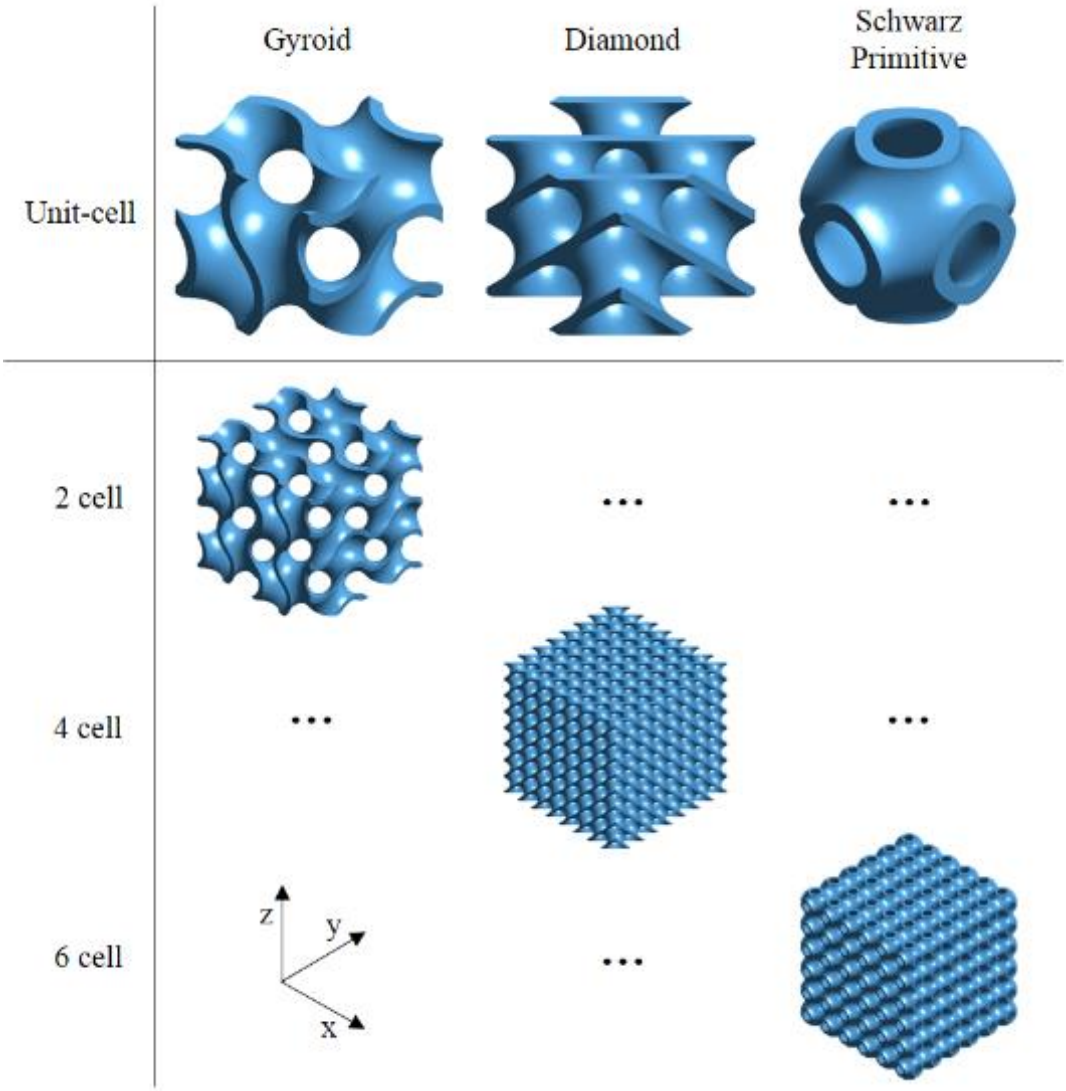


Figure 7.1 - Single unit-cell models with lattice dimensions [1, 1, 1] for each of the three unit-cell types used in this study.

Three different TPMS unit-cell types were investigated in this study: gyroid, diamond and Schwarz primitive. The lattice models were generated using in-house software, 'FLatt Pack', and output as .stl files. A single unit-cell is described as having a cell number of 1; this corresponds to an array of [1, 1, 1] unit-cells in the direction [x, y, z], as illustrated in Figure 7.1.

7.3 GEOMETRIC PROPERTIES OF THE SAMPLES

A total of 18 lattice samples were manufactured over three unit-cell types as shown in Table 7.1. Sample dimensions are 20 x 20 x 20mm with cell numbers of 2, 4 and 6, where a cell number of 4 corresponds to a [4, 4, 4] unit-cell array using the notation described in Figure 7.1. This equates to cell sizes of 10, 5 and 3.3 mm respectively to achieve a cube with side lengths of 20 mm. It is important to understand any effects that size scale may have on the thermal conductivity performance of lattice structures. This range of unit cell sizes is chosen to cover different potential component size scales – 10 mm cells may be used in components with void thicknesses > 50 mm, whilst 3.3 mm cells may be used in components with void thicknesses of < 10 mm.

The TPMS equations [116] define a mathematical surface with zero thickness. To create a sample with volume, the surface is 'thickened' to provide a proportion of solid material per volume, termed the 'volume fraction'. In this study, 0.2 and 0.5 volume fraction variants were manufactured for each unit-cell type and cell number combination. This represents the typical range of volume fractions at which lattice structures are used as below 0.2 volume fraction at 3.3 mm cell size, the features become too small to manufacture via LPBF; greater than 0.5 volume fraction, lattice structures become too dense for use as a method of lightweighting and the drawbacks of the increased design complexity outweigh the performance benefits.

Table 7.1 - Parameters used for the manufacture of a total of 18 lattice test samples

Unit-cell type	Gyroid; Diamond; Schwarz P
Volume fraction	0.2; 0.5
Cell size (mm)	0.33; 5; 10

Thermal conductivity is governed by the volume fraction, i.e. the amount of material available to enable heat transfer. It is expected that thermal conductivity will also be a function of geometry in complex structures such as the TPMS lattice types, this constituting a second order effect that must be understood for lattice implementation in components. Parameters were chosen to investigate the effect of the lattice type and XYZ dimensions on the thermal conductivity of the sample, as well as to check the relative weighting of these effects in comparison to the volume fraction.

Initial results from this range of samples were used to generate design equations that allow samples with custom thermal conductivity to be manufactured. These equations take into account the effect that each lattice geometry has on its thermal conductivity, allowing calculation of the volume fraction required for the particular application. This technique was used to manufacture three further samples, one of each unit cell type, with the target thermal conductivity values of 3.0, 3.5 and 4.0 $W.m^{-1}.K^{-1}$. The experimentally measured performance of these designed lattices was compared with the predicted performance.

The developed design equations were then used to propose some graded lattice structures in both 2-D and 3-D, with example cases given for each. To demonstrate the design concept visually, a sample with the University of Nottingham logo displayed in graded lattice was manufactured in Hastelloy-X, with the aim of producing a distinct thermal profile when viewed with a thermal camera.

7.4 SAMPLE PREPARATION AND TESTING

After manufacturing, the samples were removed from the build plate using a SiC abrasive cut-off disk and ground flat to within ± 0.1 mm of the nominal 20 x 20 x 20 mm sample dimensions using SiC grinding paper, measured using digital Vernier calipers. A final grinding step using P1200 SiC was undertaken to enhance thermal coupling and hence heat transfer. All samples were ultrasonically cleaned to remove loose powder, dried and then measured and weighed to enable the measurement of volume fraction.

The standard operating procedure for the thermal conductivity testing apparatus is outlined in section 6.2.1 and was followed for all samples presented in this Chapter.

7.5 RESULTS AND DISCUSSION

7.5.1 SOLID SAMPLES

Hastelloy-X solid samples were evaluated to determine the thermal conductivity of the bulk alloy. The expected conductivity varies with temperature as shown by the line in Figure 7.2. As the testing method uses a thermal gradient to measure conductivity, the sample is not a homogeneous temperature. The sample temperature was therefore taken as the mean temperature between the hot and cold faces of the sample, 97.2 °C. The measured conductivity for the solid as-LPBF HX sample was 11.36 $W.m^{-1}.K^{-1}$, a 2 % deviation from the expected thermal conductivity at the mean temperature. In Figure 7.2, with the error bars consistent with an error of 7 % as described earlier in section 6.2.3, it can be seen that the measured thermal conductivity for the bulk sample is well aligned with the linear relationship between thermal conductivity and temperature of Hastelloy-X given in the material specification data [185].

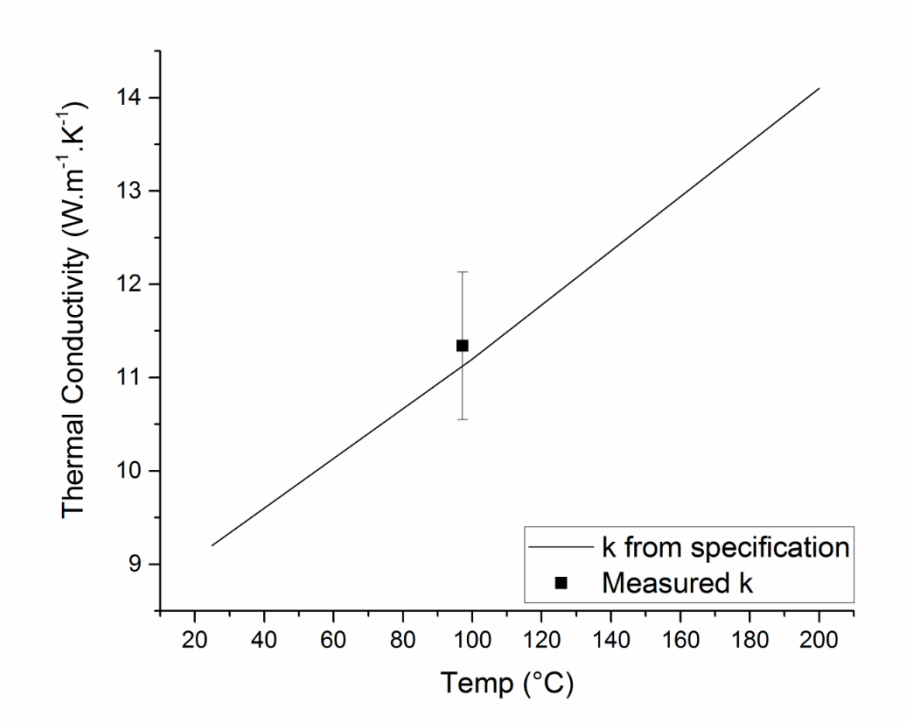


Figure 7.2 - Thermal conductivity of Hastelloy-X bulk material across the temperature range 25 - 120 °C as taken from the material data sheet [185], with the measured conductivity of the as-LPBF HX sample shown. 7 % error shown.

7.5.2 LATTICE STRUCTURE SAMPLES

Figure 7.3 shows the apparent thermal conductivity measured from the experiments as a function of actual volume fraction (volume fraction as measured from manufactured samples) and lattice cell type for the two different metal alloys. It can be seen that there is a linear relationship between the volume fraction and the thermal conductivity for all lattice types within the volume fraction range tested. This is regardless of the unit cell size. The diamond and gyroid unit cells perform similarly for both materials, whilst the Schwarz primitive unit cell has a higher thermal conductivity per volume fraction at higher volume fractions. This effect is attributed to the increase in wall thickness (or decrease in surface area to volume ratio, as evidenced in Table 7.2) seen in this unit cell compared to the gyroid and diamond unit cells. This has the effect of providing fewer but wider conduction pathways for the heat, with a lower proportion of heat energy lost due

to radiation and conduction into the air contained within the unit cell. Further, the thicker wall provides better thermal contact between the lattice sample and the reference blocks when assembled in the test stack.

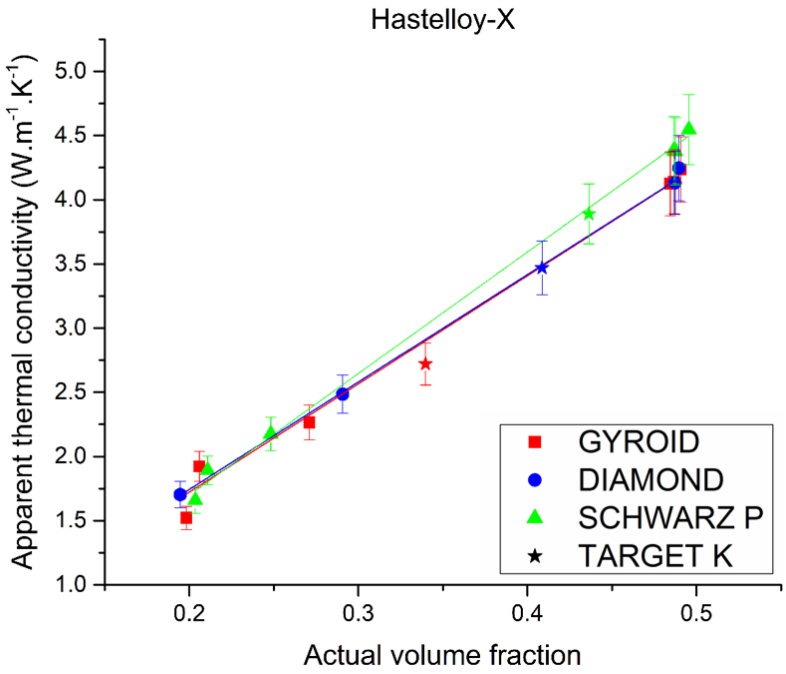


Figure 7.3 - Apparent thermal conductivity against actual volume fraction for all Hastelloy-X lattices. The unit cell type is denoted, but the cell size is ignored for this plot. The star markers are the results of the 'specified conductivity' test. Error bars consistent with 7 %.

Table 7.2 - Surface area and volume data for each lattice sample tested based upon the computer models. Note the large variation in surface area to volume ratio between the unit cell types, giving rise to the differences in conductivity seen in Figure 7.3

Unit cell	Vol. frac.	Cell size (mm)	Surface area (mm^2)	Volume (mm^3)	SA:vol	Min. wall thickness (µm)
GYROID	0.2	3.33	14960	1572	9.52	230
	0.2	5	10128	1591	6.37	355
	0.2	10	5252	1584	3.31	695
	0.5	3.33	14109	3994	3.53	610
	0.5	5	9790	3986	2.46	910
	0.5	10	5429	4008	1.35	1820
DIAMOND	0.2	3.33	18583	1509	12.31	190
	0.2	5	12485	1584	7.88	275
	0.2	10	6412	1584	4.05	555
	0.5	3.33	17131	4004	4.28	490
	0.5	5	11793	3995	2.95	730
	0.5	10	6379	4006	1.59	1480
SCHWARZ P	0.2	3.33	11399	1595	7.15	265
	0.2	5	7744	1590	4.87	400
	0.2	10	4050	1590	2.55	795
	0.5	3.33	10584	4005	2.64	685
	0.5	5	7406	3999	1.85	1030
	0.5	10	4210	4000	1.05	2070

The data in Figure 7.3 was fit to a linear line:

$$K_a = C_1 V_f + C_2 \quad (14)$$

Where K_a is apparent thermal conductivity, V_f is volume fraction and C_i are the fitting constants relating to a particular lattice cell type and material. The curve fit constants are provided in Table 7.3. To validate this linear fit, some samples with a specified thermal conductivity were manufactured and tested. The samples were varied in unit cell and cell size, and the required volume fraction was calculated from equation (14) using the constants in Table 7.3. A description of the samples manufactured in this exercise and the corresponding geometrical data is given in Table 7.4. The data from the samples manufactured at a specified thermal conductivity were also added to Figure 7.3 (star data points); it is clear that there is a good correlation between these samples and the linear fit from which the volume fractions are calculated (within 3 % of target values for Schwarz primitive and diamond, and within 10 % for gyroid). This gives confidence that the design equations can be used to manufacture lattice structures with a specific thermal conductivity. The lattice samples had a high accuracy in manufactured volume fraction with a deviation from designed value of -3.0 – -0.8 %, with correspondingly accurate thermal conductivity results to that of the design intent – the diamond 10 mm cell sample came within 1 % of the designed value. This relationship between designed volume fraction and actual volume fraction after manufacture is dependent upon geometry, material and process parameters. It is a further optimisation parameter that needs to be taken into account when designing lattice structures for a specified load, whether the load is mechanical or thermal. There is no simple correction that can be applied to all TPMS lattices to achieve 100 % accuracy between the .stl model and the manufactured sample due to variance in the LPBF manufacturing process; corrections must be developed on a case-by-case basis. These corrections may be made directly to the .stl file, such as

applying a scaling factor, or to the processing parameters to ensure the manufactured part is accurate to the digital model.

Table 7.3 - Curve fitting parameters for the linear equations relating apparent thermal conductivity to actual volume fraction for each of the unit cell types

		C_1	C_2
HX	GYR	8.631	-0.039
	SCH	9.415	-0.174
	DIA	8.507	+0.032

Design rules such as the linear fit developed here are vital for components where a load bearing wall may also be required to provide a thermally insulating layer by using lattice structures in a sandwich construction. If there is no coolant fluid passing through this layer, thermal conductivity dominates and hence it must be possible to accurately control the thermal conductivity of the structure used. Such lattice structures can alternatively be used as a heatsink to conduct heat away from high-temperature components. Whilst the materials shown in this paper may not be ideal for high-performance conductive heat transfer, they are commonly preferred for gas turbine applications. This is an application where materials with a higher thermal conductivity, aluminium or copper alloys, cannot provide adequate performance at the high operating temperatures.

Table 7.4 - Design parameters and experimental test data for the three target thermal conductivity lattice samples manufactured in Hastelloy-X.

Unit cell	Cell size (mm)	Target cond. ($W.m^{-1}.K^{-1}$)	Design vol. frac.	Actual vol. frac.	App. cond. ($W.m^{-1}.K^{-1}$)	Δ Vol. frac. (%)	Δ Cond. (%).
GYR	3.3	3.00	0.350	0.340	2.72	-3.0	-10.4
SCH	5	4.00	0.440	0.436	3.89	-0.8	-2.7
DIA	10	3.50	0.415	0.409	3.47	-1.6	-0.7

To aid analysis of unit cell type and size, the parameter ‘normalised conductivity’ was used. This was calculated by dividing the thermal conductivity by the actual volume fraction for each sample. This removes the effect of the volume fraction from the data set and hence allows for any cell size effect to be studied. The results were grouped by designed volume fraction, as presented in Figure 7.4. It can be seen that the Schwarz primitive lattice samples had a greater conductivity than gyroid or diamond based samples of the same cell size and volume fraction in 92 % of the applicable test cases, mirroring the results from Figure 7.3. This is independent of material and is attributed to the lower surface area to volume ratio seen in the Schwarz primitive cell type.

The relationship between lattice sample and the thermal conductivity is dominated by the volume fraction. However, if this was the only factor in the relationship, then the value of normalised conductivity in Figure 7.4 would be equal across all cell sizes. It can be seen however that the normalised conductivity changes across the 0.2 volume fraction samples; at 3.33 mm cell size, the normalised conductivity is typically 8 – 20 % lower than for the same unit cell type at 10 mm cell size. At small cell sizes, the wall thicknesses are significantly lower than for larger cell sizes at the same volume fraction. This geometrical relationship is clear when considering a cross-sectional area of a particular unit cell across a range of unit cell sizes whilst keeping the volume fraction

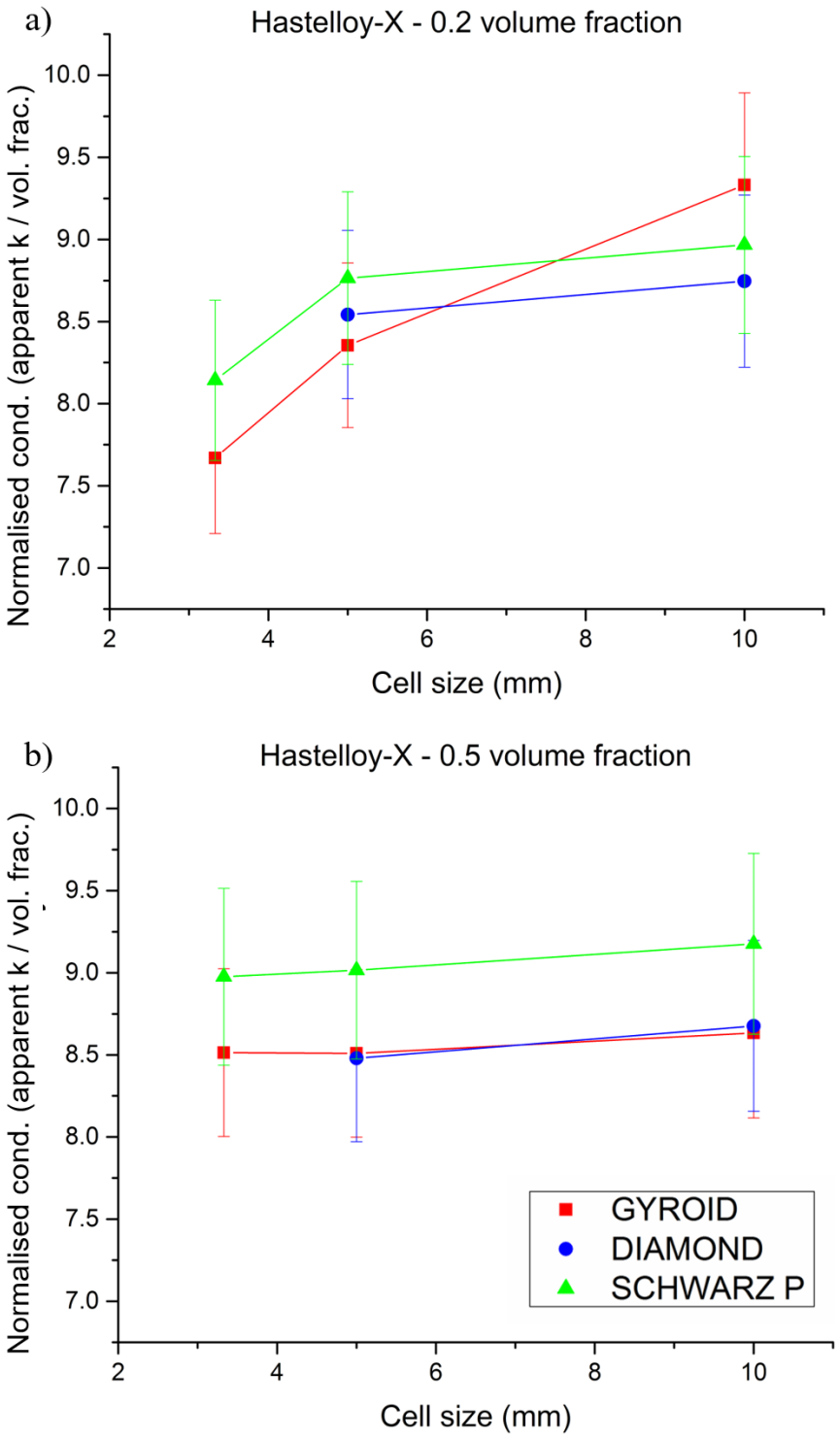


Figure 7.4 - Normalised conductivity vs cell size for Hastelloy-X lattice samples with (a) 0.2 volume fraction and (b) 0.5 volume fraction.

equal, as seen in Figure 7.5. A reduced wall thickness results in a decreased heat transfer efficiency and an increased probability of poor thermal coupling between the lattice sample and the reference blocks. Further, surface roughness of LPBF components remains relatively constant across all wall thicknesses (for each build angle relative to the build plane). For thin walls, surface roughness occupies a greater proportion of the total wall thickness than for thicker walls. Surface roughness consists of partially fused powder particles that will have limited thermal transport ability due to a lack of metallurgical bond or physical contact, effectively reducing the thermal conductivity. The geometries with a lower average wall thickness may therefore show reduced thermal conductivity. These effects act to decrease the apparent thermal conductivity of the sample.

Throughout this experiment, the contribution of convective heat transfer between cells was assumed to be negligible. This is true for the smaller cell sizes, where the tightly spaced cells prevent air currents from moving large distances in the z-direction; at larger cell sizes, the path for convection is wider, enabling easier flow of air, and so convection between the cells may increase the apparent thermal conductivity of the samples. Thermal conductivity measurement error due to natural convection is discussed in ASTM E1225-13 [132] with regards to heat flow external to solid samples. Whilst this standard does not deal with porous samples, the principles of measurement error due to natural convection can be applied to the lattice samples. This is seen particularly in the 0.2 volume fraction samples (Figure 7.4 (a)). At 0.5 volume fraction, the increase in material reduces the free volume inside each cell and constricts the pathways for convection between cells. Hence, this is why an increased cell size does not have as great an impact on the thermal conductivity for these samples (Figure 7.4 (b)). As such, if it is desirable to design a lattice that acts as a natural convection heatsink, it is important to ensure a cell size and volume fraction is chosen that allows for sufficient convection between cells and hence flow of fluid out of the heatsink structure.

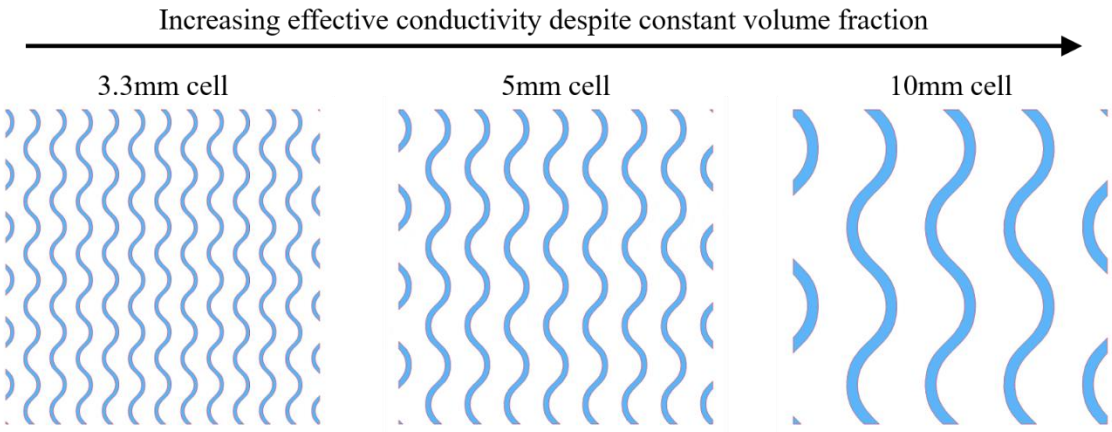


Figure 7.5 - An illustration of the change in wall thickness across different unit cell sizes despite a constant volume fraction (0.2 in this case).

7.6 DEVELOPMENT OF SAMPLES WITH GRADED THERMAL CONDUCTIVITY

The design equations previously provided were fed back into the lattice design software to create sample models with prescribed variations in thermal conductivity. As the TPMS lattices shown here are not based on nodes and elements, but instead are mathematically represented surfaces, the volume fraction can be continuously varied in 3-dimensions. This avoids the step change in volume fraction and hence thermal conductivity that would be seen if a discrete cell-by-cell variation was used. Figure 7.6 (a) illustrates a simple 1D variation in volume fraction, and hence apparent thermal conductivity, in the z-direction of the sample based on a shallow gradient parabolic function. The range of 1.875 – 4.5 $W.m^{-1}.K^{-1}$ in Hastelloy-X corresponds to 0.22 – 0.5 volume fraction and hence covers the majority of the volume fraction range tested experimentally. The effect of volume fraction on wall thickness is clearly seen by observing the expansion and contraction of the hole in the side wall of the Schwarz primitive unit cell type used in this sample. Figure 7.6 (b) introduces further complexity into the grading by using a cosine squared function.

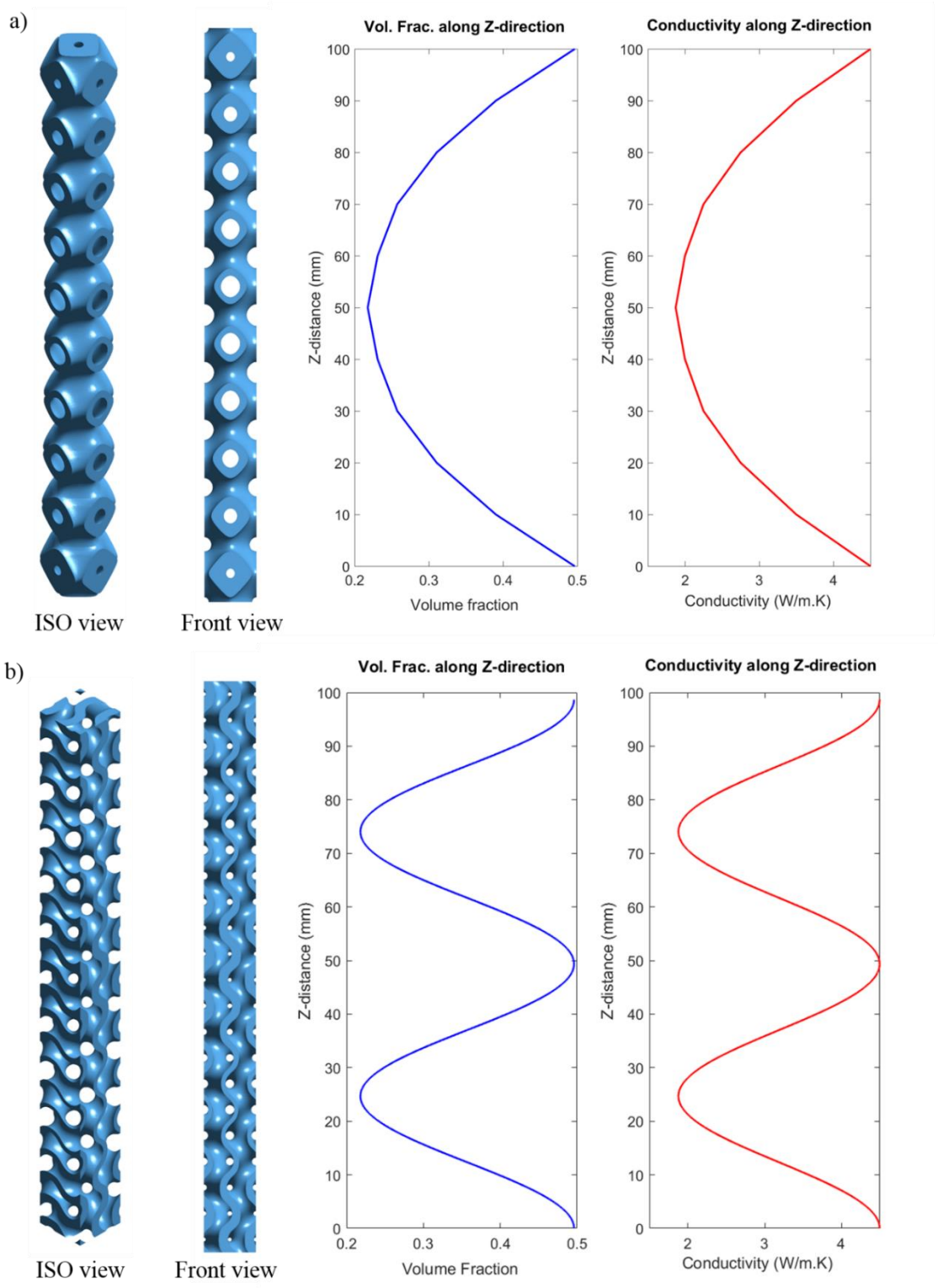


Figure 7.6 - Demonstration of 1D functional grading of Hastelloy-X lattice structures to sweep through a prescribed range of apparent thermal conductivities through variation of volume fraction following (a) a simple gradient and (b) a cosine squared gradient.

Similar design methods can be applied to generate a sample that has a 2D graded structure. Figure 7.7 illustrates a gradient based upon a 2D function, creating a sinusoidal variation in volume fraction, and hence thermal conductivity, that resonates out from the centre of the sample. Such a structure could be placed on top of a flat plate heater, with the heat being conducted through the lattice structure. Therefore, a heating device with a very specific heat distribution can be produced without requiring a custom resistive element or filament to be manufactured. Designing a conventional heating element that can vary the temperature profile with sub millimetre-scale precision is trivial to produce using graded lattice structures via LPBF.

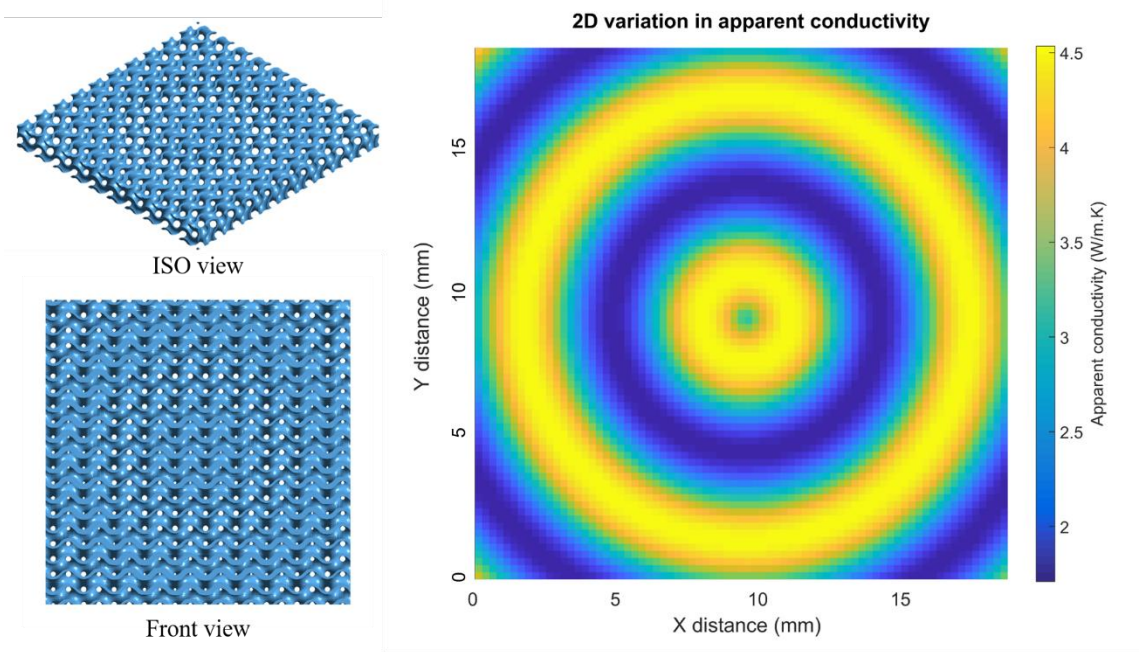


Figure 7.7 - A demonstration of 2D functional grading of Hastelloy-X lattice structures based on the $\sin(x^2 + y^2)^{-1}$ function, showing prescribed apparent thermal conductivity within the range 1.875 - 4.5 $W.m^{-1}.K^{-1}$). On the left is the digital model of the lattice structure generated and the 2D volume fraction map is shown on the right.

Using this method of varying volume fraction, a custom lattice was designed that included the University of Nottingham castle logo and 'UoN' text. The .stl model and manufactured sample, the latter coated in matt black paint to aid in capturing a thermal image, can be seen in Figure 7.8. This custom lattice sample was then placed on a heater plate and a FLIR T400 infrared camera was used to capture images as the plate heated up. Despite appearing as a near-uniform lattice sample to the naked eye, the logo and text can be distinguished from the background using the infrared imaging method (Figure 7.8, c). The high resolution and sharp definition between the logo and the background was achieved due to the continuous cell grading. This image was captured before the temperature of the sample reached steady state; the lower temperature seen in the logo region is a consequence of the higher thermal mass of this area due to the higher volume fraction. At steady state, the temperature profile would be uniform across the sample. If this sample was to be used as an interface between the heater plate and a component, heat would be conducted at a higher rate through the logo and text area (higher volume fraction areas) than the surrounding lattice.

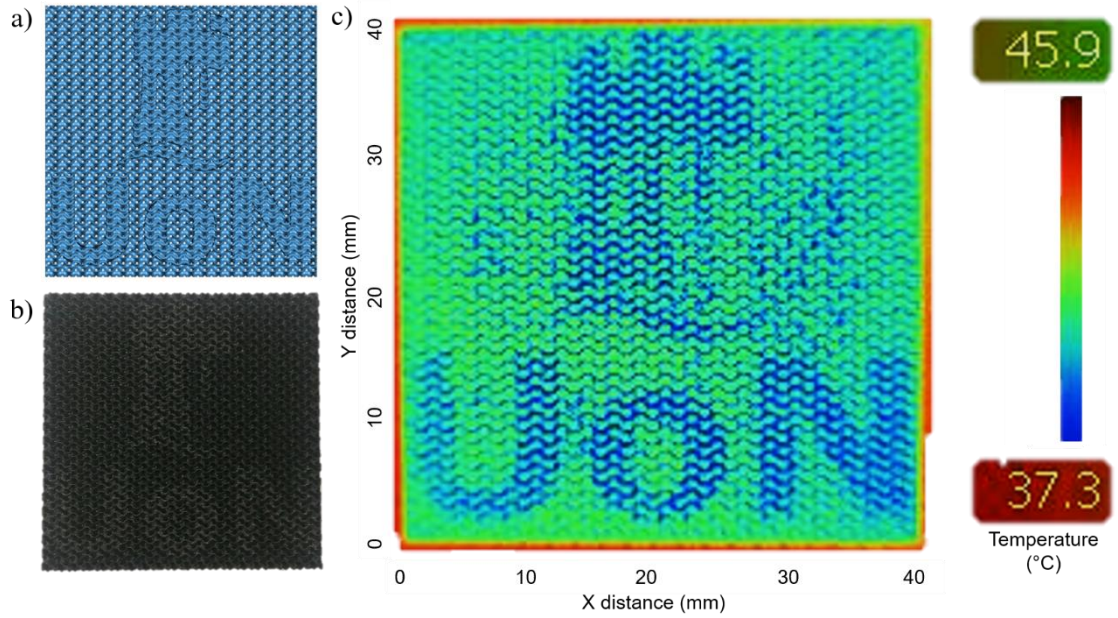


Figure 7.8 - University of Nottingham logo and text embedded into a lattice sample using variation in volume fraction. The .stl file can be seen in (a) along with the manufactured sample in (b) after spraying matt black. The logo is barely visible to the naked eye until it is heated and the variation in temperature due to the volume fraction grading is captured with an infrared camera, (c). Temperatures shown in °C.

7.7 CONCLUSIONS

In this Chapter, the 1D thermal conductivity for a range of lattice samples was experimentally measured using a custom-built test rig conforming to ASTM E1225-13. The measured results were then used to develop a set of design rules, or equations, that govern the relationship between thermal conductivity and the lattice parameters of volume fraction, unit cell type and unit cell size. From these design rules, it was possible to generate a number of demonstration models with a prescribed variation in conductivity using 1D and 2D mathematical functions. A sample was manufactured, using the University of Nottingham logo to demonstrate how varying the lattice volume fraction results in a distinct thermal profile. As a result of the experiments, heatsinks or thermal insulation layers can be developed that are optimised for thermal conductivity whilst retaining the advantages in weight reduction that lattice structures provide. Example applications across electronics, automotive and aerospace are given in the results and discussion section.

The key findings of the experimental work were as follows:

- For the lattice structures tested, thermal conductivity is primarily a function of the volume fraction, or ratio of solid material to free space inside the lattice
- Unit cell types with higher minimum wall thickness have a greater thermal conductivity than those with lower minimum wall thickness, at the same volume fraction (i.e. thermal conductivity is inversely proportional to surface area to volume ratio). It is important to note that for convective heat transfer, thermal performance is typically proportional to surface area, so thin walls are likely to be more beneficial under convection.
- Surface roughness may have a greater effect on thermal conductivity for samples with a higher surface area to volume ratio. Partially fused material

at the surface has reduced thermal conductivity, therefore does not effectively contribute to the thermal conductivity of the sample.

- Smaller unit cell sizes may constrain the air within the cells, preventing natural convection heat transfer between the cells from increasing the measured thermal conductivity.
- Larger unit cells may allow air to flow freely between cells, increasing the measured thermal conductivity. This effect is greater for unit cell types with a lower surface area to volume ratio such as Schwarz primitive

Typically, heatsinks used to cool electronics or mechanical components are independent components or assemblies. This creates complexity in manufacture and assembly, where components are joined using mechanical methods. Further, the packing of components is not optimised. This is a particular issue in aerospace and automotive components, where both volume and mass are at a premium. But most importantly, the weight of the assembly is increased by the necessity for manufacturing each component separately. Through simulation of the thermal loads, a thermal profile for the components can be derived. From this, a heatsink can be incorporated into the component itself. This design can be optimised for: minimal weight; defined thermal properties to cool hot components; structural strength if load bearing; external volume and shape for efficient packaging. In more advanced applications, a coolant flow such as compressed air can be forced through the structure. Operating as heat transfer surfaces under forced convection, lattice structures are capable of adding value to components in multiple ways. With proper design knowledge, such features can be incorporated into components via LPBF without incurring significant material cost or manufacturing time penalties. The experimental study of lattice structures as convective heat transfer devices is therefore the next research challenge.

8 ENHANCING CONVECTIVE HEAT TRANSFER USING LATTICE STRUCTURES

8.1 INTRODUCTION

The thermal conductivity of LPBF manufactured lattice structures are now known, however the maximum benefit of these geometries will come from their application in convective heat transfer. In this Chapter, the results obtained from experimental testing of the lattice structures using the apparatus described in Chapter 6 (section 6.3.2) will be presented an analysed.

Due to constraints in manufacturing these larger samples, it was decided to only manufacture a full sample set in AlSi10Mg. This material is lower cost than Hastelloy-X and was routinely available and loaded into a Renishaw AM250 LPBF machine at the University of Nottingham. This enabled trial builds be run in-house to determine optimum build orientations and parameters before final builds were performed, of which a minimum of three were required. In contrast, all Hastelloy-X samples were manufactured by Siemens Industrial Turbomachinery in Sweden and required cost estimations, budget allocation, machine scheduling and delivery lead-times, amongst other hurdles. Therefore, after initial testing was completed on the AlSi10Mg samples, a smaller batch of Hastelloy-X samples were manufactured to determine the effect of material properties on the pressure drop and convective heat transfer performance.

In this Chapter, pressure drop characteristics for the geometries are initially described. This does not include any heat transfer, however it is a key component in the overall performance of geometries for heat exchangers. The heat transfer characteristics are then given and discussed. From these, thermal performance metrics are calculated, which allow the selection of suitable geometries for the type of convective heat transfer performance required. Finally, design guidelines are provided for effective implementation of lattice structures into components under thermal loading.

For clarity: the work surrounding the AlSi10Mg samples in this thesis was performed in collaboration with Richard Sélo (PhD student at the Centre for Additive Manufacturing, University of Nottingham). Richard was responsible for the following: operation of the Renishaw AM250 LPBF machine for manufacture of the AlSi10Mg samples; writing of the Matlab script for processing of the experimental data; and performing <50 % of the AlSi10Mg experiments. Sam Catchpole-Smith was responsible for: 100 % of the design and manufacture of the convective heat transfer rig; performing >50 % of the experiments using AlSi10Mg samples; and 100 % of the work related to the HX samples. All graphs and associated results and discussion text was written wholly by Sam Catchpole-Smith with exception of some work surrounding error analysis of the experimental apparatus.

8.2 Experimental setup

This section details the setup for the experiment used to determine the convective heat transfer performance of lattice structure samples manufactured via LPBF.

8.2.1 Lattice structures under investigation

The full range of lattice unit cell types under investigation is given in Figure 8.1. Here, each illustration represents a 10 mm cube sectioned from the convective heat transfer samples. Each 10 mm cube contains a 2x2x2 array of unit cells, for a unit cell size of 5 mm. The top row in Figure 8.1 shows the isometric view of the unit cell to demonstrate the variation seen in the unit cells in 3D. The bottom row shows the frontal area seen by the flow, where the flow direction is in to the page. This aids in understanding the geometric features that result in a large variation in both pressure drop and heat transfer performance across the sample set as given later. Bar charts in Figure 8.1 provide geometrical data for all of the lattice structure samples under investigation. As cell size

decreases, the SA:vol increases exponentially. This has an impact on the flow capabilities and heat transfer performance of the samples which will be discussed in the later sections.

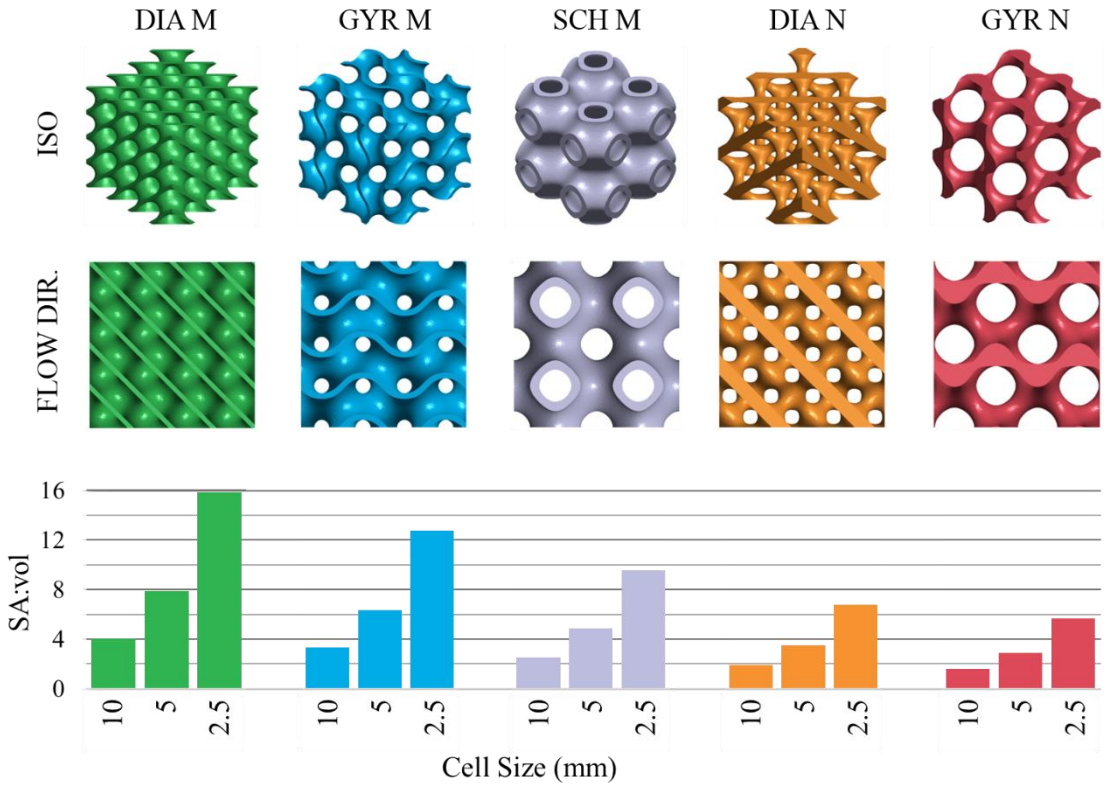


Figure 8.1 - Full set of unit cells under investigation in this study. One unit cell is shown per column, with the isometric view on the top row and the frontal view as seen by the fluid flow on the bottom row. Each represents a 10 x 10 x 10 mm section with 5 mm unit cell size. Surface area to volume ratio (SA:vol) is given in the bar charts and relates to the volume of solid material within each cell.

8.2.2 PIN-FIN BENCHMARK SAMPLE

To compare the pressure drop and heat transfer performance of the lattice structures, a classic pin-fin geometry was designed and manufactured via LPBF alongside the lattice structure samples. The pin-fin spacing and geometry can be seen in Figure 8.2. This geometry was chosen to be 20 % volume fraction, matching that of the lattice structure samples to ensure the thermal performance per unit volume can be directly compared. Throughout the following results, the data corresponding to the pin-fin benchmark is displayed as a black line.

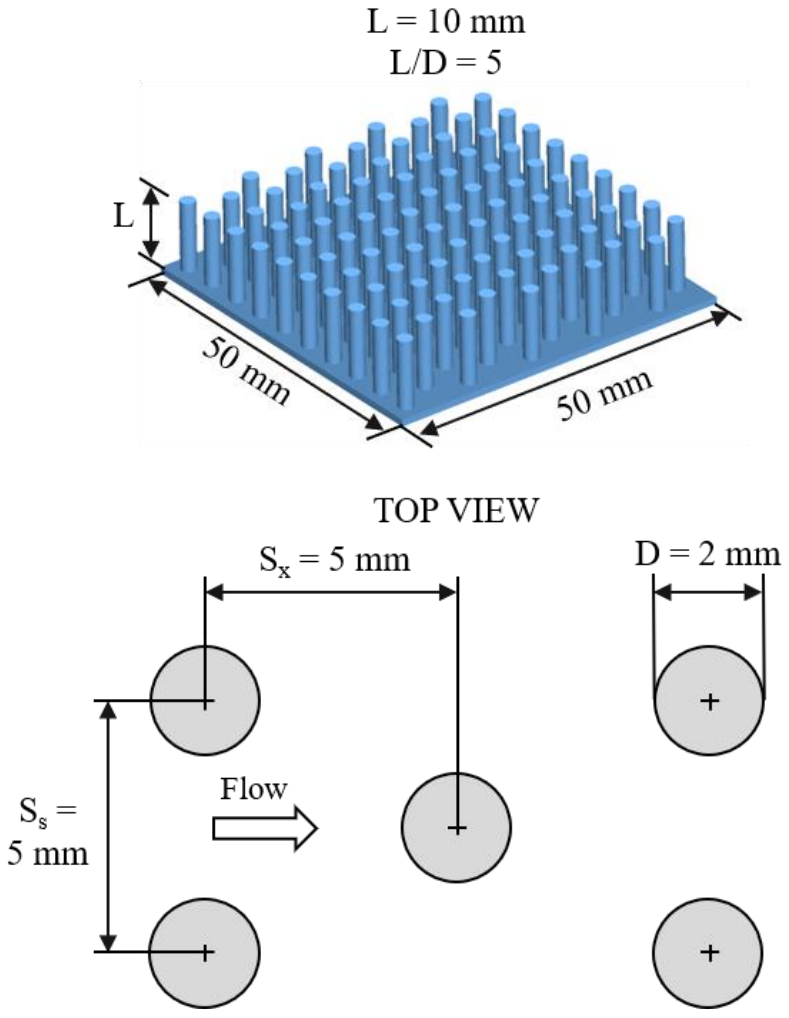


Figure 8.2 - Geometry data for the pin-fin benchmark coupon with spanwise spacing S_s = 5 mm, streamwise spacing S_x = 5 mm, pin diameter D = 2 mm and pin length L = 10 mm. This provides a ratio L/D = 5. This layout can be seen in 3D on the right-hand side (top wall removed for clarity).

8.3 EXPERIMENTAL RESULTS

8.3.1 PRESSURE DROP – AlSi10Mg

Figure 8.3 shows the friction factor augmentation results for the matrix phase lattice samples across the full Reynolds range. All samples shown here had approximately 2 – 15 times increase in friction factor augmentation compared to the pin-fin sample. There is a clear negative correlation between cell size and friction factor augmentation; large cells resulted in the lowest frictional losses and reducing cell size progressively increased the frictional losses. This was true across all matrix phase cell types. For each cell size, the GYR M cell type had the lowest friction factor augmentation of the three matrix phase unit cell types tested, whilst the SCH M cell type had the highest frictional losses. However, an interesting trend was seen for the SCH M cell type: the friction factor augmentation performance disparity compared to GYR M and DIA M decreased as cell size decreased. At 2.5 mm cell size, the SCH M performance was near parity with the other samples at higher Reynolds number flows. The SCH M may visually appear to provide an easy path for fluid through the holes in the geometry (Figure 8.1, column 3). However, this entrance region is actually highly restrictive as the fluid is forced through these holes only, whereas a more constant but meandering path is possible in the GYR M (Figure 8.1, column 2) and DIA M (Figure 8.1, column 1) unit cells. At 2.5 mm cell size, the high SA:vol of the GYR M and DIA M compared to the SCH M (Figure 8.1, bar chart) counteracts the benefits of a geometry that is less restrictive to flow, equalising the friction factor augmentation across the three unit cell types.

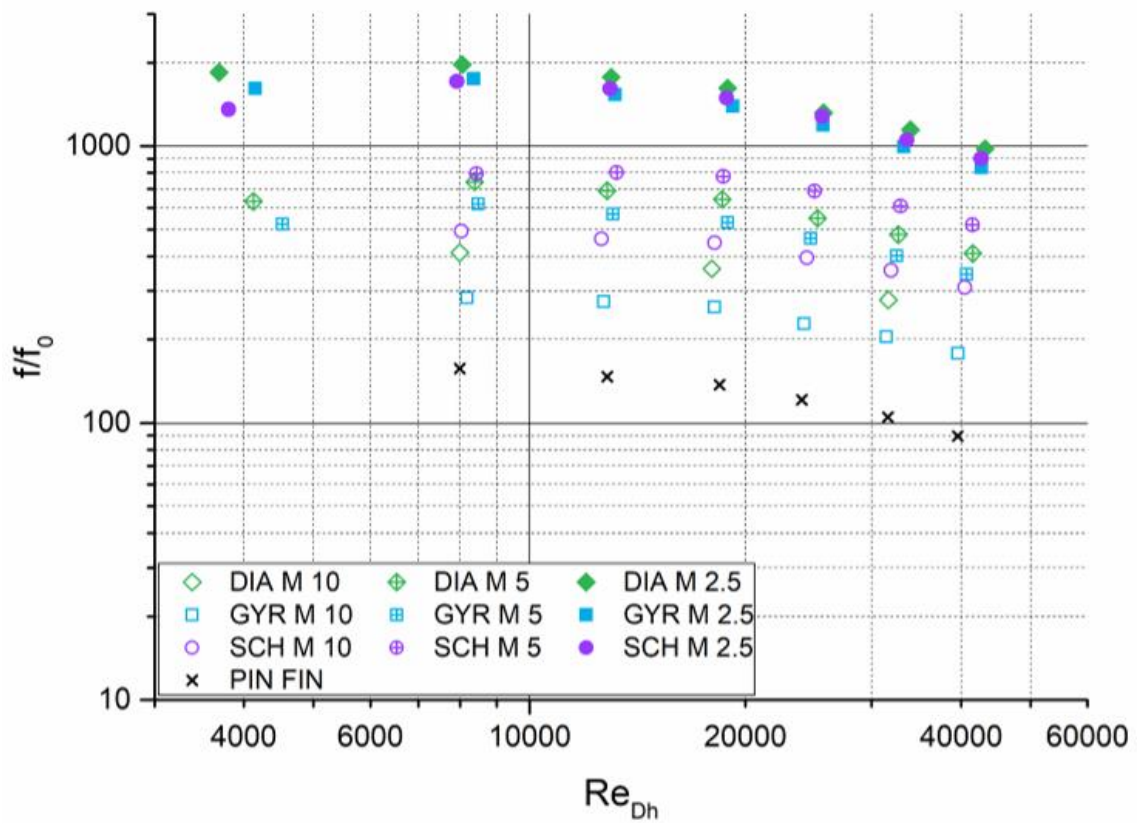


Figure 8.3 - Friction factor augmentation (f/f_0) across the Reynolds number range for all matrix phase lattice samples. Note the negative correlation between cell size and friction factor augmentation.

By extracting the results for GYR M and DIA M 2.5 mm and 10 mm cells at Re = 20,000 and plotting without the visual compression present using logarithmic scale, the impact of cell size is evident (Figure 8.4). Simply by decreasing the cell size by 75 %, there was an associated increase in friction factor augmentation of approximately four times, or an order of magnitude at low Reynolds conditions. This effect was driven by the increase in SA:vol with decreasing cell size. As the LPBF manufactured samples can be considered high roughness when compared to conventionally manufactured heat exchanger geometries, the associated fouling of the flow can be significant when the flow is forced through narrow passages or around fine features. This absolute surface roughness is improving as process understanding and optimisation is developed.

However, manufacturing process induced surface roughness will still remain constant across feature size scales in LPBF, i.e. the surface roughness will be the same for a 5 mm thick wall as it will be for a 500 µm thick wall. If the surface roughness and flow conditions remain constant, the boundary layer thickness at the surface will remain constant, occupying a larger proportion of the flow area as cell size decreases. A loss of approximately 10 % of the free flow area is seen in the GYR M example in Figure 8.5. Therefore, the relationship between feature size and friction factor augmentation is not linear.

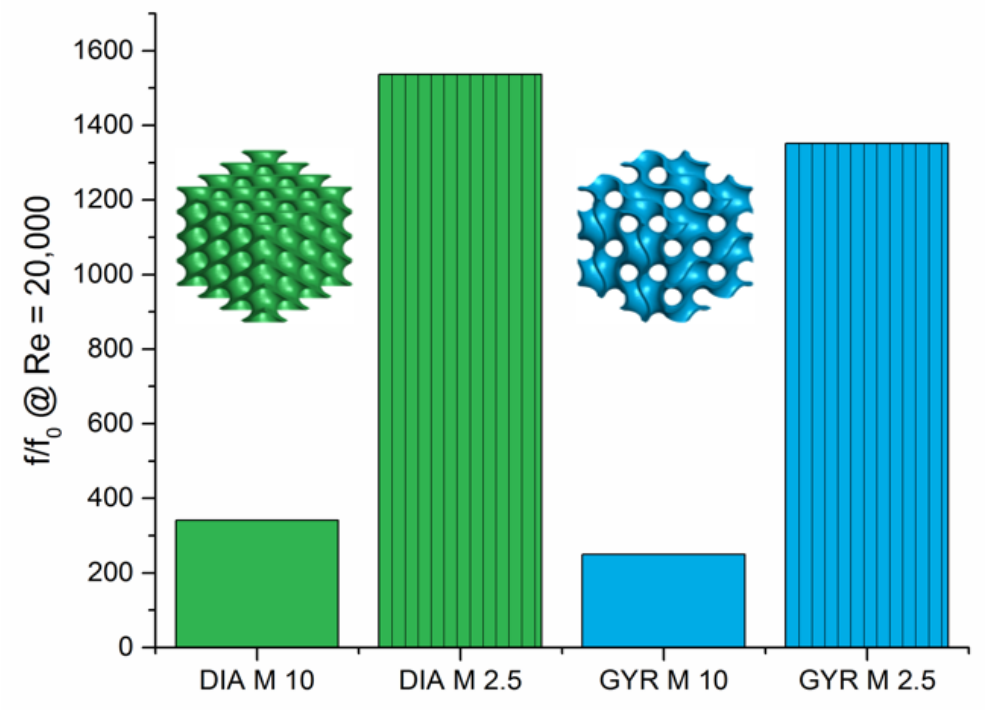
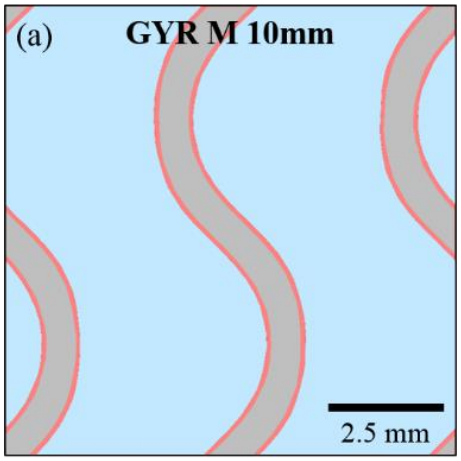


Figure 8.4 - Friction factor augmentation (f/f_0) at Re = 20,000 for the GYR M and DIA M 2.5 mm and 10 mm cells only. This demonstrates the effect on frictional losses as cell size is decreased.



	GYR M	
	10 mm	2.5 mm
Boundary (%)	4.4	12.6
Flow area (%)	79.4	72.6

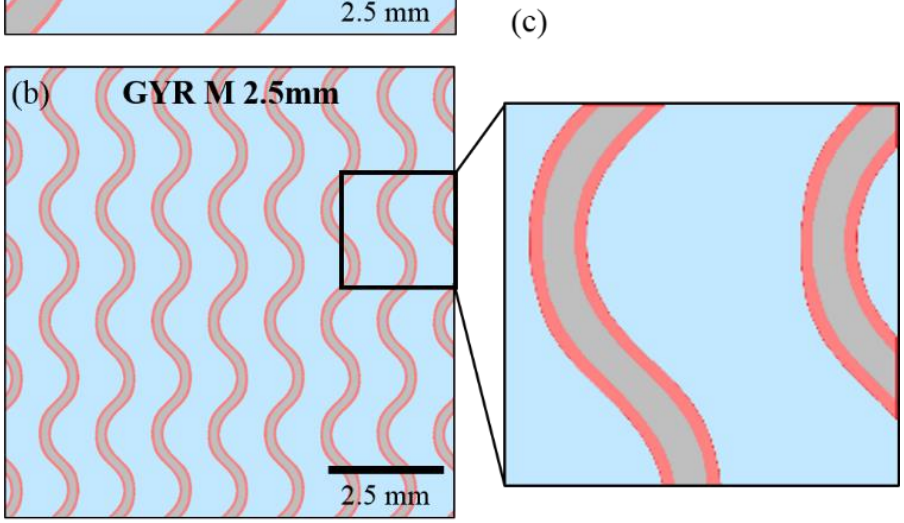


Figure 8.5 - Illustration of the change in boundary layer area (red) and free flow area (blue) when moving from 10 mm (a) to 2.5 mm (b) cell size.

The network phase samples followed the same negative correlation between friction factor augmentation and cell size (Figure 8.6). Importantly, the 10 mm cell size network lattice samples provided lower friction factor augmentation than the pin-fin benchmark across the full Re range. This indicates that despite the complex appearance of the network lattice structures, the flow path through the geometry can be relatively free, providing that a large cell size and hence low SA:vol is chosen. The GYR N had a better performance than the DIA N across all cell sizes and the performance delta between these two unit cell types was greater in the case of the network phase than for the matrix phase. Further, the performance delta remained at 2.5 mm cell size whereas in the matrix phase samples, performance delta between DIA and GYR narrowed as cell size decreased. The

DIA N 5 mm sample only provided an approximately 23 % decrease in friction factor augmentation than the GYR N 2.5 mm sample, despite the significantly lower SA:vol (Figure 8.1, bar chart). This demonstrates that geometry has a significant effect on the frictional losses and it is not SA:vol alone that dictates the pressure drop performance of a sample.

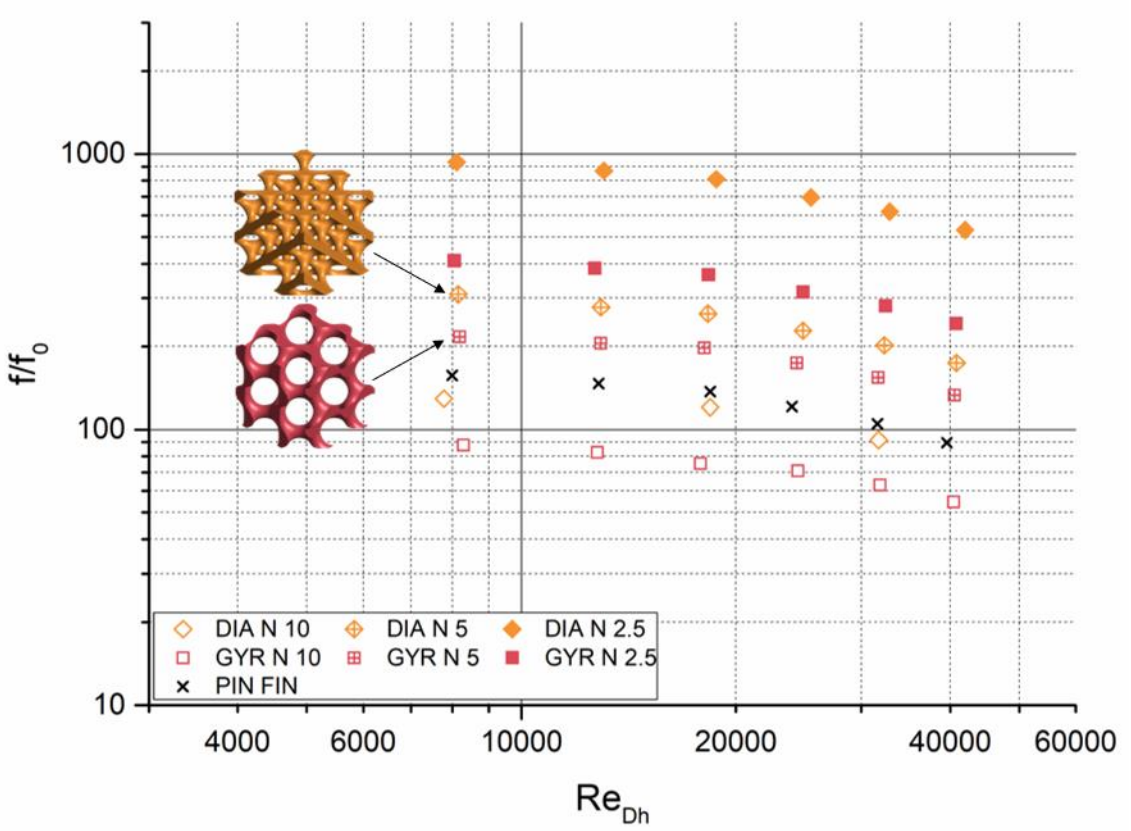


Figure 8.6 - Friction factor augmentation (f/f_0) across the Reynolds number range for all network phase lattice samples. Colours refer to unit cell type, marker fill refers to cell size. Note the improved frictional losses compared to the matrix phase (Figure 8.3).

The difference in friction factor augmentation at Re = 20,000 between the matrix and network phase lattices at 5 mm cell size is apparent in Figure 8.7. The GYR M sample had approximately 2.7 times greater friction factor augmentation than the equivalent GYR N sample, which itself had approximately twice the friction factor augmentation of the pin-fin geometry. This relationship is also true for the DIA samples but with greater frictional losses in each case. Overall, this would indicate that for applications where frictional losses need to be kept to a minimum, network cell types are the logical choice. However, the friction factor augmentation performance is only one factor to consider, with the heat transfer performance being equally as important. Once this is taken into consideration, the choice of unit cell may move towards one with a higher friction factor, but improved heat transfer. The relationship between friction factor and heat transfer performance is evaluated using a range of 'thermal performance' indices explored later in this Chapter.

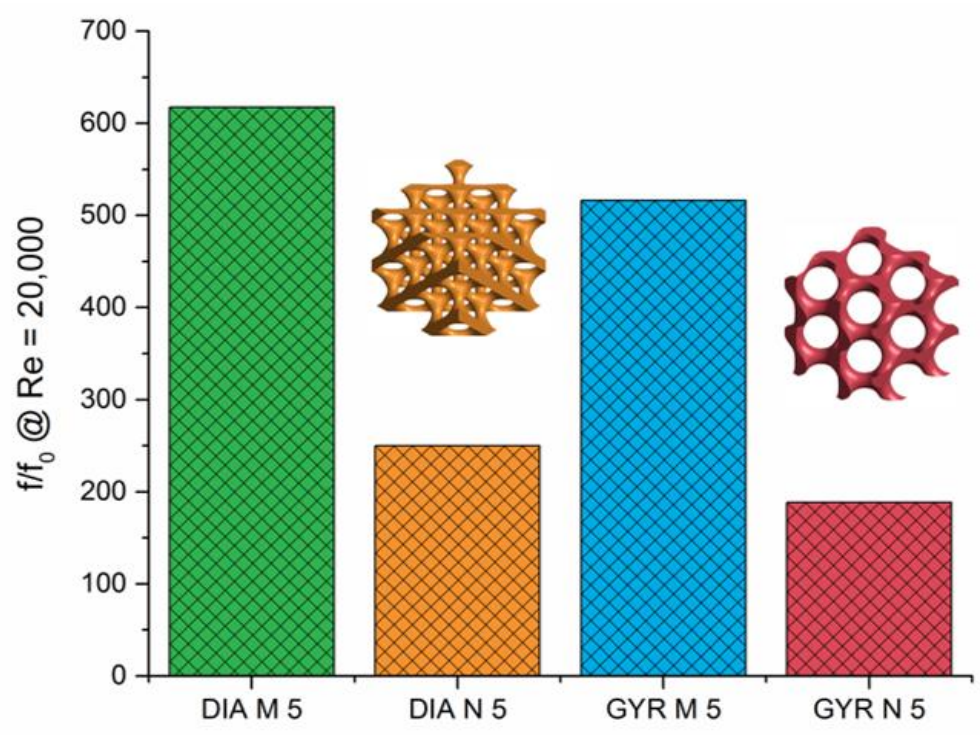


Figure 8.7 - Friction factor augmentation (f/f_0) at Re = 20,000 comparing the performance of the matrix phase against network phase for the GYR and DIA unit cell type at 5 mm cell size.

8.3.2 HEAT TRANSFER PERFORMANCE – ALSI10MG

Figure 8.8 shows the Nu for all the lattice samples tested. It illustrates the wide range of performance possible using lattice structures, where a minimum of 5 times increase in Nu compared to the pin-fin benchmark was seen. This indicates that the complex lattice geometries dictate a flow path that acts to prevent a significant thermal insulation layer of static fluid from forming at the surface of the structure. Therefore, they are highly effective at inducing convective heat transfer from the structure to the coolant flow.

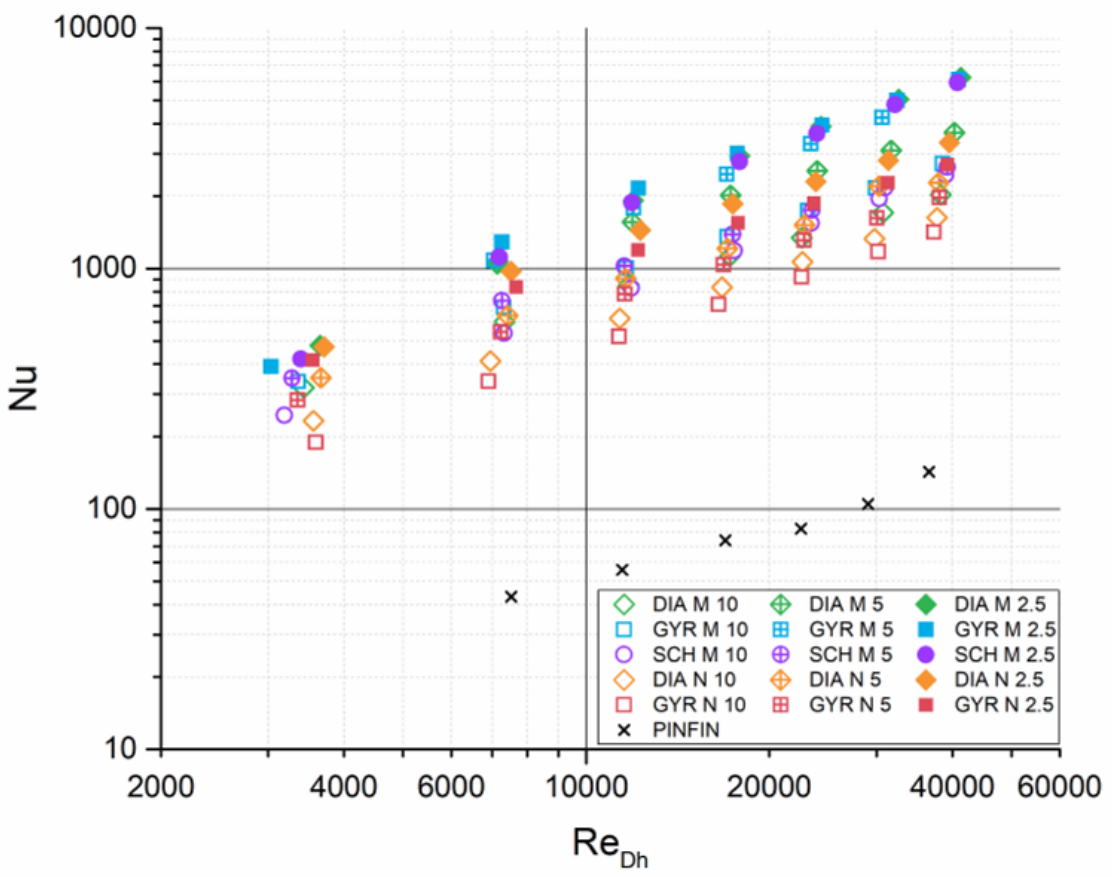


Figure 8.8 - Nusselt number for all lattice samples tested across the full Reynolds range. The minimum and maximum Nu of 300 and 7000 respectively demonstrates the wide range of operation possible using lattice heat exchange geometries.

Nusselt number augmentation (Nu/Nu_0) was greatly increased by moving from 10 mm to 5 mm cell size (Figure 8.9), as a larger SA:vol (Figure 8.1, bar charts) resulted in enhanced interaction between the fluid flow and the surface of the lattice geometry.

Little gain was seen by then decreasing cell size to 2.5 mm for the GYR M sample, however. This suggests that there is a fundamental limit to the improvement of heat transfer performance achievable via the reduction of feature size (or increase in SA:vol), beyond which the proportion of boundary layer to free flow area becomes too large. As with the friction factor augmentation results, the SCH M sample was the lowest performing geometry at 10 mm cell size. However, performance increased relative to the other matrix phase samples as cell size decreased, reaching performance parity at 2.5 mm cell size. At large cell sizes, the SCH M geometry allows for a large proportion of the air to pass directly through the structure via holes aligned with the flow direction. This prevents turbulation and mixing of the air within the cell, therefore decreasing interaction between the air and lattice surface resulting in a poor Nu. At smaller cell sizes, the free path for the air is significantly reduced, forcing increased surface interaction and hence improving Nu. Due to this relationship, the SCH M unit cell would not be chosen at cell sizes 5 mm and above due to high friction losses and poor heat transfer performance. However, below that size limit the SCH M can be as effective in convective heat transfer as the other unit cell types.

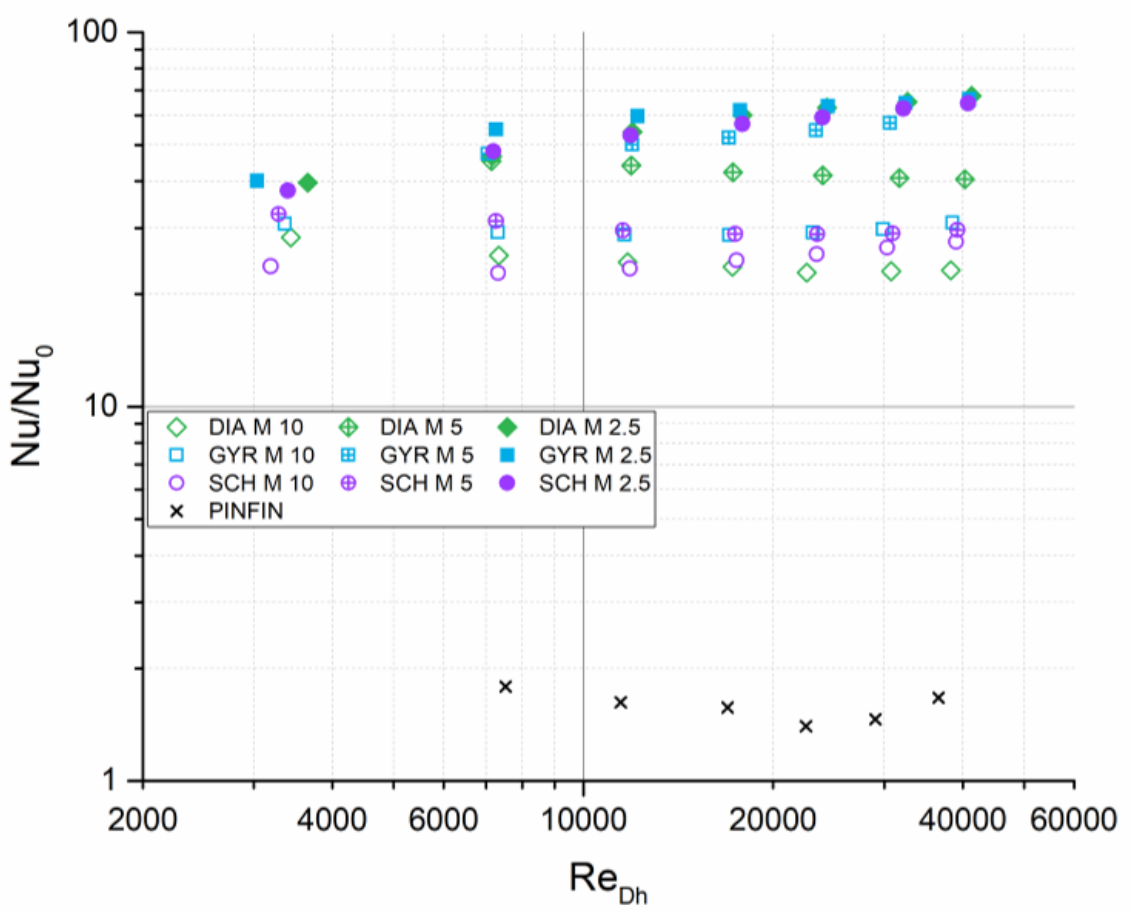


Figure 8.9 - Nusselt number augmentation plots for the matrix phase lattice samples across all unit cell sizes

The Nu augmentation results for the network phase lattice samples (Figure 8.10) overall followed the same trends as those seen for the matrix lattice phase, however there was now a flat or slightly negative correlation between Nu/Nu_0 and Re. Across all cell sizes, DIA N achieved a higher Nu augmentation than GYR N. The GYR N lattice allows for a low number of large diameter free-flow paths through the structure (Figure 8.1, column 6). In contrast, the DIA N has a larger number of small diameter paths (Figure 8.1, column 5), resulting in a higher degree of interaction between the fluid and the structure. As a result, the DIA N geometry is more effective at transferring heat into the coolant fluid, increasing the Nu values.

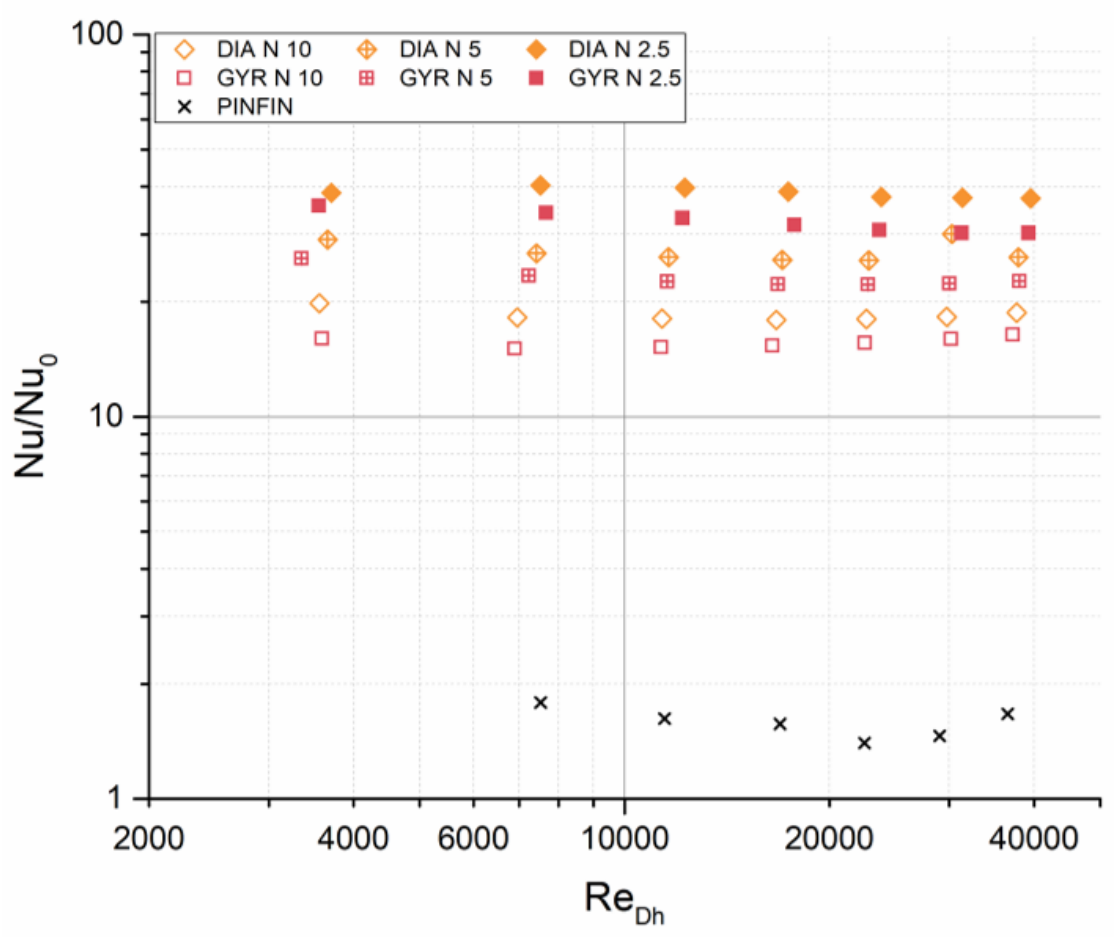


Figure 8.10 - Nusselt number augmentation for the network phase lattice structure samples across all cell sizes

8.3.3 Thermal performance indices – AlSi10Mg

The thermal performance rating of a heat exchange geometry can be represented in multiple ways and care must be taken to select the correct index for the heat exchanger application. In this section, two thermal performance indices are provided for the lattice structure dataset and the significance of each is discussed. These indices are ordered as follows:

1. $TP_{norm} = \frac{Nu}{f}$
2. $TP_{mod} = \frac{{}^{Nu}/_{Nu_0}}{\left({}^{f}/_{f_0}\right)^{1/3}}$

8.3.3.1 TP_{NORM} INDEX

TP_{norm} (Figure 8.11) attaches equal weighting, and therefore equal engineering design importance, to Nusselt number and friction factor. This TP index may be used for applications where pressure drop across the heat exchanger needs to be kept to a minimum and hence some convective heat transfer performance must be sacrificed. Using TP_{norm}, all of the lattice structure samples provided an efficiency enhancement over the pin-fin benchmark. The network phase samples performed particularly highly, providing approximately 6.5 – 16.7 times TP increase at Re = 25,000. The network phase samples had a higher thermal performance than the matrix phase due to the lower frictional losses compared to the matrix phase. Whilst the lattices showed enhanced thermal performance, performance gain may not be significant enough to outweigh the added complexity in qualifying the structural integrity of lattice structures. In contrast, pin-fin geometries are relatively simple and methods of qualification post-manufacture are well-understood.

At Re > 10,000 the 10 mm cell size samples proved to be the most efficient for the network phase lattices (Figure 8.11) using TP_{norm}, with the GYR N 10 mm having the highest TP_{norm} overall. At Re > 20,000, the GYR M 5 mm sample had the highest TP out of the matrix phase group. It is important to note that despite the 2.5 mm cell size samples providing the highest Nu augmentation, they achieved some of the lowest TP_{norm} values due to excessive pressure drop. This is a manifestation of the effects of geometry on flow fowling: small feature sizes and large flow rates result in a significant proportion of the flow path being lost to viscous boundary layers, leading to poor TP. TP_{norm} would be ideal for applications where coolant fluid is only available at low pressure, for example air delivered using an axial fan in an electronics enclosure. Here, a low pressure drop heat transfer region is required to ensure coolant can be fed through the system at high enough mass flow rates. However, in an application where coolant is supplied at high pressure, a geometry chosen based on TP_{norm} may result in a heat exchanger with too small a pressure

drop. As a result, mass flow rates through the component may be too high and overall system efficiency would be lost due to underutilisation of the coolant fluid.

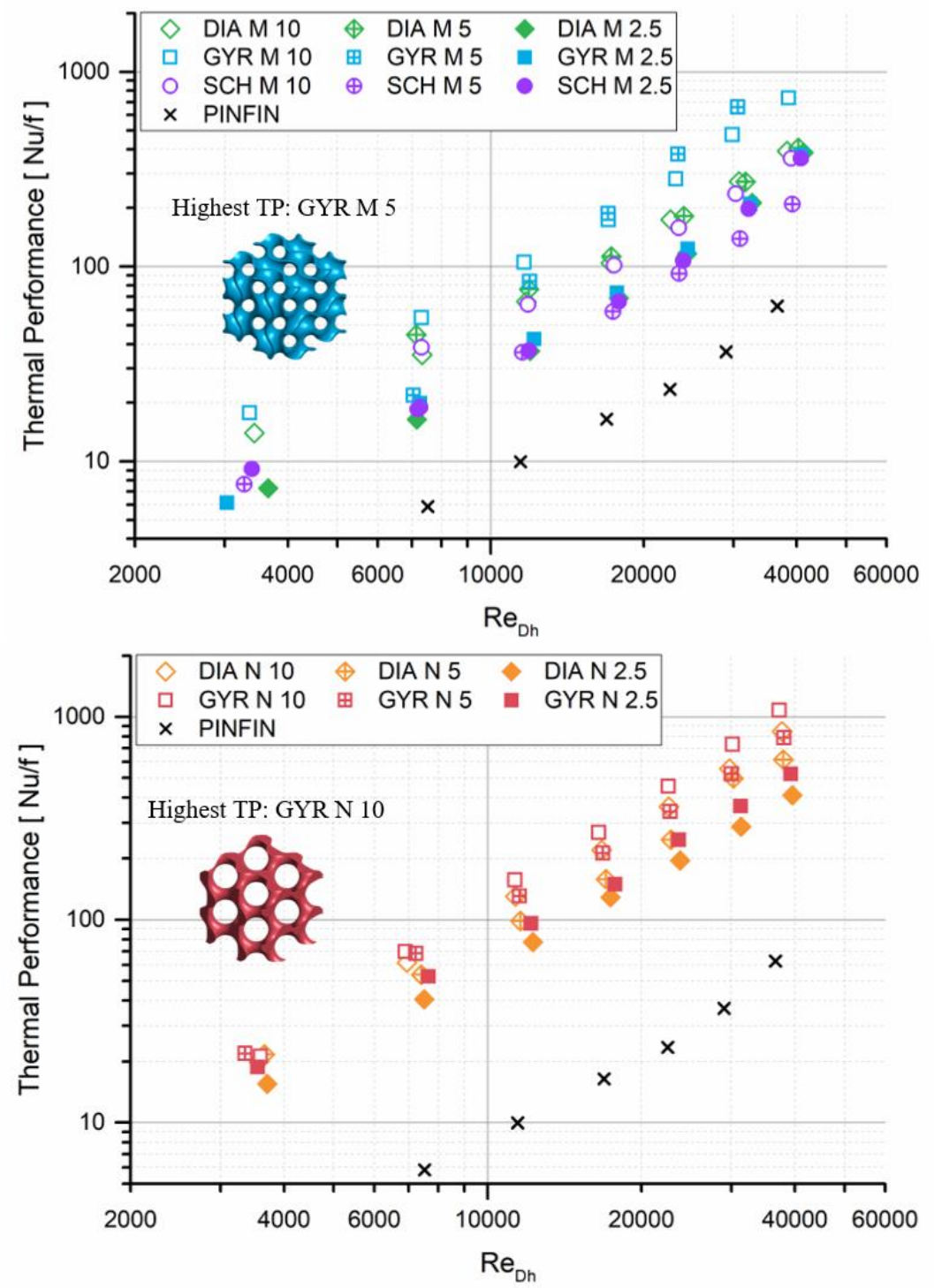


Figure 8.11 - Thermal performance metric TP_{norm} [Nu/f] against Reynolds number for the matrix phase (top) and network phase (bottom) lattice structure samples. Note the modest performance increase between the lattice samples and the pin-fin benchmark using this performance metric.

8.3.3.2 TP_{MOD} INDEX

Using the modified thermal performance index (TP_{mod}), the weight of friction factor on thermal performance value is decreased and enhanced heat transfer performance is promoted. It is clear that the lattice structure samples have a significant performance advantage over the pin-fin benchmark using this index (Figure 8.12), outweighing the added complexity involved with implementing and verifying lattice structure heat transfer geometry. The GYR M 5 mm sample provided the highest thermal performance when Re > 10,000 at 40 times that of the pin-fin, with the DIA M 5 mm giving slightly better performance at Re < 10,000. SCH M 10 mm and 5 mm and DIA M 10 mm had the worst TP_{mod} due to poor Nusselt augmentation values (Figure 8.9) and high friction factor augmentation. However, at 2.5 mm cell size, SCH M ranked equal in TP_{mod} with the other unit cell types as its low SA:vol prevented significant fouling of the flow. The network phase lattice structures have a relatively flat TP_{mod} across the Re range and as a result have a higher performance than the matrix phase at Re > 7,000 (TP_{mod}: GYR M 10 = 4.0, GYR N 2.5 = 4.4 at Re = 3,400). The 2.5 mm network samples provide the highest TP_{mod}, showing that reducing cell size below 5 mm can improve TP when using geometries that are less prone to flow fouling.

TP_{mod} is an example of how analysis of thermal performance can be modified to suit different applications – any value can be used as the exponent of friction in the equation, as required. TP_{mod} favours high heat transfer performance at the expense of pressure drop through the heat transfer region. It is ideal for applications where coolant pumping energy is not a primary system limitation and can be supplied at a high pressure. A suitable use case is in cooling of post-combustion gas turbine components such as turbine blades and guide vanes, where coolant air is supplied by the compression stage at a pressure typically 3 bar greater than the pressure of the hot gas path. Therefore, any coolant air exiting component cooling channels into the hot gas path will undergo a 3 bar pressure drop,

more than sufficient to enable effective use of any lattice structure tested here. Consequently, geometries with the greatest thermal performance according to TP_{mod} (Figure 8.12, GYR M 5) are preferred, despite their high friction factor augmentation.

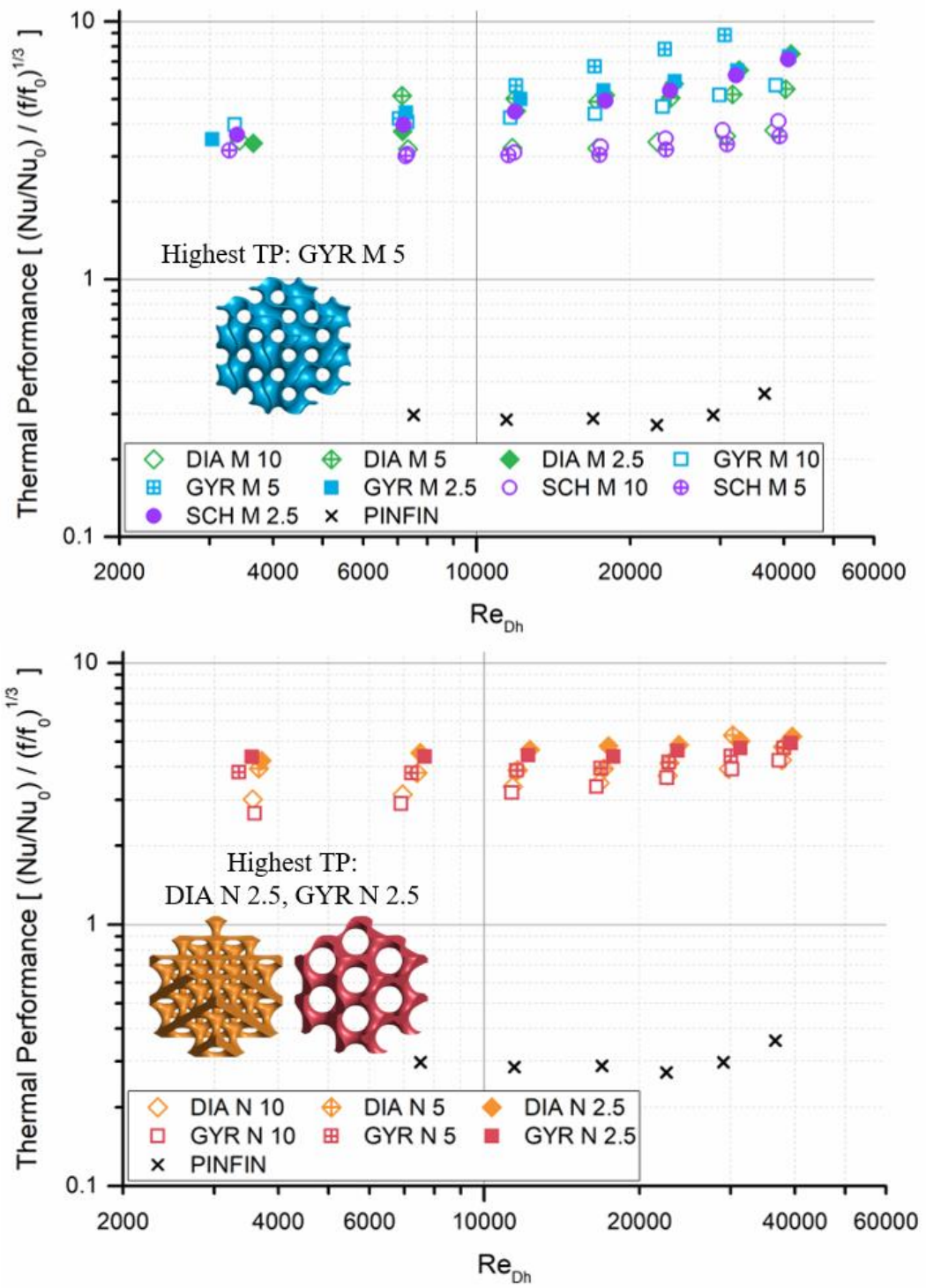


Figure 8.12 - Thermal performance metric TP_{mod} against Reynolds number for the matrix phase (top) and network phase (bottom) lattice structure samples. Note the relatively flat relationship between performance and Re using this metric.

8.4 HASTELLOY-X LATTICE CHARACTERISATION

A selection of geometries were manufactured in Hastelloy-X (HIP + HT condition) and tested using the same methodology. It was important to determine the performance of the samples manufactured in this material due to differences in the as-manufactured surface roughness (*see* Chapter 4 section 4.5.3) and properties of the bulk material, particularly thermal conductivity. This section will provide the pressure drop and heat transfer performance of the Hastelloy-X samples and also draw comparisons to the data given previously for the AlSi10Mg samples.

8.4.1 PRESSURE DROP – HASTELLOY-X

Figure 8.13 shows the friction factor augmentation values for the HX samples across the full Re range. As with the AlSi10Mg samples, there is a negative correlation between Re and f/f_0. The DIA M and DIA N 2.5 mm samples showed the highest f/f_0 as expected due to the smallest cell size tested. The GYR N 2.5 mm sample had significantly lower f/f_0 despite having the same cell size, matching that seen in the AlSi10Mg testing. The BCC AN cell also showed a low f/f_0 as like the GYR N, it has a free flow path through the geometry which provides a low pressure drop path for the air. As a result, there is less interaction with the geometry and therefore it should be expected that the BCC AN will also have a lower heat transfer performance. As seen in the Alsi10Mg samples, the GYR M 5 mm sample had similar f/f_0 performance to the 2.5 mm network phase samples despite having double the cell size. This further demonstrates how the continuous wall structure of matrix phase geometries results in a high pressure drop due to increased flow interaction. The GYR N and DIA N 5 mm performance was equal at Re > 10,000, an unexpected result that may suggest that the GYR N sample was manufactured slightly oversize, or the DIA N was manufactured slightly undersize.

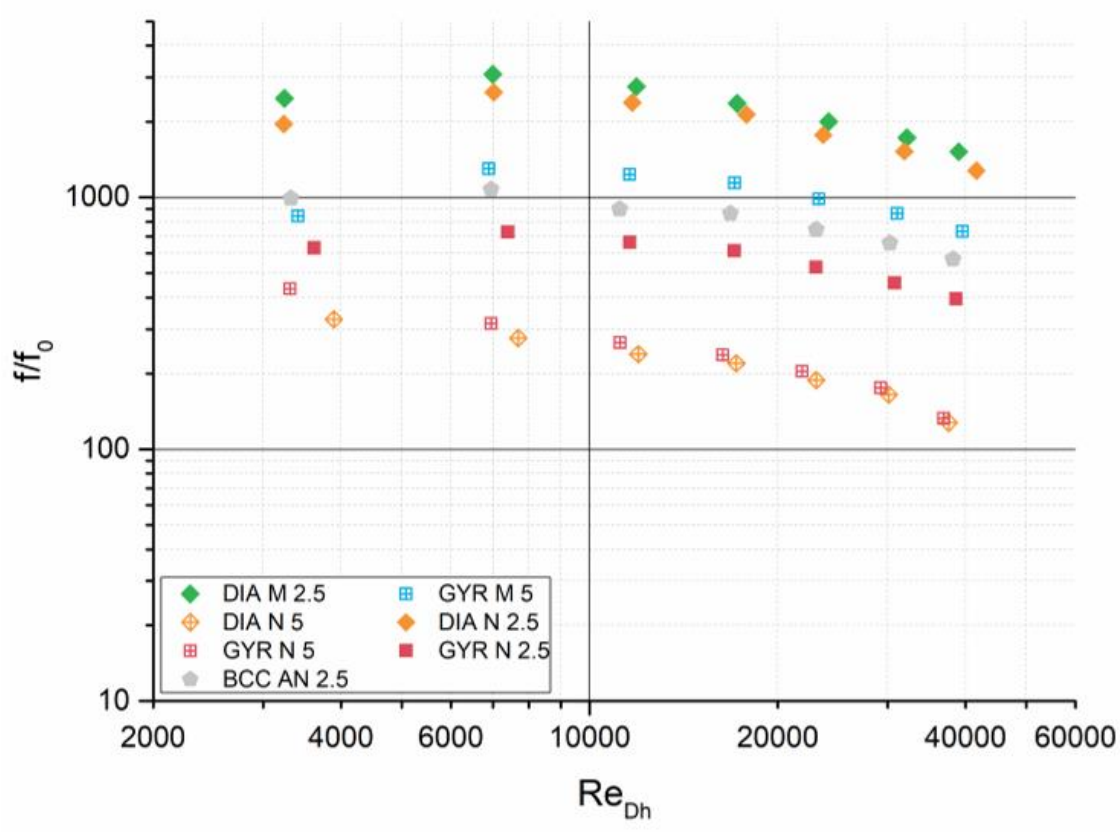


Figure 8.13 - Friction factor augmentation (f/f_0) across the Reynolds number range for all Hastelloy-X samples. Note the negative correlation between cell size and friction factor augmentation.

When comparing the f/f_0 to that of the AlSi10Mg samples (Figure 8.14) it can be seen that the HX GYR M 5 mm had greater than double the frictional losses. However, the f/f_0 increase for the DIA N 5 mm was not so significant. This is due to a combination of the increase Sa value of the HX samples (HX Sa = 17.8 µm, AlSi10Mg Sa = 15.5 µm, discussed in section 4.5.3.1) and the geometry, where the matrix phase is more susceptible to increases in surface roughness due to the higher degree of interaction between the walls of the geometry and the air. This result indicates how important surface roughness is to frictional losses in convective heat transfer applications. For increased performance of lattice structure heat exchangers, methods for reducing surface roughness should be investigated. These may be in-process optimisations such as scan strategy or process parameter modifications or may be post-processes such as abrasive particle machining.

However, it is also important to consider that surface roughness may also increase heat transfer and so overall performance in heat exchange may not be improved by reducing surface roughness.

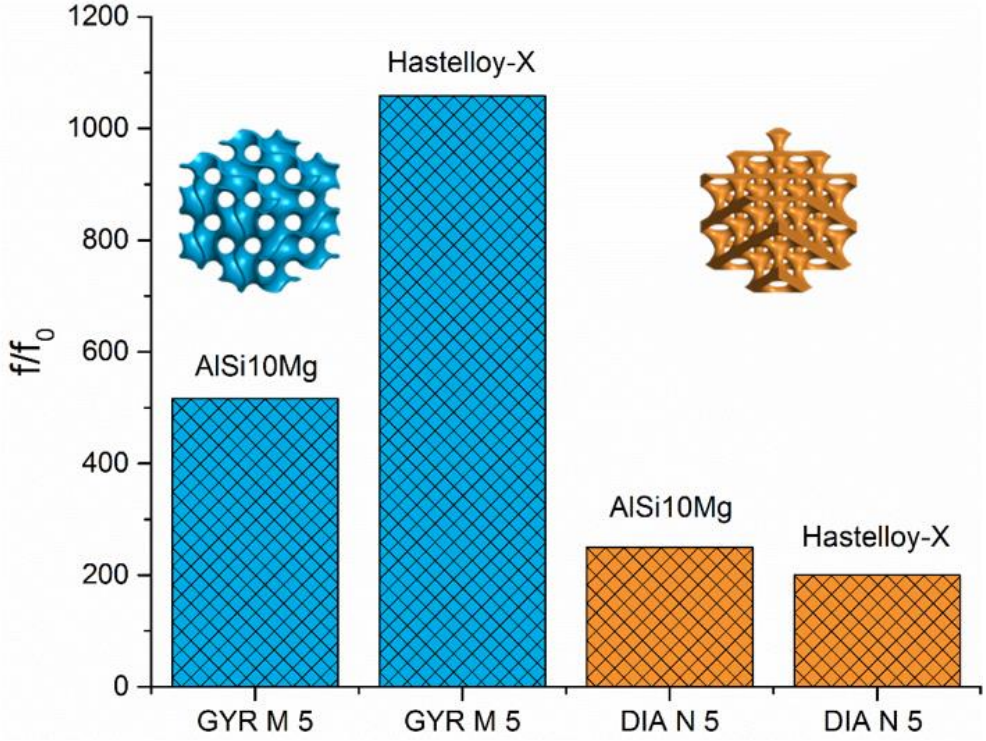


Figure 8.14 - Comparison of friction factor augmentation between HX and AlSi10Mg for the GYR M 5 mm and DIA N 5 mm samples. All data taken at Re = 20,000.

8.4.2 HEAT TRANSFER PERFORMANCE – HASTELLOY-X

The Nu augmentation results for the HX samples are given in Figure 8.15. As with the AlSi10Mg samples, the DIA N 2.5 mm sample had the highest Nu/Nu_0. However, the performance was reduced for the HX samples, ranging 5 – 26 compared to 16 – 40 for the AlSi10Mg. This is due to the reduced thermal conductivity of the HX bulk material (HX: k = 9.7 $W.m^{-1}.K^{-1}$, AlSi10Mg: k = 103 $W.m^{-1}.K^{-1}$ at 293 K). As the apparatus heats the lattice sample from the bottom surface, the heat must be conducted through the lattice geometry before it can be transferred to the air via convection. A material with a higher thermal conductivity will be able to conduct the heat more effectively, with a more even temperature distribution through the geometry in the direction perpendicular to the heated surface. The HX cannot conduct heat so effectively and so there will be a steeper temperature gradient in this direction.

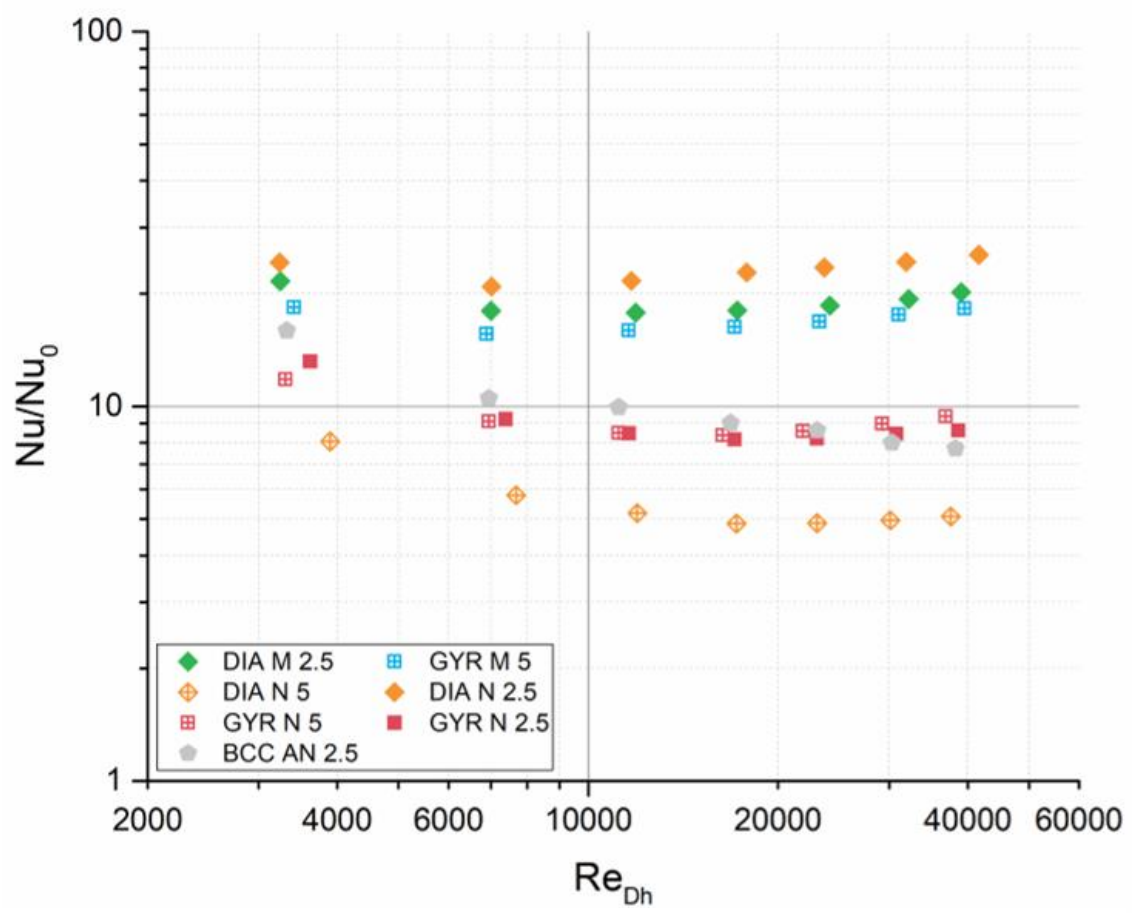


Figure 8.15 - Nusselt number augmentation for all HX samples across the full Re range.

Convective heat transfer is more efficient when the temperature differential between the geometry and the air is greater; the HX sample will be cooler towards the top and therefore less efficient at transferring heat to the air. Overall, this results in a reduced Nu/Nu_0. In a real engineering application this effect can be accounted for through design by using a graded lattice structure. If the volume fraction is higher at the hot surface and is gradually reduced in the direction perpendicular to this surface, effective thermal conductivity of the geometry will be tailored in a way that enables a more even temperature distribution. This in turn will increase the Nu (and therefore Nu/Nu_0) of the heat exchanger. This idea was explored in Chapter 6 ('Thermal conductivity of lattice structures') where graded lattices with tailored effective thermal conductivity values were modelled and manufactured.

8.4.3 THERMAL PERFORMANCE INDEX - TP_{NORM}

TP_{norm} favours low pressure drop over high heat transfer as discussed in section 8.3.3.1 and is ideal for applications requiring a low pressure drop heat transfer geometry. As a result, the 2.5 mm cell size samples had the lowest TP_{norm} performance due to their high friction factor and the larger cell size samples showed the highest performance. TP_{norm} was in the range 2 – 200 compared to the AlSi10Mg samples with the range 6 – 730. This greatly decreased performance rating is a result of the increased f/f_0 and decreased Nu/Nu_0 seen previously for the HX samples. However, at Re = 20,000 the lowest performing HX sample (DIA M 2.5 mm) was similar to that of the AlSi10Mg pin-fin benchmark sample (TP_{norm} = 17 and 20 respectively), showing that even when manufactured in a material with a significantly lower thermal conductivity, the lattice structures are an effective convective heat transfer geometry. In applications where aluminium is chosen for high heat transfer at the expense of some mechanical performance, lattice structures may provide the increase in heat transfer required to enable choice of a material with higher mechanical strength that would normally be discounted

due to poor thermal performance. This is a further degree of design freedom that can be unlocked through AM processes that enable manufacture of complex geometries that improve upon classical pin-fin or narrow channel heat exchangers.

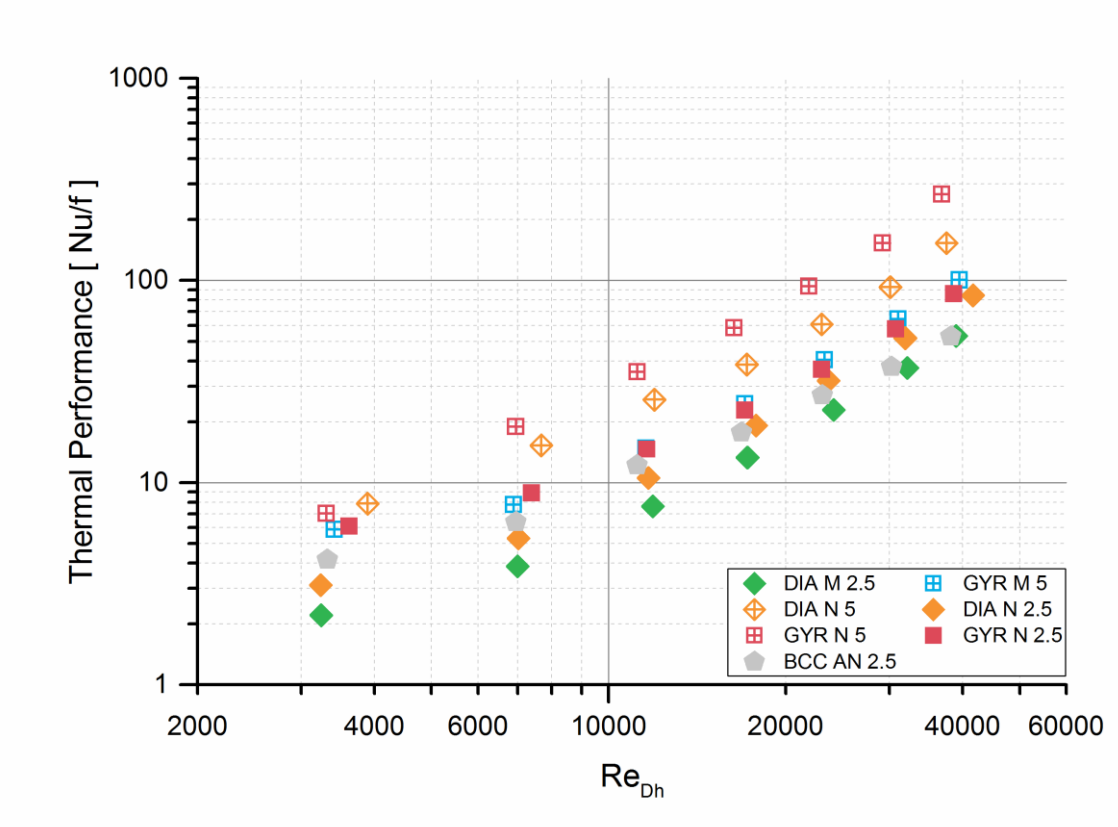


Figure 8.16 - Thermal performance metric TP_{norm} [Nu/f] against Reynolds number for the HX lattice structure samples.

The performance delta in TP_{mod} between the same geometries manufactured in HX and AlSi10Mg is made clear in Figure 8.17. The performance of the DIA M 5 mm sample is approximately an order of magnitude greater in AlSi10Mg than HX, demonstrating why aluminium alloys or alloys with high thermal conductivity are used in heat exchange applications. A nickel alloy such as HX would only be used in applications where its properties such as corrosion resistance and high strength at elevated temperatures are required. The poor TP_{mod} performance of the matrix phase HX geometry is again a result of the compounding high f/f_0 and low Nu/Nu_0 (1000 and 17 respectively at Re = 20,000_. The performance delta for the GYR N 5 mm lower at 0.28 times the AlSi10Mg equivalent

due to its lower f/f_0 (500 at Re = 20,000). This is despite the lower Nu/Nu_0 than the GYR M 5 mm (8.5 at Re = 20,000), which is an effect of the equal weighting on friction and Nu of the performance index TP_{mod}.

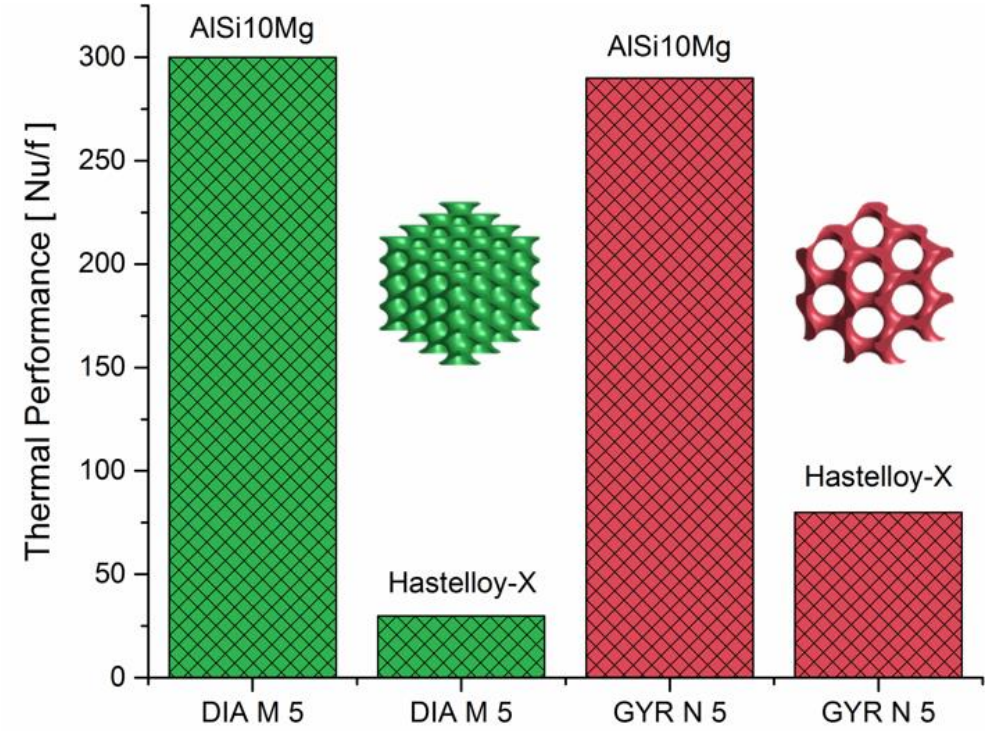


Figure 8.17 - Comparison of thermal performance index TP_{norm} between HX and AlSi10Mg for the DIA M 5 mm and GYR N 5 mm samples. All data taken at Re = 20,000.

8.4.4 THERMAL PERFORMANCE INDEX TP_{MOD}

This performance index is tailored for choosing geometries with a high heat transfer performance where a greater degree of frictional losses are acceptable as discussed in section 8.3.3.2. The TP_{mod} data for the HX samples is given in Figure 8.18. Here, the DIA N 2.5 mm sample provides the highest performance as a result of its increased Nu/Nu_0 and despite its high f/f_0. This geometry is also the highest performer in the AlSi10Mg sample set. The GYR N 2.5 mm sample provides a lower than expected TP_{mod} considering the performance of the other 2.5 mm cell size samples and is a result of its low Nu/Nu_0 performance. The GYR N geometry thins substantially at certain points through the cell,

which when coupled with the low thermal conductivity of HX, may produce areas with a high resistance to conductivity of heat. This thinning effect is exacerbated by reducing cell size with a constant volume fraction. As a consequence, the temperature gradient seen in this sample is likely to be steep, with a decreased convective heat transfer efficiency in the cells furthest away from the hot surface. This performance drop is not evident in the AlSi10Mg samples, which may be as a result of the high thermal conductivity of this material overcoming the bottleneck of the thin geometry. If this geometry was to be implemented at small cell sizes, some modifications to the unit cell may be made to increase the material thickness in these regions.

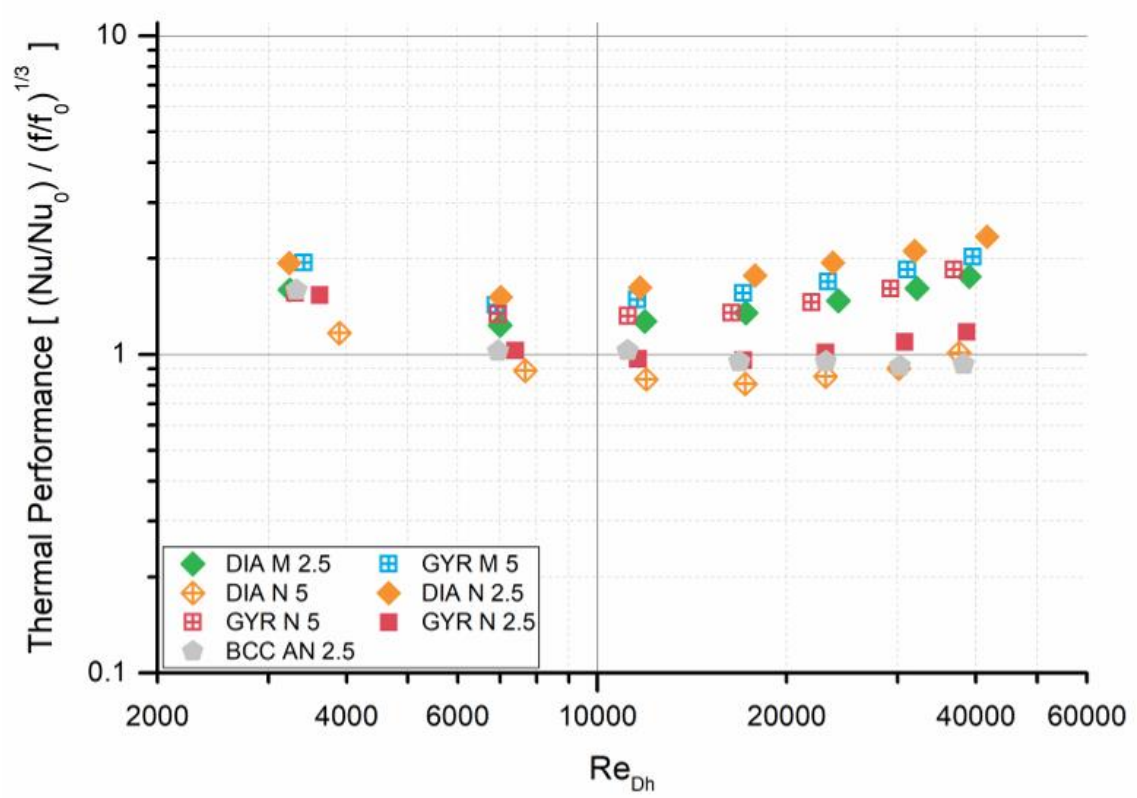


Figure 8.18 - Thermal performance metric TP_{mod} against Reynolds number for the HX lattice structure samples.

When comparing TP_{mod} results with those from the AlSi10Mg sample set, it can be seen that the performance delta is decreased compared to that for TP_{norm} (Figure 8.19). The TP_{mod} values of the HX samples are 23 % and 36 % of the AlSi10Mg for GYR M 5 mm and DIA N 2.5 mm respectively. Further, the HX samples all exceed the TP_{mod}

performance of the AlSi10Mg pin-fin benchmark by a minimum factor of 3. This demonstrates the capabilities of lattice structures for convective heat transfer in applications where frictional losses and therefore pressure drop are of less importance. Designers may now be able to specify a high specific strength alloy such as titanium in place of an aluminium alloy, where otherwise this may not be possible due to the low thermal performance of conventional heatsink designed manufactured in titanium alloys.

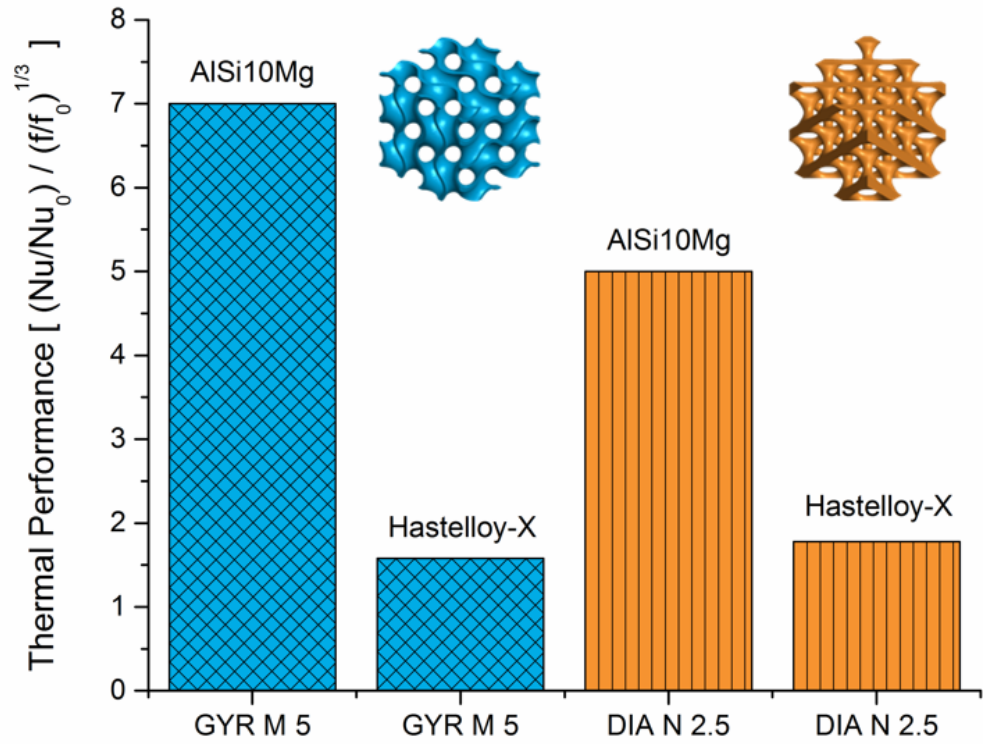


Figure 8.19 - Comparison of thermal performance index TP_{mod} between HX and AlSi10Mg for the GYR M 5 mm and DIA N 2.5 mm samples. All data taken at Re = 20,000

8.5 CONCLUSIONS

The convective heat transfer testing apparatus described in Chapter 6 was used to evaluate a total of 22 lattice structure samples across six unit cell types, three unit cell sizes, two materials and with size scales that are applicable to a wide range of components in a variety of engineering fields. It was shown that using thermal performance index TP_{mod}, the lattice structures provided significantly improved performance over pin-fins (10 – 20 times TP_{mod} increase). For applications where TP_{norm} is more applicable, the lattice structures provided a modest performance increase. The AlSi10Mg sample set showed improved performance over the HX sample set due to the high thermal conductivity of the base alloy and reduced surface roughness.

Through appropriate geometry and cell size choice, the lattice structures can be applied in a variety of applications irrespective of whether they require low pressure drop or maximum heat transfer performance (with high pressure drop penalty). The thermal performance achieved demonstrates the potential of TPMS lattice structures in high performance heat exchange applications, particularly where a high pressure drop is available. Here, convective heat transfer far exceeds that possible using a typical pin-fin geometry. For applications where pressure drop must be minimised, some network phase TPMS geometries are suitable but the argument for their implementation is less clear due to the added complexity in qualifying components that use lattice structures. Some practitioners may prefer to use well-understood pin-fins or straight channel heat exchangers. If methods are developed to reduce the surface roughness of internal geometry, it may be possible to improve the pressure drop of the geometries with the highest Nu, enabling their use in applications where only low pressure drop is acceptable. This may be via optimisation of LPBF process parameters for specific geometries or via post-processing. The thermal performance data provided here can serve as a toolbox for

design engineers in selection and implementation of lattice heat exchangers and this capability will be explored in the next Chapter.

For convective heat transfer applications, the following design recommendations are made:

- If a higher pressure drop is acceptable, choose matrix phase GYR lattices for enhanced heat transfer. Otherwise, choose network phase (DIA or GYR)
- If a higher pressure drop is acceptable, choose a smaller cell size where possible but be aware of system resolution limits – if cell size is designed too small, features will be manufactured oversize and pressure drop through the structure will increase as a result
- Where only low pressure drop is acceptable, choose the largest practical cell size for the dimensions of the region to be filled with lattice
- For low pressure drop applications, other geometries may be preferable for ease of verification. The additional benefits of lattice structures (mechanical performance, self-supporting in LPBF) should also be considered, however

Lattice structures can also provide additional mechanical performance over conventional heat exchange geometries, enhancing component value further if under thermomechanical loading. This is of particular interest for the aerospace industry, where mass of components and therefore specific properties are important. In this case, a lattice structure that provides equivalent TP to pin-fins, but using less material may be chosen. Alternatively, engine fuel efficiency may be increased by improving cooling performance and adding strength or stiffness without increasing weight. These aspects must be balanced and optimised for effective implementation of lattice structures for thermomechanical applications.

9 APPLICATION OF LATTICE STRUCTURES FOR HEAT TRANSFER

9.1 INTRODUCTION

Lattice structures have a high potential for application in heat transfer components as demonstrated in the previous Chapters. Practical insight regarding the introduction of this technology into complex engineering components is currently lacking, however. The experimental work described previously has characterised the heat transfer properties for a range of structures. In this Chapter, the data from this work was used to design and manufacture heat transfer components via LPBF. Lattice structures are used to incorporate heat transfer capability into three demonstrator components: a low-profile GPU heatsink representing applications in high-power electronics; a compact fluid-fluid heat exchanger; and a modified gas turbine nozzle guide vane. The designs presented here enable increases in performance alongside improved packaging, in both shape and volume, whilst minimising mass. This capability is evaluated in the case of the GPU, showing improved cooling performance whilst achieving a 90 % mass and 93 % volume reduction. As the understanding of and confidence in metal AM processes such as LPBF for manufacture of heat exchange components increases, the implementation of complex geometries such as lattice structures can begin to proliferate. To this end, this Chapter aims to provide a guide for the introduction of TPMS lattice structures into high value components.

9.2 APPLICATION CASE-STUDIES

9.2.1 LIGHTWEIGHT, SMALL-PACKAGE HEATSINK FOR ELECTRONIC CHIPS

The preface for this case study is given in the literature review, section 2.6.4.1, illustrating how cooling of electronic chips is limited by available package size and coolant fluid. Air cooling methods are performance limited by mass flow rates and pressures generated by bladed fans or centrifugal blowers. By using compressed air as the coolant, the pressure head of the supply can be increased and the performance of the heatsink improved through increasing the surface area available for heat transfer to the air.

In order to demonstrate the heat transfer capabilities of LPBF manufactured lattice structures, this case study uses a computer graphical processing unit (GPU) as an example of a high-power electronic chip. With the highest heat generation of any chip in a PC, the GPU requires a large conventional heatsink to ensure the die temperature does not exceed 100 °C. At this temperature, software limits are imposed that throttle the performance of the chip to reduce the temperature and prevent failure. The bulky stock heatsink (Figure 9.1) uses comparatively inefficient forced convection provided by an electronic fan with minimal ducting to direct the airflow through the finned heatsink and into the surroundings. The fins are manufactured from aluminium sheet, stamped into cross-sections and then mechanically fixed together using tabs (Figure 9.1 (a)). The fin array is in contact with heat pipes which are used to draw heat away from the GPU chip, via the surface plate, and distribute it evenly across the length of the fins. Heat pipes utilise phase change heat transfer, evaporating a coolant at the cold side, transporting the fluid through the pipe via a wick, and condensing it again at the cool side. This provides a heat transfer coefficient an order of magnitude or greater than standard forced convection heat transfer. Importantly, there is no metallurgical bonding between the surface plate, the heat pipes and the fin array (Figure 9.1 (b)). This impedes the efficiency of heat transfer away from

the GPU chip and into the coolant air when compared to the LPBF manufactured heatsink. Using LPBF, the heatsink can be formed as a solid block of aluminium with no barrier to heat flow between the GPU and the lattice.

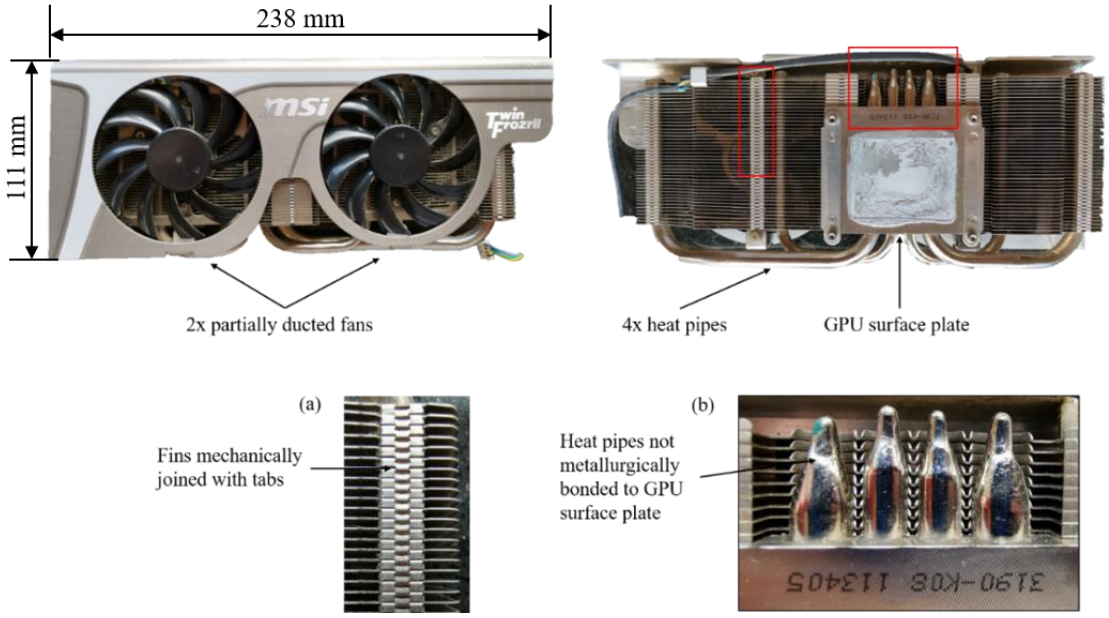


Figure 9.1 - The stock GPU heatsink with 2x fans for forced convection. Heat pipes draw heat away from the GPU which is in contact with the GPU surface plate. Heat transfer efficiency is impeded by the lack of metallurgical bond between the fins (a) and between the heat pipes and surface plate (b).

9.2.1.1 GPU HEATSINK DESIGN FOR LPBF

The stock heatsink was replaced by a low-profile aluminium block with an integrated lattice structure (Figure 9.2). The gyroid matrix lattice structure was chosen for its high heat transfer coefficient and fin-like structure which makes it ideal for short, wide heatsink applications. The high pressure drop associated with this lattice is offset by using a single channel through the heatsink rather than a snaking or S-shaped route, reducing the overall travel length of the fluid through the heatsink and minimising pressure drop. This parallel flow geometry also allows for a higher mass flow rate of air through the heatsink at any given pressure, increasing the available cooling power. An advantage of AM is the ability to grade the volume fraction (or amount of material per volume)

according to design requirements. In a heatsink that is conducting heat away from a surface and then transferring that heat to a fluid, the rate of heat transferred to the fluid is proportional to the difference in temperature between the heatsink and the fluid. This temperature difference is greatest at the hot surface, dropping as the distance from the surface increases. As you move away from the surface, less heat remains to be removed and hence the volume of material required to efficiently conduct this heat decreases. By linearly reducing the volume fraction of the lattice in the Z-direction (Figure 9.2), the mass, and therefore cost of the heatsink can be reduced whilst retaining heat transfer performance. In this instance, volume fraction grading also reduces the average pressure drop across the heatsink when compared to a constant volume fraction. Therefore, the coolant pumping power requirements are also reduced.

Table 9.1 - Properties of the GPU heatsinks analysed here. Note the difference in mass and volume between the stock and lattice heatsinks

	Mass (g)	Length (mm)	Width (mm)	Height (mm)	Volume (mm^3)	Surface area (mm^2)	SA:Vol
Stock heatsink	451	234	98	30	687960	173888	0.253
Lattice heatsink	81	71	61	10	43310	25838	0.597
Lightweight heatsink	49	71	61	10	43310	25838	0.597

The benefits of using a lattice structure heatsink in terms of mass and volume are evident from the data in Table 9.1. The mass of the lightweight lattice heatsink is < 10 % of that of the stock heatsink, a vast improvement for any application where mass results in a higher fuel burn. A lighter heatsink therefore acts to reduce cost. The significantly smaller volume, particularly the reduction in height from 30 mm to 10 mm, enables the GPU to be packaged much more efficiently. Surface-area-to-volume ratio data illustrates

how LPBF manufactured lattice structures can be used to create a heat transfer device that packs a very large surface area into a small casing. This is the key to achieving high performance for minimal mass and volume. Further, using a compressed air feed for the coolant that vents externally to the electronics enclosure ensures that the hot air passing through the heatsink is not directly dumped into the local environment of the GPU.

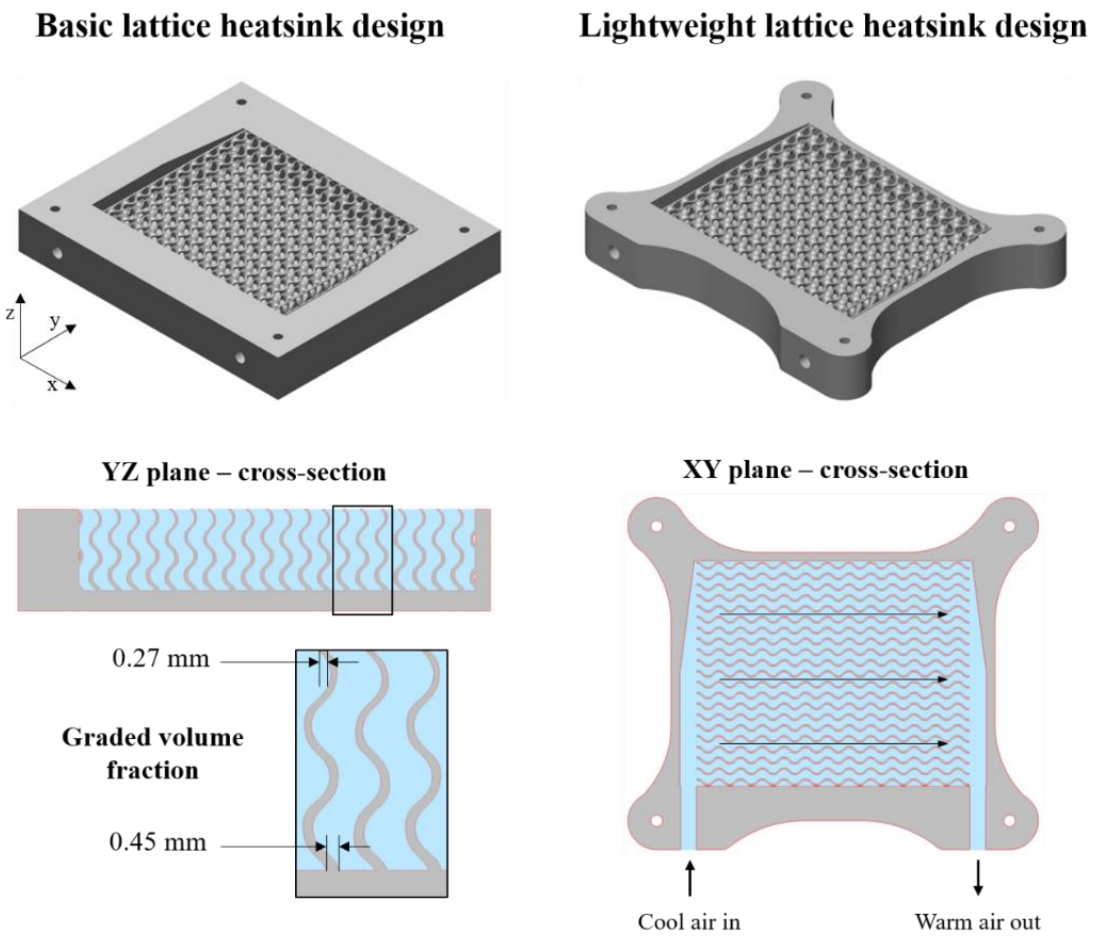


Figure 9.2 - Illustration of the lattice GPU heatsink design. A gyroid matrix lattice is used with a graded volume fraction in the Z-direction, from 30% at the hot surface to 15% at the top. Compressed air is supplied from a single inlet and travels across the heatsink in the X-direction.

9.2.1.2 GPU HEATSINK MANUFACTURE AND TESTING

The lattice heatsink was manufactured in AlSi10Mg via LPBF (Figure 9.3) (Renishaw AM250, laser power 200 W, point distance 80 µm, exposure time 140 µs, layer thickness 25 µm). To demonstrate the performance, graphical benchmark tests were performed with simultaneous temperature logging of the GPU die. The testing package GpuTest from Geeks3D includes GiMark geometry instancing test and PixMark Piano pixel shader test. Each test places a 100 % load condition on the GPU, representing the greatest possible thermal demands on the heatsink for this chip. The GPU was allowed to reach thermal steady state at idle (29 – 31 °C for stock heatsink, 24 – 26 °C for lattice heatsink) before each test was run for 60 s. After the test, a further 60 s period was recorded to trace the temperature response after the 100 % load condition was removed.

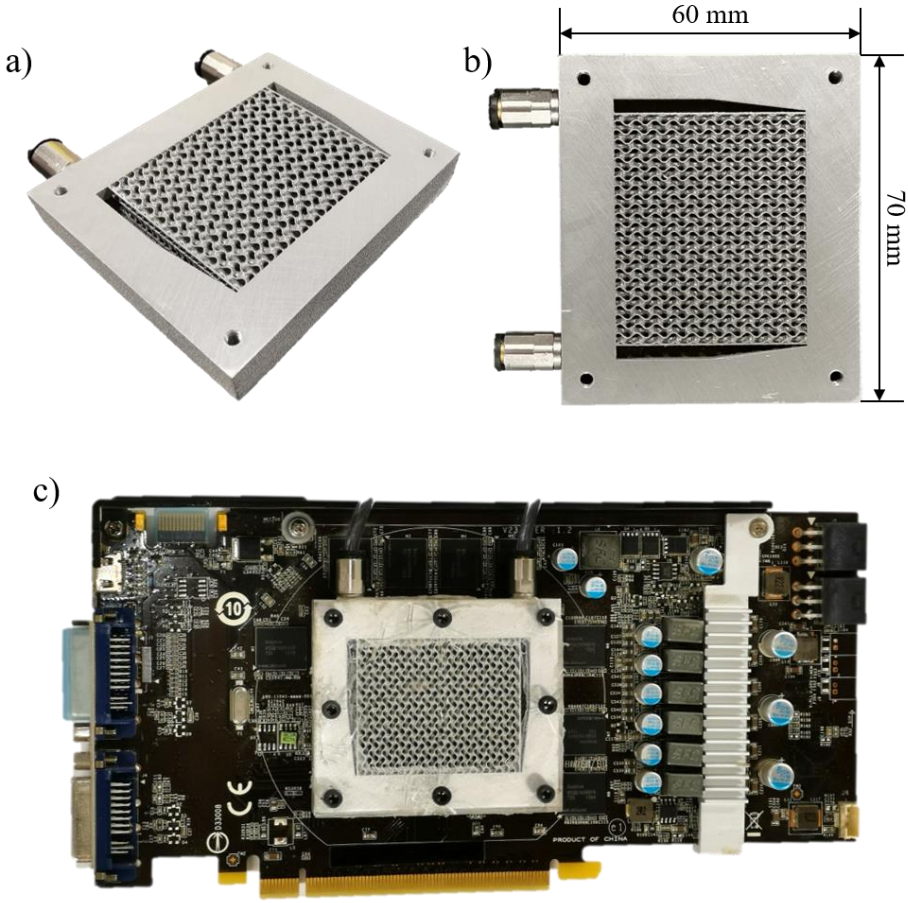


Figure 9.3 - AlSi10Mg lattice GPU heatsinks after manufacture via LPBF (a), (b). The heatsink as installed in place on the GPU is shown in (c). The small volume occupied by the heatsink is evident when compared to the stock heatsink.

The results of this testing can be seen in Figure 9.4, where the lattice heatsink improved on the cooling performance in both test cases with a reduction in maximum temperature of 2 °C in the GiMark benchmark. Further, the lattice heatsink provides better response to changes in load as indicated by the ramp-up and ramp-down of temperatures under switching loading conditions. At the start of each benchmark test, the stock heatsink undergoes a sharper positive temperature gradient than the lattice heatsink. After loading is removed, the GPU temperature returns to idle temperature within 60 s

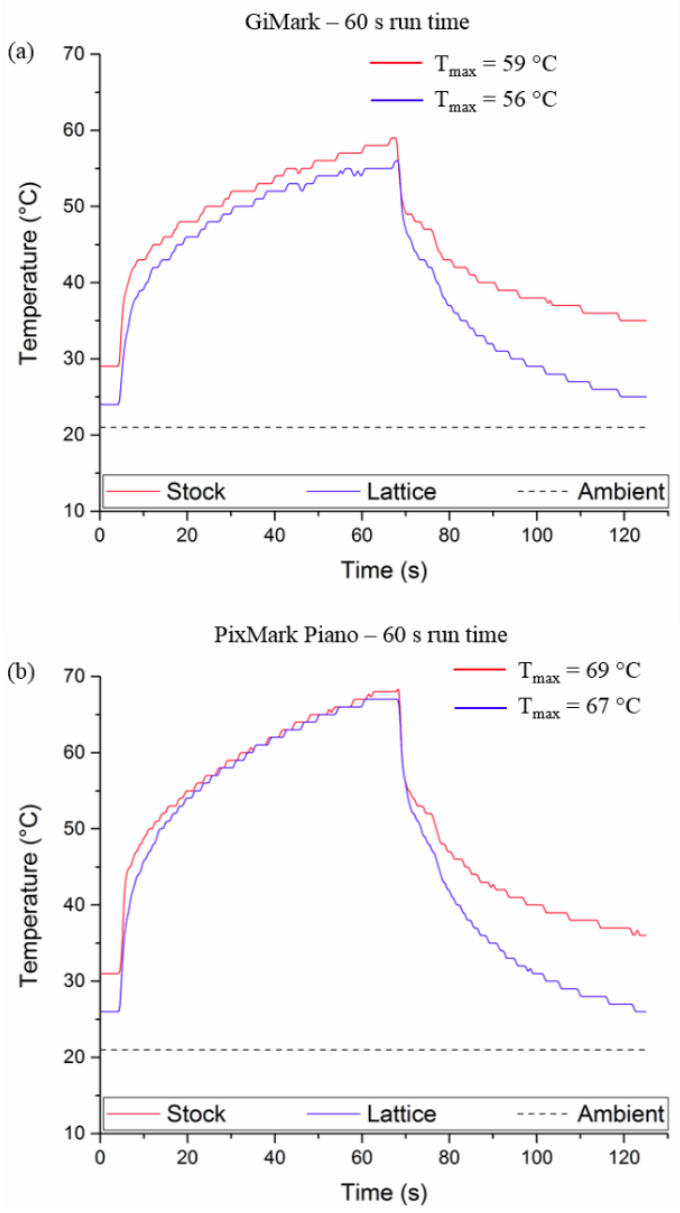


Figure 9.4 - Temperature vs. time plots comparing the stock heatsink (blue) to the lattice heatsink (orange) whilst running GiMark and PixMark Piano benchmarking tests. Throughout, ambient temperature is 21 °C.

using the lattice heatsink, whilst the stock heatsink remains $5 – 7$ °C above idle temperatures.

Whilst the temperature reductions seen here are not profound, this case study represents a non-optimised demonstration of the possibilities of using lattice structures as heatsinks for electronic chips. The reduction in size of the heatsink is particularly valuable for the electronics industry where packing constraints limit the performance of the cooling solution. Further, for applications in aerospace and automotive, a lattice-based heatsink may be useful where space is at a premium and any excess mass results in fuel efficiency losses and therefore cost increases. Utilising thermal modelling and optimisation studies, the geometry of the heatsink can be modified to ensure that the best performance is achieved. For some applications, a higher mass and volume may be permitted for higher heat transfer performance, for example if temperatures can be reduced by > 15 °C. In other cases, mass and volume may be minimised as a means of providing sufficient cooling power but with the smallest possible footprint for applications where component packing density is important.

9.2.2 GAS TURBINE NOZZLE GUIDE VANE WITH MODIFIED INTERNAL COOLING

In this case study, two base NGV geometries were explored – a single wall NGV section with an empty core region, and a double-wall NGV section with a narrow channel for heat transfer augmentation. The double wall example also features an open trailing edge. It is desirable to make the trailing edge as thin as possible for aerodynamic efficiency [205]. However, reducing the wall thickness comes at the risk of oxidisation reaching unsafe limits in this region, effectively burning through the walls of the vane, leading to failure. To prevent this, the thin trailing edge is protected from oxidation from the hot combustion gases impinging on the surface by ejecting coolant air through a slot. Addition of this slot typically requires ribs or 'lands' to retain the structural integrity of the NGV, which decrease the effectiveness of the cooling. By using lattice structures in the trailing edge region, the mechanical integrity is retained. The lattice also acts to turbulate the air exiting the slot in the same way as the pin-fins that are conventionally used. This use-case leverages the performance of lattice structures in heat transfer and mechanical (thermo-mechanical) loading. A further feature of the double wall NGV example is separation of the lattice region into sections dependent on the expected surface temperatures. This allows for individual coolant paths through the NGV, where a higher mass flow rate can be directed through the walls of hottest regions (leading edge, mid-span pressure side, trailing edge) whilst reducing the mass flow rate where cooling demands are not as high (vacuum side). Using the heat transfer performance data presented earlier, cooling strategies are presented that can provide enhancement over those present in classic NGV geometries. Three examples are then manufactured in a nickel superalloy via LPBF (Xi'an Bright Laser Technologies S210, laser power 195 W, scan speed 950 $mm.s^{-1}$, layer thickness 40 μm), demonstrating the feasibility of applying lattice structures in NGV designs.

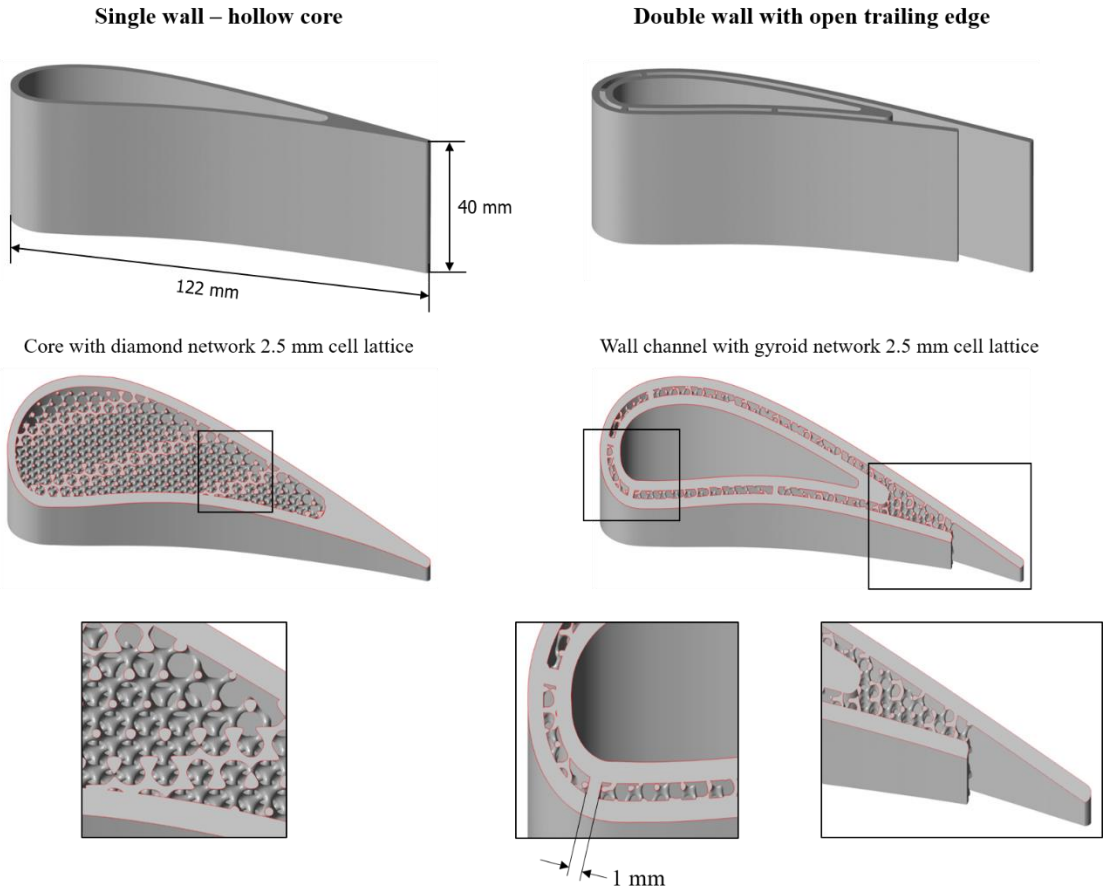


Figure 9.5 - Demonstration nozzle guide vane models: (a) a single wall geometry with a core region filled with diamond network lattice with constant volume fraction; (b) a double wall geometry with gyroid network lattice region sandwiched between the walls; (c) a trailing edge featuring a slot for film cooling.



Figure 9.6 - Demonstrator NGV sections manufactured in Inconel 718 superalloy via LPBF. These sections show the capability of incorporating fine lattice features into a high-value component.

Lattice structures may play an important part in advancing the cooling capabilities of turbine NGV. By replacing conventional features such as pin-fins that are largely limited by investment casting, new design possibilities can be explored. The thermo-mechanical performance of lattice structures presents the opportunity to create NGV sections with thinner walls than normally possible, especially in the trailing edge region where an aerodynamic advantage is gained from doing so. An important finding in this case-study is that of applying lattice structures to thin sections – in small gas turbine engines, the first stage NGV may well be too small to effectively implement lattice due to the resolution limits of the LPBF process. Lattice features below 150 µm are difficult to manufacture accurately and also may have lower mechanical properties than expected due to the inaccurate manufacture.

9.3 CONCLUSIONS

Laser powder bed fusion enables the manufacture of complex lattice structures that until now have mainly been utilised for mechanical performance enhancement. The case studies given in this Chapter demonstrate how TPMS lattice structures can also be used as heat transfer surfaces in a variety of applications. The potential for replacement of bulky conventional heatsinks for high-power electronic chips with lightweight, low-profile lattice heatsinks is attractive for the aerospace and automotive industry. However, design optimisation studies must be utilised to ensure that the required performance is achieved and the benefits of using lattice structures are fully exploited.

Gas turbine nozzle guide vanes may have significantly increased thermal and mechanical performance with the implementation of lattice structures. Pin-fins are a compromise based on manufacturing limits, which can be improved upon through optimisation of lattice structures for heat transfer in these high-temperature environments. LPBF overall is an important manufacturing advancement for this industry, but there are many problems that must be addressed before critical components such as an NGV or turbine blade are used in service. Overall, lattice structures present an opportunity for improvements in a wide range of components that require heat transfer, however optimisation will play an important role in ensuring maximum performance is obtained.

10 CONCLUSIONS AND FUTURE WORK

10.1 FINAL CONCLUSIONS

The LPBF process has unique capabilities that see its increasing adoption across high-value industries. It enables manufacture of components with a high degree of complexity and with performance enhancing features that cannot be made in any other way. One example of such complexity is lattice structures, that beyond proof of concept parts, are to date mainly used to reduce component mass. Existing academic and industrial research has developed lattice structure knowledge in the area of mechanical performance, but their potential in heat transfer applications had not been explored. This may be due to the non-standard apparatus required for experimental evaluation of these structures. It was proposed that a new method for evaluating heat transfer in additively manufactured structures was required. Both a conductive and convective heat transfer apparatus was built for this purpose. This study has shown that through development of such apparatus, the performance of lattice structures in thermal conductivity and convective heat transfer can be characterised. Thermal evaluation was performed alongside mechanical testing of samples in the Hastelloy-X, creating a toolbox of performance characteristics that can be used for design of components under thermomechanical loading.

The fundamentals of LPBF manufacture were explored in Chapter 4 – process parameter development. Attempts were made to develop novel scan strategies for manufacture of a Ni-alloys that is considered unweldable, using fractal or area filling curves. Ultimately it was not possible to achieve acceptable material quality in this alloy. Fractal scan strategies for metal LPBF were demonstrated experimentally and solid samples were successfully manufactured (albeit with cracking, but this is a material-dependent problem). Further, knowledge on the cracking phenomena in LPBF was improved, with it being shown that the order in which a scan strategy is followed can

result in specific areas having a higher propensity for cracking. This is an important finding for further process development of unweldable alloys or others that also suffer from high thermally induced stresses as a result of the rapid cooling in the LPBF process. It can also be used to inform how scan strategies should be modified depending upon geometrical features. For example, an intersection between two scan regions should not be placed at sharp corners in any build layer, to prevent concentration of residual stresses.

Mechanical testing in Chapter 5 demonstrated the effect of HIP + HT on the performance of the bulk alloy and lattice structure samples. The microstructure of as-LPBF material is not desirable in many applications due to degraded creep and fatigue performance that decrease the service life of a component. HT cycles are used to increase the grain size and homogenise the grain structure of the material, but as a result, the compressive yield strength of the bulk material was decreased by >38 %. Further, the lattice structure modulus and yield strength values were also decreased, but importantly, mechanical behaviour could be dictated through choice of geometry. The knowledge gained here was that mechanical performance of lattice structures is driven by both material condition (with or without HT) and geometry. Therefore, consideration of both must be made for implementation of lattice structures in components.

Chapter 6 outlined the design and manufacture of custom thermal testing apparatus to determine thermal conductivity and convective heat transfer performance of lattice structures. ASTM standards guided the design for the thermal conductivity testing apparatus but was the first apparatus seen in the literature for measurement of lattice structure properties. Although it is based upon an ASTM standard, it will provide other researchers with knowledge in how to measure similar samples in this way.

No standard was identified for convective heat transfer evaluation. Hence, a review of the existing apparatus in the literature was used to guide the design of a new apparatus,

but with modifications for the specific sample geometries and size scale required for this work. The apparatus were successful and performed as expected and demonstrate a suitable overall design for evaluation of lattice structures that can be used to inform other researchers in designing similar apparatus.

The thermal conductivity properties of a range of lattice structures were determined in Chapter 7. The thermal conductivity value of the material used for manufacture was found to be the biggest driver for lattice thermal conductivity, however some interesting geometrical effects were also discussed. The knowledge gained here was that structures with thicker walls or struts, and larger connected internal void regions, provide a higher effective thermal conductivity. This is due in part to internal natural convection currents, a finding that validated the use of experimental measurement of thermal conductivity as this second order effect could have been easily missed in computer simulations if CFD was not implemented. Using the data from this Chapter, design engineers can specify custom thermal profile components for either high conductivity, or for heat shielding applications. This is a unique capability for TPMS structures that was made possible from this work.

In Chapter 8, convective heat transfer performance of the lattice structures was demonstrated. This is the most important work in this thesis and has the potential to enable increased performance of heat exchange components across a range of industries. It was shown that at nearly 100 % of the flow conditions tested, TPMS lattice structures exceeded the performance of a pin-fin benchmark sample. This indicates that lattice structures are a real candidate to replace conventional heat transfer geometries when manufacturing via AM. AlSi10Mg and HX alloys were evaluated, showing how performance curves for the geometries are shifted in the Y-axis when the thermal properties of the base alloy is changed. The knowledge gained from the samples in these alloys could then be extended to other alloys as required, enhancing the value of the

experimental data. Further, the distinction was made between applications where pressure drop is important, and those where pressure drop can be sacrificed for improved thermal performance. Using performance metrics that account for this, recommendations for TPMS geometries were made that aim to expedite the choice of lattice structure when developing a component.

Finally, in Chapter 9, three case study components using lattice structures were given. Despite the overall focus on the gas turbine industry in this thesis, it was important to demonstrate how wide the applicability of lattice structures is. Hence, the case studies focussed on a heatsink for high-power electronic chips and a gas turbine NGV with modified internal cooling passages. Experimental evaluation of the electronic chip heatsink resulted in an improved performance over the stock heatsink, whilst allowing 90 % reduction in mass and 94 % reduction in volume. This showcases the capabilities of LPBF manufacture for high-performance heatsinks. The custom NGV cooling channels would represent a complete revision of existing designs, replacing pin-fins and ribs with a lattice structure, made possible by LPBF. The important element in this design is that the lattice structure also aids the mechanical integrity of the component – secondary design improvements may be possible by implementing lattice structures, such as reduction of wall thickness that were previously required for strength. Not only can the component be made lighter, but the surface temperatures will also be decreased as the internal cooling effectiveness increases with proximity to the hot surface.

This thesis developed the use-case for TPMS lattice structures in thermomechanical applications. Through demonstrating how TPMS structures are superior to strut-type lattices in mechanical performance, and to conventional geometries such as the pin-fin in heat transfer, it is hoped that incorporation of these structures in end-use components will be accelerated. By evaluating the performance of these geometries experimentally, the data now exists to build computational models of the complex TPMS structures in heat

transfer with a higher degree of confidence. This is an important step as without a robust digital modelling and optimisation platform, design iterations of high-value components would not be possible.

10.2 FUTURE WORK

Several areas of future work have been identified from the work in this thesis:

Regarding the fractal scan strategies in Chapter 4, it would be interesting to process an alloy that is more suitable for LPBF using this method to determine the effect on residual stress. This would not be a robust experiment for the CM247LC samples as a proportion of the residual stress is relieved through cracking. Ti6Al4V would be a good candidate for this – existing process parameters can prevent the material from cracking and de-laminating in LPBF, but the remaining residual stresses are sufficiently large that, in many cases, it is mandatory for components to undergo stress relief heat treatment prior to removal from the build platform. Cantilever specimens such as those by Kruth et al. [97] would be a relatively trivial first step in assessing any benefit of fractal scan strategies for stress relief.

If single crystal alloys could be manufactured successfully via LPBF then printing of first-stage turbine blades with current-class component life expectancy would be feasible. This may be achieved by using a single crystal seed in the LPBF machine base plate, through controlled cooling rates via inductive cooling or with multiple lasers dedicated to maintaining high temperatures during printing. Single crystal lattice structures would present an ideal geometry for lightweight components in all manner of high-temperature environments where creep is important. The type of controlled cooling required for single crystal manufacture may also be transferrable to ceramic matrix composites or bulk metallic glasses in LPBF. LPBF would represent a step-change in the geometric complexity possible using these material systems.

For thermal conductivity, targeting geometries for thermal insulation or isolation would be of interest. This may include modification of the lattice structures to enclose internal volumes, preventing natural convection currents from increasing the effective thermal conductivity of the structure. The network phase TPMS structures may also be of use here as they can be manufactured at lower volume fractions without minimum features sizes falling below the resolution limits of LPBF. The geometries investigated here could also be manufactured in alternative materials that are chosen for thermal insulation properties, for example alumina or a similar ceramic. This would also require a different manufacturing method such as ceramic loaded stereolithography (SLA) or binder jetting as these materials are not yet manufacturable via LPBF. However, some thermal control methods outlined above, in combination with new laser technology that can target the peak absorptivity levels of these materials, may make LPBF a feasible option. Applications for such structures may be high-temperature components for the nuclear or defence industry, or low temperature components in cryogenic applications such as storage tanks for liquid fuels in rocket propulsion.

Regarding the convective heat transfer evaluation of lattice structures, a second-generation testing apparatus with high-temperature capability (~500 °C) would be of interest. These structures have the most potential in high-temperature applications and therefore it is important to characterise their performance at near the intended operating temperature. A future application of such structures may be regeneratively cooled rocket nozzles where the cryogenic temperature fuel loops through a lattice structure sandwich structure that makes up the nozzle walls. Additionally, manufacture of lattice structures in materials with high thermal conductivity, such as copper alloys, would demonstrate the maximum performance of these structures. With the possibility of manufacturing small components in copper alloys using binder jet processes at a far lower cost than LPBF, lattice structure heat exchangers in the electronics industry may be economically viable

in some applications. Further, LPBF material quality is more desirable than that of binder jetting due to increased density (lower porosity). As a result, LPBF manufacture of a number of lower cost components would be possible.

Evaluation of graded volume fraction lattice structures may also be of interest to maximise thermal performance whilst minimising component mass. This was not included in this thesis as it would add too many variables for experimentation, however these structures are trivial to design and manufacture using existing software tools. This work could also include optimising the wall thickness of the matrix phase TPMS structures for maximum heat transfer performance. Further design features could be included such as constraining flows within the structure by blocking movement of fluid through the unit cells in one direction. This was explored somewhat in the NGV case-study in this thesis but would require real operating condition data to enable design to target specific performance regimes. Alongside volume fraction grading, unit cell type grading could also be explored, moving from a high pressure drop, high performance structure in one region, to a low pressure drop structure where heat transfer demands are lower. Shape memory alloys may pose an interesting design possibility with lattice structure channels, where flow of coolant may be controlled passively by ‘valves’ actuated by change in temperature. This may dynamically change the hydraulic diameter of the structure to provide the cooling performance needed to maintain a constant component temperature.

Development of CFD models for the lattice structure convective heat transfer work is the logical next step from a simulation perspective. This is beyond the scope of this thesis and hence was not explored, but the experimental data given here can be used to validate the models. With this, the design of components using lattice structures could be iterated at a faster rate than is possible using experimental work, and optimisation tools can be used to automatically vary volume fraction or unit cell to provide the highest

performance. However, development of methodologies to reduce the computational requirements of simulating flow within complex geometries may be required; currently, CFD of models beyond a small number of unit cells is very computationally expensive and limits the design of components with large volumes of lattice structures that are non-uniform.

REFERENCES

1. Kruth, J.-P., X. Wang, T. Laoui, and L. Froyen, *Lasers and materials in selective laser sintering.* Assembly Automation, 2003. **23**(4): p. 357-371.

2. Schmidt, M., D. Pohle, and T. Rechtenwald, *Selective laser sintering of PEEK.* CIRP annals, 2007. **56**(1): p. 205-208.

3. Raja, B. K., R. J. P. Raja, K. Karan, R. Soundararajan, and P. Ashokavarthanan, *Parameter Optimization for Polyamide in Selective Laser Sintering Based on Mechanical Behavior*, in *3D Printing and Additive Manufacturing Technologies*. 2019, Springer. p. 217-231.

4. Special Metals Corporation, *INCONEL alloy 625*. 2013.

5. King, W. E., A. T. Anderson, R. Ferencz, N. Hodge, C. Kamath, S. A. Khairallah, and A. M. Rubenchik, *Laser powder bed fusion additive manufacturing of metals; physics, computational, and materials challenges.* Applied Physics Reviews, 2015. **2**(4): p. 041304.

6. Rosen, D. W., *Research supporting principles for design for additive manufacturing: This paper provides a comprehensive review on current design principles and strategies for AM.* Virtual and Physical Prototyping, 2014. **9**(4): p. 225-232.

7. Jared, B. H., M. A. Aguilo, L. L. Beghini, B. L. Boyce, B. W. Clark, A. Cook, B. J. Kaehr, and J. Robbins, *Additive manufacturing: Toward holistic design.* Scripta Materialia, 2017. **135**: p. 141-147.

8. Hossain, M. S., J. A. Gonzalez, R. M. Hernandez, M. a. I. Shuvo, J. Mireles, A. Choudhuri, Y. Lin, and R. B. Wicker, *Fabrication of smart parts using powder bed fusion additive manufacturing technology.* Additive Manufacturing, 2016. **10**: p. 58-66.

9. Salmi, A., F. Calignano, M. Galati, and E. Atzeni, *An integrated design methodology for components produced by laser powder bed fusion (L-PBF) process.* Virtual and Physical Prototyping, 2018. **13**(3): p. 191-202.

10. Kantareddy, S., B. Roh, T. Simpson, S. Joshi, C. Dickman, and E. Lehtihet. *Saving weight with metallic lattice structures: Design challenges with a real-world example*. in *Proceedings of the Solid Freeform Fabrication Symposium*. 2016.

11. Yang, L., O. Harrysson, D. Cormier, H. West, S. Zhang, H. Gong, and B. Stucker. *Design for additively manufactured lightweight structure: a perspective*. in *Proceedings of the Solid Freeform Fabrication Symposium*. 2016.

12. Schmelzle, J., E. V. Kline, C. J. Dickman, E. W. Reutzel, G. Jones, and T. W. Simpson, *(Re) Designing for part consolidation: understanding the challenges of metal additive manufacturing.* Journal of Mechanical Design, 2015. **137**(11): p. 111404.

13. Hällgren, S., L. Pejryd, and J. Ekengren, *Additive Manufacturing and High Speed Machining-Cost comparison of short lead time manufacturing methods.* Procedia CIRP, 2016. **50**: p. 384-389.

14. Gibson, I., D. W. Rosen, and B. Stucker, *Additive Manufacturing Technologies : Rapid Prototyping to Direct Digital Manufacturing*. 2009, Springer.

15. Ciobota, N.-D., *Standard tessellation language in rapid prototyping technology*, in *The Scientific Bulletin of Valahia University – Materials and Mechanics*. 2012.

16. Tanaka, H. *New File Format for 3D Printing, its extensions and applications*. in *NIP & Digital Fabrication Conference*. 2015. Society for Imaging Science and Technology.

17. Iancu, C., *About 3MF file format for 3D printing.* Fiability and Durability, 2019(1).

18. Iancu, C., *About 3D printing file formats.* Annals of the Constantin Brancusi University of Targu Jiu-Letters & Social Sciences Series, 2018(2).

19. Gaynor, A. T., N. A. Meisel, C. B. Williams, and J. K. Guest. *Topology optimization for additive manufacturing: considering maximum overhang constraint*. in *15th AIAA/ISSMO Multidisciplinary Analysis and Optimization Conference*. 2014.

20. Zwier, M. P. and W. W. Wits, *Design for additive manufacturing: Automated build orientation selection and optimization.* Procedia CIRP, 2016. **55**: p. 128-133.

21. Gaynor, A. T. and J. K. Guest, *Topology optimization considering overhang constraints: Eliminating sacrificial support material in additive manufacturing through design.* Structural and Multidisciplinary Optimization, 2016. **54**(5): p. 1157-1172.

22. Pham, D. T. and R. S. Gault, *A comparison of rapid prototyping technologies.* International Journal of machine tools and manufacture, 1998. **38**(10-11): p. 1257-1287.

23. Karapatis, N., J. Van Griethuysen, and R. Glardon, *Direct rapid tooling: a review of current research.* Rapid prototyping journal, 1998. **4**(2): p. 77-89.

24. Gibson, I., T. Kvan, and L. Wai Ming, *Rapid prototyping for architectural models.* Rapid Prototyping Journal, 2002. **8**(2): p. 91-95.

25. Yan, X. and P. Gu, *A review of rapid prototyping technologies and systems.* Computer-Aided Design, 1996. **28**(4): p. 307-318.

26. Bellini, A. and S. Güçeri, *Mechanical characterization of parts fabricated using fused deposition modeling.* Rapid Prototyping Journal, 2003. **9**(4): p. 252-264.

27. Hull, C. W., *Apparatus for production of three-dimensional objects by stereolithography,* 1986, Patent number US5059359A

28. Jacobs, P. F., *Rapid prototyping & manufacturing: fundamentals of stereolithography*. 1992: Society of Manufacturing Engineers.

29. Jacobs, P. F. *Fundamentals of stereolithography*. in *Proceedings of the Solid Freeform Fabrication Symposium*. 1992.

30. Maskery, I., A. O. Aremu, M. Simonelli, C. Tuck, R. D. Wildman, I. A. Ashcroft, and R. J. M. Hague, *Mechanical Properties of Ti-6Al-4V Selectively Laser Melted Parts with Body-Centred-Cubic Lattices of Varying cell size.* Experimental Mechanics, 2015. **55**(7): p. 1261-1272.

31. Simonelli, M., Y. Y. Tse, and C. Tuck, *On the Texture Formation of Selective Laser Melted Ti-6Al-4V.* Metallurgical and Materials Transactions A, 2014. **45**(6): p. 2863-2872.

32. Garibaldi, M., I. Ashcroft, M. Simonelli, and R. Hague, *Metallurgy of high-silicon steel parts produced using Selective Laser Melting.* Acta Materialia, 2016. **110**: p. 207-216.

33. Liu, B., *Further process understanding and prediction on selective laser melting of stainless steel 316L*. 2013, Loughborough University.

34. Mumtaz, K. A., P. Erasenthiran, and N. Hopkinson, *High density selective laser melting of Waspaloy®.* Journal of Materials Processing Technology, 2008. **195**(1–3): p. 77-87.

35. Vilaro, T., C. Colin, J. D. Bartout, L. Nazé, and M. Sennour, *Microstructural and mechanical approaches of the selective laser melting process applied to a nickel-base superalloy.* Materials Science and Engineering: A, 2012. **534**: p. 446-451.

36. Aboulkhair, N. T., N. M. Everitt, I. Ashcroft, and C. Tuck, *Reducing porosity in AlSi10Mg parts processed by selective laser melting.* Additive Manufacturing, 2014. **1–4**: p. 77-86.

37. Aboulkhair, N. T., I. Maskery, C. Tuck, I. Ashcroft, and N. M. Everitt, *The microstructure and mechanical properties of selectively laser melted AlSi10Mg: The effect of a conventional T6-like heat treatment.* Materials Science and Engineering: A, 2016. **667**: p. 139-146.

38. Boig, C., *The Application of Additive Manufacturing to Nickel-Base Superalloys for Turbocharger Applications*. 2019, University of Sheffield.

39. Mullen, L., R. C. Stamp, W. K. Brooks, E. Jones, and C. J. Sutcliffe, *Selective Laser Melting: A regular unit cell approach for the manufacture of porous, titanium, bone in-growth constructs, suitable for orthopedic applications.* Journal of Biomedical Materials Research B: Applied Biomaterials, 2009. **89B**(2): p. 325-334.

40. Nakano, T. and T. Ishimoto, *Powder-based additive manufacturing for development of tailor-made implants for orthopedic applications.* KONA Powder and Particle Journal, 2015. **32**: p. 75-84.

41. Liu, R., Z. Wang, T. Sparks, F. Liou, and J. Newkirk, *Aerospace applications of laser additive manufacturing.* Laser Additive Manufacturing, 2017: p. 351-371.

42. Brøtan, V., O. Å. Berg, and K. Sørby, *Additive manufacturing for enhanced performance of molds.* Procedia CIRP, 2016. **54**: p. 186-190.

43. Klocke, F., K. Arntz, M. Teli, K. Winands, M. Wegener, and S. Oliari, *State-of-the-art laser additive manufacturing for hot-work tool steels.* Procedia CIRP, 2017. **63**: p. 58-63.

44. Badini, C., D. E. Padovano, D. F. D'aiuto, and G. Di Matteo, *Selective laser melting aluminum alloys for automotive component*. 2018, Politecnico di Torino.

45. Weller, C., R. Kleer, and F. T. Piller, *Economic implications of 3D printing: Market structure models in light of additive manufacturing revisited.* International Journal of Production Economics, 2015. **164**: p. 43-56.

46. Hague, R. and P. Reeves, *Additive manufacturing and 3D printing.* Ingenia, 2013. **55**: p. 39-40.

47. Baumers, M., P. Dickens, C. Tuck, and R. Hague, *The cost of additive manufacturing: machine productivity, economies of scale and technology-push.* Technological Forecasting and Social Change, 2016. **102**: p. 193-201.

48. Fu, W., C. Haberland, E. Klapdor, D. Rule, and S. Piegert, *Streamlined frameworks for advancing metal based additive manufacturing technologies.* Journal of the Global Power and Propulsion Society, 2018.

49. Sims, C. T., *A history of superalloy metallurgy for superalloy metallurgists.* Superalloys, 1984. **1984**: p. 399-419.

50. Badran, O. O., *Gas-turbine performance improvements.* Applied Energy, 1999. **64**(1-4): p. 263-273.

51. Reed, R. C. and C. M. F. Rae, *Physical Metallurgy of the Nickel-Based Superalloys.* Physical Metallurgy 2014: p. 2215-2290.

52. Furrer, D. and H. Fecht, *Ni-based superalloys for turbine discs.* Journal of Materials, 1999. **51**(1): p. 14-17.

53. Harris, K., G. Erickson, S. Sikkenga, W. Brentnall, J. Aurrecoechea, and K. Kubarych, *Development of the rhenium containing superalloys CMSX-4® & CM 186 LC® for single crystal blade and directionally solidified Vane applications in advanced turbine engines.* Superalloys 1992, 1992. **297**.

54. Pask, G., *Turbine shroud and turbine shroud assembly*, 1985, Patent number US4551064A

55. Lee, C. S., *Hardening mechanisms in a cobalt-base superalloy*. 1966, The University of Arizona.

56. Mouritz, A. P., *Introduction to aerospace materials*. 2012: Elsevier.

57. Sims, C. T., *A history of superalloy metallurgy for superalloy metallurgists.* Superalloys, 1984.

58. Jena, A. K. and M. C. Chaturvedi, *The role of alloying elements in the design of nickel-base superalloys.* Journal of Materials Science, 1984. **19**(10): p. 3121-3139.

59. Al-Jarba, K. and G. Fuchs, *Carbon-containing single-crystal nickel-based superalloys: segregation behavior and carbide formation.* Journal of Materials, 2004. **56**(9): p. 50-55.

60. Liu, L. R., T. Jin, N. R. Zhao, X. F. Sun, H. R. Guan, and Z. Q. Hu, *Formation of carbides and their effects on stress rupture of a Ni-base single crystal superalloy.* Materials Science and Engineering: A, 2003. **361**(1): p. 191-197.

61. Fu, H. Z. and L. Liu. *Progress of directional solidification in processing of advanced materials*. in *Proceedings of the Materials Science Forum*. 2005.

62. Wagner, A., B. Shollock, and M. Mclean, *Grain structure development in directional solidification of nickel-base superalloys.* Materials Science and Engineering: A, 2004. **374**(1-2): p. 270-279.

63. Koizumi, Y., T. Kobayashi, T. Yokokawa, J. Zhang, M. Osawa, H. Harada, Y. Aoki, and M. Arai, *Development of next-generation Ni-base single crystal superalloys.* Superalloys 2004, 2004: p. 35-43.

64. Caron, P. and T. Khan, *Evolution of Ni-based superalloys for single crystal gas turbine blade applications.* Aerospace Science and Technology, 1999. **3**(8): p. 513-523.

65. Rongzhang, C., *Development status of single crystal superalloys [J]*. Journal of Materials Engineering, 1995. **8**.

66. Harris, K., G. Erickson, and R. Schwer. *MAR M 247 Derivations—CM 247 LC DS Alloy, CMSX® Single Crystal Alloys, Properties and Performance*. in *5th International Symposium on Superalloys*. 1984.

67. Huang, H.-E. and C.-H. Koo, *Characteristics and Mechanical Properties of Polycrystalline CM 247 LC Superalloy Casting.* Materials Transactions, 2004. **45**(2): p. 562-568.

68. Henderson, M., D. Arrell, R. Larsson, M. Heobel, and G. Marchant, *Nickel based superalloy welding practices for industrial gas turbine applications.* Science and Technology of Welding and Joining, 2004. **9**(1): p. 13-21.

69. The International Nickel Company Inc., *Alloy IN-738 Technical Data*. 1997.

70. Wahl, J. and K. Harris, *Advanced Ni base superalloys for small gas turbines.* Canadian Metallurgical Quarterly, 2011. **50**(3): p. 207-214.

71. Neonickel, *Alloy C263 Technical Datasheet*. 2019.

72. Neonickel, *Rene 41 Technical Datasheet*. 2019.

73. Carter, L. N., M. M. Attallah, and R. C. Reed, *Laser Powder Bed Fabrication of Nickel-Base Superalloys: Influence of Parameters; Characterisation, Quantification and Mitigation of Cracking.* Superalloys 2012, 2012: p. 577-586.

74. Kunze, K., T. Etter, J. Grässlin, and V. Shklover, *Texture, anisotropy in microstructure and mechanical properties of IN738LC alloy processed by selective laser melting (SLM).* Materials Science and Engineering: A, 2015. **620**: p. 213-222.

75. Zhao, X., X. Lin, J. Chen, L. Xue, and W. Huang, *The effect of hot isostatic pressing on crack healing, microstructure, mechanical properties of Rene88DT superalloy prepared by laser solid forming.* Materials Science and Engineering: A, 2009. **504**(1–2): p. 129-134.

76. Zhao, J.-C., M. Larsen, and V. Ravikumar, *Phase precipitation and time–temperature-transformation diagram of Hastelloy X.* Materials Science and Engineering: A, 2000. **293**(1-2): p. 112-119.

77. Aquaro, D. and M. Pieve, *High temperature heat exchangers for power plants: Performance of advanced metallic recuperators.* Applied Thermal Engineering, 2007. **27**(2-3): p. 389-400.

78. Nguyen, O. and S. Samuelsen. *The effect of discrete pilot hydrogen dopant injection on the lean blowout performance of a model gas turbine combustor*. in *ASME 1999 International Gas Turbine and Aeroengine Congress and Exhibition*. 1999. American Society of Mechanical Engineers Digital Collection.

79. Wozaldo, G. and W. L. Pearl, *General corrosion of stainless steels and nickel base alloys exposed isothermally in superheated steam.* Corrosion, 1965. **21**(11): p. 355-369.

80. Wang, F., X. H. Wu, and D. Clark, *On direct laser deposited Hastelloy X: dimension, surface finish, microstructure and mechanical properties.* Materials Science and Technology, 2011. **27**(1): p. 344-356.

81. Wang, F., *Mechanical property study on rapid additive layer manufacture Hastelloy® X alloy by selective laser melting technology.* The International Journal of Advanced Manufacturing Technology, 2011. **58**(5): p. 545-551.

82. Tomus, D., T. Jarvis, X. Wu, J. Mei, P. Rometsch, E. Herny, J.-F. Rideau, and S. Vaillant, *Controlling the microstructure of Hastelloy-X components manufactured by Selective Laser Melting.* Physics Procedia, 2013. **41**: p. 823-827.

83. Abuzaid, W. Z., M. D. Sangid, J. D. Carroll, H. Sehitoglu, and J. Lambros, *Slip transfer and plastic strain accumulation across grain boundaries in Hastelloy X.* Journal of the Mechanics and Physics of Solids, 2012. **60**(6): p. 1201-1220.

84. Tomus, D., P. A. Rometsch, M. Heilmaier, and X. Wu, *Effect of minor alloying elements on crack-formation characteristics of Hastelloy-X manufactured by selective laser melting.* Additive Manufacturing, 2017. **16**: p. 65-72.

85. Harrison, N. J., I. Todd, and K. Mumtaz, *Reduction of micro-cracking in nickel superalloys processed by Selective Laser Melting: A fundamental alloy design approach.* Acta Materialia, 2015. **94**: p. 59-68.

86. Pourbabak, S., M. L. Montero-Sistiaga, D. Schryvers, J. Van Humbeeck, and K. Vanmeensel, *Microscopic investigation of as built and hot isostatic pressed Hastelloy X processed by Selective Laser Melting.* Materials Characterization, 2019. **153**: p. 366-371.

87. Rosenthal, S., S. Platt, R. Hölker-Jäger, S. Gies, S. Kleszczynski, A. E. Tekkaya, and G. Witt, *Forming properties of additively manufactured monolithic Hastelloy X sheets.* Materials Science and Engineering: A, 2019. **753**: p. 300-316.

88. Louvis, E., P. Fox, and C. J. Sutcliffe, *Selective laser melting of aluminium components.* Journal of Materials Processing Technology, 2011. **211**(2): p. 275-284.

89. Kruth, J.-P., L. Froyen, J. Van Vaerenbergh, P. Mercelis, M. Rombouts, and B. Lauwers, *Selective laser melting of iron-based powder.* Journal of Materials Processing Technology, 2004. **149**(1-3): p. 616-622.

90. Sadowski, M., L. Ladani, W. Brindley, and J. Romano, *Optimizing quality of additively manufactured Inconel 718 using powder bed laser melting process.* Additive Manufacturing, 2016. **11**: p. 60-70.

91. Li, S., Q. Wei, Y. Shi, Z. Zhu, and D. Zhang, *Microstructure characteristics of Inconel 625 superalloy manufactured by selective laser melting.* Journal of Materials Science & Technology, 2015. **31**(9): p. 946-952.

92. Yasa, E., J. Deckers, T. Craeghs, M. Badrossamay, and J.-P. Kruth. *Investigation on occurrence of elevated edges in selective laser melting*. in *International Solid Freeform Fabrication Symposium, Austin, TX, USA.* 2009.

93. Biffi, C., J. Fiocchi, and A. Tuissi, *Selective laser melting of AlSi10 Mg: Influence of process parameters on Mg2Si precipitation and Si spheroidization.* Journal of Alloys and Compounds, 2018. **755**: p. 100-107.

94. Dai, D., D. Gu, H. Zhang, J. Xiong, C. Ma, C. Hong, and R. Poprawe, *Influence of scan strategy and molten pool configuration on microstructures and tensile properties*

of selective laser melting additive manufactured aluminum based parts. Optics & Laser Technology, 2018. **99**: p. 91-100.

95. Simchi, A., *Direct laser sintering of metal powders: Mechanism, kinetics and microstructural features.* Materials Science and Engineering: A, 2006. **428**(1-2): p. 148-158.

96. Yasa, E., J. Deckers, J.-P. Kruth, M. Rombouts, and J. Luyten. *Investigation of sectoral scanning in selective laser melting*. in *ASME 2010 10th Biennial Conference on Engineering Systems Design and Analysis*. 2010. American Society of Mechanical Engineers Digital Collection.

97. Kruth, J.-P., J. Deckers, E. Yasa, and R. Wauthlé, *Assessing and comparing influencing factors of residual stresses in selective laser melting using a novel analysis method.* Proceedings of the Institution of Mechanical Engineers, Part B: Journal of Engineering Manufacture, 2012. **226**(6): p. 980-991.

98. Parry, L., I. A. Ashcroft, and R. D. Wildman, *Understanding the effect of laser scan strategy on residual stress in selective laser melting through thermo-mechanical simulation.* Additive Manufacturing, 2016. **12, Part A**: p. 1-15.

99. Lu, Y., S. Wu, Y. Gan, T. Huang, C. Yang, L. Junjie, and J. Lin, *Study on the microstructure, mechanical property and residual stress of SLM Inconel-718 alloy manufactured by differing island scanning strategy.* Optics & Laser Technology, 2015. **75**: p. 197-206.

100. Carter, L. N., C. Martin, P. J. Withers, and M. M. Attallah, *The influence of the laser scan strategy on grain structure and cracking behaviour in SLM powder-bed fabricated nickel superalloy.* Journal of Alloys and Compounds, 2014. **615**: p. 338-347.

101. Ma, L. and H. Bin, *Temperature and stress analysis and simulation in fractal scanning-based laser sintering.* The International Journal of Advanced Manufacturing Technology, 2006. **34**(9): p. 898-903.

102. Yang, J., H. Bin, X. Zhang, and Z. Liu, *Fractal scanning path generation and control system for selective laser sintering (SLS).* International Journal of Machine Tools and Manufacture, 2003. **43**(3): p. 293-300.

103. Catchpole-Smith, S., N. Aboulkhair, L. Parry, C. Tuck, I. Ashcroft, and A. Clare, *Fractal scan strategies for selective laser melting of 'unweldable'nickel superalloys.* Additive Manufacturing, 2017. **15**: p. 113-122.

104. Gibson, L. J., *Biomechanics of cellular solids.* Journal of Biomechanics, 2005. **38**(3): p. 377-399.

105. Gibson, L. J. and M. F. Ashby, *Cellular solids: structure and properties*. 1999: Cambridge university press.

106. Du Plessis, A., C. Broeckhoven, I. Yadroitsava, I. Yadroitsev, C. H. Hands, R. Kunju, and D. Bhate, *Beautiful and Functional: A Review of Biomimetic Design in Additive Manufacturing.* Additive Manufacturing, 2019. **27**: p. 408-427.

107. Johnson, D. E., C. M. Krutchen, and G. V. Sharps Jr, *Polymer foam process,* 1984, Patent number US4424287A

108. Howard, K. A., *Method for manufacturing expanded polystyrene foam components from used polystyrene materials,* 1993, Patent number US5217660A

109. Banhart, J., *Manufacturing routes for metallic foams.* Journal of Materials, 2000. **52**(12): p. 22-27.

110. Miyoshi, T., M. Itoh, S. Akiyama, and A. Kitahara, *ALPORAS aluminum foam: production process, properties, and applications.* Advanced Engineering Materials, 2000. **2**(4): p. 179-183.

111. Gu, X., J. Zhu, and W. Zhang, *The lattice structure configuration design for stereolithography investment casting pattern using topology optimization.* Rapid Prototyping Journal, 2012. **18**(5): p. 353-361.

112. Li, Q., E. Y. Chen, D. R. Bice, and D. C. Dunand, *Mechanical properties of cast Ti-6Al-4V lattice block structures.* Metallurgical and Materials Transactions A, 2008. **39**(2): p. 441-449.

113. Fonda, R., M. Scherr, A. Geltmacher, and K. Sharp, *Soldering a 3D wire lattice structure.* Journal of Materials Engineering and Performance, 2013. **22**(11): p. 3376-3380.

114. Sypeck, D. and H. Wadley, *Multifunctional microtruss laminates: textile synthesis and properties.* Journal of Materials Research, 2001. **16**(3): p. 890-897.

115. Lee, Y.-H., B.-K. Lee, I. Jeon, and K.-J. Kang, *Wire-woven bulk Kagome truss cores.* Acta Materialia, 2007. **55**(18): p. 6084-6094.

116. Shi, J., L. Zhu, L. Li, Z. Li, J. Yang, and X. Wang, *A TPMS-based method for modeling porous scaffolds for bionic bone tissue engineering.* Scientific Reports, 2018. **8**(1): p. 7395.

117. Maskery, I., L. Sturm, A. O. Aremu, A. Panesar, C. B. Williams, C. J. Tuck, R. D. Wildman, I. A. Ashcroft, and R. J. M. Hague, *Insights into the mechanical properties of several triply periodic minimal surface lattice structures made by polymer additive manufacturing.* Polymer, 2017.

118. Lim, T. S., C. S. Lee, and D. G. Lee, *Failure modes of foam core sandwich beams under static and impact loads.* Journal of Composite Materials, 2004. **38**(18): p. 1639-1662.

119. Yan, L., B. Yu, B. Han, C. Chen, Q. Zhang, and T. Lu, *Compressive strength and energy absorption of sandwich panels with aluminum foam-filled corrugated cores.* Composites Science and Technology, 2013. **86**: p. 142-148.

120. Xiong, J., R. Mines, R. Ghosh, A. Vaziri, L. Ma, A. Ohrndorf, H. J. Christ, and L. Wu, *Advanced micro-lattice materials.* Advanced Engineering Materials, 2015. **17**(9): p. 1253-1264.

121. Ataee, A., Y. Li, D. Fraser, G. Song, and C. Wen, *Anisotropic Ti-6Al-4V gyroid scaffolds manufactured by electron beam melting (EBM) for bone implant applications.* Materials & Design, 2018. **137**: p. 345-354.

122. Leary, M., M. Mazur, H. Williams, E. Yang, A. Alghamdi, B. Lozanovski, X. Zhang, D. Shidid, L. Farahbod-Sternahl, G. Witt, I. Kelbassa, P. Choong, M. Qian, and M. Brandt, *Inconel 625 lattice structures manufactured by selective laser melting (SLM): Mechanical properties, deformation and failure modes.* Materials & Design, 2018. **157**: p. 179-199.

123. Yan, C., L. Hao, A. Hussein, and D. Raymont, *Evaluations of cellular lattice structures manufactured using selective laser melting.* International Journal of Machine Tools and Manufacture, 2012. **62**: p. 32-38.

124. Maskery, I., N. T. Aboulkhair, A. O. Aremu, C. J. Tuck, and I. A. Ashcroft, *Compressive failure modes and energy absorption in additively manufactured double gyroid lattices.* Additive Manufacturing, 2017. **16**: p. 24-29.

125. Maskery, I., N. Aboulkhair, A. Aremu, C. Tuck, I. Ashcroft, R. Wildman, and R. Hague, *A mechanical property evaluation of graded density Al-Si10-Mg lattice*

structures manufactured by selective laser melting. Materials Science and Engineering: A, 2016.

126. Van Grunsven, W., E. Hernandez-Nava, G. Reilly, and R. Goodall, *Fabrication and mechanical characterisation of titanium lattices with graded porosity.* Metals, 2014. **4**(3): p. 401-409.

127. Al-Ketan, O., R. Rowshan, and R. K. Abu Al-Rub, *Topology-mechanical property relationship of 3D printed strut, skeletal, and sheet based periodic metallic cellular materials.* Additive Manufacturing, 2018. **19**: p. 167-183.

128. Challis, V. J., X. Xu, L. C. Zhang, A. P. Roberts, J. F. Grotowski, and T. B. Sercombe, *High specific strength and stiffness structures produced using selective laser melting.* Materials & Design, 2014. **63**: p. 783-788.

129. Jin, N., F. Wang, Y. Wang, B. Zhang, H. Cheng, and H. Zhang, *Failure and energy absorption characteristics of four lattice structures under dynamic loading.* Materials & Design, 2019. **169**: p. 107655.

130. Al-Saedi, D. S. J., S. H. Masood, M. Faizan-Ur-Rab, A. Alomarah, and P. Ponnusamy, *Mechanical properties and energy absorption capability of functionally graded F2BCC lattice fabricated by SLM.* Materials & Design, 2018. **144**: p. 32-44.

131. Chen, J. K., M. W. Wu, T. L. Cheng, and P. H. Chiang, *Continuous compression behaviors of selective laser melting Ti-6Al-4V alloy with cuboctahedron cellular structures.* Materials Science and Engineering: C, 2019. **100**: p. 781-788.

132. ASTM E1225-13, *Standard Test Method for Thermal Conductivity of Solids Using the Guarded-Comparative-Longitudinal Heat Flow Technique*. 2013, ASTM International.

133. ASTM E1530-11, *Standard Test Method for Evaluating the Resistance to Thermal Transmission of Materials by the Guarded Heat Flow Meter Technique*. 2016, ASTM International.

134. ASTM D7896-16, *Standard Test Method for Thermal Conductivity, Thermal Diffusivity, and Volumetric Heat Capacity of Engine Coolants and Related Fluids by Transient Hot Wire Liquid Thermal Conductivity Method*. 2019, ASTM International.

135. ASTM E1461-11, *Standard Test Method for Thermal Diffusivity by the Flash Method*. 2013, ASTM International.

136. ASTM E2584-14, *Standard Practice for Thermal Conductivity of Materials Using a Thermal Capacitance Slug Calorimeter*. 2014, ASTM International.

137. ASTM C518-17, *Standard Test Method for Steady-State Thermal Transmission Properties by Means of the Heat Flow Meter Apparatus*. 2017, ASTM International.

138. Thompson, A., N. Senin, C. Giusca, and R. Leach, *Topography of selectively laser melted surfaces: A comparison of different measurement methods.* CIRP Annals, 2017. **66**(1): p. 543-546.

139. Kirsch, K. L. and K. A. Thole, *Heat Transfer and Pressure Loss Measurements in Additively Manufactured Wavy Microchannels.* Journal of Turbomachinery, 2016. **139**(1): p. 011007-011007-9.

140. Kirsch, K. L. and K. A. Thole, *Pressure loss and heat transfer performance for additively and conventionally manufactured pin fin arrays.* International Journal of Heat and Mass Transfer, 2017. **108, Part B**: p. 2502-2513.

141. Marques, C. and K. W. Kelly, *Fabrication and Performance of a Pin Fin Micro Heat Exchanger.* Journal of Heat Transfer, 2004. **126**(3): p. 434-444.

142. Wong, M., S. Tsopanos, C. J. Sutcliffe, and I. Owen, *Selective laser melting of heat transfer devices.* Rapid Prototyping Journal, 2007. **13**(5): p. 291-297.

143. Wong, M., I. Owen, C. J. Sutcliffe, and A. Puri, *Convective heat transfer and pressure losses across novel heat sinks fabricated by Selective Laser Melting.* International Journal of Heat and Mass Transfer, 2009. **52**(1–2): p. 281-288.

144. Tian, J., T. Kim, T. J. Lu, H. P. Hodson, D. T. Queheillalt, D. J. Sypeck, and H. N. G. Wadley, *The effects of topology upon fluid-flow and heat-transfer within cellular copper structures.* International Journal of Heat and Mass Transfer, 2004. **47**(14–16): p. 3171-3186.

145. Joo, J. H., K. J. Kang, T. Kim, and T. J. Lu, *Forced convective heat transfer in all metallic wire-woven bulk Kagome sandwich panels.* International Journal of Heat and Mass Transfer, 2011. **54**(25–26): p. 5658-5662.

146. Kim, T., C. Y. Zhao, T. J. Lu, and H. P. Hodson, *Convective heat dissipation with lattice-frame materials.* Mechanics of Materials, 2004. **36**(8): p. 767-780.

147. Kim, T., H. P. Hodson, and T. J. Lu, *Fluid-flow and endwall heat-transfer characteristics of an ultralight lattice-frame material.* International Journal of Heat and Mass Transfer, 2004. **47**(6–7): p. 1129-1140.

148. Kim, T., H. Hodson, and T. Lu, *Pressure loss and heat transfer mechanisms in a lattice-frame structured heat exchanger.* Proceedings of the Institution of Mechanical Engineers, Part C: Journal of Mechanical Engineering Science, 2004. **218**(11): p. 1321-1336.

149. Kim, T., H. P. Hodson, and T. J. Lu, *Contribution of vortex structures and flow separation to local and overall pressure and heat transfer characteristics in an ultralightweight lattice material.* International Journal of Heat and Mass Transfer, 2005. **48**(19–20): p. 4243-4264.

150. Boyce, M. P., *Gas turbine engineering handbook.* 2011: Elsevier.

151. Giampaolo, T., *Gas turbine handbook: principles and practice*. 2002: Fairmont Press.

152. Han, J.-C., S. Dutta, and S. Ekkad, *Gas turbine heat transfer and cooling technology*. 2012: CRC press.

153. Cuta, J., C. Mcdonald, and A. Shekarriz, *Forced convection heat transfer in parallel channel array microchannel heat exchanger*. 1996: American Society of Mechanical Engineers.

154. Brandner, J. J., E. Anurjew, L. Bohn, E. Hansjosten, T. Henning, U. Schygulla, A. Wenka, and K. Schubert, *Concepts and realization of microstructure heat exchangers for enhanced heat transfer.* Experimental Thermal and Fluid Science, 2006. **30**(8): p. 801-809.

155. Shah, R. K. and D. P. Sekulic, *Fundamentals of heat exchanger design*. 2003: John Wiley & Sons.

156. Thulukkanam, K., *Heat exchanger design handbook.* 2013: CRC Press.

157. Mazur, Z., A. Luna-Ramirez, J. Juárez-Islas, and A. Campos-Amezcua, *Failure analysis of a gas turbine blade made of Inconel 738LC alloy.* Engineering Failure Analysis, 2005. **12**(3): p. 474-486.

158. Han, J.-C., *Turbine blade cooling studies at Texas A&M University: 1980-2004.* Journal of Thermophysics and Heat Transfer, 2006. **20**(2): p. 161-187.

159. Han, J.-C., *Recent studies in turbine blade cooling.* International Journal of Rotating Machinery, 2004. **10**(6): p. 443-457.

160. Lu, T. J., *Heat transfer efficiency of metal honeycombs.* International Journal of Heat and Mass Transfer, 1999. **42**(11): p. 2031-2040.

161. Wen, T., J. Tian, T. Lu, D. Queheillalt, and H. Wadley, *Forced convection in metallic honeycomb structures.* International Journal of Heat and Mass Transfer, 2006. **49**(19): p. 3313-3324.

162. Krishnan, S., D. Hernon, M. Hodes, J. Mullins, and A. M. Lyons, *Design of complex structured monolithic heat sinks for enhanced air cooling.* IEEE Transactions on Components, Packaging and Manufacturing Technology, 2012. **2**(2): p. 266-277.

163. Bhattacharya, A. and R. L. Mahajan, *Finned metal foam heat sinks for electronics cooling in forced convection.* Journal of Electronic Packaging, 2002. **124**(3): p. 155-163.

164. Bhattacharya, A., V. V. Calmidi, and R. L. Mahajan, *Thermophysical properties of high porosity metal foams.* International Journal of Heat and Mass Transfer, 2002. **45**(5): p. 1017-1031.

165. Hwang, J.-J. and C.-C. Lui, *Measurement of endwall heat transfer and pressure drop in a pin-fin wedge duct.* International Journal of Heat and Mass Transfer, 2002. **45**(4): p. 877-889.

166. Queheillalt, D. T., G. Carbajal, G. P. Peterson, and H. N. G. Wadley, *A multifunctional heat pipe sandwich panel structure.* International Journal of Heat and Mass Transfer, 2008. **51**(1–2): p. 312-326.

167. Smith, M., Z. Guan, and W. J. Cantwell, *Finite element modelling of the compressive response of lattice structures manufactured using the selective laser melting technique.* International Journal of Mechanical Sciences, 2013. **67**: p. 28-41.

168. Gu, S., T. J. Lu, and A. G. Evans, *On the design of two-dimensional cellular metals for combined heat dissipation and structural load capacity.* International Journal of Heat and Mass Transfer, 2001. **44**(11): p. 2163-2175.

169. Lu, T. J., *Thermal management of high power electronics with phase change cooling.* International Journal of Heat and Mass Transfer, 2000. **43**(13): p. 2245-2256.

170. Hopton, P. and J. Summers. *Enclosed liquid natural convection as a means of transferring heat from microelectronics to cold plates*. in *29th IEEE Semiconductor Thermal Measurement and Management Symposium*. 2013.

171. Eiland, R., J. Fernandes, M. Vallejo, D. Agonafer, and V. Mulay. *Flow Rate and inlet temperature considerations for direct immersion of a single server in mineral oil*. in *Fourteenth Intersociety Conference on Thermal and Thermomechanical Phenomena in Electronic Systems (ITherm)*. 2014.

172. Meng, X., J. Zhu, X. Wei, and Y. Yan, *Natural convection heat transfer of a straight-fin heat sink.* International Journal of Heat and Mass Transfer, 2018. **123**: p. 561-568.

173. Iyengar, M. and A. Bar-Cohen, *Design for manufacturability of SISE parallel plate forced convection heat sinks.* IEEE Transactions on Components and Packaging Technologies, 2001. **24**(2): p. 150-158.

174. Padture, N. P., M. Gell, and E. H. Jordan, *Thermal Barrier Coatings for Gas-Turbine Engine Applications.* Science, 2002. **296**(5566): p. 280-284.

175. Han, J.-C., *Fundamental Gas Turbine Heat Transfer.* Journal of Thermal Science and Engineering Applications, 2013. **5**(2): p. 021007-021007-15.

176. Pattnaik, S., D. B. Karunakar, and P. Jha, *Developments in investment casting process—a review.* Journal of Materials Processing Technology, 2012. **212**(11): p. 2332-2348.

177. Loeber, L., S. Biamino, U. Ackelid, S. Sabbadini, P. Epicoco, P. Fino, and J. Eckert. *Comparison of selective laser and electron beam melted titanium aluminides*. in *Proceedings of the Solid Freeform Fabrication Symposium*. 2011.

178. Kempen, K., B. Vrancken, L. Thijs, S. Buls, J. Van Humbeeck, and J.-P. Kruth. *Lowering thermal gradients in Selective Laser melting by pre-heating the baseplate*. in *Proceedings of the Solid Freeform Fabrication Symposium*. 2013.

179. Caprio, L., G. Chiari, A. Demir, and B. Previtali. *Development of Novel High Temperature Laser Powder Bed Fusion System for the Processing of Crack-Susceptible Alloys*. in *Proceedings of the Solid Freeform Fabrication Symposium*. 2018.

180. Leung, C. L. A., R. Tosi, E. Muzangaza, S. Nonni, P. J. Withers, and P. D. Lee, *Effect of preheating on the thermal, microstructural and mechanical properties of*

selective electron beam melted Ti-6Al-4V components. Materials & Design, 2019. **174**: p. 107792.

181. Schneider, C. A., W. S. Rasband, and K. W. Eliceiri, *NIH Image to ImageJ: 25 years of image analysis.* Nature Methods, 2012. **9**(7): p. 671-675.

182. Schindelin, J., I. Arganda-Carreras, E. Frise, V. Kaynig, M. Longair, T. Pietzsch, S. Preibisch, C. Rueden, S. Saalfeld, B. Schmid, J.-Y. Tinevez, D. J. White, V. Hartenstein, K. Eliceiri, P. Tomancak, and A. Cardona, *Fiji: an open-source platform for biological-image analysis.* Nature Methods, 2012. **9**(7): p. 676-682.

183. ASTM E92-17, *Standard Test Methods for Vickers Hardness and Knoop Hardness of Metallic Materials*. 2017, ASTM International.

184. ASTM B213-13, *Standard Test Methods for Flow Rate of Metal Powders Using the Hall Flowmeter Funnel*. 2013, ASTM International.

185. Haynes International, *H-3009E HASTELLOY X alloy - Principal Features*. 2019.

186. Carter, L. N., K. Essa, and M. M. Attallah, *Optimisation of selective laser melting for a high temperature Ni-superalloy.* Rapid Prototyping Journal, 2015. **21**(4): p. 423-432.

187. Hilbert, D., *Ueber die stetige Abbildung einer Line auf ein Flächenstück.* Mathematische Annalen, 1891. **38**(3): p. 459-460.

188. Mandelbrot, B., *Fractals: form, chance and dimension*. Vol. 1. 1979: WH Freeman & Co.

189. Mitchell, T. P., R. Sanderson, and B. G. Dance. *Electron beam welding of crack sensitive nickel super alloy MAR-M-002*. in *Proceedings of the Materials Science Forum*. 2007.

190. Ploshikhin, V., A. Prikhodovsky, M. Makhutin, A. Ilin, and H.-W. Zoch, *Integrated mechanical-metallurgical approach to modeling of solidification cracking in welds*, in *Hot cracking phenomena in welds*. 2005, Springer. p. 223-244.

191. Kou, S., *Solidification and liquation cracking issues in welding.* Journal of Materials, 2003. **55**(6): p. 37-42.

192. Divya, V. D., R. Muñoz-Moreno, O. M. D. M. Messé, J. S. Barnard, S. Baker, T. Illston, and H. J. Stone, *Microstructure of selective laser melted CM247LC nickel-*

based superalloy and its evolution through heat treatment. Materials Characterization, 2016. **114**: p. 62-74.

193. Cloots, M., P. J. Uggowitzer, and K. Wegener, *Investigations on the microstructure and crack formation of IN738LC samples processed by selective laser melting using Gaussian and doughnut profiles.* Materials & Design, 2016. **89**: p. 770-784.

194. Zhong, M., H. Sun, W. Liu, X. Zhu, and J. He, *Boundary liquation and interface cracking characterization in laser deposition of Inconel 738 on directionally solidified Ni-based superalloy.* Scripta Materialia, 2005. **53**(2): p. 159-164.

195. Yadroitsev, I., P. Bertrand, and I. Smurov, *Parametric analysis of the selective laser melting process.* Applied Surface Science, 2007. **253**(19): p. 8064-8069.

196. Sun, M.-S. M., J. J. Beaman, and J. W. Barlow. *Parametric analysis of the selective laser sintering process*. in *Proceedings of the Solid Freeform Fabrication Symposium*. 1990.

197. Carter, L. N., X. Wang, N. Read, R. Khan, M. Aristizabal, K. Essa, and M. M. Attallah, *Process optimisation of selective laser melting using energy density model for nickel based superalloys.* Materials Science and Technology, 2016. **32**(7): p. 657-661.

198. Newton, L., N. Senin, and R. Leach, *Focus variation measurement of metal additively manufactured surfaces*, in *2018 ASPE and euspen Summer Topical Meeting Advancing Precision in Additive Manufacturing*. 2018.

199. Newton, L., N. Senin, C. Gomez, R. Danzl, F. Helmli, L. Blunt, and R. Leach, *Areal topography measurement of metal additive surfaces using focus variation microscopy.* Additive Manufacturing, 2019. **25**: p. 365-389.

200. Hansen, N., *Hall–Petch relation and boundary strengthening.* Scripta Materialia, 2004. **51**(8): p. 801-806.

201. Tomus, D., Y. Tian, P. A. Rometsch, M. Heilmaier, and X. Wu, *Influence of post heat treatments on anisotropy of mechanical behaviour and microstructure of Hastelloy-X parts produced by selective laser melting.* Materials Science and Engineering: A, 2016. **667**: p. 42-53.

202. Sadd, M. H., *Elasticity: theory, applications, and numerics*. 2009: Academic Press.

203. Xiao, H. and H. Liu. *An empirical formula of mean specific heat capacity of ideal gases*. in *Proceedings of the 2015 International Conference on Education, Management, Information and Medicine*. 2015.

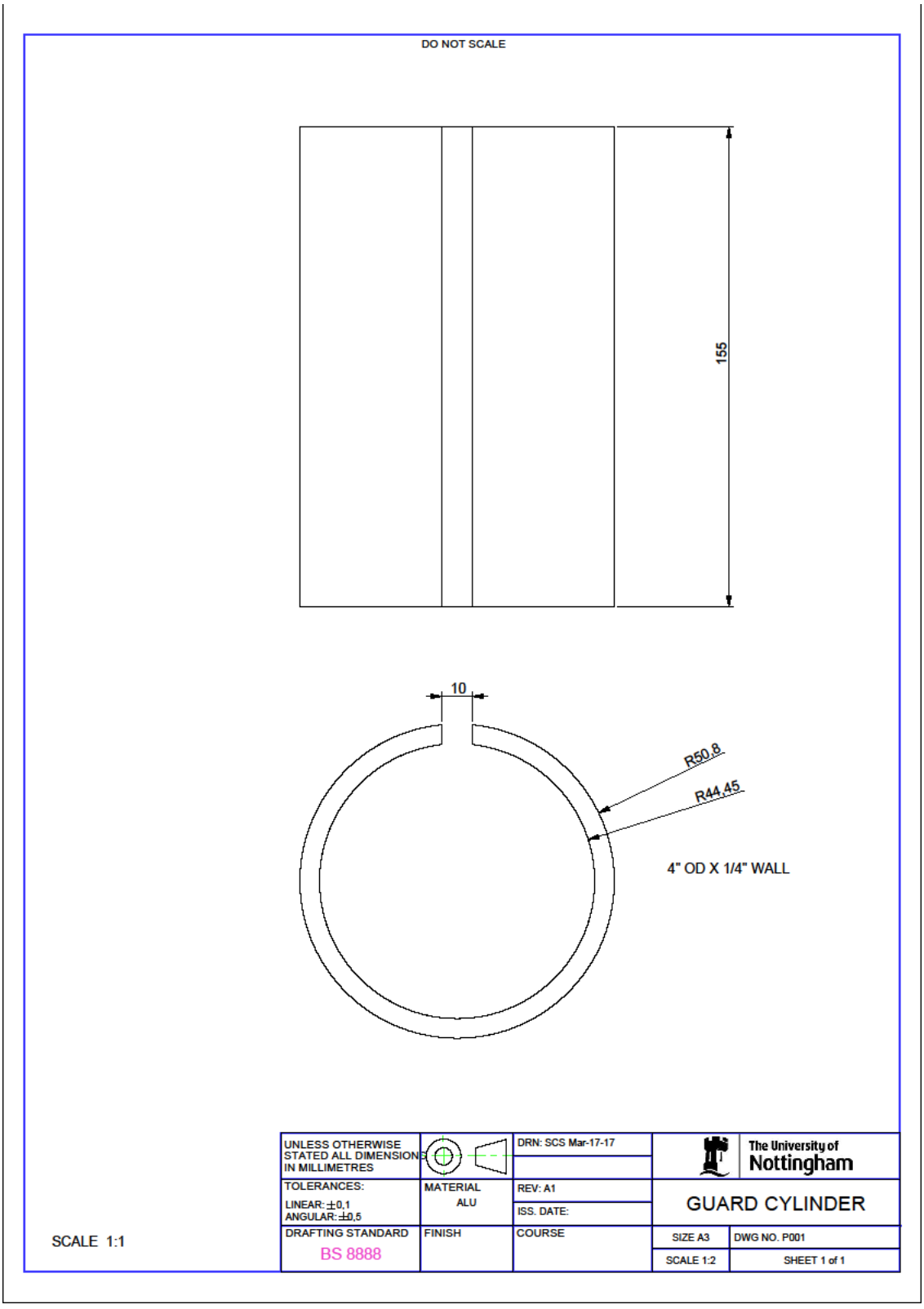
204. Han, J. C., Y. M. Zhang, and C. P. Lee, *Augmented Heat Transfer in Square Channels With Parallel, Crossed, and V-Shaped Angled Ribs.* Journal of Heat Transfer, 1991. **113**(3): p. 590-596.

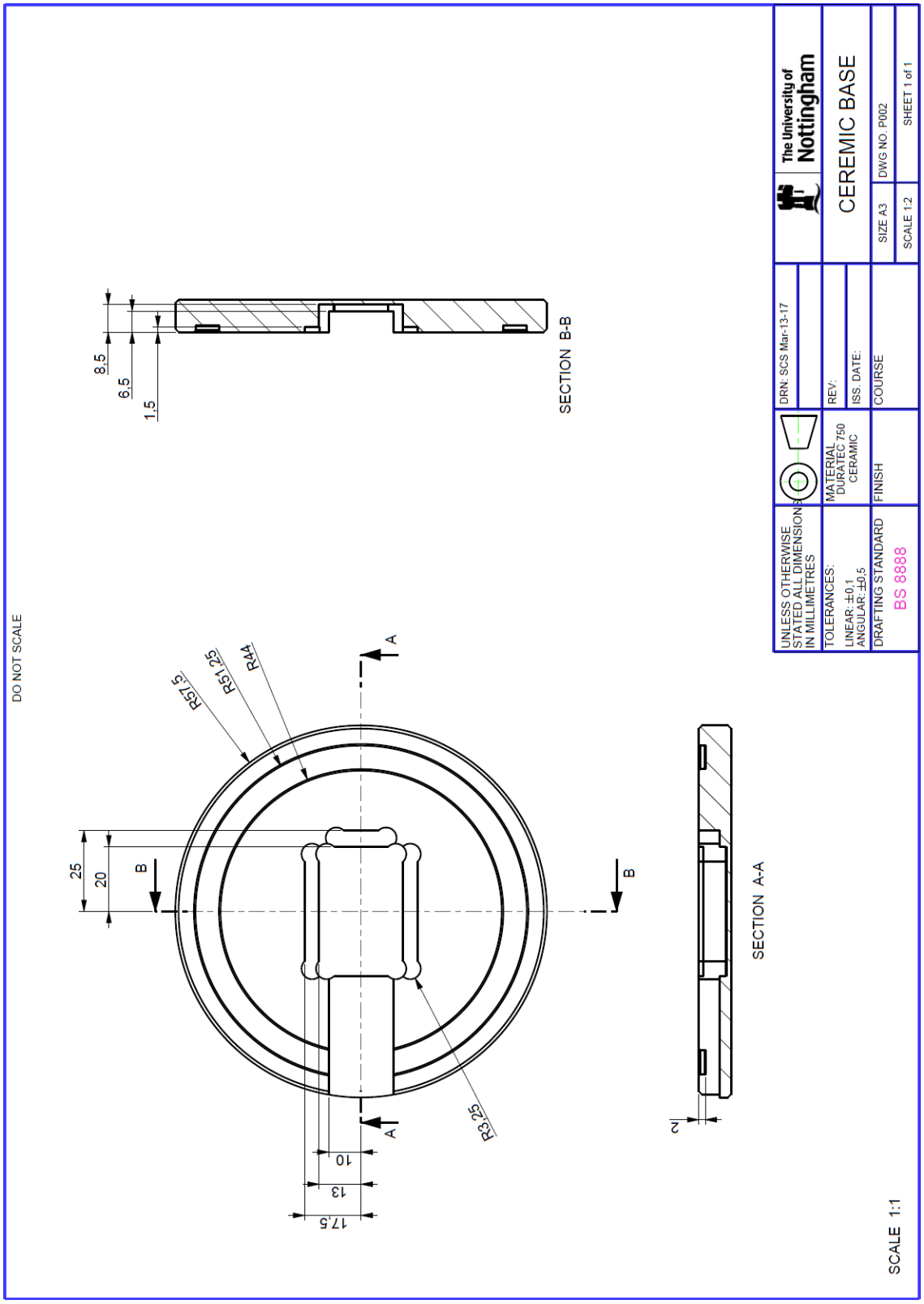
205. Horbach, T., A. Schulz, and H. J. Bauer, *Trailing Edge Film Cooling of Gas Turbine Airfoils—External Cooling Performance of Various Internal Pin Fin Configurations.* Journal of Turbomachinery, 2011. **133**(4): p. 041006-041006-9.

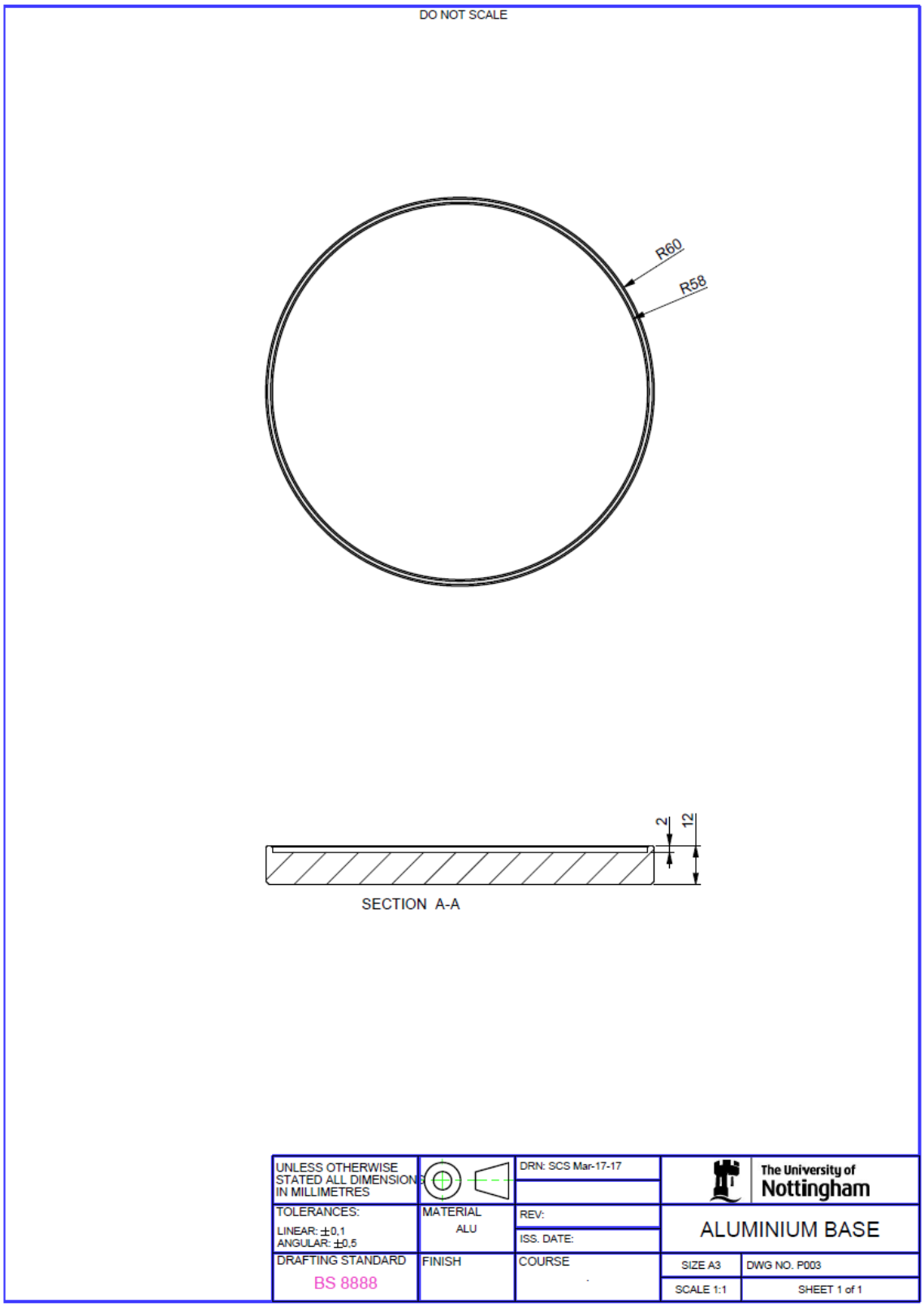
APPENDIX

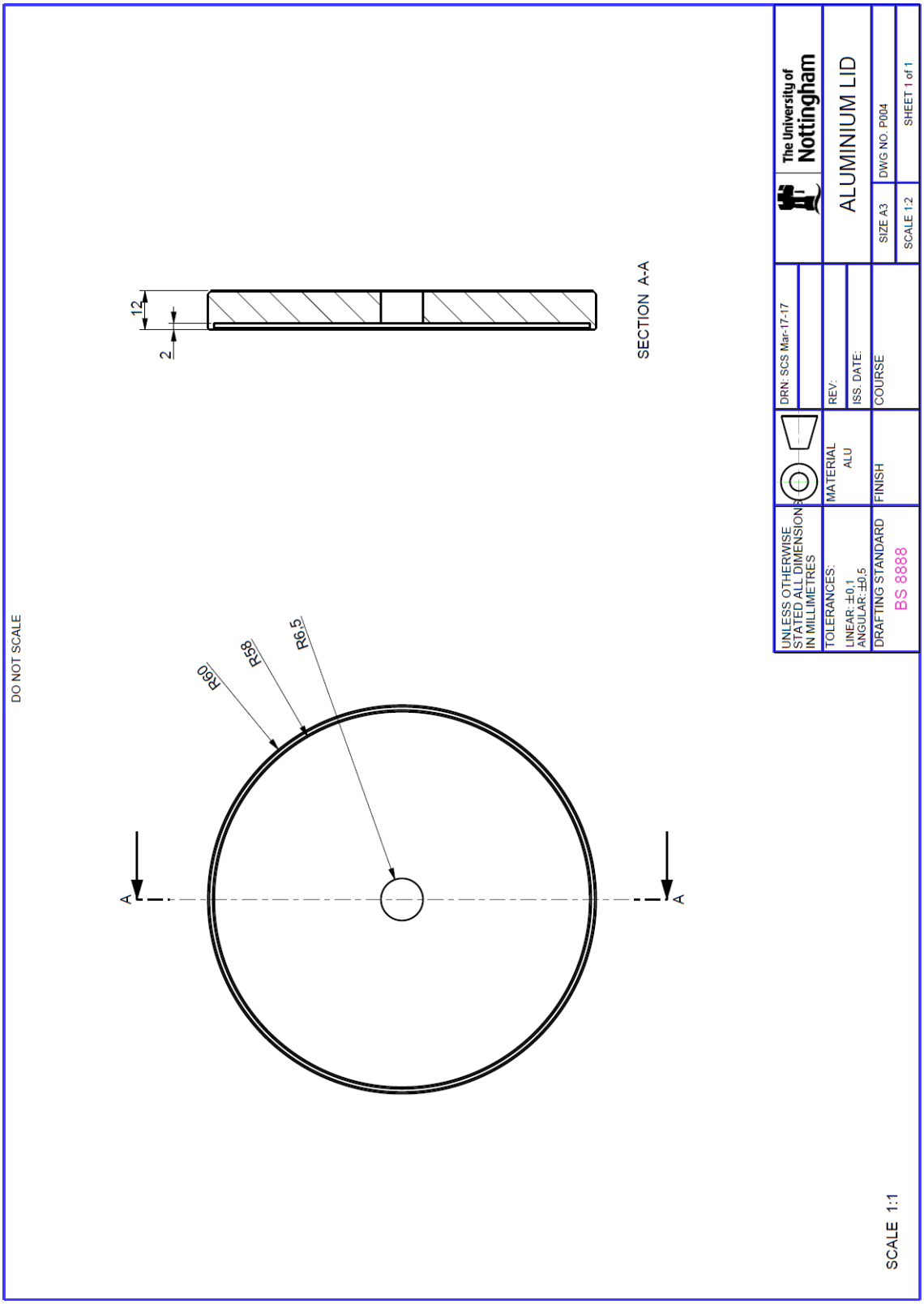
SECTION 1 – CONDUCTIVE HEAT TRANSFER APPARATUS

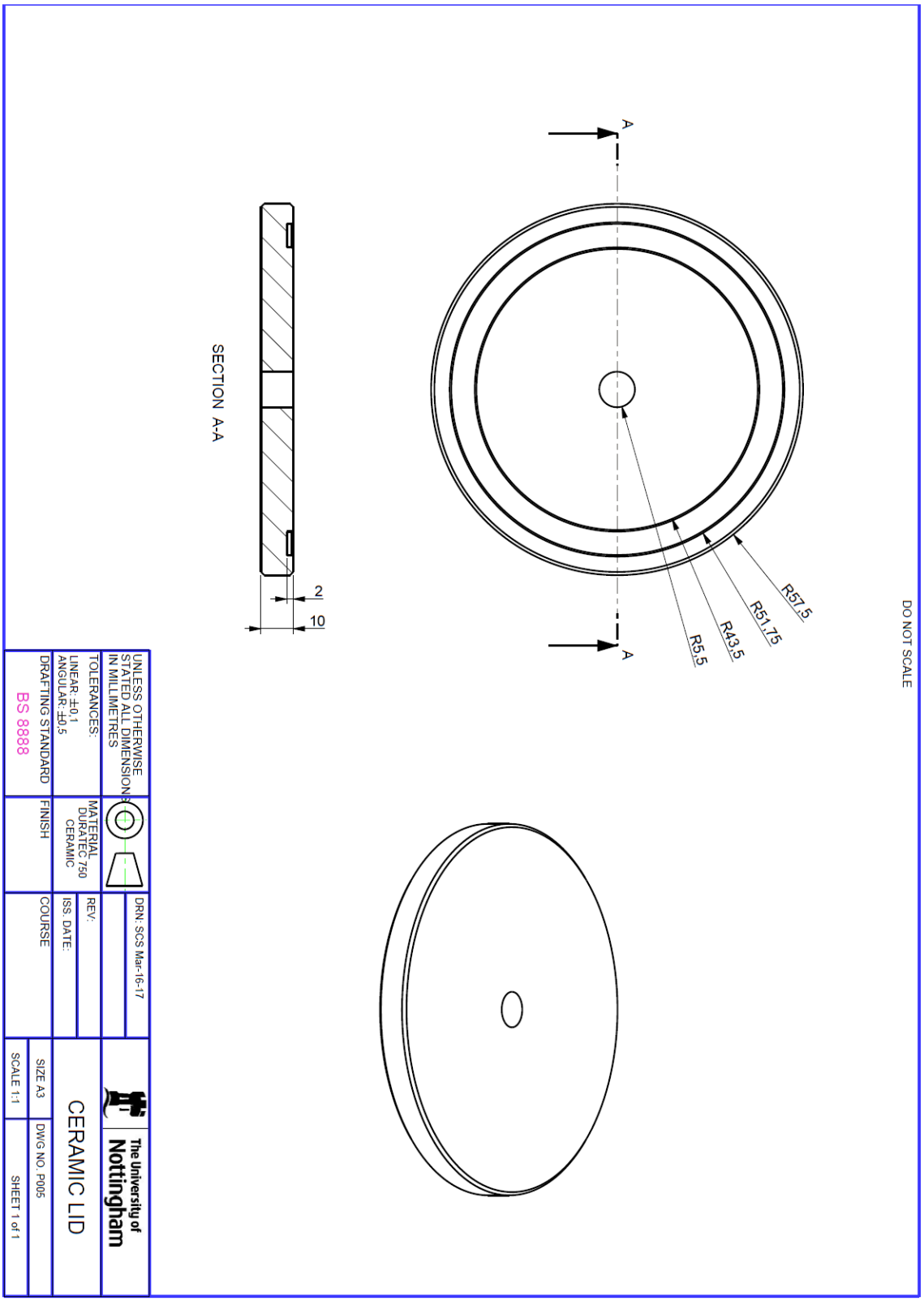
This section provides the set of engineering drawings required to replicate the conductive heat transfer apparatus.

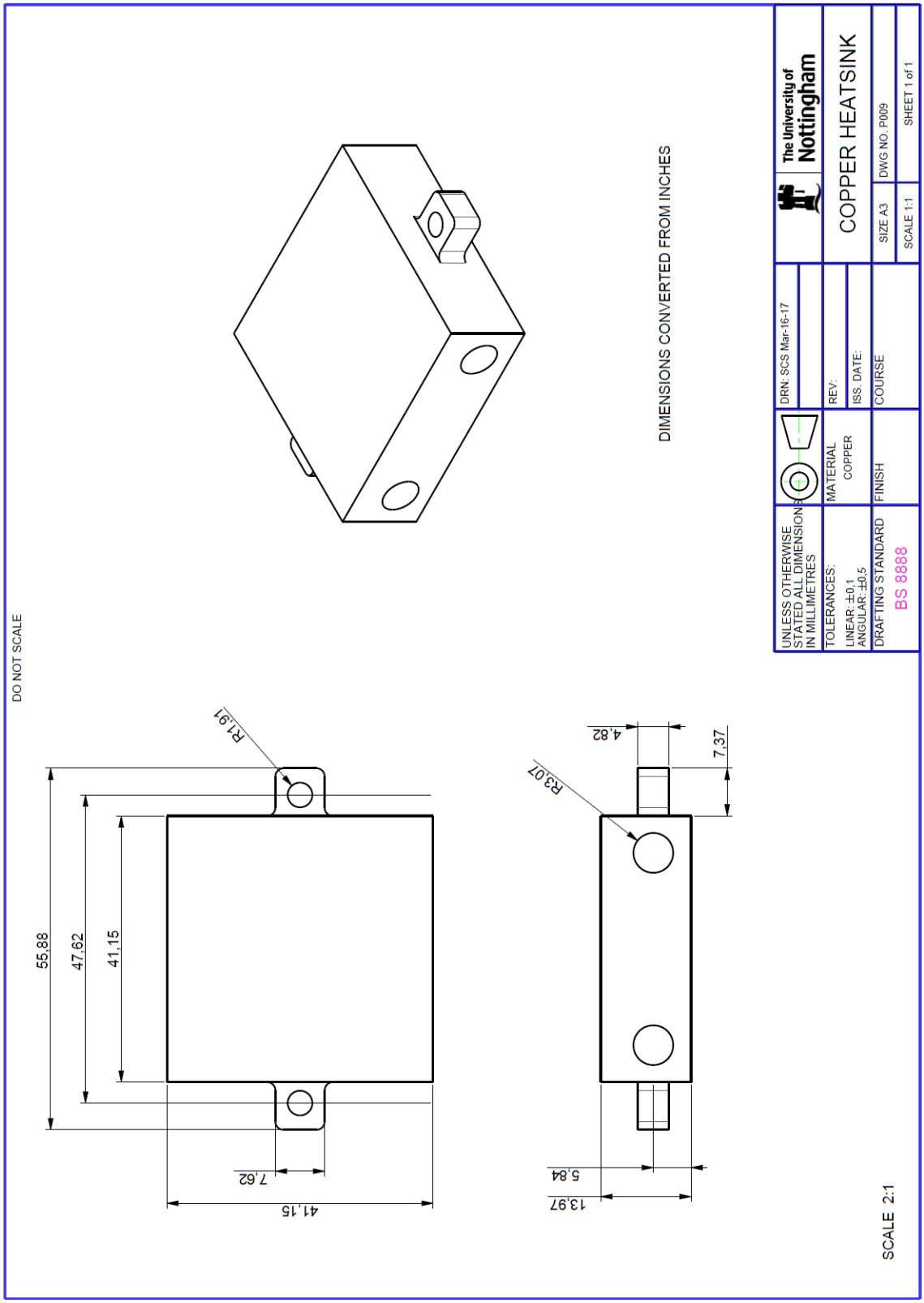


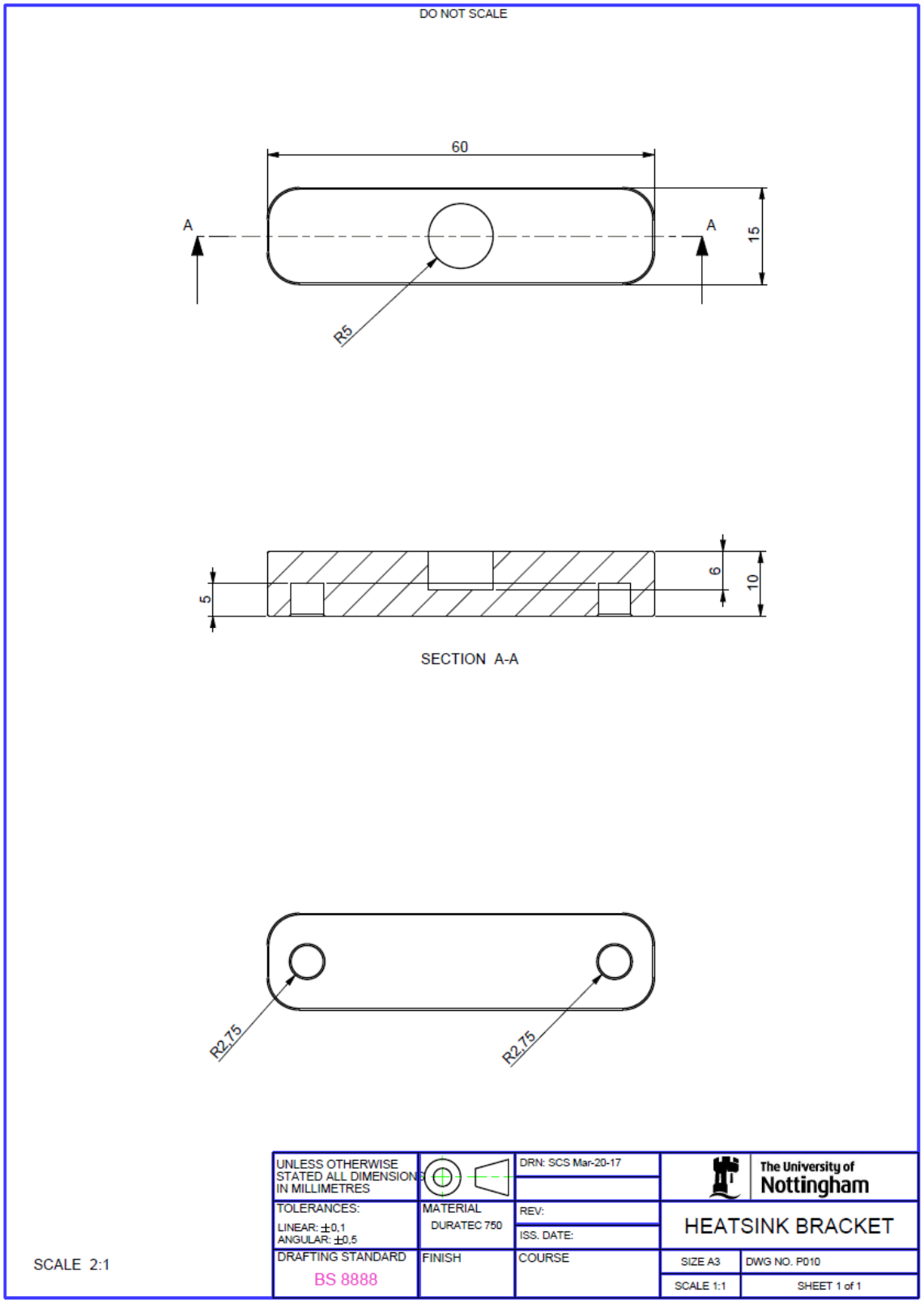

DO NOT SCALE
SECTION B-B
8.5
6.5
1.5
R57.5
R51.25
R44
A
B
25
20
10
13
17.5
R3.25
SECTION A-A
2
SCALE 1:1
UNLESS OTHERWISE STATED ALL DIMENSIONS IN MILLIMETRES
TOLERANCES:
LINEAR: ±0.1
ANGULAR: ±0.5
DRAFTING STANDARD
BS 8888
MATERIAL
DURATEC 750
CERAMIC
FINISH
DRN: SCS Mar-13-17
REV:
ISS. DATE:
COURSE
The University of Nottingham
CEREMIC BASE
SIZE A3
SCALE 1:2
DWG NO. P002
SHEET 1 of 1


DO NOT SCALE
R60
R58
2
12
SECTION A-A
UNLESS OTHERWISE STATED ALL DIMENSIONS IN MILLIMETRES
TOLERANCES:
LINEAR: ±0,1
ANGULAR: ±0,5
DRAFTING STANDARD
BS 8888
MATERIAL
ALU
FINISH
DRN: SCS Mar-17-17
REV:
ISS. DATE:
COURSE
The University of Nottingham
ALUMINIUM BASE
SIZE A3
DWG NO. P003
SCALE 1:1
SHEET 1 of 1


DO NOT SCALE
SECTION A-A
12
2
R60
R58
R6.5
A
A
SCALE 1:1
UNLESS OTHERWISE STATED ALL DIMENSIONS IN MILLIMETRES
TOLERANCES:
LINEAR: ±0.1
ANGULAR: ±0.5
DRAFTING STANDARD
BS 8888
MATERIAL
ALU
FINISH
DRN: SCS Mar-17-17
REV:
ISS. DATE:
COURSE
The University of Nottingham
ALUMINIUM LID
SIZE A3
DWG NO. P004
SCALE 1:2
SHEET 1 of 1

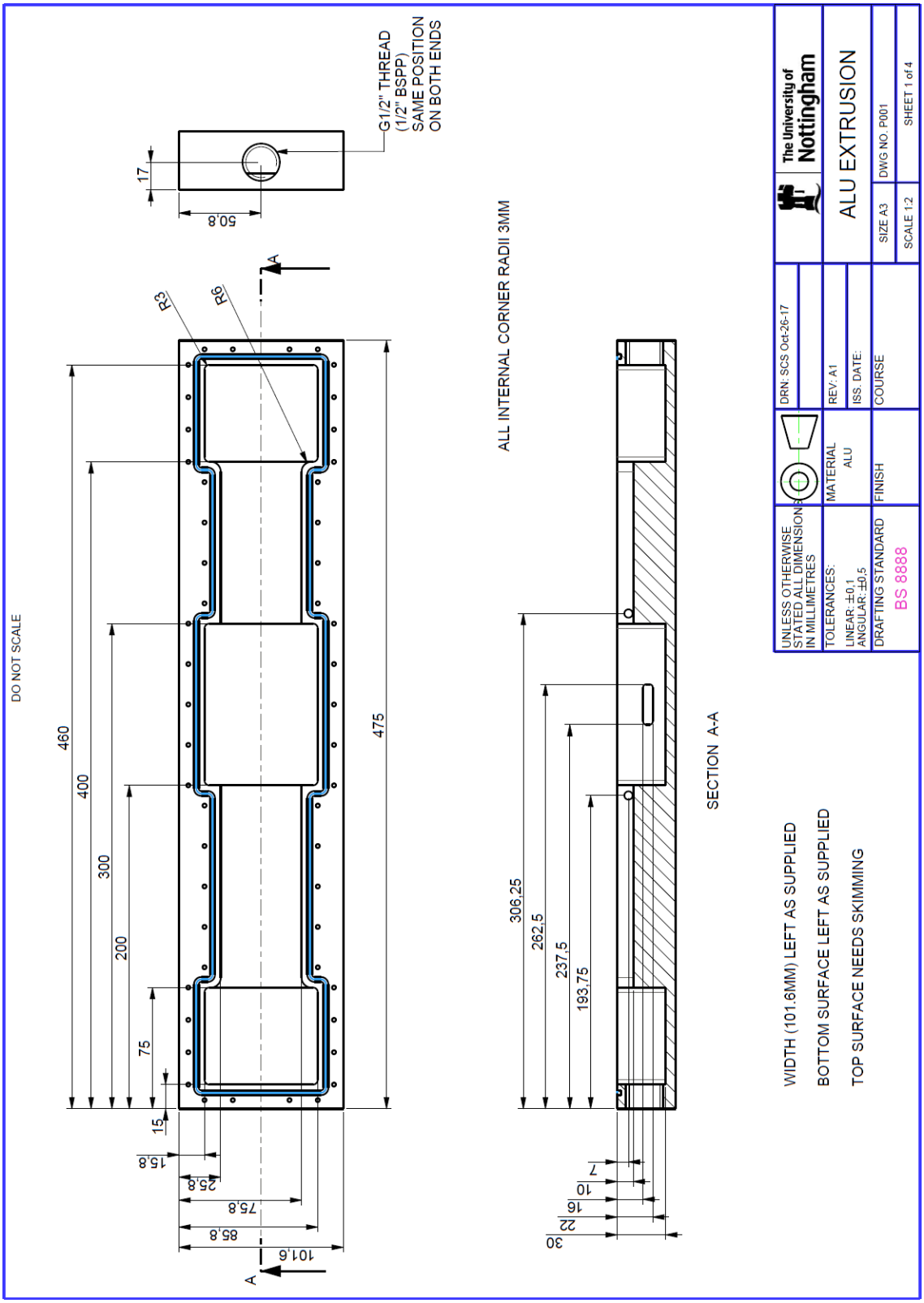

SECTION A-A
2
10
A
A
R57.5
R51.75
R43.5
R5.5
DO NOT SCALE
UNLESS OTHERWISE STATED ALL DIMENSIONS IN MILLIMETRES
DRN: SCS Mar-16-17
TOLERANCES:
LINEAR: ±0.1
ANGULAR: ±0.5
MATERIAL
DURATEC 750 CERAMIC
REV:
ISS. DATE:
FINISH
COURSE
DRAFTING STANDARD
BS 8888
The University of Nottingham
CERAMIC LID
SIZE A3
DWG NO. P005
SCALE 1:1
SHEET 1 of 1

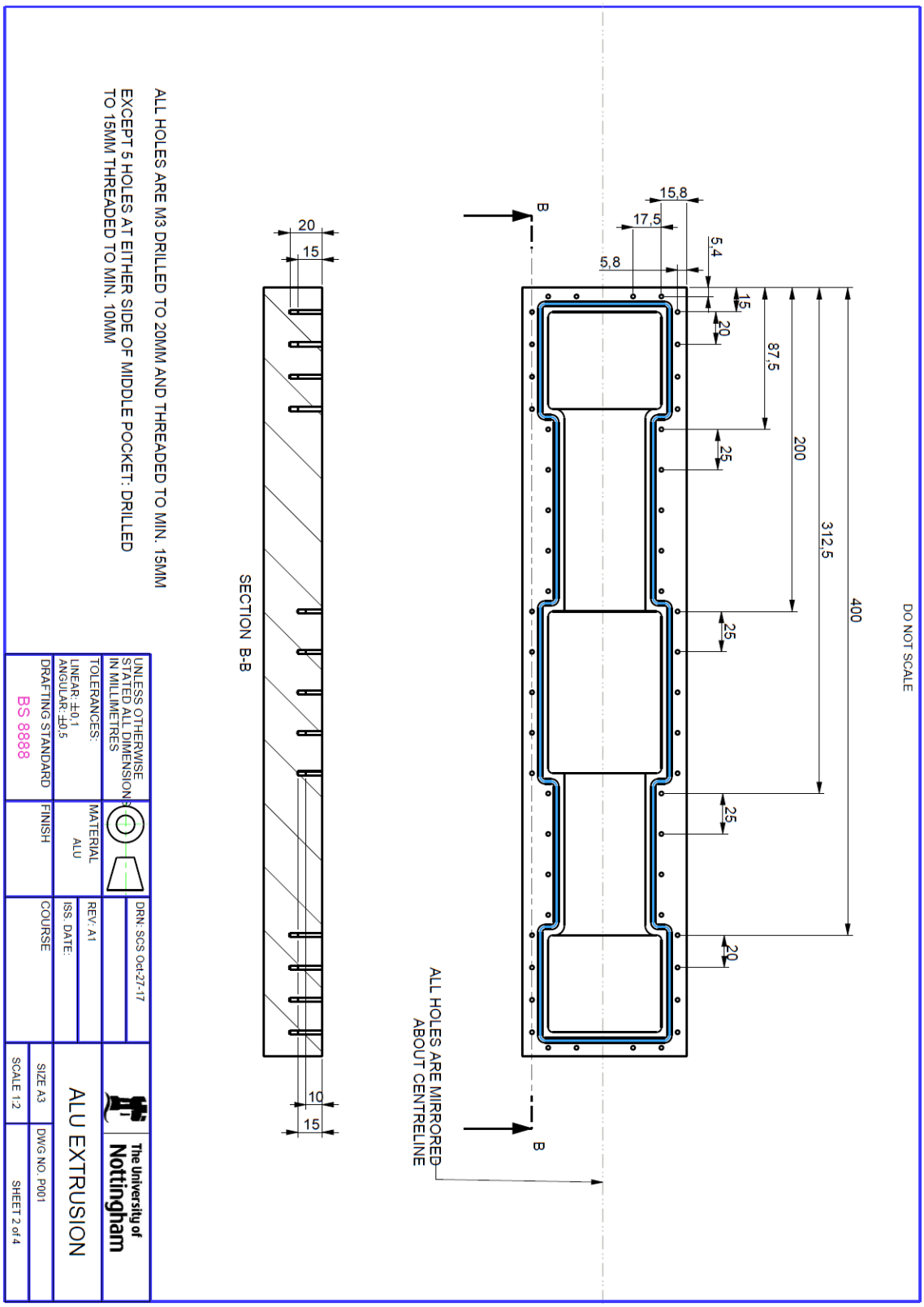

DO NOT SCALE
DIMENSIONS CONVERTED FROM INCHES
UNLESS OTHERWISE STATED ALL DIMENSIONS IN MILLIMETRES
TOLERANCES:
LINEAR: ±0.1
ANGULAR: ±0.5
DRAFTING STANDARD
BS 8888
MATERIAL
COPPER
FINISH
DRN: SCS Mar-16-17
REV:
ISS. DATE:
COURSE
The University of Nottingham
COPPER HEATSINK
SIZE A3
DWG NO. P009
SCALE 1:1
SHEET 1 of 1
R1.91
55.88
47.62
41.15
7.62
41.15
R3.07
4.82
7.37
5.84
13.97
SCALE 2:1

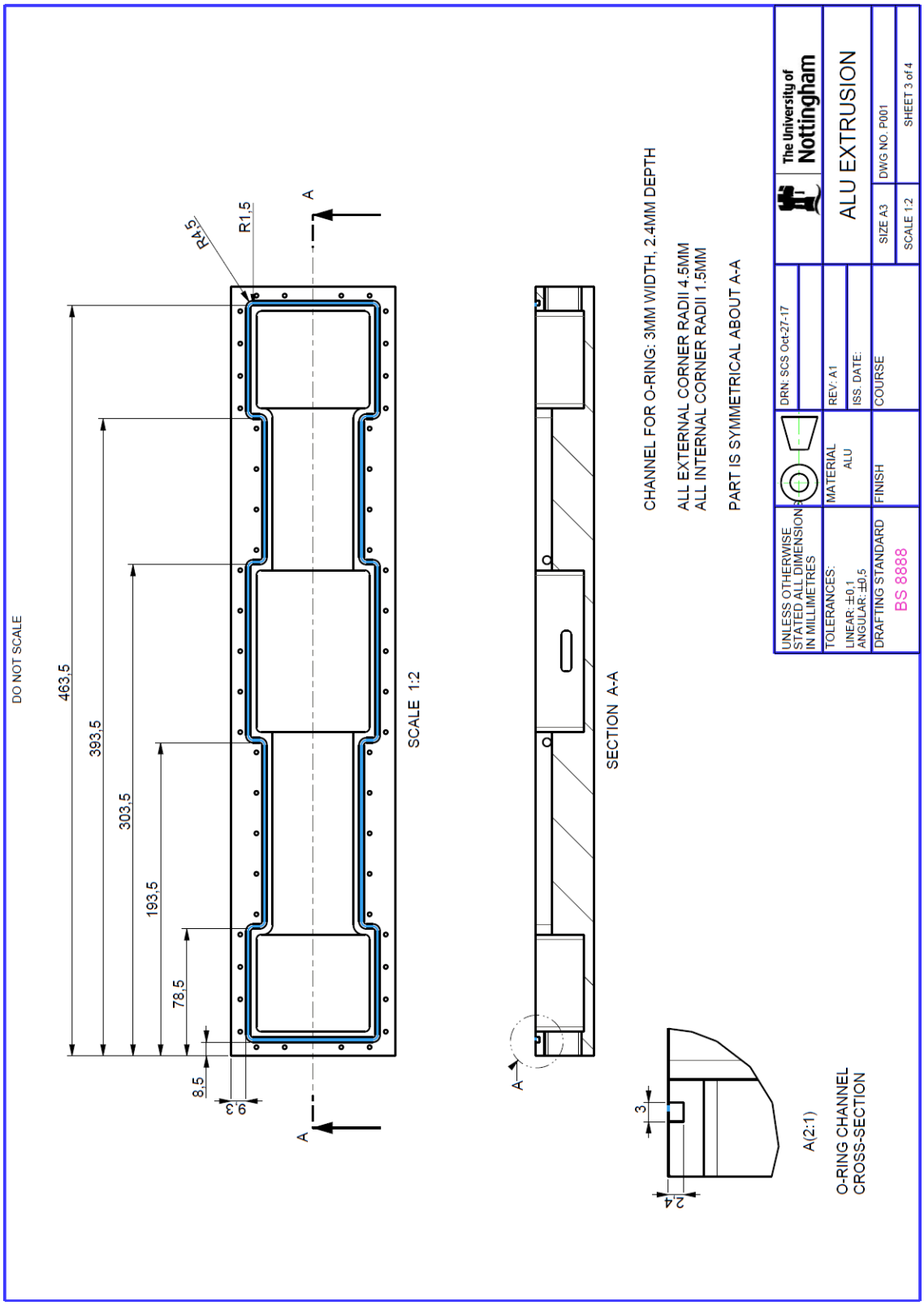

DO NOT SCALE
60
A
A
15
R5
6
10
5
SECTION A-A
R2.75
R2.75
SCALE 2:1
UNLESS OTHERWISE STATED ALL DIMENSIONS IN MILLIMETRES
TOLERANCES:
LINEAR: ±0,1
ANGULAR: ±0,5
DRAFTING STANDARD
BS 8888
MATERIAL
DURATEC 750
FINISH
DRN: SCS Mar-20-17
REV:
ISS. DATE:
COURSE
The University of Nottingham
HEATSINK BRACKET
SIZE A3
DWG NO. P010
SCALE 1:1
SHEET 1 of 1

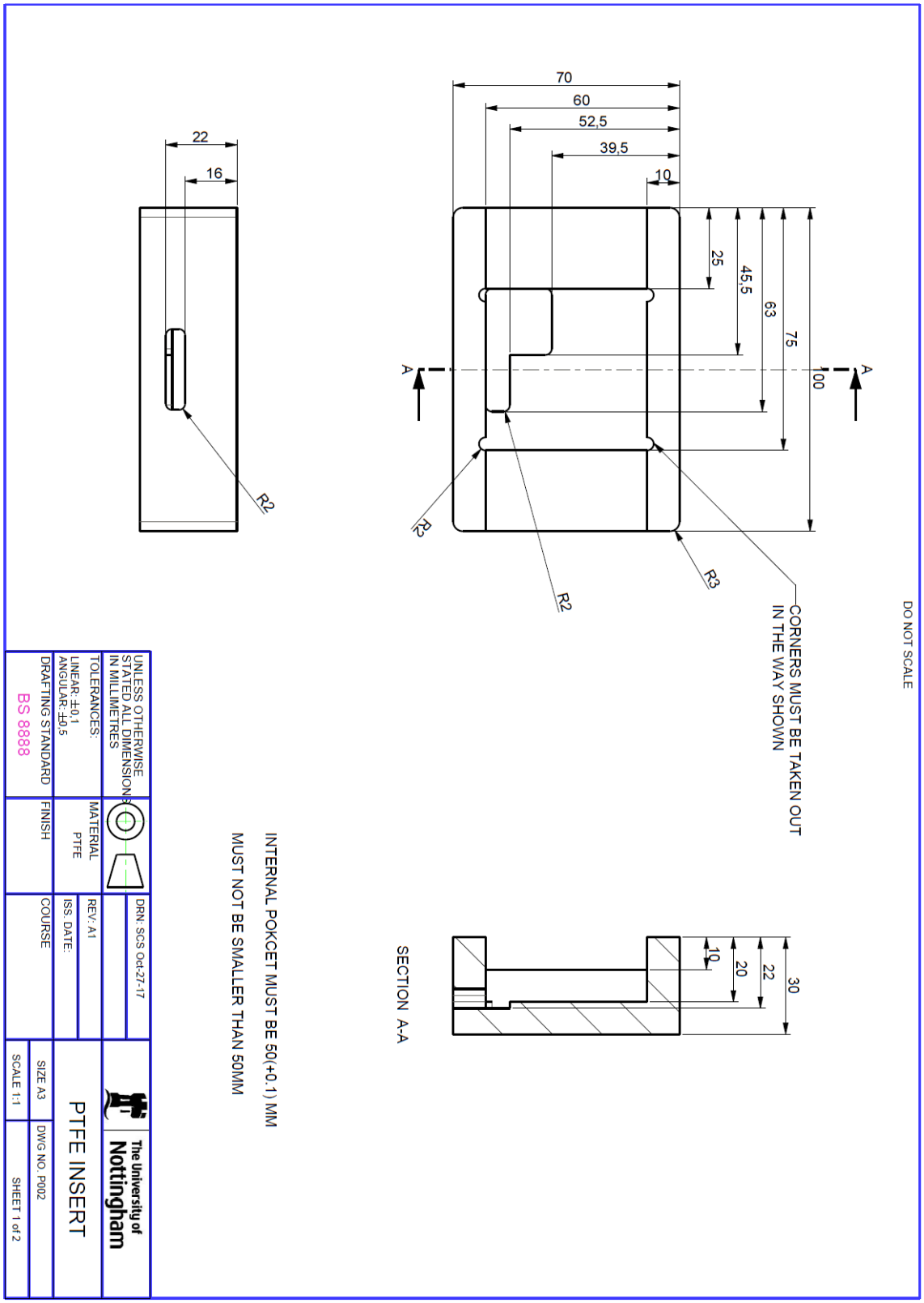
SECTION 2 – CONVECTIVE HEAT TRANSFER APPARATUS

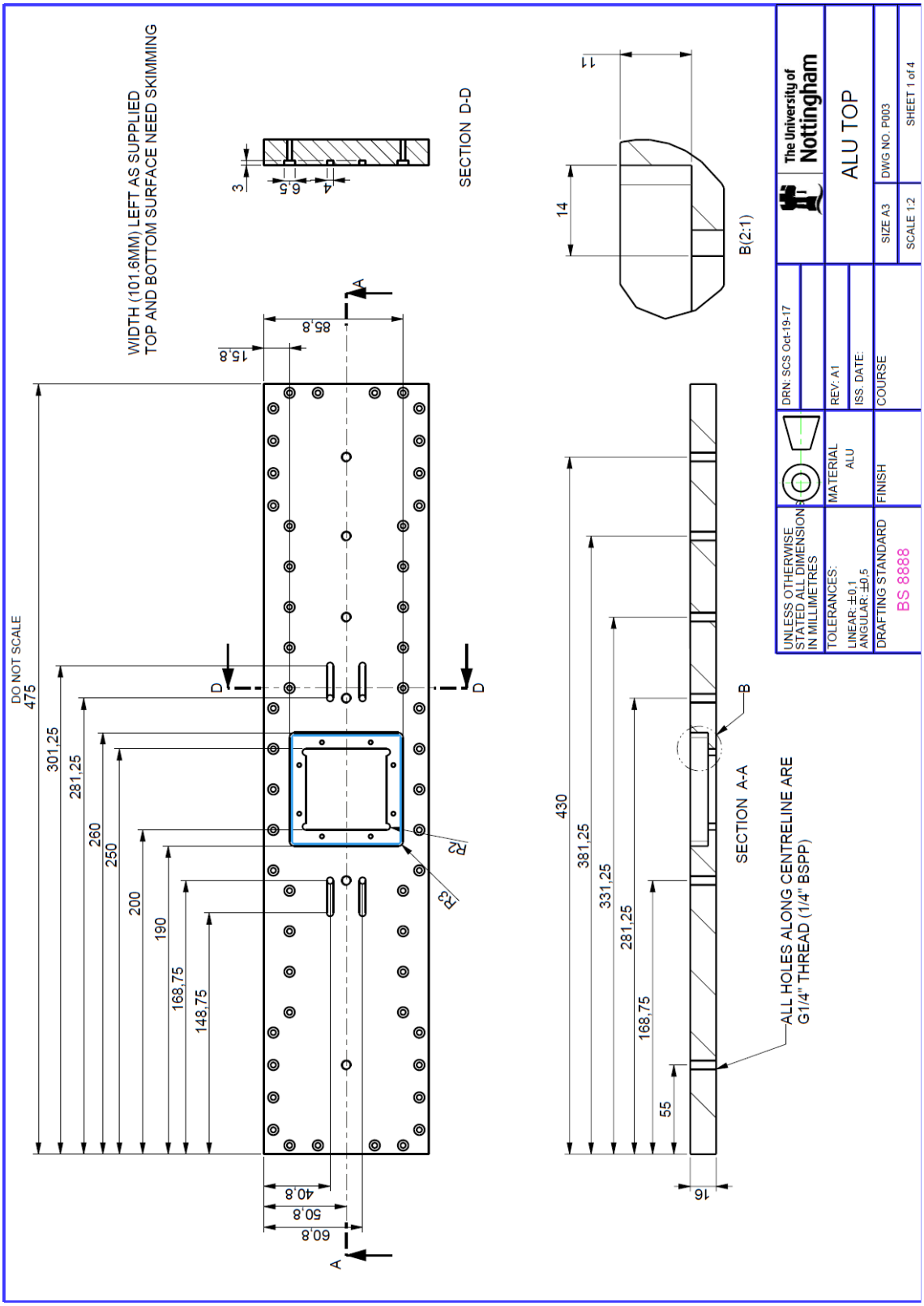
This section provides the set of engineering drawings required to replicate the convective heat transfer apparatus.

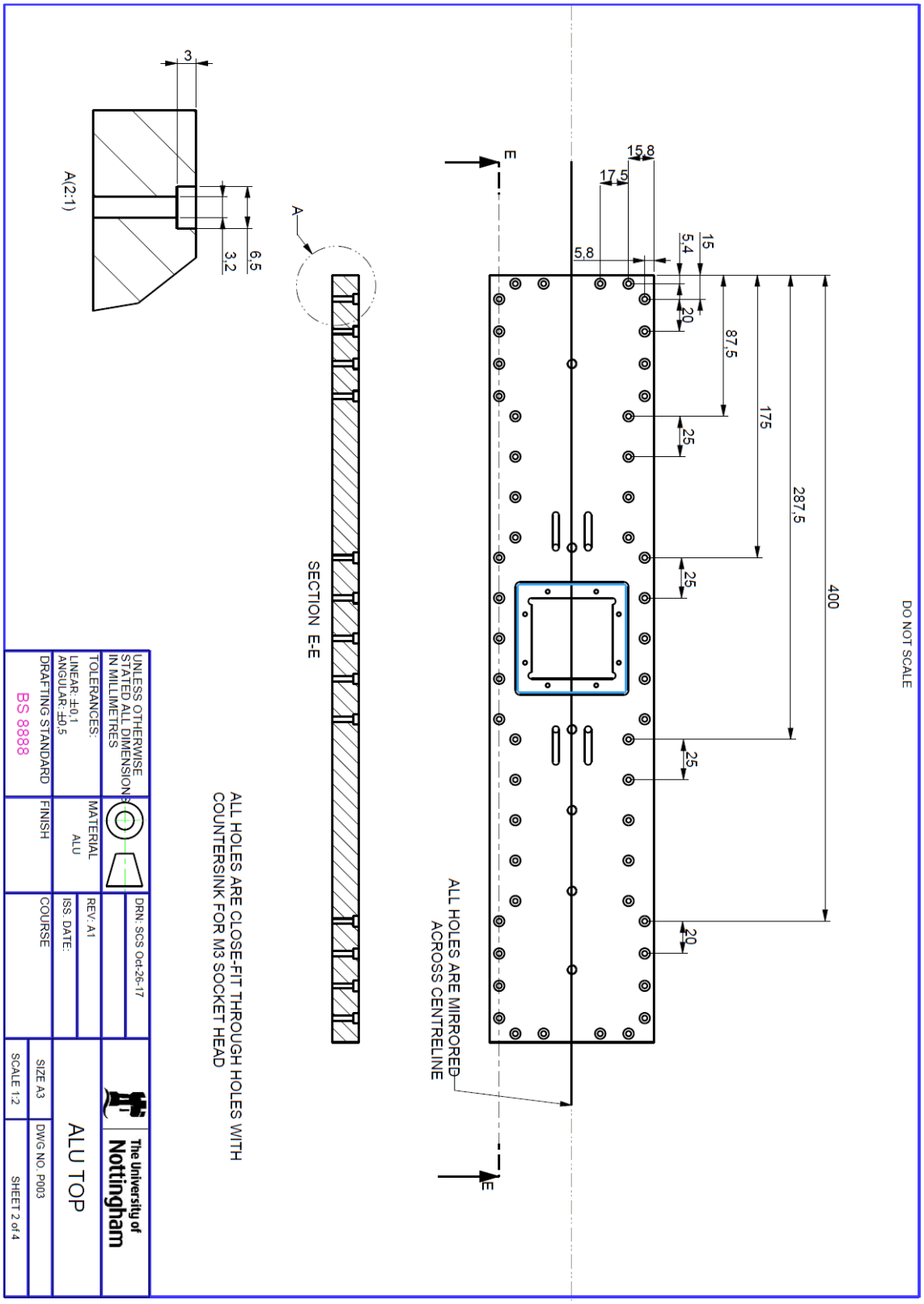


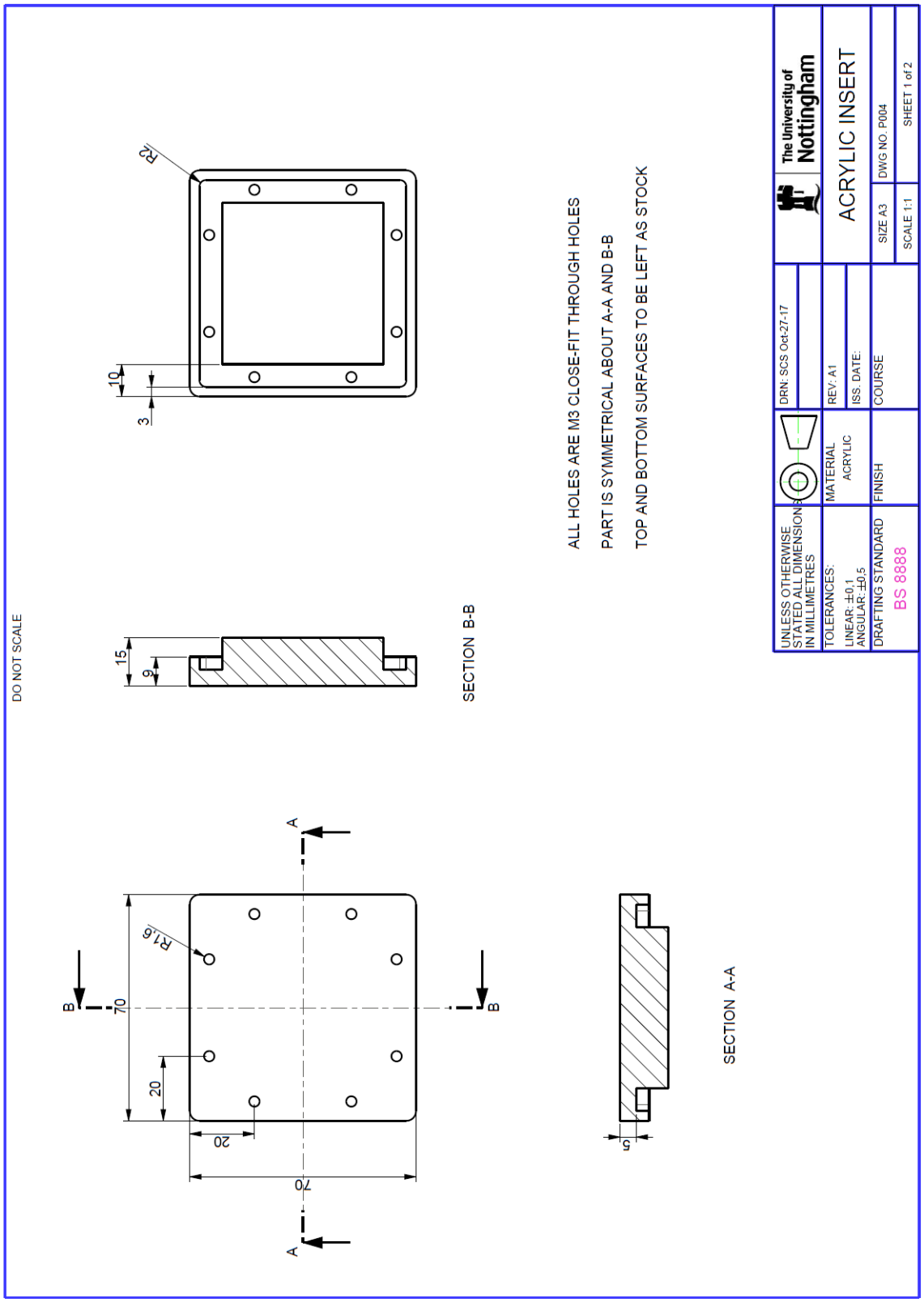

DO NOT SCALE
400
312.5
200
87.5
15
20
25
25
25
20
15.8
17.5
5.8
5.4
B
B
ALL HOLES ARE MIRRORED ABOUT CENTRELINE
SECTION B-B
20
15
10
15
ALL HOLES ARE M3 DRILLED TO 20MM AND THREADED TO MIN. 15MM
EXCEPT 5 HOLES AT EITHER SIDE OF MIDDLE POCKET: DRILLED TO 15MM THREADED TO MIN. 10MM
UNLESS OTHERWISE STATED ALL DIMENSIONS IN MILLIMETRES
TOLERANCES: LINEAR: ±0.1 ANGULAR: ±0.5
DRAFTING STANDARD BS 8888
MATERIAL ALU
FINISH
COURSE
DRN: SCS Oct-27-17
REV: A1
ISS. DATE:
The University of Nottingham
ALU EXTRUSION
SIZE A3
DWG NO. P001
SCALE 1:2
SHEET 2 of 4


DO NOT SCALE
463,5
393,5
303,5
193,5
78,5
8,5
9,3
R4,5
R1,5
A
A
SCALE 1:2
SECTION A-A
A
CHANNEL FOR O-RING: 3MM WIDTH, 2.4MM DEPTH
ALL EXTERNAL CORNER RADII 4.5MM
ALL INTERNAL CORNER RADII 1.5MM
PART IS SYMMETRICAL ABOUT A-A
3
2,4
A(2:1)
O-RING CHANNEL
CROSS-SECTION
UNLESS OTHERWISE STATED ALL DIMENSIONS IN MILLIMETRES
TOLERANCES:
LINEAR: ±0.1
ANGULAR: ±0.5
DRAFTING STANDARD
BS 8888
DRN: SCS Oct-27-17
MATERIAL
ALU
FINISH
REV: A1
ISS. DATE:
COURSE
The University of Nottingham
ALU EXTRUSION
SIZE A3
SCALE 1:2
DWG NO. P001
SHEET 3 of 4


70
60
52,5
39,5
10
25
45,5
63
75
100
A
A
R2
R2
R3
22
16
R2
CORNERS MUST BE TAKEN OUT
IN THE WAY SHOWN
DO NOT SCALE
SECTION A-A
10
20
22
30
INTERNAL POKCET MUST BE 50(+0.1) MM
MUST NOT BE SMALLER THAN 50MM
UNLESS OTHERWISE
STATED ALL DIMENSIONS
IN MILLIMETRES
TOLERANCES:
LINEAR: ±0.1
ANGULAR: ±0.5
DRAFTING STANDARD
BS 8888
MATERIAL
PTFE
FINISH
COURSE
DRN: SCS Oct-27-17
REV: A1
ISS. DATE:
The University of
Nottingham
PTFE INSERT
SIZE A3
DWG NO. P002
SCALE 1:1
SHEET 1 of 2


WIDTH (101.6MM) LEFT AS SUPPLIED
TOP AND BOTTOM SURFACE NEED SKIMMING
SECTION D-D
B(2:1)
DO NOT SCALE
475
301.25
281.25
260
250
200
190
168.75
148.75
85.8
15.8
40.8
50.8
60.8
R2
R3
430
381.25
331.25
281.25
168.75
55
16
SECTION A-A
ALL HOLES ALONG CENTRELINE ARE
G1/4" THREAD (1/4" BSPP)
The University of Nottingham
ALU TOP
DRN: SCS Oct-19-17
REV: A1
ISS. DATE:
COURSE
SIZE A3
DWG NO: P003
SCALE 1:2
SHEET 1 of 4
UNLESS OTHERWISE STATED ALL DIMENSIONS IN MILLIMETRES
TOLERANCES:
LINEAR: ±0.1
ANGULAR: ±0.5
MATERIAL
ALU
FINISH
DRAFTING STANDARD
BS 8888


DO NOT SCALE
15.8
17.5
15
5.4
5.8
20
87.5
175
287.5
400
25
25
25
20
E
E
ALL HOLES ARE MIRRORED ACROSS CENTRELINE
A
SECTION E-E
3
6.5
3.2
A(2:1)
ALL HOLES ARE CLOSE-FIT THROUGH HOLES WITH COUNTERSINK FOR M3 SOCKET HEAD
UNLESS OTHERWISE STATED ALL DIMENSIONS IN MILLIMETRES
TOLERANCES:
LINEAR: ±0.1
ANGULAR: ±0.5
DRAFTING STANDARD
BS 8888
MATERIAL
ALU
FINISH
REV: A1
ISS. DATE:
COURSE
DRN: SCS Oct-26-17
The University of Nottingham
ALU TOP
SIZE A3
DWG NO. P003
SCALE 1:2
SHEET 2 of 4


DO NOT SCALE
R2
10
3
15
9
SECTION B-B
ALL HOLES ARE M3 CLOSE-FIT THROUGH HOLES
PART IS SYMMETRICAL ABOUT A-A AND B-B
TOP AND BOTTOM SURFACES TO BE LEFT AS STOCK
A
B
R1.6
70
20
20
70
A
B
5
SECTION A-A
UNLESS OTHERWISE STATED ALL DIMENSIONS IN MILLIMETRES
TOLERANCES:
LINEAR: ±0.1
ANGULAR: ±0.5
DRAFTING STANDARD
BS 8888
MATERIAL
ACRYLIC
FINISH
DRN: SCS Oct-27-17
REV: A1
ISS. DATE:
COURSE
The University of Nottingham
ACRYLIC INSERT
SIZE A3
DWG NO. P004
SCALE 1:1
SHEET 1 of 2

DO NOT SCALE
ITEM
DWG or PART NO.
DESCRIPTION
MATERIAL
QTY
1 P001 ALU EXTRUSION ALU 1
2 P002 PTFE INSERT PTFE 1
3 P003 ALU TOP ALU 1
4 P004 ACRYLIC INSERT ACRYLIC 1
(2) FITS WITHIN (1) - LOCATIONAL CLEARANCE FIT
(4) FITS WITHIN (3) - SLIDING FIT
TOLERANCE ON INDIVIDUAL COMPONENTS NOT IMPORTANT PROVIDING THEY ASSEMBLE WITH ABOVE FITS
(2) HAS SPECIFIC FIT FOR INTERNAL POCKET - PLEASE SEE DRW002 (DRAWING FOR P002)
UNLESS OTHERWISE STATED ALL DIMENSIONS IN MILLIMETRES
DRN: SCS Nov-06-17
The University of Nottingham
TOLERANCES:
LINEAR: ±0.1
ANGULAR: ±0.5
MATERIAL
REV:A1
ISS. DATE: 06/11/2017
CONVECTIVE RIG ASSEMBLY
DRAFTING STANDARD
BS 8888
FINISH
COURSE
SIZE A3
DWG NO. D010
SCALE 1:4
SHEET 1 of 1